Barriers and impurity transport in tokamak's plasmas

Guillaume Lo-Cascio

Barrières et transport des impuretés dans les plasmas de Tokamak

Thèse

présentée et soutenue publiquement le 29 septembre 2023
pour l'obtention du titre de

Docteur de l'Université de Lorraine

Mention : Physique. Spécialité : Physique des plasmas

par

Guillaume Lo-Cascio

Composition du jury

Rapporteurs:	Mme. Pascale Hennequin	Directrice de recherche CNRS - LPP, Ecole polytechnique
	M. Peter Beyer	Professeur des universités, PIIM, Aix-Marseille Université
Examinateurs:	M. Guilhem Dif-Pradalier	Chercheur CEA - HDR, IRFM, CEA Cadarache
Président du jury:	M. Stéphane Heuraux	Professeur des universités, IJL, Université de Lorraine
Directeur:	M. Etienne Gravier	Professeur des universités, IJL, Université de Lorraine
Co-directeur:	M. Thierry Réveillé	Maitre de conférences, IJL Université de Lorraine
Invité:	M. Maxime Lesur	Maitre de conférences - HDR, IJL Université de Lorraine

Institut Jean Lamour | UMR CNRS 7198, Nancy, France
Université de Lorraine

Remerciements

Premièrement, je souhaiterais remercier les membres du jury Pascale Hennequin, Peter Beyer, Guilhem Dif-Pradalier et Stéphane Heuraux d'avoir accepté les rôles de rapporteurs et d'examinateurs de mon travail de thèse. Vos retours ont été précieux et les discussions que nous avons eues durant ma soutenance ont permis d'éclaircir certains points critiques de mes résultats.

J'aimerais aussi très vivement remercier Etienne Gravier et Thierry Réveillé de m'avoir fait confiance pour réaliser cette thèse, j'ai bien conscience de la chance que j'ai eu de travailler avec vous. Vous m'avez beaucoup apporté durant ces trois années, que ce soit humainement ou professionnellement. Merci pour votre patience et votre aide pendant les moments de doute qui ont pu avoir lieu durant cette thèse, votre guidance et vos conseils avisés m'ont permis de finir dans les temps et avec la forme ces trois années de recherches.

Merci infiniment à Maxime Lesur, Xavier Garbet et Yanick Sarazin d'avoir supporté des réunions de deux heures toutes les trois semaines, d'avoir relu de (très) nombreuses fois cet article qui semblait interminable, et surtout d'avoir toujours eu la patience de donner des explications claires et limpides aux questions auxquelles je n'avais pas de réponse. J'ai énormément apprécié de travailler avec vous, et je ne doute pas que nos chemins se recroisent à l'avenir.

Merci énormément à Kyungtak, tu as été un pilier très important dans la réussite de ma thèse, pour tous les conseils et les informations que tu m'as prodigué mais aussi le temps conséquent que tu as consacré aux corrections de mes manuscrits. Ton aide a été cruciale, et j'espère un jour pouvoir te rendre la pareille.

J'aimerais aussi prendre le temps de remercier tous les membres de l'équipe 107, Stéphane (lucky-LOC, maitre des jeux de mots), Frédéric, Jérôme, Eric, Daniele, Anne-Sophie, Juvert, Louis et Nicolas, avec qui j'ai partagé de très bons moments que je ne suis pas près d'oublier.

Merci aussi à Alejandro, ami et collègue avec qui j'ai partagé un bureau et des idées pendant trois ans, et qui a toujours été là lorsque j'avais besoin d'un avis éclairé sur un point de physique qui me dérangeait. Merci aussi pour tous ces débats et discussions endiablés sur les films et jeux du moment, ça a été un réel plaisir.

Anil my dear friend, this part will be in english just for you. Thank you for all the moments we shared, for the discussions we had and trips we made. You are a great researcher but also a great singer (and photographer, you really are doing everything aren't you ?) and I cannot wait to go to Garching with you.

Merci aussi à Luigui et Sarah, vous avez toujours été une source de positivité pour moi par votre enthousiasme et bonne humeur.

Merci Timothé d'avoir apporté un peu de fraicheur pendant ma dernière année de thèse, ça a été un réel plaisir de t'initier à GYSELA, et je suis sûr que l'on continuera à être en contact dans le futur.

Merci ***Maxence***, je ne sais pas ***quoi*** dire.

Evidemment, je remercie tous mes amis que j'ai rencontrés à l'IJL et au bad-

minton avec qui j'ai partagé des moments difficilement oubliable; Jade, Thibaut, Baptiste, JB, Victorien, Killian, Loris, Nathan, Maryam, Adèle, Anna, Agathe, Antoine, Clovis, Corentin(s), Quentin, Clélia, Pierre, Azise, Omer, Amel, Juàn, Victor, Marine, Hélène, Nico, Mauricio, Sébastien(s), Thomas, Alberto, Jude, Akilan, Jon, Valentin et Tobias. Je ne sais pas si j'ai réussi à citer tout le monde, mais vous avez toujours été là pour me soutenir, merci pour tout.

Merci à mes proches, Maxime, Maxence, Arnaud, Paulin, Axel, Laëtitia, Bérenger, Lucie, Lucas, vous n'imaginez pas à quel point vous avez été important durant cette thèse, vous m'avez supporté dans les pires moments tout en en créant des inoubliables, et je vous en suis éternellement reconnaissant.

Sans oublier ma famille, mes parents et mon frère qui m'ont supporté durant toutes mes études pour enfin les finir après neuves longues années, je vous dois beaucoup.

Et enfin, car ça devient un peu long, j'aimerais dire humblement "merci pour tout" à Héloïse, qui a toujours été là tout au long de cette thèse pour m'entendre râler sur des équations trop compliquées ou un supercalculateur capricieux. Tu aurais mérité que ton nom figure sur tous mes travaux, mais j'aurais été accusé d'augmenter artificiellement ton H-index. Tout aurait été beaucoup plus difficile et déplaisant sans toi, mais surtout personne n'aurait pu m'aider à finir toutes ces tartiflettes.

Contents

Résumé

Introduction

La fusion nucléaire est le processus qui anime le plasma de cœur des étoiles et consiste à fusionner des noyaux légers, typiquement des isotopes de l'hydrogène, en un noyau plus lourd comme l'hélium. Le déficit de masse engendré via ce type réaction donne en sortie une quantité d'énergie importante, le tout sans émettre de gaz à effet de serre. Cette réaction de fusion via un confinement gravitationnel est impossible à effectuer sur Terre et il est donc nécessaire de trouver un autre moyen de confiner un plasma à plusieurs millions de Kelvin si l'on souhaite exploiter cette source d'énergie.

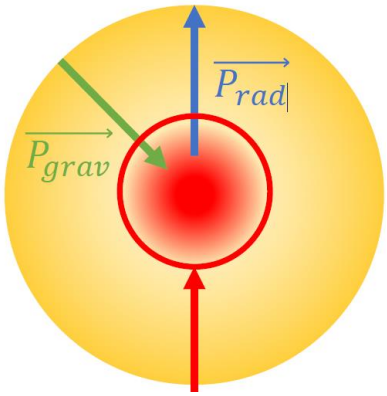

Figure 1: Equilibre entre pression gravitationnelle et pression radiative due aux réactions de fusion nucléaire dans une étoile. La zone encerclée en rouge correspond à la région où les conditions permettant la fusion nucléaire sont réunies.

Le moyen le plus étudié pour atteindre cet objectif aujourd'hui est la fusion par confinement magnétique. En effet, les particules chargées suivent une trajectoire hélicoïdale autour des lignes de champ magnétique. Il est donc possible de construire un réacteur, usuellement de forme toroïdale, permettant de confiner un plasma moins dense que dans le cœur des étoiles, mais à des températures 10 fois plus élevées. Un champ magnétique dans l'axe principal du tore est généré par des bobines externes transverses (i.e. poloïdales). Une série de bobines complémentaires permet par induction d'injecter un courant dans ce même axe toroïdal qui génère à la fois un chauffage ohmique du plasma et un champ magnétique transverse qui, une fois combiné avec le premier champ, créent un champ total hélicoïdal reposant sur des surfaces toroïdales imbriquées. Les particules qui évoluent sur ces surfaces fermées sont alors dites confinées. Cependant, le confinement du plasma

dans un tokamak n'est pas parfait; les collisions Coulombiennes permettent aux ions de dériver vers les parois en traversant la dernière surface de flux fermée du tokamak (i.e. la séparatrice). Ce phénomène de transport est appelé transport « néoclassique ». Cependant, les coefficients de transports calculés à partir de la théorie néoclassique sont 1 à 2 ordres de grandeurs en dessous des valeurs expérimentales.

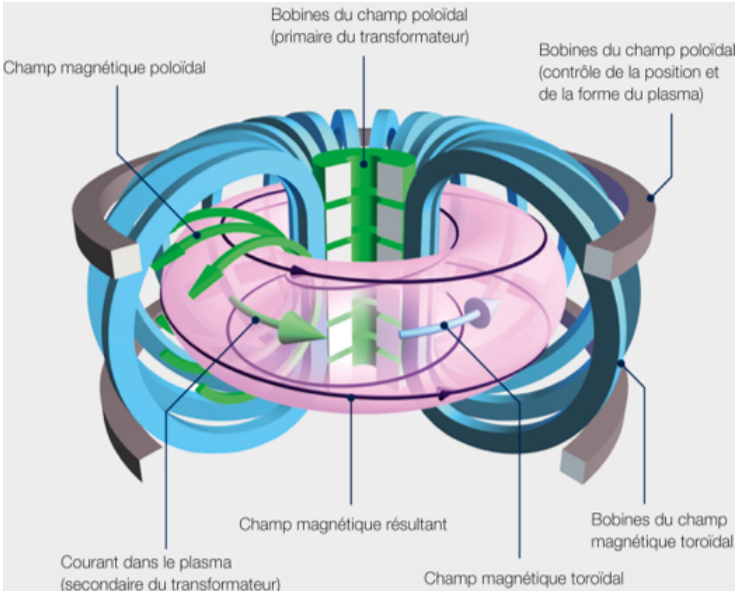

Figure 2: Représentation d'un tokamak moderne en 3D. Image tirée de [1].

Le transport observé dans les tokamaks est dû principalement à des instabilités se développant en turbulence en puisant dans l'énergie libre stockée dans les gradients de température notamment, augmentant ainsi grandement le transport de chaleur et de particules vers les parois du tokamak. Ce transport peut toutefois être limité en déclenchant une bifurcation de l'état du système qui s'opère en injectant suffisament d'énergie dans le tokamak via divers méthodes de chauffage. Une réduction très importante du transport et un raidissement des profils de pression au bord est alors observé ; une « barrière de transport » s'est mise en place. Cette transition L-H (i.e. « Low - High ») est reproductible expérimentalement dans de nombreux tokamaks et est le mode de fonctionnement standard envisagé pour ITER. Cependant, même en mode H, des flux importants de particules et de chaleur peuvent atteindre la paroi et l'endommager. Des impuretés peuvent alors contaminer le cœur du plasma et entraîner une disruption. C'est notamment le cas du tungstène qui n'est pas complètement ionisé dans les conditions des plasmas de cœur et réémet alors une grande partie de l'énergie qu'il absorbe sous forme de rayonnement. Dans cette thèse, nous avons étudié via GYSELA, un code gyrocinétique 5D massivement parallélisé développé par le CEA Cadarache, les différents mécanismes permettant de générer les barrières de transport. Pour cela, une source de cisaillement poloïdal a été utilisée afin de réduire localement l'intensité turbulente. La réduction importante de la taille moyenne des structures turbulentes a engendré une réduction équivalente du flux de chaleur et du coefficient de diffusivité associé, permettant d'établir clairement la formation d'une barrière de transport. Enfin, des simulations en présence d'impuretés (He, Ar, W) en présence de cette barrière de transport ont montré que la barrière de transport ainsi générée empêche

les impuretés lourdes venant de l'extérieur de contaminer le plasma de cœur en augmentant notamment l'effet d'écrantage thermique, améliorant ainsi la qualité du confinement.

Transport néoclassique et turbulent

Pour comprendre le transport *néoclassique*, il est nécessaire de comprendre le transport dit *classique*. Ce dernier, schématiquement représenté sur la figure 3, consiste simplement à traiter le transport collisionnel en présence d'un champ magnétique. Les particules auront alors tendance à être transportées perpendiculairement au champ magnétique après chaque collision. En prenant alors en compte la géométrie torique du tokamak (i.e. sa courbure), et donc le gradient de champ magnétique qui en découle naturellement, on entre alors dans la théorie dite *néoclassique*. Cette dernière montre alors qu'une partie du transport observé dans les tokamaks est dû en partie à ce canal de transport.

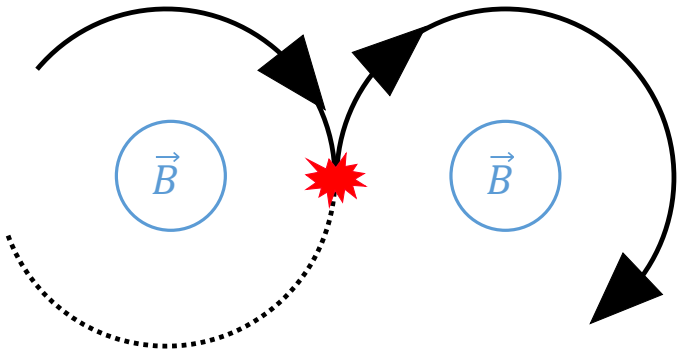

Figure 3: Représentation schématique d'une collision entre deux particules chargées dans un plan perpendiculaire au champ magnétique. Cette représentation est schématique; En effet, les collisions sont à faible déflexion et la situation schématisée ici représente l'effet cumulatif d'un grand nombre de collisions.

Le transport turbulent est, de manière analogue à ce qui est observé en hydrodynamique, dû à des structures de type "tourbillon" qui engendrent, dans les tokamaks, un flux d'énergie, de moment et de particules orienté vers les parois. La turbulence sous-jacente peut avoir de multiples origines, comme des instabilités macroscopiques liées à la magnétohydrodynamique (MHD) et à l'équilibre global du plasma qui peuvent entraîner des disruptions du plasma. Aussi, des micro-instabilités, d'une échelle allant de la longueur de Debye au rayon de Larmor, peuvent croître exponentiellement dans le plasma et engendrer ces structures favorisant le transport de chaleur et de particules.

Il est important de noter que ces micro-instabilités sont, le plus souvent, dues à des écarts à la neutralité électrique, d'où la nécessité de modéliser les plasmas avec une approche multi-espèces en prenant en compte les électrons et les ions séparemment. Ces écarts à la quasi-neutralité entraînent donc des petites fluctuations de charge d'espace qui augmenteront en retour l'intensité des fluctuations initiales. La phase de croissance linéaire (i.e. exponentielle) de ces instabilités prendra alors fin

lorsque des interactions non-linéaires entreront en jeu et permettront la saturation en intensité de la turbulence.

Dans les tokamaks, il existe de nombreuses instabilités dont certaines sont communes à l'hydrodynamique. C'est le cas notamment des instabilités de type Kelvin-Helmholtz (cisaillement de vitesse entre deux couches de fluides/plasma dont les vitesses moyennes sont différentes) ou encore de type Rayleigh-Taylor (deux couches de fluides de densité différentes).

Cependant, dans cette étude, nous nous concentrerons sur les micro-instabilités de type ITG (*Ion Temperature Gradient*), qui puisent leur énergie dans l'énergie libre stockée dans le gradient de température des ions. Cette instabilité engendre des structures radiales le long desquelles le transport de chaleur et de particules s'opère. Elle est responsable d'une grande partie du transport de chaleur turbulent observé dans les tokamaks et explique notamment les coefficients de transport élevés mesurés.

Barrière de transport et transport d'impuretés

Bien que le confinement soit mis à mal par le transport turbulent, le mécanisme de transition L-H permet, au moins localement, de réduire ce transport. Dans ces conditions, le transport néoclassique domine dans la région où la barrière de transport est présente. Il est donc nécessaire, si l'on souhaite étudier le transport d'impuretés dans les tokamaks, d'utiliser un modèle prenant en compte ces deux canaux de transport.

C'est pour cette raison que cette étude s'appuie sur GYSELA, un code gyrocinétique 5D massivement parallélisé, qui a pour avantage de traiter de manière cinétique plusieurs espèces ioniques dans un plasma de coeur. La théorie gyrocinétique permet de réduire la dimensionnalité du système, et donc son accessibilité aux supercalculateurs, en faisant la moyenne sur le mouvement cyclotronique des particules chargées et en changeant habilement de coordonnées via la définition d'invariants (i.e. le moment magnétique μ).

En utilisant une source qui simule les effets d'un chauffage externe, un cisaillement de vitesse poloïdale (i.e. transverse à l'axe principal du tore) a pu être généré pour l'espèce principale, ici du deuterium. Ce cisaillement, généralement observé au niveau des barrières de transport durant les transitions L-H, a généré par conséquent une barrière de transport radialement localisée. Cette barrière a eu plusieurs effets notables;

- Une réduction locale très importante du flux de chaleur turbulent et du coefficient de transport associé.
- Une réduction de la taille moyenne des structures turbulentes au voisinage de la barrière.
- Une augmentation légère de la température au coeur ainsi qu'un raidissement du gradient de température au niveau de la barrière.

Une fois les caractéristiques de la barrière comprises, des simulations similaires ont pu être conduites, cette fois-ci en présence d'impuretés. En fonction du choix des impuretés, différents régimes de collisionalité sont pris en compte :

- L'hélium, qui de par sa faible masse sera plus sujet à la turbulence et moins au transport néoclassique (i.e. collisionnel), subira un régime de collisionalité faible appelé régime "Banane" et sera principalement transporté vers les parois.

- L'argon, injecté au niveau des parois et du diverteur pour réduire le flux de chaleur reçus par ces composants, et qui subira un régime de collisionalité intermédiaire nommé "Plateau" et aura tendance à être transporté vers le coeur.

- Le tungstène, qui provient de la pulvérisation des parois du diverteur, et qui ne doit pas s'accumuler dans le coeur du plasma. Par sa masse élevée, cette espèce est dans un régime de collisionalité élevé appelé "Pfirsch-Schlutter" et aura tendance à être transporté vers le coeur du plasma à cause du transport néoclassique. Cette espèce, de par son numéro atomique élevé, absorbera une grande partie de l'énergie du plasma pour s'ioniser jusqu'à disruption du plasma.

En injectant des impuretés en présence de la barrière de transport, une réduction très importante du transport turbulent de particules est observé pour les impuretés, de manière analogue aux observations faites pour le flux de chaleur du deuterium. Concernant le transport néoclassique, ce dernier est affecté par l'asymétrie poloïdale de la source elle-même, en plus de l'effet de la barrière de transport. En revanche, le raidissement du profil de température de l'espèce principale entraîne, pour les impuretés les plus lourdes, un effet "d'écrantage thermique" permettant de repousser ces impuretés vers l'extérieur et donc d'améliorer le confinement et l'efficacité du tokamak.

Cette étude pourrait être poursuivie en utilisant notamment des électrons cinétiques et non adiabatiques. La synergie entre les instabilités ITG et TEMs (*Trapped Electron Modes*) pourrait donner des résultats plus réalistes, la turbulence TEM pouvant avoir un rôle très important sur le transport. Il serait aussi souhaitable d'utiliser une version électromagnétique du code prenant en compte les effets des variations du champ magnétique de manière auto-cohérente. Des conditions au bord et une configuration magnétique plus réalistes, comme une configuration diverteur par exemple, seraient aussi souhaitables. Coupler GYSELA avec un code de bord plus adéquat afin de créer un modèle intégré permettrait de répondre à ce besoin.

Abstract

Nuclear fusion is the process that powers stars and consists in fusing light nuclei, typically hydrogen isotopes, into a heavier nucleus such as helium. The mass deficit obtained through this type of reaction yields significant amount of energy without emitting greenhouse gases. Fusion through gravitational confinement is impossible to do on Earth. Another way of confining fusion plasma, which are at several millions Kelvin, is required if we want to operate this source of energy.

Nowadays, the most widely studied way of achieving fusion is by magnetically confining the plasma. Since charged particles follow an helical trajectory around magnetic field lines, it is therefore possible to build a reactor, usually toroidal in shape, to confine a plasma that is less dense than in the cores of stars, but at temperatures 10 times higher. A magnetic field along the main axis of the torus is generated by external transverse (i.e. poloidal) coils. A plasma current along the same toroidal axis is induced by auxiliary coils. This current generates a transverse magnetic field which, when combined with the first field, creates a total helical field relying on closed nested toroidal surfaces. The particles evolving in these closed surfaces are then said to be confined.

However, plasma confinement in a tokamak is not perfect; Coulomb collisions allow ions to drift towards the walls by crossing the last closed flux surface of the tokamak (i.e. the separatrix). This transport phenomenon is known as "neoclassical" transport. However, the transport coefficients calculated using neoclassical theory are 2 to 3 orders of magnitude lower than the experimental values.

The transport observed in tokamaks is mainly due to instabilities evolving in turbulence using the free energy stored in the temperature and density gradients, thus greatly increasing the transport of heat and particles towards the walls of the tokamak.

Nonetheless, this transport can be limited by a state transition triggered by injecting energy into the tokamak via fast neutrals. A very significant reduction in transport and a stiffening of the pressure profiles at the edge is then observed; a "transport barrier" has been set up. This L-H (i.e. "Low - High") transition is experimentally reproducible in many tokamaks and is the standard operating mode considered for ITER.

However, even in H mode, large flows of particles and heat can reach and damage the wall. Impurities (i.e. species not involved in the fusion reaction) can then contaminate the plasma core and dilute or even extinguish it. This is particularly the case with tungsten, which is not completely ionized under core plasma conditions and therefore radiates much of the energy it absorbs.

In this thesis, we used GYSELA, a 5D gyrokinetic massively parallelized code developed by CEA Cadarache, in order to investigate the various mechanisms that

generate transport barriers. To this end, a sheared poloidal momentum source was used to reduce turbulent intensity locally. The resulting quench of turbulent structures' size led to an equivalent reduction in heat flux and associated diffusivity coefficients. Those elements led us to conclude that a transport barrier was successfully triggered in our simulations. Finally, simulations with impurities (He, Ar, W) with and without a transport barrier showed that the transport barrier successfully prevented heavy impurities from outside the barrier to penetrate and contaminate the core plasma. Thermal screening effect is mainly responsible for the resulting confinement enhancement we observed.

Chapter 1

Introduction

1.1 Plasma and energy

Plasmas can be defined as *a collection of charged particles with a collective behaviour which is, from an external point of view, electrically quasi-neutral.* This definition describes more than 99% of matter in the Universe. This plasma state is often described as the fourth state of matter which can take various forms, going from cold and sparse interstellar clouds which evolve on time scales of millions of years, to stars like our Sun which temperature and density are both extremely high, or even electric arcs and polar lights observed on our planet. Many criteria can be used to characterize a plasma:

- Its ionization rate $\tau_i = \frac{n_e}{n_e+n_n}$ with n_e and n_n the electronic and neutral densities in m^{-3}. This value measures the ion proportion in the considered plasma cloud.
- The grain factor $g = 1/N_D$, which evaluates the effectiveness of the Debye shielding of the particles composing the plasma on a test charge plunged in the plasma. g depends on macroscopic parameters such as density n and temperature T through the equation $N_D = n_e \frac{4\pi}{3} \lambda_D^3$ with $\lambda_D = \sqrt{\frac{\epsilon_0 k_B T_e}{e^2 n_e}}$ the Debye length. A small grain factor corresponds to a plasma for which screening effect and collective behaviour are strong.
- Whether there is a magnetic field $\mathbf{B}$ and/or a particular geometry in which the plasma is contained and evolves.

Weakly ionized plasmas ($\tau_i \ll 1$) with a strong grain factor ($g < 1$) correspond to laboratory plasmas often nicknamed "cold plasmas" where neutrals play a significant role through collisions. Also, electrons are usually hotter than ions and neutrals ($T_e \gg T_i, T_n$) in such plasmas. They are also called reactive plasma because ions and neutrals undergo a lot of chemical reactions through electron exchanges. It can refer to industry plasma used for coating (i.e. nitriding, Plasma Vapor Deposition - PVD for example), describe electric arcs in the atmosphere, the magnetosphere of planets or even hall-effect thrusters for space probes.

In this thesis, we will focus on "hot plasmas" where ions and electrons both reach same temperature levels of $T_e \approx T_i \geqslant 0.1$ keV $\leftrightarrow 10^6$ K. Thus, such plasmas

are usually strongly ionized ($\tau_i \approx 1$) with a prominent collective behaviour ($g \ll 1$). This is the type of plasmas where fusion reactions can be obtained.

Nuclear fusion reactions require huge amounts of energy; in fact, to make two nuclei fuse together, it is mandatory to overcome the electrostatic repulsion between the two light nuclei. Our Sun is the best and closest example; the ionized hydrogen composing 75% of the Sun's core is pushed to temperatures of around $1.5 \cdot 10^7$K and densities of 10^{32} m^{-3} thanks to its own gravitationnal pull. Then, the following series of fusion reactions happen:

$$ {}_1^1\mathrm{H}^+ + {}_1^1\mathrm{H}^+ + {}_{-1}^{0}\mathrm{e}^- \rightarrow {}_1^2\mathrm{D}^+ + {}_0^0\nu_e + 1.442\,MeV, \tag{1.1} $$

$$ {}_1^2\mathrm{D}^+ + {}_1^1\mathrm{H}^+ \rightarrow {}_2^3\mathrm{He}^{2+} + {}_0^0\gamma + 5.493\,MeV, \tag{1.2} $$

$$ {}_2^3\mathrm{He}^{2+} + {}_2^3\mathrm{He}^{2+} \rightarrow 2\,{}_1^1\mathrm{H}^+ + {}_2^4\mathrm{He}^{2+} + 17.35\,MeV. \tag{1.3} $$

This series of reactions only uses 4 hydrogen atoms and 2 electrons to produce a helium nucleus (or α particle) as well as 26.73 MeV. With 1g of hydrogen, it is possible to produce the equivalent of 711 MWh of energy, meaning 61 TOE (Tonnes of Oil Equivalent, see table 1.1). In other terms, 1g of hydrogene could produce through nuclear fusion as much energy as 61 tonnes of oil while producing few nuclear wastes (when compared to nuclear fission) or greenhouse gases (when compared to fossil fuels). This is the main reason why so many efforts are put into nuclear fusion reasearch.

Fuel / reactant	Mass kg	Mechanism	Produced energy MWh	Produced energy TOE
Coal (anthracite)	1000	Chemical combustion	9.17	0.79
Coal (lignite)	1000	Chemical combustion	5	0.43
Oil	1000	Chemical combustion	11.63	1
Natural gas	1000	Chemical combustion	14.44	1.24
Uranium	0.001	Nuclear fission	20.17	1.73
Hydrogen	0.001	Nuclear fusion	711	61

Table 1.1: Summary of the energetic equivalences between different energy sources. Fission and fusion reactions are much more effective than fossile fuels.

1.2 Nuclear fusion devices

To produce energy through nuclear fusion on Earth, the plasma and its charged particles must be heated and confined efficiently. A useful metric to know if a

reactor is suitable for energy production through fusion is the Lawson criterion which leads to the famous triple product

$$nT\tau_E \geqslant 10^{21}\text{keV m}^{-3}\text{s}, \tag{1.4}$$

with τ_E the confinement time of energy. It represents the time for the confined plasma to cool down without any heating source. One way to make fusion on Earth is to use lasers to heat D-T (deuterium-tritium) pellets as presented in Figure 1.1. A recent breakthrough at NIF (National Ignition Facility) [2] managed to get 3.15 MJ output from fusion energy while injecting 2.05 MJ to the pellet. This method leads to both extremely high temperature ($T \geqslant 20$keV) and density ($n \sim 10^{31}\text{m}^{-3}$) but low confinement times ($\tau_E \sim 10^{-11}$s).

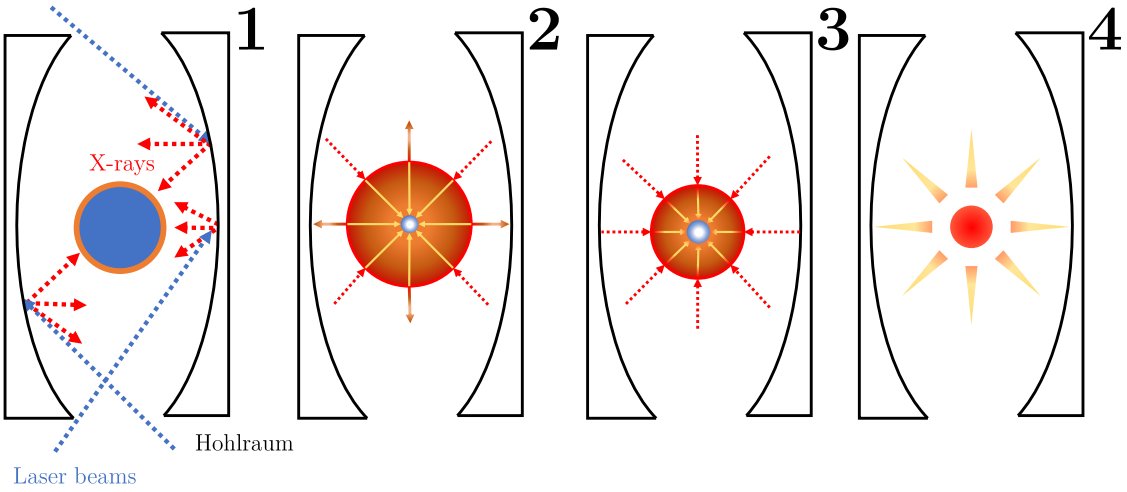

Figure 1.1: Step for inertial confinement fusion process inspired from [3]. **1:** Lasers heat the inner layer of the Hohlraum containing a D-T pellet which reemits energy as X-rays. The X-rays emitted by the Hohlraum generates a thin plasma coat on the fuel pellet. **2:** Rapid expansion of the plasma layer compresses the unburnt fuel. **3:** The pellet imploses, leading the fuel to get extremely dense until ignition at around 100 MK (i.e $\sim 10 - 20keV$). **4:** The entire pellet burns, giving more output energy than the input.

Another way to confine and heat the plasma is by using magnetic field lines. The idea is to use the fact that charged particles, when plunged in a magnetic field, will follow an helical path along the magnetic field line as shown in Figure 1.2a. This can be used to create a specific geometry in which magnetic field lines are closing on themselves, effectively forcing particles to circulate in a closed volume *indefinitely*. Such a magnetic field can be written as

$$\mathbf{B} = B_\varphi \mathbf{e}_\varphi + B_\theta \mathbf{e}_\theta \tag{1.5}$$

in the simplified toroidal coordinate system presented in Figure 1.2b. Its magnitude can be written $B_\varphi = B_0 / \left(1 + \frac{r}{R_0}\cos\theta\right)$, meaning its amplitude decays with R, the major radius. Such field creates nested magnetic flux surfaces, i.e. concentric

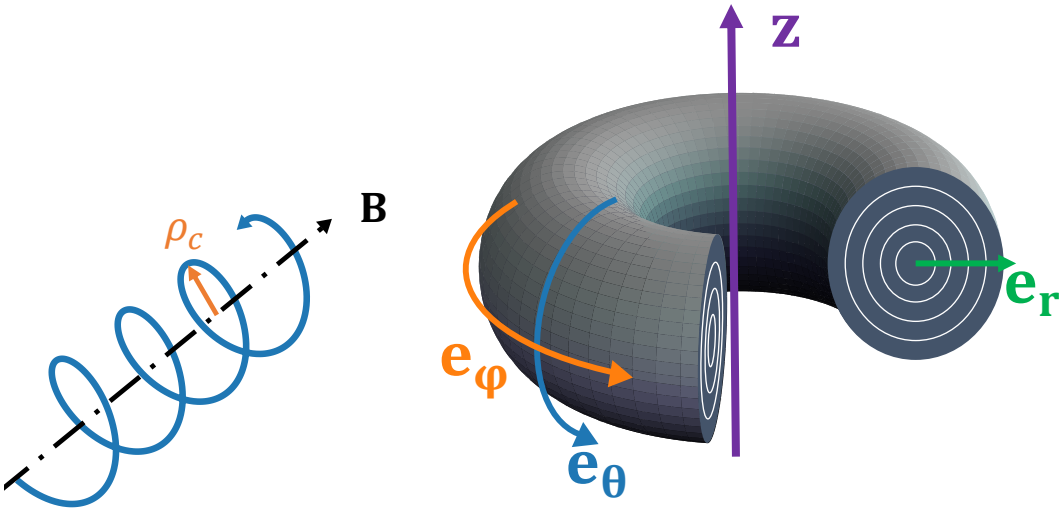

Figure 1.2: **Left:** Charged particle trajectory when a magnetic field line is present. The direction of rotation will depend on the sign of the charged particle. $\rho_c = \frac{\sqrt{k_B T}}{MqB}$ is the Larmor radius. **Right:** Tokamak with a circular shaped cross-section. Toroidal coordinate system unit vectors are shown here for clarity.

surfaces on which helical magnetic field lines lie on. This leads, on paper, to an ideal confinement provided the magnetic field is both strong and stable enough. A complex system of coils is mandatory to create such a complex arrangement of magnetic field lines; the main coils are around the poloidal surfaces and generate the toroidal magnetic field coils. A toroidal plasma current generates the poloidal field and a central solenoid is placed at the center of the tokamak to drive current as well as stabilization purposes. Modern tokamaks use a more complex geometry with a D-shaped cross-section and an X-point divertor configuration as presented in Figure 1.3. This method leads to lower densities ($n \sim 10^{20}\mathrm{m}^{-3}$) but much higher confinement times ($\tau_E \sim 1 - 10\mathrm{s}$) when compared to inertial confinement devices.

This magnetic configuration leads to different phenomena and trajectories that will be described in the next subsection.

1.3 Particle and guiding-center trajectories in tokamaks

Due to the magnetic configuration, particles will follow a trajectory that will be the sum of multiple motions with various origins. The first one is the cyclotron motion as presented before; since particles are plunged in a magnetic field with an initial velocity $\mathbf{v} = \mathbf{v}_\parallel + \mathbf{v}_\perp$ (i.e. $\parallel$ and $\perp$ directions refers to the magnetic field line considered), they will follow a helical trajectory along magnetic field lines. This movement can be easily derived from the equation of motion. One can then look at the motion of the *average* position of the particle on its trajectory called the guiding-center to study its average movement.

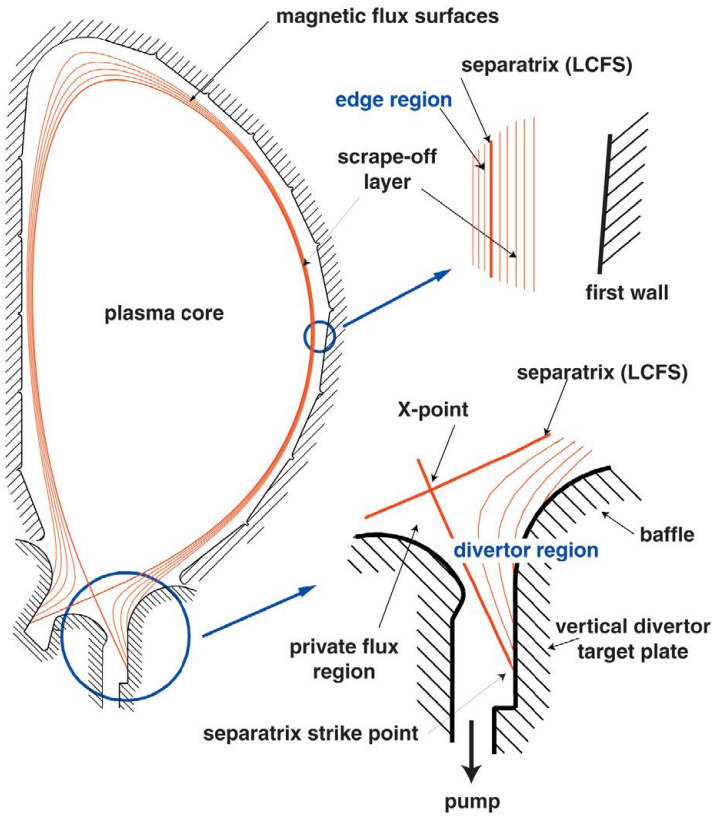

Figure 1.3: Modern tokamak geometry configuration [4]. The scrape-off layer (SOL) is the region where magnetic field lines are opened and intercept the walls in the divertor region, which is usually made of tungsten. The separatrix between the plasma core and SOL is defined by the LCFS (Last Closed Flux Surface) which forms an X-point in the divertor region.

When an electric field is added,

$$m_s \frac{d\mathbf{v}_s}{dt} = q_s \left(\mathbf{E} + \mathbf{v}_s \times \mathbf{B}\right), \tag{1.6}$$

the motion of the guiding-center of a species s is modified. It undergoes a *drift* motion perpendicular to both the magnetic $\mathbf{B}$ and electric $\mathbf{E}$ fields with the familiar expression

$$\mathbf{v}_{E\times B} = \frac{\mathbf{E} \times \mathbf{B}}{B^2}. \tag{1.7}$$

Interestingly, this drift velocity does not depend on particle charge nor mass, thus all guiding-centers (or particles) will drift with the exact same velocities. Equation (1.7) can then be generalized for any force perpendicular to $\mathbf{B}$:

$$\mathbf{v}_{F\times B,s} = \frac{1}{q_s} \frac{\mathbf{F}_s \times \mathbf{B}}{B^2}. \tag{1.8}$$

A typical example is gravity, which gives a dependance on both the mass (i.e. $\mathbf{F}_s = m_s\mathbf{g}$) and the charge. This creates what is called a *polarization* drift, meaning particles of opposite charges will go to opposite directions, thus generating charge separation and a resulting current.

However, two important effects are heavily modifying guiding-center trajectories; the curvature and the gradient drifts. Both effects are linked because if a magnetic field is curved, then a gradient of $|\mathbf{B}|$ must exist as well. This leads to two drifts,

$$\mathbf{v}_{c,s} = \frac{m_s v_{\parallel,s}^2}{q_s} \frac{\mathbf{R_c} \times \mathbf{B}}{R_c^2 B^2}, \tag{1.9}$$

$$\mathbf{v}_{\nabla,s} = \frac{m_s v_{\perp,s}^2}{2q_s} \frac{\mathbf{b} \times \boldsymbol{\nabla} B}{B^2}, \tag{1.10}$$

with $\mathbf{R_c}$ the curvature radius. This drift leads to guiding-centers (and thus particles) to drift vertically out of the tokamak; towards the top and bottom respectively for positive and negative particles. This is the main reason why the poloidal field exist; since particle will rotate poloidally, it will compensate this vertical drift phenomenon by keeping the orbits within the device. The sum of both contributions can then be written

$$\mathbf{v}_{D,s} = \frac{m_s}{q_s B^2} \left(v_{\parallel,s}^2 \frac{\mathbf{R_c} \times \mathbf{B}}{R_c^2} + \frac{v_{\perp,s}^2}{2} \mathbf{b} \times \boldsymbol{\nabla} B \right). \tag{1.11}$$

Other drifts can be taken into account if, for example, $\mathbf{E}$ varies with time or depends on space (i.e. polarization drift $\mathbf{v}_{pol,s}$ and Larmor radius effects respectively). All those contributions can be combined with the motion of the guiding-centers along the magnetic field line $v_\parallel$ to get

$$\mathbf{v}_{GC,s} = \mathbf{v}_{\parallel,s} + \underbrace{\overbrace{\frac{\mathbf{E} \times \mathbf{B}}{B^2}}^{\mathbf{v}_{E\times B}} + \overbrace{\frac{m_s}{q_s B^2} \left(v_{\parallel,s}^2 \frac{\mathbf{R_c} \times \mathbf{B}}{R_c^2} + \frac{v_{\perp,s}^2}{2} \mathbf{b} \times \boldsymbol{\nabla} B \right)}^{\mathbf{v}_{D,s}} + \overbrace{\frac{1}{\omega_{c,s} B} \frac{d\mathbf{E}_\perp}{dt}}^{\mathbf{v}_{pol,s}}}_{\mathbf{v}_{\perp,s}}. \tag{1.12}$$

However, even with those drifts taken into account, one cannot explain the confinement times observed in tokamaks. This is due to radial transport which can be generated by collisions and, as we will see later, turbulence.

1.4 Diffusion processes in magnetized plasmas

1.4.1 Classical diffusion and magnetic field influence

Fusion plasmas in tokamaks have ion and electron densities of the order of $\sim 10^{19}$ m^{-3} and thus collisions, which are primarly coulombian, play an important role in particle transport. Those elastic collisions can be intra-species (ion-ion and electron-electron) or inter-species (ion-electron), but the latter prominently leads to

particle diffusion in the presence of a magnetic field. As a first approach to evaluate diffusion transport due to ion-electron collisions, one can take the fluid momentum conservation equation in the steady-state, isothermal and isotropic limit:

$$\mathbf{v}_s = -D_{classic,s}\frac{\boldsymbol{\nabla} n_s}{n_s}, \tag{1.13}$$

where $D_{classic,s} = \frac{k_B T_s}{m_s \nu_{e,s}}$ is the classic diffusion coefficient without magnetic field. Here, collisions tend to *lower* radial diffusion as density gradient is expected to be along $\mathbf{r}$. However, we can look at the effect of a magnetic field perpendicular to the density gradient, similarly as in tokamaks. This modifies equation (1.13) such that we get

$$\mathbf{v}_s = -\frac{D_{classic,s}}{1+\omega_{c,s}^2/\nu_{e,s}^2}\frac{\boldsymbol{\nabla} n_s}{n_s} - \frac{\omega_{c,s}^2}{\nu_{e,s}^2+\omega_{c,s}^2}\mathbf{v}_{\wedge,s}, \tag{1.14}$$

with $\mathbf{v}_{\wedge,s} = -\frac{\boldsymbol{\nabla} P_s \times \mathbf{B}}{q_s n_s B^2}$ the diamagnetic drift. This time diffusion is modified such that $D_{\perp,s} \equiv \frac{D_{classic,s}}{1+\omega_{c,s}^2/\nu_{e,s}^2}$. When collisions are dominant (i.e. weakly magnetized plasma, $\nu_{e,s} \gg \omega_{c,s}$), we retrieve $D_{\perp,s} \approx D_{classic,s}$ where transport *decreases* with the collision rate. However, when the plasma is strongly magnetized (i.e. $\nu_{e,s} \ll \omega_{c,s}$), we get $D_{\perp,s} \approx D_{classic,s}\nu_{e,s}^2/\omega_{c,s}^2 = k_B T_s \nu_{e,s}/m_s\omega_{c,s}^2$ where this time transport *increases* with the collision rate, showing that collisions enhance particle transport perpendicular to the magnetic field (i.e. towards the walls of the tokamak's vessel).

A more accurate and historical computation has been done by Braginskii [5],

$$D_{Brag} = 2\times 10^{-3}\frac{n_{20}}{B_0^2 T_k^{1/2}}\ \mathrm{m}^2/\mathrm{s}, \tag{1.15}$$

using a kinetic approach to the said problem. However for typical tokamak values, $D_{Brag} \approx 10^{-5}\ \mathrm{m}^2/\mathrm{s}$, which is extremely undervalued compared to what is usually measured experimentally: $D_{exp} \approx 1\ \mathrm{m}^2/\mathrm{s}$, 5 orders of magnitude higher. As we will see later in this manuscript, a huge part of this transport is due to turbulence born from micro-instabilities, but a more accurate and complete approach can still be done regarding collisional transport through neoclassical theory.

1.4.2 Magnetic trapping and neoclassical diffusion

This theory takes into account the toroidal geometry effect on collisional transport and can become more challenging to derive. Due to the complex magnetic field geometry, charged particles can be trapped because of the B gradient along the major radius creating a *low field side* ($\theta = 0$, outer side) and a *high field side* ($\theta = \pi$). Since particles undergo a poloidal orbit in addition to their toroidal movement, they will experience a variation in the magnetic field amplitude. To understand this trapping effect, we can write the total energy of particles

$$E_{k,s} = \frac{1}{2}m_s v_{\parallel,s}^2 + \mu_s B \tag{1.16}$$

where $\mu_s = m_s v_{\perp,s}^2/2B$ the magnetic moment. Note that the latter is an invariant of motion like $E_{k,s}$. The parallel velocity can then be written

$$v_{\parallel,s} = \pm\sqrt{\frac{2}{m_s}\left(E_{k,s} - \mu_s B\right)}. \tag{1.17}$$

If $\mu_s B_{\theta=\pi} < E_{k,s}$, the particle will be orbiting poloidally without any disturbance on its orbit. However, if at a certain point during its orbit $\mu_s B > E_{k,s}$, the particle will be trapped. This can be expressed through the inequality $\mu_s B_{\theta=\pi} = \frac{1}{2} m_s v_{\parallel,s,\theta=0}^2 + \mu_s B_{\theta=0}$, which gives

$$\begin{aligned} f_{t,s}^2 &= \frac{v_{\parallel,s,\theta=0}^2}{v_{\perp,s,\theta=0}^2} < 2\frac{r}{R_0}\left(1 - \frac{r}{R_0}\right)^{-1}, \\ f_{t,s} &= \left|\frac{v_{\parallel,s,\theta=0}}{v_{\perp,s,\theta=0}}\right| \lesssim \sqrt{2\epsilon}, \end{aligned} \tag{1.18}$$

with $\epsilon = r/R_0$ the inverse aspect ratio of the tokamak. $f_{t,s}$ represents the limit between the fraction of trapped and passing particles, the former being trapped in the low field side with *banana* orbits and toroidal precession (i.e. $v_{\parallel,s}$ changes sign) while the latter follow the magnetic field line with full poloidal orbits.

However, particles can also be detrapped due to collisions. A random walk model can be used to deduce an *effective* collision rate $\nu_{eff} = \nu_{coll}/2\epsilon$, which represents the detrapping rate of particles. It takes into account the fact that since ϵ is small, it is easier to detrap particles by changing their parallel velocity through collisions, hence the 2ϵ factor. Invariants of motion can be used to derive a bouncing frequency $\nu_{b,s} = v_{T,s}\sqrt{\epsilon}/2\pi qR\sqrt{2}$ with $v_{T,s} = \sqrt{k_B T_s/m_s}$ the thermal velocity and $q = B_\theta r/B_\varphi R$ the safety factor. The latter will be further detailed in chapter 2. *Collisionality* can then be defined as

$$\nu_s^\star \equiv \frac{\nu_{eff}}{\nu_{b,s}} = \frac{qR}{v_{T,s}}\epsilon^{-3/2}\nu_{coll}. \tag{1.19}$$

This dimensionless ratio represents the rate at which particles undergo collisions over a banana orbit. Particles can then get into different regimes:

Banana regime: For low collisionality ($\nu_s^\star \ll 1$), particles keep their trajectories and disturbances due to collisions are very low. The neoclassical diffusion coefficient can then be written [6]

$$D_{NC-B,s} \approx q^2\epsilon^{-3/2} D_{\perp,s}, \tag{1.20}$$

with $D_{\perp,s} \approx \frac{k_B T_s \nu_{e,s}}{m_s \omega_{c,s}^2}$. Usually we get $D_{NC-B,s} \sim 50 D_{\perp,s} \sim 2 \cdot 10^{-3}$ m^2 s^{-1}, which is better than previous estimates but is still insufficient to explain the values measured experimentally.

Plateau regime: This regime corresponds to intermediate collisionality ($\nu_s^\star \sim 1$), which does not affect greatly passing particles but is more proeminent on trapped particles. The corresponding neoclassical diffusion coefficient is given by [6]

$$D_{NC-P,s} \approx D_{NC-B,s}/\nu_s^\star = q^2 \nu_s^{\star -1} \epsilon^{-3/2} D_{\perp,s}. \tag{1.21}$$

Pfirsch-Schlüter regime: This regime is of high collisionality where particles are detrapped before completing their orbits. The diffusion coefficient is usually given by [6]

$$D_{NC-PS,s} \approx q^2 D_{\perp,s}. \tag{1.22}$$

Those regimes and effects on trajectories are shown in Figure 1.4. As mentionned earlier, trapped trajectories are subject to collisional diffusion. Those results can be found and summarized in the work of Galeev and Sagdeev [6] and later Hinton and Hazeltine [7]. Unfortunately, the diffusion coefficients estimated through neoclassical physics do not yield realistic confinement times either and are still too optimistic. An additionnal *anomalous* transport is measured and finds its origin in micro-instabilities and gradients present in the system. This transport, commonly labeled as *turbulent* transport, will be introduced in the next subsection.

For neoclassical transport however, the heavier the particles, the more likely they will undergo a higher collisionality regime since $D_{\perp,s} \propto m_s$. This means the main ion species, deuterium, tritium and helium, are usually in the banana regime while medium and high-Z species like tungsten will be in the plateau or Pfirsch-Schlüter regime. This effect can lead to unwanted species in the core, reducing its efficiency up to a possible disruption and complete shutdown.

1.4.3 Turbulent diffusion

In tokamaks, there is an additionnal turbulent transport channel due to fluctuations and instabilities in the plasma that can grow exponentially into eddies and thus lead to more mixing in the plasma itself. It is defined as a state of the plasma where radial transport process is mainly due to micro-instabilities rising from the free energy available in the system, mainly in the form of gradients similarly as in fluid dynamics (i.e. Rayleigh-Taylor or Kelvin-Helmoltz instabilities).

Even though turbulence is a non-linear phenomenon, it is possible to do a linear analysis of its formation by taking the variables characterizing the problem and expressing them under the following form

$$A = A_0 + A_1 = A_0 + \tilde{A} \exp\left[i\left(\mathbf{k}\cdot\mathbf{r} - \omega t\right)\right] \tag{1.23}$$

where A_0 is the considered value at equilibrium, usually depending on space only and $\tilde{A}$ the amplitude of the perturbation A_1 which usually depends on space only as well. The exponential part represents the space variation and scaling through the wave vector $\mathbf{k}$ and time evolution through ω. Usually $\omega\left(\mathbf{k}\right) = \omega_r\left(\mathbf{k}\right) + i\gamma\left(\mathbf{k}\right)$ is complex, and if $\gamma > 0$, the perturbation will grow exponentially with time; this is the

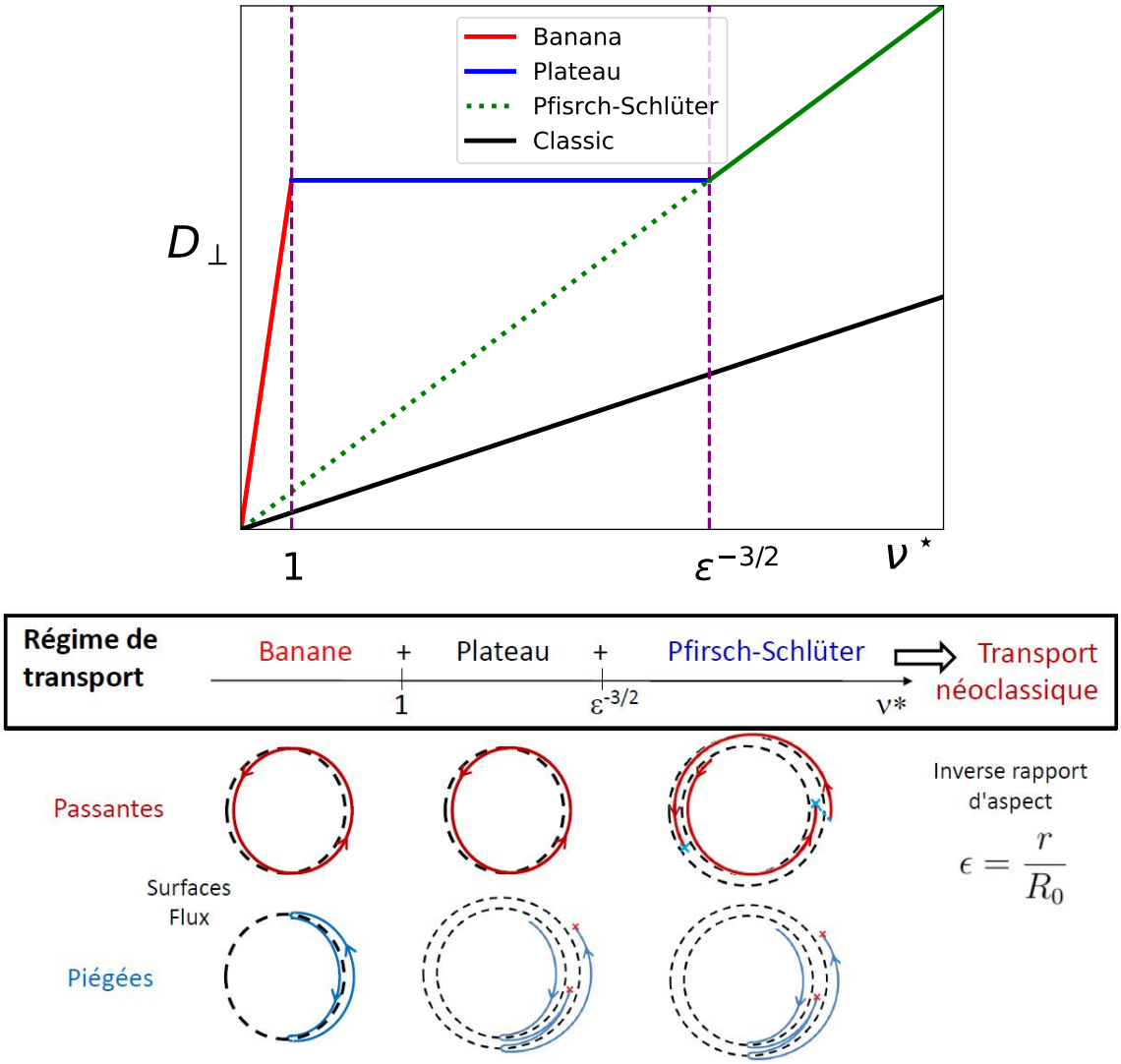

Figure 1.4: **Top:** Neoclassical diffusion coefficient as a function of collisionality, reproduced from [6] and [8] **Bottom:** Particle trajectories depending on collisionality regimes. Trapped particles are more easily affected by collisions, hence their proeminence in neoclassical transport physics. Taken from [9].

linear growth part of the instability. Note that if $\gamma < 0$, the considered perturbation mode is damped and decays to 0. Linearizing and combining all the equations of the considered system usually gives a dispersion relation $D(\mathbf{k}, w) = 0$ that helps understand how the instability behaves as a function of the plasma parameters.

In tokamaks, some instabilities are of the same nature as the two mentionned earlier but are deeply altered due to the tokamak geometry. The gradient and curvature drifts lead to a mechanism that stabilizes the inner side of the tokamak (strong field side) and destabilizes the outer side (weak field side). This means the instabilities will grow faster and stronger on the outer side.

Turbulent diffusion can then be partially modelled through a *mixing length* model. It aims at evaluating the level of fluctuations for a specific field by knowing the typical length over which the said field varies. For example, let us look at pressure fluctuations which can be written

$$|\delta P| \sim \frac{P_0}{k_r L_P}, \tag{1.24}$$

where P_0 is the average profile density, L_P is the pressure gradient length and k_r is the radial wavelength of the perturbation. It can be shown that turbulent diffusion is the same order of magnitude of

$$D \sim \sum_{\mathbf{k},\gamma_\mathbf{k}} \frac{\gamma_\mathbf{k}}{k_r^2}, \tag{1.25}$$

where the sum is over all the wavelengths with positive growth rates. It can be viewed as a sum over all the individual diffusion coefficient $D_\mathbf{k} = \gamma_\mathbf{k}/k_r^2$ following a random walk model of radial step k_r^{-1} and time step $\gamma_\mathbf{k}^{-1}$. This crude approach helps estimate the order of magnitude for turbulent diffusion, which happens to be much higher than neoclassical diffusion in tokamaks. This transport channel explains the confinement times observed in tokamaks. A more in-depth analysis will be conducted in the next chapter.

1.5 Impurity in tokamaks and scope of this thesis

In tokamaks, all species that do not contribute to fusion reactions are considered to be impurities. That means apart from deuterium and tritium ions (i.e. the fuel) as well as electrons, other species must be avoided in the plasma. Those impurities can be byproducts of the fusion reaction itself (helium), the walls (tungsten and/or beryllium) or from injected noble gas (argon and/or neon) near plasma-facing components to mitigate the heat flux received.

The main problem due to impurities is the diluting effect on the fuel; this means the fuel density will decrease just like the rate at which fusion reactions occur and render the tokamak less efficient as an energy production device. Moreover, heavy impurities like tungsten may not be fully ionized when reaching the core and thus

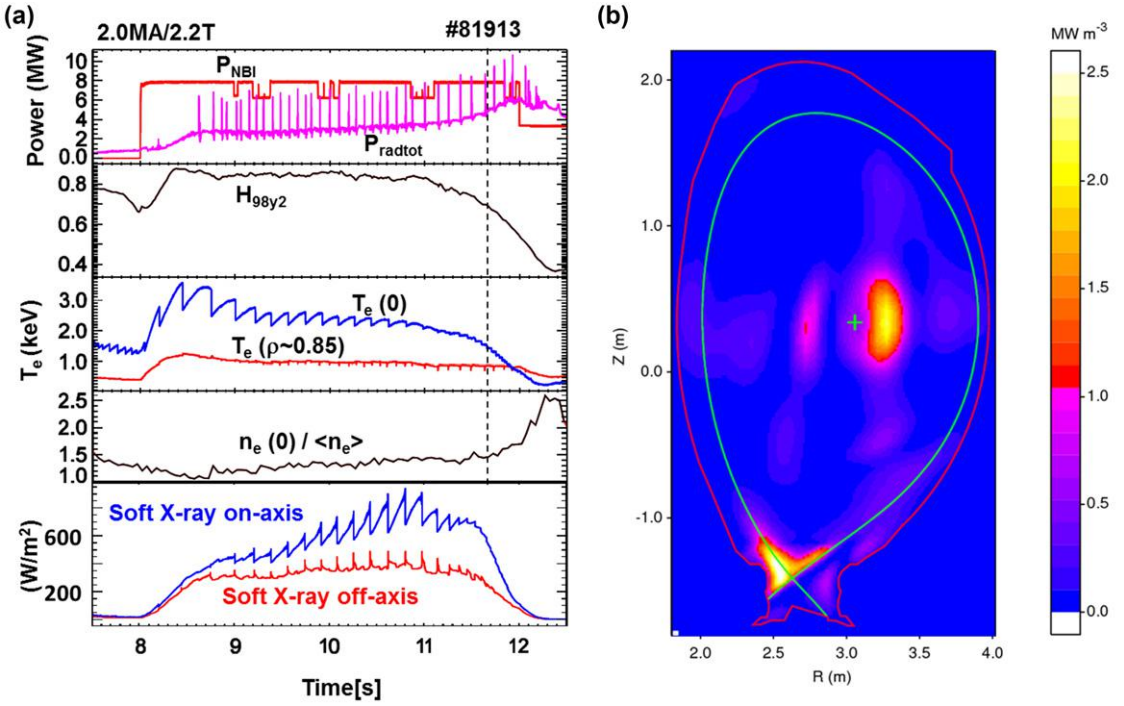

Figure 1.5: **Left:** Time evolution of the injected power in the plasma, electron temperature and density. **Right:** Radiative emission in a transverse plan of the tokamak. Two bright spots are visible, one in the X-point vicinity, mainly due to tungsten sputtering of the divertor. A second bright spot in the core shows a contamination mainly due to tungsten transported from the edge. This particular experiment underwent a radiative collapse. [10]

radiating a lot of the absorbed energy through radiation. An example of a radiative collapse in JET (Joint European Torus) is shown in Figure 1.5 with a prominent core plasma contamination by tungsten.

Unfortunately, impurities are impacted by transport just like the main species, being neoclassical (i.e. collisional) or turbulent. As discussed earlier, heavy impurities will be more subject to inward neoclassical transport due to the main species gradient and to an outward turbulent flux due to the temperature gradient, hence the possible accumulation of heavy particles in the core and radiation collapse.

Avoiding this impurity accumulation is then of upmost importance for controlled fusion devices and a clear understanding of their transport processes is required. The aim of this thesis is to study transport of impurity both numerically and theoretically and try to control it using different methods. Chapter 2 is dedicated to the introduction of neoclassical transport in a more refined way as well as turbulent transport and the instabilities present in tokamaks. A way of reducing turbulent transport experimentally, namely transport barriers, is also described as well as theoretical elements which explain part of the physics involved. In chapter 3, the gyrokinetic framework is introduced as well as GYSELA, a heavily parallelized numerical code able to simulate a 5D (3D in space, 2 in velocity) tokamak. The control of turbulent transport using poloidal shearing in GYSELA is discussed. Chapter 4 is dedicated to the study of impurity transport in a reduced turbulence regime. The last chapter draws conclusions on the work presented here.

Chapter 2

Transport and confinement

2.1 Introduction

The aim of this chapter is to provide a broad overview of the transport processes that impurities undergo in tokamaks. Since transport of particles can usually be separated between two channels such that

$$\Gamma_s^{tot} = \Gamma_s^{neo} + \Gamma_s^{turb}, \tag{2.1}$$

respectively the neoclassical and turbulent channels, both will be explored and reviewed. Their expression as a function of the geometrical configuration of tokamaks as well as thermodynamical forces due to temperature, density, pressure and electrostatic potential will be derived through two main different approaches; fluid and kinetic.

2.2 Neoclassical transport

2.2.1 Flux surface and safety factor

While classical transport treats the effect of Coulomb collisions, neoclassical transport takes into account the complex geometrical effects taking place in tokamaks due to its toroidal shape and resulting curvature. Trapped particles, in particular, play an important role as mentionned in the introduction. The main goal here is to provide a coherent theoretical review of particle fluxes along the radial direction due to neoclassical effects. For this purpose, another representation in cylindrical coordinates can be used to describe axisymmetric magnetic fields in tokamaks [11]:

$$\mathbf{B} = \overbrace{\mathbf{e}_\varphi B_\varphi}^{\mathbf{B}_\varphi} + \overbrace{\mathbf{e_R} B_R + \mathbf{e_z} B_z}^{\mathbf{B}_\theta} = \boldsymbol{\nabla} \times \mathbf{A}. \tag{2.2}$$

By using $\mathbf{e}_\varphi = R\boldsymbol{\nabla}\varphi$ and introducing a *poloidal flux function* $\psi(R,z) \equiv -RA_\varphi(R,z)$[1], the magnetic field can be recasted as

[1] This comes from the curl of the potential vector $\mathbf{A}$: $B_R = \frac{\partial A_\varphi}{\partial z}$ and $B_z = -\frac{1}{R}\frac{\partial (RA_\varphi)}{\partial R}$.

$$\mathbf{B} = \overbrace{I(\psi)\,\boldsymbol{\nabla}\varphi}^{\mathbf{B}_\varphi} + \overbrace{\boldsymbol{\nabla}\varphi \times \boldsymbol{\nabla}\psi}^{\mathbf{B}_\theta}. \tag{2.3}$$

Figure 2.1 helps vizualize and understand this notation for the magnetic field as the poloidal flux passes through the red surface (i.e. *in* a poloidal plane) while the toroidal flux is conversely passing through the blue surface (i.e. *through* a poloidal plane). The total magnetic flux through the total flux surface is then 0. One may note that field lines can close on themselves like the green line in Figure 2.1. In that case, they will be referred as *rational* surfaces whereas field lines not closing on themselves will be referred as *irrational*. This will be of importance regarding perturbations and turbulent transport.

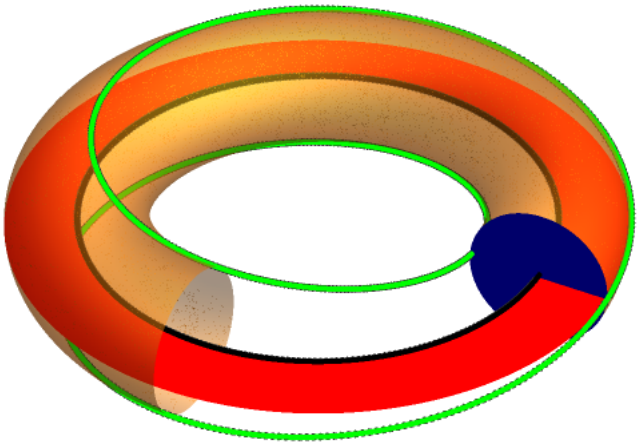

Figure 2.1: Solid black line represents the magnetic axis. The poloidal magnetic flux goes through the red surface while the toroidal one goes through the blue surface. Green line represents a magnetic field line which, in that particular case, is rational. Figure downloaded from [12].

From these equations, it readily appears that the poloidal flux function ψ remains constant along magnetic field lines ($\mathbf{B}\cdot\boldsymbol{\nabla}\psi = 0$), which means the magnetic field $\mathbf{B}$ lies on nested torus of constant ψ. One can note that flux surfaces are, in the case of tokamaks with circular cross sections (i.e. as the one showed in Figure 1.2), colinear to radial coordinates in the simplified toroidal coordinate system. The poloidal coordinate can then be built from $\boldsymbol{\nabla}\theta\cdot\boldsymbol{\nabla}\varphi = 0$ (i.e. the poloidal plane is orthogonal to the toroidal axis). This is helpful to introduce the concept of *flux-surface average*, which for a given quantity $G(\psi,\theta,\varphi)$ is written as

$$\langle G\rangle_{FS}(\psi) \equiv \int_{\theta=0}^{\theta=2\pi}\int_{\varphi=0}^{\varphi=2\pi} G(\psi,\theta,\varphi)\,J_\chi d\theta d\varphi \Big/ \int_{\theta=0}^{\theta=2\pi}\int_{\varphi=0}^{\varphi=2\pi} J_\chi d\theta d\varphi, \tag{2.4}$$

with $J_\chi = (\mathbf{B}\cdot\boldsymbol{\nabla}\theta)^{-1}$ the flux-surface Jacobian. This is analogous, but not the same, as an angle-average of a function and thus a radial profile for a given quantity. This allows us to define a *safety factor* profile

$$q\left(\psi\right)=\frac{\left\langle \mathbf{B}\cdot\boldsymbol{\nabla}\varphi\right\rangle_{FS}}{\left\langle \mathbf{B}\cdot\boldsymbol{\nabla}\theta\right\rangle_{FS}}=\frac{d\varphi}{d\theta}, \tag{2.5}$$

which counts the number of toroidal rotation for each poloidal rotation (i.e. also referred to as the *pitch* of the magnetic field). For example, rational surfaces can be expressed as $q\equiv n/m$ with n and m being integers.

2.2.2 Main ion particle flux

Helander and Sigmar [11] derived a simple relation regarding particle flux across magnetic flux surfaces (i.e. radial flux) using both the continuity and momentum balance equations for ions:

$$\frac{\partial N_i}{\partial t}+\boldsymbol{\nabla}\cdot\boldsymbol{\Gamma}_i=0, \tag{2.6}$$

$$M_i\frac{\partial\boldsymbol{\Gamma}_i}{\partial t}+\boldsymbol{\nabla}\cdot\bar{\boldsymbol{\Pi}}_i=N_iq_i\left(\mathbf{E}+\mathbf{V}_i\times\mathbf{B}\right)+\mathcal{F}, \tag{2.7}$$

with $\mathbf{V}_i$ the average fluid velocity, N_i the ion density, M_i the ion mass, $\boldsymbol{\Gamma}_i$ the ion particle flux, $\bar{\boldsymbol{\Pi}}_i$ the pressure tensor and $\mathcal{F}$ [2] the friction force. Gauss's law[3] can be applied to the continuity equation (2.6)

$$-\int_V dV\frac{\partial N_i}{\partial t}=\int_V dV\boldsymbol{\nabla}\cdot\boldsymbol{\Gamma}_i=\oint_S\frac{\left(\boldsymbol{\Gamma}_i\cdot\boldsymbol{\nabla}\psi\right)d\theta d\varphi}{\mathbf{B}\cdot\boldsymbol{\nabla}\theta}=\left\langle \boldsymbol{\Gamma}_i\cdot\boldsymbol{\nabla}\psi\right\rangle_{FS}\int\left(\mathbf{B}\cdot\boldsymbol{\nabla}\theta\right)^{-1}d\theta d\varphi,$$

where the term $\left\langle \boldsymbol{\Gamma}_i\cdot\boldsymbol{\nabla}\psi\right\rangle_{FS}$ represents the flux-surface averaged particle flux along across flux-surface. In other terms, this is the quantity we want to derive since it is equivalent to a radial flux of particles. By using some of the useful relations given in appendix A.1, we can rewrite the particle flux as

$$\left\langle \boldsymbol{\Gamma}_i\cdot\boldsymbol{\nabla}\psi\right\rangle_{FS}=\left\langle R^2\boldsymbol{\nabla}\varphi\cdot\left(\boldsymbol{\Gamma}_i\times\mathbf{B}\right)\right\rangle_{FS}.$$

Interestingly, one can get this term out of equation (2.7) by projecting it along the toroidal axis before averaging the result over a flux surface:

$$\frac{\partial\left\langle M_i\boldsymbol{\Gamma}_i\cdot\boldsymbol{\nabla}\varphi\right\rangle_{FS}}{\partial t}+\left\langle\left(\boldsymbol{\nabla}\cdot\bar{\boldsymbol{\Pi}}_i\right)\cdot\boldsymbol{\nabla}\varphi\right\rangle_{FS}=\left\langle\left(q_iN_i\mathbf{E}+q_i\overbrace{N_i\mathbf{V}_i}^{\boldsymbol{\Gamma}_i}\times\mathbf{B}\right)\cdot\boldsymbol{\nabla}\varphi\right\rangle_{FS}+\left\langle\mathcal{F}\cdot\boldsymbol{\nabla}\varphi\right\rangle_{FS}$$

[2] $\mathcal{F}=\int d^3v_im\mathbf{v}_iC\left(f_i\right)$, where $\mathbf{v}_i$ is the ion velocity , f_i the distribution function of the considered species and $C\left(f\right)$ is the collision operator. It conserves the number of particles as well as energy, but generates an internal friction term (i.e. intra-species collisions). This operator could encompass collisions with other species (i.e. inter-species collisions), but the considered problem only posesses one species for now.

[3] $\int_V dV\boldsymbol{\nabla}\cdot\mathbf{G}=\oint_S\mathbf{G}\cdot d\mathbf{S}$. In our case, we recall that $dV=J_\chi d\psi d\theta d\varphi$ and the surface vector element is $d\mathbf{S}=\boldsymbol{\nabla}\psi J_\chi d\theta d\varphi$.

By neglecting viscosity in $\bar{\bar{\mathbf{\Pi}}}_i$ and assuming both stationary state ($\partial_t = 0$) and an axisymmetric torus ($\partial_\varphi = 0$), one can get (see appendix A.2.1)

$$\langle \mathbf{\Gamma}_i \cdot \boldsymbol{\nabla}\psi \rangle_{FS} = \overbrace{-\left\langle \frac{I}{B}\left(N_i E_\parallel + \frac{\mathcal{F}_\parallel}{q_i}\right)\right\rangle_{FS}}^{\text{Neoclassic}} + \overbrace{\left\langle \frac{\boldsymbol{\nabla}\psi \cdot (\mathcal{F}\times\mathbf{B})}{q_i B^2}\right\rangle_{FS}}^{\text{Classic}} + \overbrace{\left\langle N_i \boldsymbol{\nabla}\psi \cdot \frac{\mathbf{E}\times\mathbf{B}}{B^2}\right\rangle_{FS}}^{\text{Turbulent}} \tag{2.8}$$

where three different components of the particle flux can be recognized. The neoclassical term is linked to parallel friction of guiding centres, while the classical term can be seen as a *perpendicular friction drift*, analogous to equation (1.8) with $\mathbf{F} \to \mathcal{F}$. The last term is the radial component of the $\mathbf{E}\times\mathbf{B}$ flux usually associated to turbulent transport. This component will be tackled in the next section.

The neoclassical part of equation (2.8) can be further developped by separating it into two terms corresponding to different collisionality regimes as shown in appendix A.2.1

$$\langle \mathbf{\Gamma}_i \cdot \boldsymbol{\nabla}\psi \rangle_{FS}^{neo} = \underbrace{-I\left\langle \frac{1}{q_i B}\left(q_i N_i E_\parallel + \mathcal{F}_\parallel\right)\left(1 - \frac{B^2}{\langle B^2\rangle_{FS}}\right)\right\rangle_{FS}}_{\langle \mathbf{\Gamma}_i\cdot\nabla\psi\rangle_{FS}^{PS}} \underbrace{-I\frac{\left\langle B\left(q_i N_i E_\parallel + \mathcal{F}_\parallel\right)\right\rangle_{FS}}{q_i \langle B^2\rangle_{FS}}}_{\langle \mathbf{\Gamma}_i\cdot\nabla\psi\rangle_{FS}^{BP}}, \tag{2.9}$$

where it readily appears that the Pfirsch-Schlüter component is entirely due to the toroidal geometry of the magnetic field and the dependency of B with the major radius R of the tokamak. In a cylindrical geometry and with an axisymmetric B field, the term $B^2/\langle B^2\rangle_{FS}$ would vanish since the flux-surface averaging would give B^2, leading to $\langle \mathbf{\Gamma}_i \cdot \boldsymbol{\nabla}\psi \rangle_{FS}^{PS} = 0$. The banana-plateau flux is linked to the parallel components of the friction and electric field. This can be further expanded to make a link with pressure anisotropy by using the fluid momentum equation (2.7) and the CGL tensor [13] as detailed in appendix A.2.2.

2.2.3 Impurity particle flux

While previous developments are useful for the main species neoclassical particle flux, we want to express impurities' neoclassical flux in a trace regime (i.e. $N_s/N_i \ll 1$). For this purpose, we start from the continuity equation (2.6) for impurities in a steady-state to get $\nabla \cdot \mathbf{\Gamma}_s = 0$. This guiding center flux can be separated in parallel and perpendicular components to the magnetic field $\mathbf{\Gamma}_s = \Gamma_{\parallel,s}\mathbf{b} + \mathbf{\Gamma}_{\perp,s}$, the latter being written as

$$\mathbf{\Gamma}_{\perp,s} = \underbrace{N_s \mathbf{v}_\mathbf{E}}_{\mathbf{\Gamma}_{E,s}} + \underbrace{N_s \langle \mathbf{v}_{D,s}\rangle_v}_{\mathbf{\Gamma}_{D,s}} \underbrace{- \boldsymbol{\nabla} \times \overbrace{\left[N_s \left\langle \frac{\mu_s}{q_s}\mathbf{b}\right\rangle_v\right]}^{\mathbf{M}_s/q_s}}_{\mathbf{\Gamma}_{mag,s}} \tag{2.10}$$

with

$$\mathbf{v}_E = \frac{\mathbf{B}\times\boldsymbol{\nabla}\bar{\phi}}{B^2}, \tag{2.11}$$

$$\mathbf{v}_{D,s} = \mathbf{v}_{\nabla,s} + \mathbf{v}_{c,s} = \frac{\mu_s}{q_s}\frac{\mathbf{B}\times\boldsymbol{\nabla}B}{B^2} + \frac{M_s v_{\parallel,GC,s}^2}{q_s B^2}\frac{\mathbf{R_c}\times\mathbf{B}}{R_c^2}, \tag{2.12}$$

$$\mathbf{v}_{\parallel,GC,s} = v_{\parallel,GC,s}\mathbf{b}, \tag{2.13}$$

$$\boldsymbol{\Gamma}_{mag,s} = \mathbf{j}_{mag,s}/q_s = \boldsymbol{\nabla}\times\mathbf{M}_s/q_s, \tag{2.14}$$

which are respectively the $E\times B$, gradient plus curvature drifts as well as the parallel motion to the magnetic field. The magnetization flux $\boldsymbol{\Gamma}_{mag,s}$[4] is a mandatory correction to have the full particle flux[5]. Developping equation (2.10) using the appropriate definitions developped in appendix A.3 combined with the CGL tensor notation gives the total flux of impurities

$$\boldsymbol{\Gamma}_\mathbf{s} = \underbrace{\left[N_s v_{\parallel,GC,s} - \frac{P_{\perp,s}}{q_s B}\mathbf{b}\cdot(\boldsymbol{\nabla}\times\mathbf{b})\right]\mathbf{b}}_{\boldsymbol{\Gamma}_{\parallel,s}} + \underbrace{N_s\frac{\mathbf{b}\times\boldsymbol{\nabla}\phi}{B}}_{\boldsymbol{\Gamma}_{E,\perp,s}} + \underbrace{\frac{\mathbf{b}\times\boldsymbol{\nabla}\cdot\boldsymbol{\Pi}_s}{q_s B}}_{\boldsymbol{\Gamma}_{D,\perp,s}}, \tag{2.15}$$

where we recognize the parallel and perpendicular components of the flux. The former is composed of the classical parallel velocity term. The perpendicular flux is the sum of the $E\times B$ drift term with the diamagnetic term. The former will be mainly treated in the next section while the latter is the one of interest for this section. In fact, this term is directly related to neoclassical effects (i.e. collisions and geometrical factors) and can be further expanded by averaging it over flux-surfaces and splitting it in BP and PS terms. The flux-surface average gives

$$\langle\boldsymbol{\Gamma}_{\perp,s}\cdot\boldsymbol{\nabla}\psi\rangle_\psi = \underbrace{-\frac{I}{q_s}\left\langle\left(\frac{1}{B} - \frac{B}{\langle B^2\rangle_\psi}\right)\mathbf{b}\cdot(\boldsymbol{\nabla}\phi N_s q_s + \boldsymbol{\nabla}\cdot\boldsymbol{\Pi}_s)\right\rangle_\psi}_{\boldsymbol{\Gamma}_{BP,s}} \underbrace{-\frac{I\langle\mathbf{B}\cdot\boldsymbol{\nabla}\cdot\boldsymbol{\Pi}_s\rangle_\psi}{q_s\langle B^2\rangle_\psi}}_{\boldsymbol{\Gamma}_{PS,s}}, \tag{2.16}$$

in which we retrieve the main effects dominating in each regime. In the BP regime, anistropy is the dominating phenomenon while collisions dominate through parallel friction in the PS regime [14]. However, as computed by C. Angioni and P. Helander [15] and used by both P.Donnel [16] and K. Lim [17], this expression can be further refined to take into account poloidal asymmetries by starting from equation (2.15), the full impurity flux expression, and write the gradient terms as

$$\boldsymbol{\nabla}P_{\perp,s} = \frac{\partial P_{\perp,s}}{\partial\theta}\boldsymbol{\nabla}\theta + \frac{\partial P_{\perp,s}}{\partial\psi}\boldsymbol{\nabla}\psi, \tag{2.17}$$

$$\boldsymbol{\nabla}\phi = \frac{\partial\phi}{\partial\theta}\boldsymbol{\nabla}\theta + \frac{\partial\phi}{\partial\psi}\boldsymbol{\nabla}\psi. \tag{2.18}$$

[4]The bracket $\langle\ldots\rangle_v = \int dv\ldots\bar{F}_s/\int dv\bar{F}_s$ represents an average over the velocity space with $\bar{F}_s$ the distribution function of the considered impurities species and $\int dv\bar{F}_s = N_s$, the density of impurities.

[5]This term does not impact the continuity equation; it is divergenceless by nature since $\boldsymbol{\nabla}\cdot(\boldsymbol{\nabla}\times\mathbf{A}) = 0$.

Injecting those expressions in equation (2.15) gives

$$\mathbf{\Gamma_s} = K_s\mathbf{B} - N_s\Omega_s R^2\boldsymbol{\nabla}\varphi + \underbrace{\Pi_{\parallel,s}\frac{\mathbf{b}\times\mathbf{k}}{q_sB} + \frac{\mathbf{b}\times\boldsymbol{\nabla}\theta}{B}\left(N_s\frac{\partial\phi}{\partial\theta} + \frac{1}{q_s}\frac{\partial P_{\perp,s}}{\partial\theta}\right)}_{\tilde{\mathbf{\Gamma}}_\mathbf{s}}, \tag{2.19}$$

with $K_s = \frac{\Gamma_{\parallel,s}}{B} + \frac{IN_s\Omega_s}{B}$, which is a function that varies poloidally, $\Omega_s = \frac{\partial\phi}{\partial\psi} + \frac{1}{N_sq_s}\frac{\partial P_{\perp,s}}{\partial\psi}$ and $\Pi_{\parallel,s} = P_{\parallel,s} - P_{\perp,s}$ the pressure anisotropy. An equation for particles crossing flux-surfaces for the BP and PS channels, similarly as equation (2.16), can be obtained by combining equations (2.19) and (A.35), this time taking into account poloidal asymmetries. Details about computations can be found in the work of Hirshman and Sigmar [14] as well as P. Donnel [16] and succinctly summarized in appendix A.4. It finally writes

$$\langle\mathbf{\Gamma}\cdot\boldsymbol{\nabla}\psi\rangle^{neo}_{FS,s} = \langle\mathbf{\Gamma}\cdot\boldsymbol{\nabla}\psi\rangle^{BP}_{FS,s} + \langle\mathbf{\Gamma}\cdot\boldsymbol{\nabla}\psi\rangle^{PS}_{FS,s} \tag{2.20}$$

with each channels detailed as

$$\langle\mathbf{\Gamma}\cdot\boldsymbol{\nabla}\psi\rangle^{BP}_{FS,s} = -\frac{I}{q_s}\left\langle\frac{B^2}{N_s}\right\rangle_\psi^{-1}\left\langle\frac{\mathbf{B}\cdot\boldsymbol{\nabla}\theta}{N_s}\left[\frac{\partial P_{\perp,s}}{\partial\theta}\right]\right\rangle_\psi \longrightarrow \Gamma^{P_{\perp,s}} \tag{2.21}$$

$$-\frac{I}{q_s}\left\langle\frac{B^2}{N_s}\right\rangle_\psi^{-1}\left\langle\frac{\mathbf{B}\cdot\boldsymbol{\nabla}\theta}{N_s}\left[B\frac{\partial}{\partial\theta}\left(\frac{\Pi_{\parallel,s}}{B}\right)\right]\right\rangle_\psi \longrightarrow \Gamma^{\Pi_{\parallel,s}} \tag{2.22}$$

$$\langle\mathbf{\Gamma}\cdot\boldsymbol{\nabla}\psi\rangle^{PS}_{FS,s} = \frac{I}{q_s}M_s\nu_{si}\left\{\frac{T_i}{e}\frac{I}{L_{\psi,i}}\left(\left\langle\frac{N_s}{B^2}\right\rangle_\psi - \left\langle\frac{B^2}{N_s}\right\rangle_\psi^{-1}\right)\right\} \longrightarrow \Gamma^{\nabla N_i} \tag{2.23}$$

$$-\frac{I}{q_s}M_s\nu_{si}\left\{u\left(\langle N_s\rangle_\psi - \frac{\langle B^2\rangle_\psi}{\langle B^2/N_s\rangle_\psi}\right)\right\} \longrightarrow \Gamma^{u_s} \tag{2.24}$$

$$+\frac{I}{q_s}M_s\nu_{si}\left\{\frac{T_iI}{e}\left(\left\langle\frac{N_s}{B^2L_{\psi,s}}\right\rangle_\psi - \left\langle\frac{1}{L_{\psi,s}}\right\rangle_\psi\left\langle\frac{B^2}{N_s}\right\rangle_\psi^{-1}\right)\right\} \longrightarrow \Gamma^{\nabla N_s} \tag{2.25}$$

$$+\frac{I}{q_s}M_s\nu_{si}\left\{\frac{\left\langle\frac{B}{N_s}\frac{\partial}{\partial\psi}\left(\frac{I\Pi_{\parallel,s}}{q_sB}\right)\right\rangle_{FS}}{\langle B^2/N_s\rangle_{FS}} - \frac{1}{B}\frac{\partial}{\partial\psi}\left(\frac{I\Pi_{\parallel,s}}{q_sB}\right)\right\} \longrightarrow \Gamma^{K_s} \tag{2.26}$$

with $L^{-1}_{\psi,s} = -\partial_\psi P_{\perp,s}/T_iZ_sN_s$ and $L^{-1}_{\psi,i} = \partial_\psi\ln P_i - H_{TS}\partial_\psi\ln T_i$. H_{TS} is called the thermal screening factor and is taken as $3/2$ later on.

As shown on equations (2.21) to (2.26), the BP and PS components of the neoclassical flux can be detailed even further in different terms to highlight some behaviours depending on the species or local plasma conditions.

For the BP component of the flux, the term $\Gamma^{P_{\perp,s}}$ is linked to the poloidal asymmetries of the perpendicular pressure. This term is usually lower in ordering than the term $\Gamma^{\Pi_{\parallel,s}}$, the poloidal asymmetry of pressure anisotropy term. In contrast

to the PS component, the BP one does not explicitly depend on the collosion rate ν_{si}, hence its dominance when impurities are light.

The PS flux will however be mainly driven by the pressure gradients of both the impurity and main ion species, the latter being the dominant term we expect for heavy impurities such as tungsten. One can expand the $L_{\psi,i}^{-1} = \partial_\psi \ln N_i - 0.5\partial_\psi \ln T_i$ term to evidence the thermal screening effect; if the temperature gradient ($\partial \ln T_i < 0$ in tokamaks usually) is strong enough to overcome the density gradient ($\partial \ln N_i < 0$ in tokamaks also), then the term $L_{\psi,i}^{-1}$ will be positive; in other terms, with a sufficiently strong temperature gradient of the main species, heavy impurities in the PS regime will be repelled and not penetrate the core plasma. One must note that this value of H_{TS} can vary with collisionality [18, 19], but the value was set to the same as K. Lim's study to make the comparisons easier. This is the ideal scenario envisioned for ITER to avoid core plasma contamination by tungsten for instance [20]. This phenomenon has already been observed in JET [21] where an efflux (i.e. outward flux / loss) has been measured during H-mode experiments. A good agreement is found between this analytical derivation and simulation as already shown [16, 17, 22, 23] and also in this thesis in chapter 4.

2.3 Turbulent transport

2.3.1 ITG

Slab kinetic approach

One of the first micro-instability encountered in fusion plasma is called the ITG (i.e. Ion Temperature Gradient) instability. Micro-instabilities originate at smaller scales than MHD macro-instabilities, namely the Larmor radius ρ_c or Debye length λ_d scale, and can rise from small charge separations leading to perturbations of the electrostatic potential. As a result, a perturbed electric field will enhance the existing fluctuations and lead to turbulence growth. ITG modes more specifically draw their energy from the ion temperature gradient and lead to large radial transport coefficients, especially ion heat diffusivity. This instability is of the "interchange" type as shown in Figure 2.2 and is due, in tokamaks, to the magnetic drift velocity $\mathbf{v}_D$. If a perturbation in the pressure profile appears on a magnetic surface, a small difference in $\mathbf{v}_D$ shall appear and be amplified by the $\mathbf{v}_{E\times B}$ drift velocity in the weak $\mathbf{B}$ region, also called the "bad curvature" or "unstable" region for this kind of instability. This leads to extended radial structures in potential along which particles are able to be transported, hence the augmentation in radial transport and loss of confinement.

One of the first mention of temperature gradient-driven instability is by Rudakov and Sagdeev [25]. Their main motivation was to explain instabilities observed during ohmic heating discharges through which the current was directed along a strong magnetic field. Those instabilities could not be explained within an ideal MHD framework and required a two-fluid model approach or a kinetic model. The presence of small charge separation and therefore potential fluctuations are required to get ITG modes as shown in Figure 2.2. This analysis uses a slab geometry in

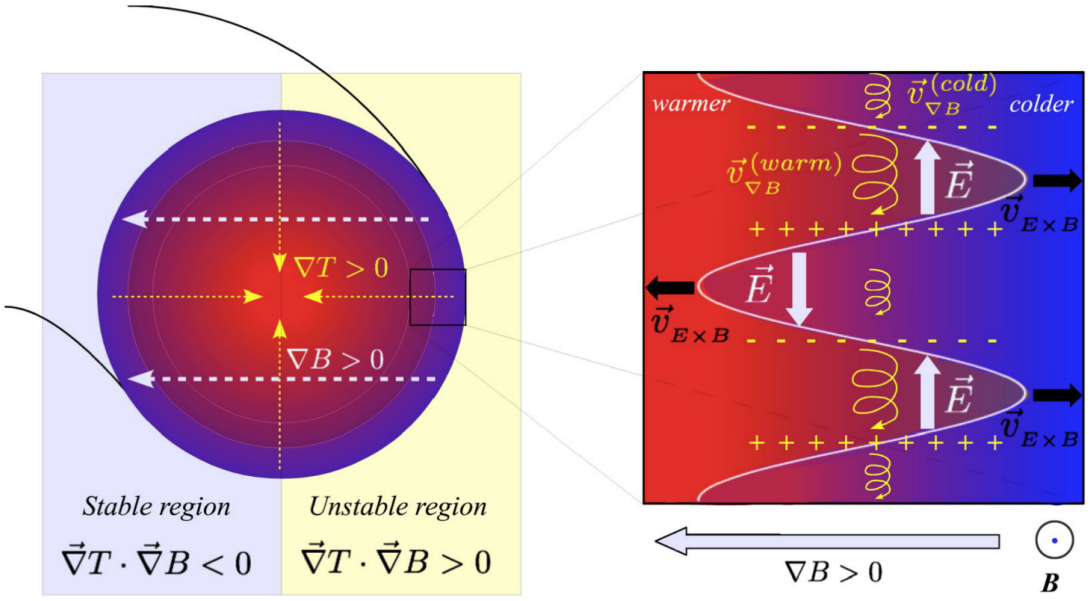

Figure 2.2: **Left:** Poloidal section of a tokamak with temperature (yellow dotted arrows) and magnetic field gradients (white dashed arrows) direction shown for clarity. **Right:** Basic mechanisms for drift-kinetic instabilities with $\mathbf{v}_{\nabla B,s} \equiv \mathbf{v}_{\nabla,s} = \frac{M_s}{q_s}\frac{\mathbf{R_c}\times\mathbf{B}}{R_c^2 B^2}\frac{1}{2}v_{\perp,s}^2$, which is proportionnal to the temperature through $v_\perp^2$, similarly as in equation (1.10). The B gradient is equivalent to gravity in Rayleigh-Taylor instabilities. Figure taken from [24].

presence of an electric field $\mathbf{E}$,

$$\frac{\partial f_s}{\partial t} + \mathbf{v}_s \cdot \boldsymbol{\nabla} f_s + \frac{q_s \mathbf{E}}{M_s} \cdot \boldsymbol{\nabla}_{\mathbf{v_s}} f_s = 0, \tag{2.27}$$

where f_s and $\mathbf{v}_s = \frac{\mathbf{E}\times\mathbf{B}}{B^2} + \mathbf{v}_{s,\parallel}$ are respectively the distribution function and velocity of the gyro-center of the species considered (e = electrons, i = ions), where only the $\mathbf{E}\times\mathbf{B}$ and parallel components are not zero. The magnetic field $\mathbf{B}$ is constant and directed along the z direction, meaning that $\mathbf{B} = B_0\mathbf{b} = B_0\mathbf{e_z}$. Equation (2.27) is called the Vlasov drift-kinetic equation and is valid for guiding-centers without larmor radius effects taken into account.

The system was considered isothermal ($T_e = T_i \equiv T_0$) with a non-zero temperature gradient ($T_0 = T_0(x)$) but with a flat density profile ($n_0 = cst$). This set of assumptions ultimately led to the following dispersion relation

$$\int_{-\infty}^{+\infty} \frac{v_z dv_z}{\omega - k_z v_z} \left\{ \underbrace{\left[\frac{M_i}{M_e}\frac{\partial f_{0e}}{\partial v_z} + \frac{\partial f_{0i}}{\partial v_z}\right]}_{\text{Velocity gradient}} + \underbrace{\frac{k_y}{k_z}\frac{1}{\omega_c}\frac{\partial}{\partial x}(f_{0i} - f_{0e})}_{\text{Space gradient}} \right\} = 0, \tag{2.28}$$

where f_{0s} is the unperturbed (Maxwellian) distribution function of the considered species, v_z is the velocity along the magnetic field, ω and $k_{y,z}$ are respectively the

pulsation and wave vectors of the perturbation, $\omega_c = q_i B/M_i$ is the ion Larmor pulsation and M_s is either the ion or electron mass. Since the analysis was done locally, $k_x \equiv 0$. Equation (2.28) posesses a velocity gradient part, reminiscent of the ion acoustic oscillations, while the space gradient part is related to inhomogeneity in the plasma (i.e. temperature gradient in the present case). In the hydrodynamic limit $v_{T,i} = \sqrt{\frac{T_0}{M_i}} \ll \frac{\omega}{k_z} \ll \sqrt{\frac{T_0}{M_e}} = c_s$ and without density gradient, the solution to the dispersion relation writes

$$\omega = \frac{1}{\sqrt{3}}(1+2i)\left(\frac{k_y}{k_z}\frac{d\log T}{dx}k_z^3\frac{2T^2}{M^2\omega_c}\right)^{1/3} \tag{2.29}$$

where the only possible way to have a non-zero imaginary part, thus a growth rate for the instability, is to have a non-zero temperature *and* temperature gradient. This can be easily understood since larger temperature gradients increase the amount of free energy available for the unstable modes to grow. However, heavier particles as well as larger magnetic field are, in this framework, more likely to linearly stabilize - or at least reduce the growth rate - of ITG modes.

This simple approach shows the importance of gradients in tokamak plasmas and their impact on the stability of the system. However, this approach is not a fully kinetic one as the resonnance is discarded through the hydrodynamic limit approach. Also, the effect of a density gradient is not taken into account here. Nonetheless, Rudakov and Sagdeev have shown in their work that in a slab geometry, this temperature drift instability is dominant in terms of scale as well as in transport coefficient magnitude.

Kadomtsev and Pogutse [26] derived a more refined fluid criterion which takes into account the stabilizing effects of density gradient on ITG modes. More precisely, they found that higher $\eta \equiv \kappa_T/\kappa_n = \partial_r \log T_i/\partial_r \log N_i$ factors further excites the said instability. They further investigated plasma drift instabilities [27] by adding sheared lines of force in their model to better describe toroidal geometry for both electrons and ions in a localized radial region. Further investigations done by Coppi, Rosenbluth and Sagdeev [28] were able to establish an integral equation describing and governing the structure of the instability for a complex magnetic configuration in a slab geometry. In that case, strong magnetic shear is found to stabilize ITG modes.

Guzdar et al. [29] explored the stability of ITG modes in a similar toroidal configuration using a ballooning mode formalism. This allowed them to treat the full kinetic problem and derive an equation which governs ITG modes and different limits were explored, both analytically and numerically. The main output from their work is the destabilizing effect of toroidal geometry on ITG modes for $\eta > 1$.

Expansion with density gradient

The previous analysis is unfortunately not taking into account the effect of the density gradient. We therefore propose to extend this analysis by adding the aforementionned density gradient and explore *both* the kinetic framework and the hy-

drodynamic limit. For this purpose, we start from equation (2.27) and explore the two following paths:

1. Linearize equation (2.27) and the quasi-neutrality equation to extract a kinetic dispersion relation $D(k,\omega)$. This should give us more information on the instability, but may not be analytically solvable.

2. Derive fluid equations by integrating over the velocity space and linearize the resulting set of equations as well as the quasi-neutrality equation.

First, let's investigate the kinetic case by linearizing equation (2.27). The main assumptions are as follows:

- $f = f_M + f_1$ with the unperturbed term being an equilibrium Maxwellian distribution function $f_M\left(r, v_\parallel\right) = \frac{n_0}{\sqrt{2\pi}v_{T,i}} \exp\left(-\frac{v_\parallel^2}{2v_{T,i}^2}\right)$ with $v_{T,i} = \sqrt{\frac{T}{M}}$ the thermal velocity while the perturbed one is taken as $f_1 = \sum_{k_\parallel,m,\omega} \hat{f}_{k_\parallel,m,\omega} \exp\left[i\left(k_\parallel z + m\theta - \omega t\right)\right]$.
  We recall that in our analysis, the space variables are such that $x \leftrightarrow r$, $r\theta \leftrightarrow y$ and $\parallel \leftrightarrow z$, making this study similar to the slab approach.

- The electrostatic potential is also written $\phi = \phi_0 + \phi_1$ with the perturbed term written as $\phi_1 = \phi_0(r) + \sum_{k_\parallel,m,\omega} \hat{\phi}_{k_\parallel,m,\omega} \exp\left[i\left(k_\parallel z + m\theta - \omega t\right)\right]$

- The analysis is done locally such that $k_r \equiv 0$, similarly as the study presented previously.

- Velocity is such that $\mathbf{v} = \mathbf{v}_{E\times B} + v_\parallel \mathbf{b}$. Here, the $\mathbf{E}\times\mathbf{B}$ velocity is only dependant on space through the electrostatic potential and is written $\mathbf{v}_{E\times B} = \frac{(\mathbf{E}_0+\mathbf{E}_1)\times\mathbf{B}}{B^2}$ with $\mathbf{E}_0 = -\boldsymbol{\nabla}\phi_0$ and $\mathbf{E}_1 = -\boldsymbol{\nabla}\phi_1$.

- Since we also consider a thermal equilibrium between electrons and ions, the former are faster than the latter, leading to the ordering $\sqrt{\frac{T_0}{M_i}} \ll \frac{\omega}{k_\parallel} \ll \sqrt{\frac{T_0}{M_e}}$ and to a Boltzmann distribution for the electrons such that $n_e/n_0 \approx 1 + \frac{e\phi}{T_0}$.

Linearizing equation (2.27) with this set of assumptions and discarding non-linear terms (i.e. quadratic terms and above), we get a relationship between f_1 and the perturbed electrostatic potential ϕ_1

$$\hat{f}_{k_\parallel,m_\theta,\omega} = -\frac{q\hat{\phi}_{k_\parallel,m,\omega}}{M_i v_{T,i}^2} f_0 \frac{k_\theta \rho_c v_{T,i}\left[\frac{\partial_r n_0}{n_0} + \frac{\partial_r T_0}{2T_0}\left(\frac{v_\parallel^2}{v_{T,i}^2} - 1\right)\right] - k_\parallel v_\parallel}{\omega - \frac{k_\theta}{B}\partial_r\phi_0 - k_\parallel v_\parallel}. \tag{2.30}$$

To get a dispersion relation, we need to close the system of equation with the quasi-neutrality equation

$$n_e \approx n_i \longrightarrow 1 + \frac{e\phi}{T_0} \approx \frac{1}{n_0}\int_{-\infty}^{+\infty} f_i dv_\parallel + \frac{n_{pol}}{n_0}, \tag{2.31}$$

with n_{pol} the polarization density of the ions. This correction is due to the change of electric field amplitude on the Larmor radius trajectory of the considered particle and can be written as

$$n_{pol} = \boldsymbol{\nabla}_\perp \cdot \left[\frac{n_0}{\omega_c B_0} \boldsymbol{\nabla}_\perp \phi \right], \tag{2.32}$$

and is equivalent to adding the polarization density $\mathbf{v}_{pol}$ to the total guiding-center velocity in equation (1.12). We combine equation (2.30) with equations (2.31) and (2.32) to get the dispersion relation

$$D(\mathbf{k}, \omega) = 2 + k_\perp^2 \rho_c^2 - \int_{-\infty}^{+\infty} f_M dv_\parallel \frac{\omega^\star - k_\parallel v_\parallel}{\omega - \frac{k_\theta}{B} \partial_r \phi_0 - k_\parallel v_\parallel}, \tag{2.33}$$

with

$$\omega_{n,T}^\star = \frac{k_\theta \rho_c v_{T,i}}{\{n_0, T_0\}} \frac{\partial \{n_0, T_0\}}{\partial r} \tag{2.34}$$

the gradient length frequency. Other terms are $k_\perp^2 \equiv k_\theta^2$ the perpendicular wavevector, $\rho_c^2 = \frac{T_0 M}{q_i^2 B_0^2}$ the squared ion Larmor radius and $\omega^\star = \omega_n^\star + \omega_T^\star \left(\frac{v_\parallel^2}{2 v_{T,i}^2} + \frac{1}{2} \right)$ the diamagnetic frequency.

Equation (2.33) shows a resonnance (i.e. a singularity) at $v_\parallel = \omega / k_\parallel + \frac{k_\theta}{k_\parallel B} \partial_r \phi_0$ which indicates an energy transfer between the instability wave and particles when this criterion is fullfilled. The ϕ_0 component only modifies the equation by applying a Doppler shift on the resonnance. One can try to solve this integral for 3 different cases for ω. When ω is such that its imaginary part is negative, this integral can be solved and the instability is damped. The pole at $v_\parallel = \omega / k_\parallel + \frac{k_\theta}{k_\parallel B} \partial_r \phi_0$ can be avoided and we are in a stable case. If its imaginary part is zero, then the pole must be taken into account when integrating by using the Residue theorem. This corresponds to the threshold for which the instability can grow and will depend on the plasma parameters, mainly $\omega_n^\star$ and $\omega_T^\star$. In this particular case, equation (2.33) can be separated into two distinct equations; one for the imaginary part, another one for the real part, which gives

$$\Re \left[D(\mathbf{k}, \omega) \right] = 0 = 2 + k_\perp^2 \rho_c^2 + \mathcal{P} \int_{-\infty}^{+\infty} f_M dv_\parallel \frac{\omega^\star - v_\parallel k_\parallel}{\omega - \frac{k_\theta}{B} \partial_r \phi_0 - k_\parallel v_\parallel}, \tag{2.35}$$

$$\Im \left[D(\mathbf{k}, \omega) \right] = 0 = \pi \delta \left(\omega - \frac{k_\theta}{B} \partial_r \phi_0 - k_\parallel v_\parallel \right) f_M \left[\omega_n^\star - \frac{k_\theta}{B} \partial_r \phi_0 - v_\parallel k_\parallel \right] \tag{2.36}$$

by using Cauchy's integral formula where $\mathcal{P}$ refers to the main part of the integral (i.e. without the pole). This equation does not admit any "obvious" solution but can be solved numerically for different sets of density and temperature gradient. This gives us the local linear threshold of the ITG instability in a slab geometry. An alternative approach, called *multi water-bag* [30], can also be used to solve this problem numerically in an elegant way.

Fluid approach

To study the fluid case, one can average over the velocity space the different moments of equation (2.27) for ions by computing

$$\int_{-\infty}^{+\infty} Adv_{\parallel} \frac{\partial f_i}{\partial t} + \int_{-\infty}^{+\infty} Adv_{\parallel} \mathbf{v}_i \cdot \boldsymbol{\nabla} f_i + \int_{-\infty}^{+\infty} Adv_{\parallel} \frac{q_i \mathbf{E}}{M_i} \cdot \boldsymbol{\nabla}_{\mathbf{v_i}} f_i = 0, \tag{2.37}$$

where A is replaced by 1 to get the continuity equation, $M_i v_{i,\parallel}$ to get the momentum conservation equation and $M_i v_{i,\parallel}^2$ to get the pressure conservation equation. Hereafter, we drop the i subscript since we will only tackle ions while electrons will be considered adiabatic. When required, an e subscript will be used for electrons. Computation details are available on appendix B.2. Ultimately, one can get the following set of fluid equations:

$$\frac{\partial n}{\partial t} + \frac{\mathbf{E} \times \mathbf{B}}{B^2} \cdot \boldsymbol{\nabla} n + \frac{\partial}{\partial z}\left(n u_{\parallel}\right) = 0, \tag{2.38}$$

$$Mn\left[\frac{\partial}{\partial t} + \frac{\mathbf{E} \times \mathbf{B}}{B^2} \cdot \boldsymbol{\nabla} + u_{\parallel}\frac{\partial}{\partial z}\right] u_{\parallel} = q_i E_z n - \frac{\partial P_{\parallel}}{\partial z}, \tag{2.39}$$

$$\left[\frac{\partial}{\partial t} + \frac{\mathbf{E} \times \mathbf{B}}{B^2} \cdot \boldsymbol{\nabla}\right] P + \frac{\partial Q_{\parallel}}{\partial z} + \frac{\partial u_{\parallel} P_{\parallel}}{\partial z} + 2P_{\parallel}\frac{\partial u_{\parallel}}{\partial z} = 0, \tag{2.40}$$

where $n = \int_{-\infty}^{+\infty} f dv_{\parallel}$ is the guiding-center density of ions, $Mnu_{\parallel} = \int_{-\infty}^{+\infty} v_{\parallel} f M dv_{\parallel}$ is the parallel momentum of the guiding-center with $u_{\parallel}$ the parallel fluid velocity of the guiding-center, $P = \int_{-\infty}^{+\infty} \left(v_{\parallel} - u_{\parallel}\right)^2 M f dv_{\parallel}$ is the pressure and $Q = \int_{-\infty}^{+\infty} \left(v_{\parallel} - u_{\parallel}\right)^3 M f dv_{\parallel}$ is the heat flux.

This set of equations needs to be completed by a closure equation as well as an evolution equation for the electrostatic potential (i.e. the electric field / force). The latter is the quasi-neutrality equation (2.31) just as the kinetic approach while the former is imposing a null heat flux.

The linearization step is then similar to the kinetic one, except this time averaged quantities are linearized as follows;

- $n = n_0(r) + n_1$ and $T = T_0(r) + T_1$, where n_0 and T_0 are the initial, unperturbed radial density and temperature profiles of guiding-centers respectively.
- $u_{\parallel} = u_0 + u_1 \equiv u_1$ is the parallel fluid velocity of the guiding-center. We consider the equilibrium parallel flow to be zero.
- $\phi = \phi_0 + \phi_1 \equiv \phi_1$ is the electrostatic potential. As opposite to the kinetic case, we consider the equilibrium electrostatic potential to be $\phi_0 \equiv 0$.
- $P = \underbrace{n_0 T_0}_{1} + \underbrace{n_0 T_1 + n_1 T_0}_{\epsilon}$ is the guiding-center pressure. We used $P = nT$ as a state equation and discarded the $n_1 T_1 \sim \epsilon^2$ part.

After some algebra (see appendix B.3), we can extract the *local* fluid dispersion relation of ITG in a cylindrical configuration:

$$\hat{\omega}^3\left[\frac{\tau_i}{Z_i^2}+\rho_c^2k_\perp^2\right]-\hat{\omega}^2\hat{\omega}_n^\star-\hat{\omega}\left[3\left(\frac{\tau_i}{Z_i^2}+\rho_c^2k_\perp^2\right)+1\right]+(2\hat{\omega}_n^\star-\hat{\omega}_T^\star)=0 \quad (2.41)$$

where $\tau_i = T_0/T_e$, $\hat{\omega} = \omega/\Omega_\parallel$ and $\hat{\omega}^\star_{n,T} = \omega^\star_{n,T}/\Omega_\parallel$ with $\Omega_\parallel = k_\parallel v_T$. This equation admits three solutions; one real and two conjugated. The threshold for the fluid instability is the $(\hat{\omega}_n^\star, \hat{\omega}_T^\star)$ couple for which we switch from one real solution to three as shown in Figure 2.3.1, left plot. One can see that when gradient lengths tend to infinity, we retrieve the instability threshold $\eta = 2$ (green dashed line, Figure 2.3.1). One important thing to note is the effect of the Larmor radius in this dispersion relation; if those corrections are discarded (i.e. $\rho_c \to 0$ in equation (2.41)), the growth rate γ becomes positive on the whole spectrum as shown in Figure 2.3.1, right plot, which is not physical regarding the available energy as it would mean all scales gain energy indefinitely. Larmor radius corrections allows to have a finite spectrum and are therefore key to ITG modes stabilization.

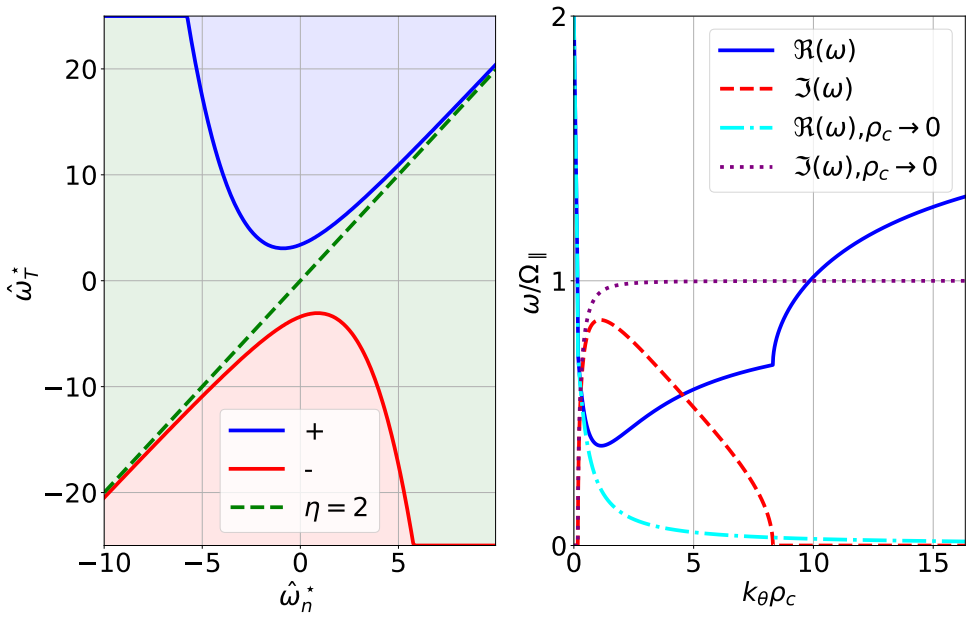

Figure 2.3: **Left:** ITG threshold map using equation (2.41) with both positive (blue) and negative (red) solutions for poloidal mode number $m = 50$, $r/a = 0.5$, $\tau_i = 1$, $B_0 = 5T$ and $T_0 = 10keV$. The limit $\hat{\omega}_{n,T} \to \pm\infty$ is the dashed green line. The region of stability is colored in green while the unstable ones are in blue and red depending on the sign of the temperature gradient. **Right:** poloidal spectrum for $r/a = 0.5$, $\tau_i = 1$, $B_0 = 5T$, $T_0 = 10keV$, $\kappa_T = 3$ and $\kappa_n = 1$ with Larmor radius effects (solid blue line for the real part of ω, dashed red line for the imaginary one, computed using (2.41)) and without (dashed-dotted cyan line for the real part of ω, dotted purple line for the imaginary one, computed using (2.41) with $\rho_c \to 0$.

Since in tokamaks, temperature and density decrease with respect to the radius, the section of interest is in the bottom left of Figure 2.3.1 (i.e. $\partial_r \{n, T\} < 0$). This

means in tokamaks, steeper density gradients will tend to stabilize ITG modes for a given temperature gradient. A more precise criterion [31] can be determined for toroidal geometry and is written

$$\kappa_{T,i}^{crit} = max \left\{ \begin{array}{c} (1+\tau)\left(1.33+1.91\frac{s}{q}\right)(1-1.5\epsilon)\left(1+0.3\epsilon\frac{d\kappa}{d\epsilon}\right) \\ 0.8\kappa_{n,i}, \end{array} \right\} \tag{2.42}$$

which depends on $\tau = Z_i \frac{T_e}{T_i}$ as well as the safety factor q, magnetic shearing s, elongation κ and inverse aspect ratio ϵ.

2.3.2 Quasi-linear approach and transport

One can extend the previous linear kinetic approach with a *quasi-linear* approach. The idea is to keep the linear solution obtained for the perturbed distribution function f_1 and derive a slow time evolution equation for f_0, meaning $\left|\frac{\partial f_0}{\partial t}\right| \ll \omega \left|f_1\right|$. For this, we start again from equation (2.27) which we developped using $f = f_0 + f_1$ and $\phi = \phi_0 + \phi_1$ before removing the linear terms (See appendix B.1.2). This leads to a phase-space flux that can be written

$$\Lambda_{QL}^r = \langle -f_1 \partial_\theta \phi_1 / Br \rangle_\theta \,. \tag{2.43}$$

This term can be further refined by writing the full perturbed terms as Fourier series and averaging over θ

$$\Lambda_{QL}^r = \sum_{k_\parallel, k_\theta, \omega} -\frac{ik_\theta}{B} \left|\hat{\phi}_{k_\parallel, k_\theta, \omega}\right|^2 f_M \frac{q_i}{T_0} \frac{k_\theta \rho_c v_T \left[\frac{\partial_r n_0}{n_0} + \frac{\partial_r T_0}{2T_0}\left(\frac{v_\parallel^2}{v_T^2} - 1\right)\right] - \frac{k_\theta}{B}\partial_r \phi_0 - k_\parallel v_\parallel}{\omega - \frac{k_\theta}{B}\partial_r \phi_0 - k_\parallel v_\parallel} \tag{2.44}$$

before integrating over the velocity space to get a particle flux (see appendix B.1.3)

$$\Gamma_{QL}^r = \int dv_\parallel \sum_{k_\parallel, k_\theta, \omega} -\frac{\gamma k_\theta}{B} \left|\hat{\phi}_{k_\parallel, k_\theta, \omega}\right|^2 f_M \frac{q_i}{T_0} \frac{k_\theta \rho_c v_T \left[\frac{\partial_r n_0}{n_0} + \frac{\partial_r T_0}{2T_0}\left(\frac{v_\parallel^2}{v_T^2} - 1\right)\right] - \frac{k_\theta}{B}\partial_r \phi_0 - k_\parallel v_\parallel}{\left(\Omega_R - k_\parallel v_\parallel\right)^2 + \gamma^2}, \tag{2.45}$$

with $\Omega_R = \omega_r - \frac{k_\theta}{B}\partial_r \phi_0$ and γ the linear growth rate of the considered instability. This expression gives very important information about turbulence behaviour. First, one can see it is proportionnal to the linear growth rate of the instability γ as well as the potential fluctuations $\left|\phi_{k_\parallel, k_\theta, \omega}\right|^2$; this means the particle flux only exists if the instability *can grow* and more specifically *if it has already developped* (i.e. the linear growth of the instability has already taken place).

Second, the flux here is *outward* since the gradient of density and temperature are negative (i.e. it decreases going outward). To make this more obvious, we can rewrite equation (2.45) with $\kappa_n = -\partial_r \ln n_0$ and $\kappa_T = -\partial_r \ln T_0$

$$\Gamma^r_{QL} = \int dv_\parallel \sum_{k_\parallel,k_\theta,\omega} \frac{\gamma k_\theta}{B} \left|\hat{\phi}_{k_\parallel,k_\theta,\omega}\right|^2 f_M \frac{q_i}{T_0} \frac{k_\theta \rho_c v_T \left[\kappa_n + \frac{\kappa_T}{2}\left(\frac{v_\parallel^2}{v_T^2} - 1\right)\right] + \frac{k_\theta}{B}\partial_r\phi_0 + k_\parallel v_\parallel}{\left(\Omega_R - k_\parallel v_\parallel\right)^2 + \gamma^2}. \tag{2.46}$$

This form also allows us to see two terms often discussed in litterature; namely the turbulent diffusion $\Gamma^{turb}_{diff} = D^{turb}_{QL} n_0 \kappa_n$ and thermo-diffusion $\Gamma^{turb}_{thermo} = -C^{turb}_{QL} T_0 \kappa_T$. By identification, those coefficients write

$$D^{turb}_{QL} = \int dv_\parallel \sum_{k_\parallel,k_\theta,\omega} \frac{\gamma k_\theta}{B} \left|\hat{\phi}_{k_\parallel,k_\theta,\omega}\right|^2 f_M \frac{q_i}{n_0 T_0} \frac{k_\theta \rho_c v_T}{\left(\Omega_R - k_\parallel v_\parallel\right)^2 + \gamma^2}, \tag{2.47}$$

$$C^{turb}_{QL} = -\int dv_\parallel \sum_{k_\parallel,k_\theta,\omega} \frac{\gamma k_\theta}{B} \left|\hat{\phi}_{k_\parallel,k_\theta,\omega}\right|^2 f_M \frac{q_i}{2T_0^2} \frac{k_\theta \rho_c v_T \left(\frac{v_\parallel^2}{v_T^2} - 1\right)}{\left(\Omega_R - k_\parallel v_\parallel\right)^2 + \gamma^2}, \tag{2.48}$$

where it readily appears that D^{turb}_{QL} will always be positive and is reduced with higher values of the magnetic field thanks to its dependance in B^{-2}. However, C^{turb}_{QL} can change sign depending on the parallel velocity value. If the distribution function is not Maxwellian or at least with non-negligeable fast particles populations, thermo-diffusion can increase outward particle flux.

The last term, written

$$\Gamma^r_{QL,\parallel} = \int dv_\parallel \sum_{k_\parallel,k_\theta,\omega} \frac{\gamma k_\theta}{B} \left|\hat{\phi}_{k_\parallel,k_\theta,\omega}\right|^2 f_M \frac{q_i}{T_0} \frac{\frac{k_\theta}{B}\partial_r\phi_0 + k_\parallel v_\parallel}{\left(\Omega_R - k_\parallel v_\parallel\right)^2 + \gamma^2}, \tag{2.49}$$

is an exchange/pumping term between parallel and perpendicular fluxes.

It is interesting to note that the resonnance with this model appears on the parallel velocity as opposed to the gyro-bounce model [32], which captures the perpendicular dynamics with a resonnance depending on the precession frequency. This leads to another interesting effect; It seems that there is no obvious scaling with the charge in the presented work, which only treats passing particles since there is no B gradient and thus no magnetic trapping effect. Conversely, the gyro-bounce model only treats the trapped particles and shows a dependance on the ion charge number.

2.3.3 Other instabilities

Generic instabilities

Streaming instabilities can arise in tokamaks because of the difference in plasma frequency between electrons $\omega_{p,e} = \sqrt{ne^2/m_e\epsilon_0}$ and ions $\omega_{p,i} = \sqrt{m_e/M_i}\omega_{p,e}$; if

the perturbations have a wavelength such that $\omega_{p,e} + kV_e \approx \omega_{p,i}$, then the density fluctuations can be in phase for both species and waves in both fluides (i.e. ions and electrons) can grow simultaneously.

Equivalently to neutral fluids, Rayleigh-Taylor (see Figure 2.4 for the classical fluid Rayleigh-Taylor instability) instabilities can grow in tokamak's plasmas due to the centrifugal force pushing particles from the core (denser and thus heavier fluid) to the outside (sparse and therefore lighter fluid). It appears clearly that this problem only occurs on the outer part of the tokamak since density gradient and centrifugal force are directed the same way. This instability starts from small oscillations on pressure isocontours which are enhanced by the difference in centrifugal force felt by the perturbed regions. It results in waves propagating in the poloidal direction and leads to flute-shaped structures (See Figure 2.5, left). They are similar to drift-wave instabilities discussed in the previous section (i.e. ITG modes) but do not propagate along the magnetic field.

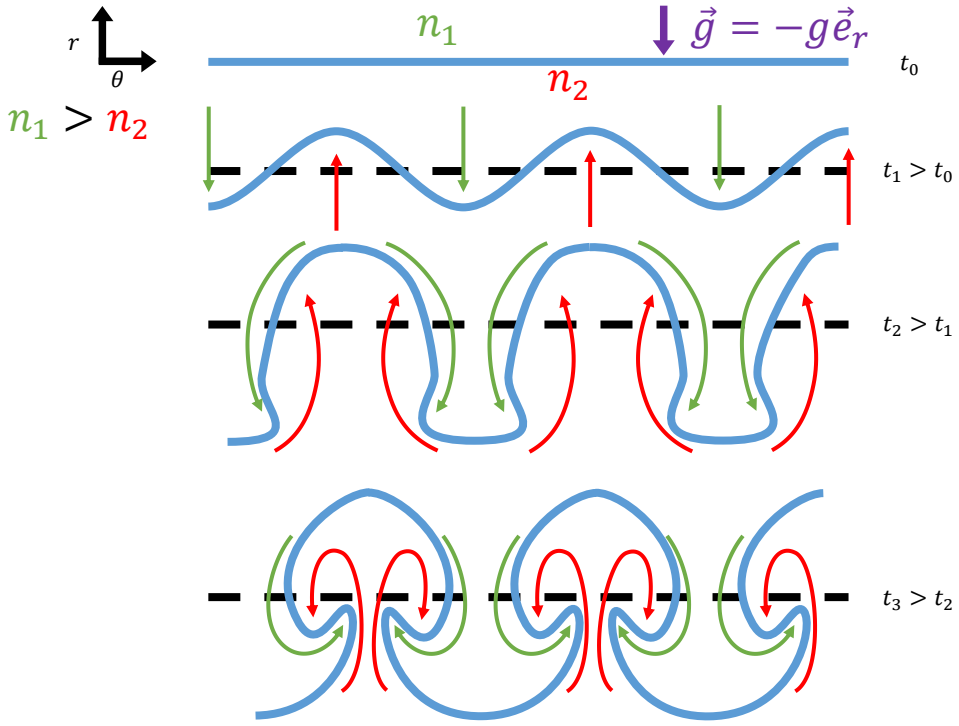

Figure 2.4: Schematic representation of Rayleigh-Taylor instability structures with two fluid layers of different densities, the heavier being on top of the lighter. If small fluctuations appear at the boundary between the two layers, the heavier fluid will drop in the lighter one and vice-versa, resulting in this type of structure. Note that gravity can in fact impact tokamaks by adding a drift velocity $\mathbf{v}_g = \frac{M_s}{q_s}\frac{\mathbf{g}\times\mathbf{B}}{B}$ by using equation (1.8) and replacing $\mathbf{F}$ by $M_s\mathbf{g}$. This will lead to similar effects as the one shown in Figure 2.2.

TEM

Though ITG modes and ion heat transport are intensely studied, electron particle and heat transport is slightly less documented. However, it has been shown that

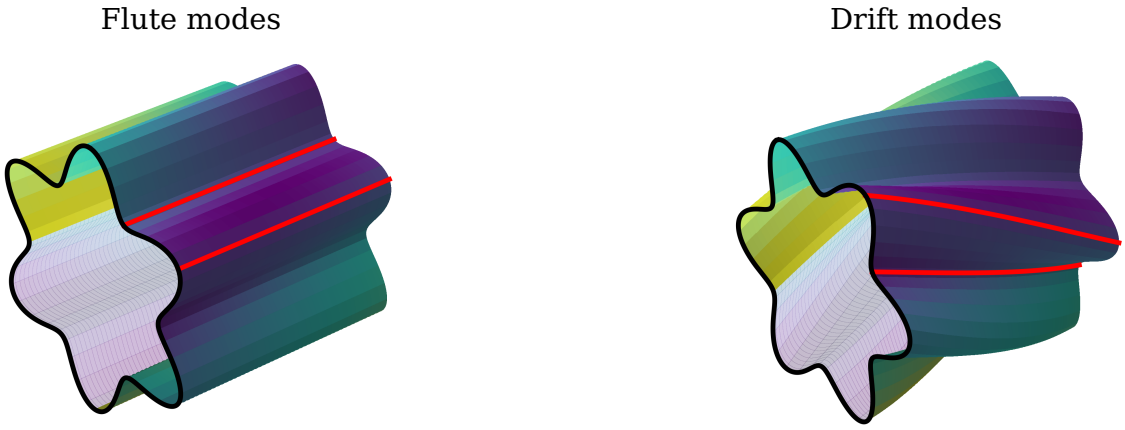

Figure 2.5: Flute (left) and drift (right) instability modes in a cylinder. Here, modes of $m = 6$ are represented with no parallel component to the magnetic field (i.e. $n = 0$, flute modes) and with an arbitrary parallel mode (i.e. $n \neq 0$, drift modes). Red lines are isocontours of the considered quantity, like pressure for example, and are twisted if $n \neq 0$.

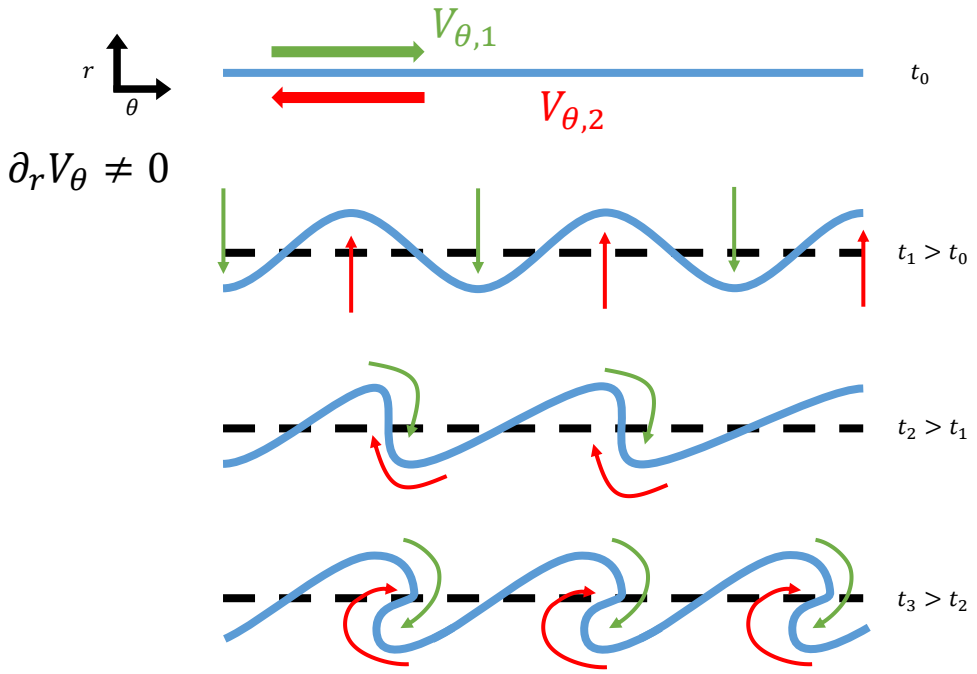

Figure 2.6: Schematic representation of Kelvin-Helmholtz instability structures with two fluid layers going opposite directions. If a slight disturbance appears at the boundary between the layers, it will result in eddy formation. This type of instability is common in our atmosphere.

TEM (i.e. Trapped Electron Modes) instability is a suitable candidate to explain the electron fluxes observed in experiments, especially when the primary source of heating is electron heating (i.e. through ECRH - Electron Resonance Cyclotron Heating -). This instability is similar to ITG modes with a drift-mode like structure as in Figure 2.5 and takes its source in electron temperature and/or density gradients depending on the experiment itself. However usual TEM turbulence scale ($0.01 < k_\perp \rho_i < 1$) overlaps that of ITG ($0.1 < k_\perp \rho_i < 1$) [33], which makes it more difficult to distinguish them apart in real experiments. Some indicators were found to be suitable to discriminate TEMs signature from ITG [34]. Also, numerical simulations of TEM turbulence were able to reproduce the wavelength spectrum measured in an Alcator C-Mod experiment [35]. In this experiment, TEMs were expected to be dominant relative to other instabilities. A number of models and simulations investigating this instability [36, 37] showed how it differenciates from ITG modes by reaching saturation based on different mechanisms.

TEMs are expected to play a major role especially in bigger tokamaks, like ITER [38], where electron heating systems are more powerful than in existing experiments.

Note that the counterpart of TEMs and ITG exist, namely TIMs (Trapped Ion Modes) and ETG (Electron Temperature Gradient), but are far less impacting tokamak turbulence.

However, since electrons are taken adiabatic in the model we use for the study presented here, TEMs will not be part of the instabilities we may encounter.

PVG and TVG

Parallel Velocity Gradient (PVG in short) instability was first introduced by D'Angelo [39] and is, in fact, analogous to the Kelvin-Helmholtz instability (flute modes, see Figure 2.5). It originates from radial layers of fluid with different parallel velocity. In other terms, it comes from strong radial gradients of parallel velocity as shown in its relatively simple instability criterion [40] $\left|\frac{ML_n}{L_\Gamma}\right| > 1$, with $L_\Gamma = \left[\frac{1}{n_{eq}V_{\parallel,eq}}\frac{d\left(n_{eq}V_{\parallel,eq}\right)}{dr}\right]^{-1}$ and $L_n = \left[\frac{1}{n_{eq}}\frac{dn_{eq}}{dr}\right]^{-1}$, respectively the parallel flux and density gradient lengths. More in-depth studies on this instability, which may be relevant for linear machines, are conducted by T. Rouyer whose PhD started at IJL in december 2022.

Transverse Velocity Gradient (i.e. TVG) instability is not discussed as much as PVG and was first introduced by Kent [41] and further studies [42]. This instability is theoretically possible in tokamaks provided the radial gradient of poloidal velocity (i.e. $\partial_r v_\theta$) is strong enough to trigger a Kelvin-Helmoltz-like instability as illustrated in Figure 2.6. However, poloidal shearing can be beneficial for plasma confinement and help creating *transport barriers*.

2.4 Transport barrier

Turbulent transport significantly reduces confinement time in tokamaks due to the increased particle and heat fluxes. The normal state of a tokamak is therefore

considered as a "Low-confinement" mode, commonly referred to as L-mode, which is highly turbulent. However, overall transport can be reduced (i.e. increasing confinement time) by triggering a plasma transition to an improved confinement state. Such a transition involves the creation of a transport barrier which can be localized in the plasma core (ITB for Internal Transport Barrier) or at the edge (ETB for Edge Transport Barrier) and may involve strong poloidal $E \times B$ shear in some cases.

2.4.1 Edge Transport Barriers (ETBs) and L-H transition

The first case of such a transition was reported by Wagner et Al. in 1982 [43] in ASDEX, a tokamak formerly based in Garching, Germany and continued as HL-2A by the China National Nuclear Corporation at Chengdu, China. This transition was triggered by neutral beam injection (i.e. **NBI**). Neutrals are injected into the plasma in a straight line at high energy levels, usually tangentially to the plasma current present in the plasma to further enhance the said current as well as toroidal momentum. Through hard collisions with ions, the light neutrals injected deposit their energy in the plasma and increase the ions kinetic energy (i.e. their temperature). Also, this method is useful to partially fuel the said plasma with specific species since neutrals that collide in the plasma will get ionized and be part of the plasma as a result. In the case of the presented ASDEX discharge, the confinement enhancement was characterized by a sudden increase in both electron density and temperature in the core plasma shortly after NBI activation. Example of pressure and density profiles in presence of an ETB is presentend in Figure 2.7. This indicates the formation of an ETB, meaning transport coefficients are severely reduced at the plasma edge hence the influx reduction observed at the divertor plate.

However, the higher confinement regime (called H mode hereafter) reached in ASDEX presented some problems in the outer region of the plasma near the separatrix. Short bursts of density and temperature reduction were observed indicating losses due to quasi-periodic ETB collapses which later got called *Edge Localized Modes* (ELMs).

Similar results were soon observed in DIII-D [44] in a similar divertor magnetic configuration by also using NBI.

First hints of the ingredients needed to trigger L-H transitions were later found by the DIII-D team [45] who was able to measure the radial electric field at the separatrix position during the whole shot. As it turns out, a huge increase in the electric field amplitude is observed during the L-H transition and stays at around 4 times the L mode value during the whole H mode time interval before dropping back to its L mode value at the end. Even more interesting was that during ELMs events, the radial electric field dropped back to its L mode values. In other terms, strong $E \times B$ poloidal velocity (i.e. radial electric field) is correlated with the presence of an active transport barrier.

The JFT-2M [46] team was able to measure the radial electric field radial profile at the edge and showed that not only the E_r well amplitude was larger, but also its radial derivative $\partial_r E_r$. The position of this strongly sheared radial electric field

also coincides with strong electron and ion pressure gradients. Similar results were obtained afterwards for DIII-D [47] with E_r width of a few centimeters, which is around 10 Larmor radius for both DIII-D and JFT-2M.

Results from ASDEX Upgrade [48, 49], Alcator C-mod [50], COMPASS [51], JET [52] and MAST [53] all converge with similar radial electric field and pressure profiles (See appendix C.1 for data about the electric field characteristics), meaning the ETBs created during those experiments are probably related to the same physics phenomena.

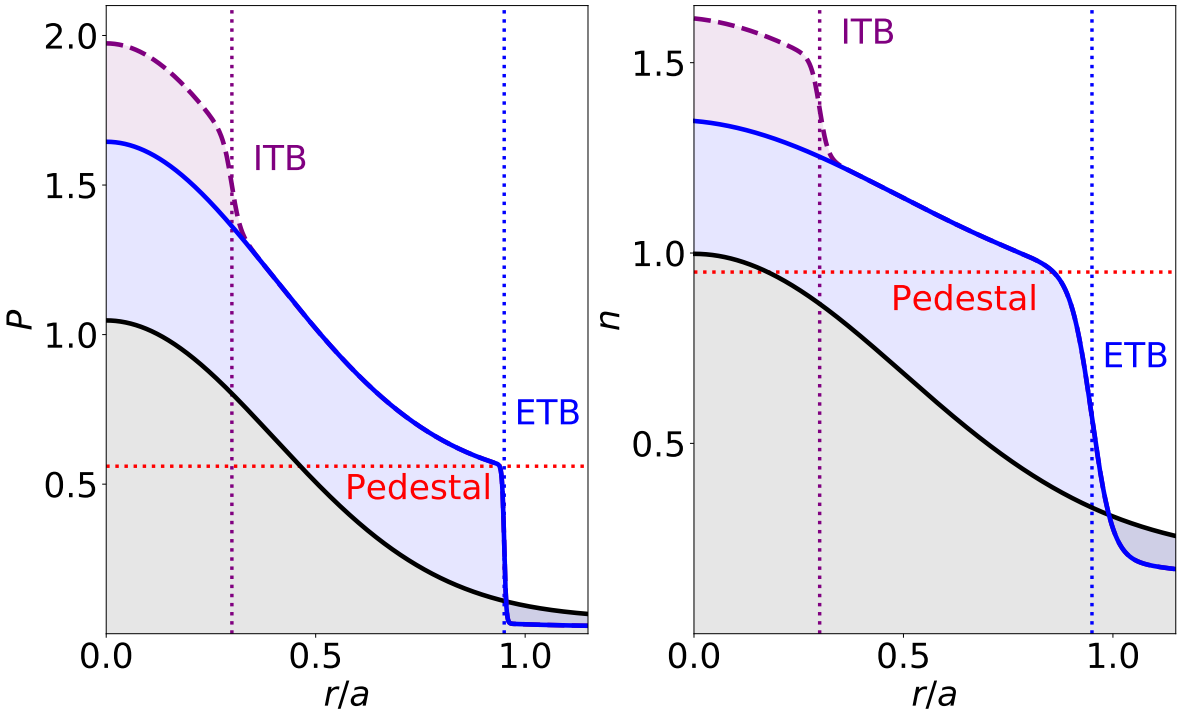

Figure 2.7: Examples of pressure (left) and density (right) profiles expected during ITB (purple) and ETB (blue) events. Black line represent the standard L-mode. Vertical lines correspond to the position of the corresponding transport barriers.

2.4.2 Internal transport barriers

In addition to ETBs, barriers localized in the core plasma can also be triggered through different means. As opposite to ETBs, it is more complicated to define exactly what ingredients generate ITBs. However, it is generally admitted that when the temperature gradient increases significantly in a thin radial region in the core (i.e. $r/a \lesssim 0.6$) combined with a strongly reduced turbulent activity indicate that an ITB event has been triggered. Typical profiles are shown in Figure 2.7.

The TFTR (Tokamak Fusion Test Reactor) team reported a first successful ITB event [54] by using a reversed magnetic shear profile (i.e. $s(r) = rq^{-1}\partial_r q$) in the core and by using a NBI heating system. Ion thermal diffusivity dropped by a factor of 40 (i.e. even lower than predicted neoclassical values) in the reversed shear radial region leading to peaked density and temperature profiles in the core.

Similar results were found almost at the same time by the DIII-D team [55, 56] with a strong confinement enhancement in the radial region of reversed magnetic shear. However, they found that reversed magnetic shear alone is not sufficient to trigger this ITB. In fact, shear reversal is present *before* the ITB is observed, indicating other phenomena play a role here.

Other tokamaks were able to reach such enhanced confinement states with reversed magnetic shear configuration like JT-60U [57, 58], JET [59, 60], EAST [61] or KSTAR [62]. Some tokamaks were also able to produce both kinds of transport barriers at the same time like in JET [63] or more recently HL-2A [64].

2.4.3 Mechanisms involved

One of the shared characteristics of ITBs and ETBs is the presence of poloidally sheared $E \times B$ flows either generated by the mean electric field at the separatrix (i.e. for ETBs) or the reversed magnetic shear profile.

Part of this $E \times B$ shearing (i.e. zonal flows [65, 66, 67]) is generated by turbulence and leads to a self-regulated state through a prey-predator mechanism [68]. Those flows are radial layers of plasma which are toroidally axisymmetric (i.e. $n = 0$) and rotating in a similar fashion as Jupiter's cloud or our own atmosphere on Earth which originate from turbulence itself. Non-linear interactions and energy transfer from drift-waves modes (i.e. $(m, n) \neq (0, 0)$) and $n = 0$ modes are responsible for zonal flow triggering. This means that if the zonal flow is strong enough to reduce turbulence and thus the drift-wave modes energy by pumping it, less energy can be transferred to the zonal flows. As a result, zonal flows decay and turbulence can rise again for energy to be transferred back to $n = 0$ modes to trigger zonal flows back again, thus the prey-predator mechanism evoked earlier. Those modes cannot be sustained in the absence of turbulence and thus cannot explain transport barrier mechanisms by themselves. However, they are part of the saturation mechanism of turbulence and its regulation.

Mean $E \times B$ shear flows are the best candidates to explain L-H transitions and turbulence quench mechanisms at ETBs and ITBs events. As discussed earlier, an important increase of these flows is measured during L-H transition on every tokamak. This explains why their effects on a turbulent plasma have been widely studied [69, 70, 71, 72, 73] using different theoretical explanations for the underlying mechanisms leading to a transport quench.

First, it is very different from zonal flow since its origin is not found in turbulence itself but is generally caused by externally injected momentum. This is done by injecting heat through NBI or I/ECRH for example, and thus is not converting turbulent energy in momentum. This means that for example, even if temperature gradient can drive ITG modes and lead to a self-regulated state with zonal flow, a transport barrier triggered by $E \times B$ sheared flows will not pump energy from turbulence. It will rather reduce turbulence intensity and make the system converge towards a new equilibrium.

The effect of shear flow in general is tackled with great pedagogy by Terry [71] from which a simple phenomenological approach is proposed to understand how shear flows can suppress turbulence. A visual representation of the process is

shown in Figure 2.8 in a poloidal plane. Turbulent structures - eddies for example - can loose their coherence after some time even without background sheared flows; this defines the eddy turnover time or turbulence coherent time. However, when the velocity difference at the eddy edges is sufficiently strong, structures are elongated in the flow direction way above its "natural" (i.e. without flow shear) coherence length, hence the lifetime reduction. Also, structures elongated parallelly to the flow also undergo a reduction in perpendicular length (i.e. radial length in the case presented in Figure 2.8). Since transport occurs along those turbulent structures, a local reduction in their radial length means transport will occur on shorter radial length and time scales. Ultimately, if we consider a random walk process for transport as a first approximation (i.e. like in section 1.4.3 and equation (1.25)), the diffusion process will be severely diminished by the effects of sheared flows. An empiric criterion gives an estimate of the needed $\omega_{E\times B}$, the $E \times B$ shear rate, which should be within the same order of magnitude as γ_{lin}^{max}, the maximum linear growth rate of the instability [74], to suppress turbulence. This time scale (i.e. γ_{lin}^{-1}) is the time scale for which a particle trapped in such turbulent eddy will be transported along its contour, therefore a shear flow with a similar time scale (i.e. $\omega_{E\times B}^{-1}$) should efficiently decorrelate the structure and reduce transport.

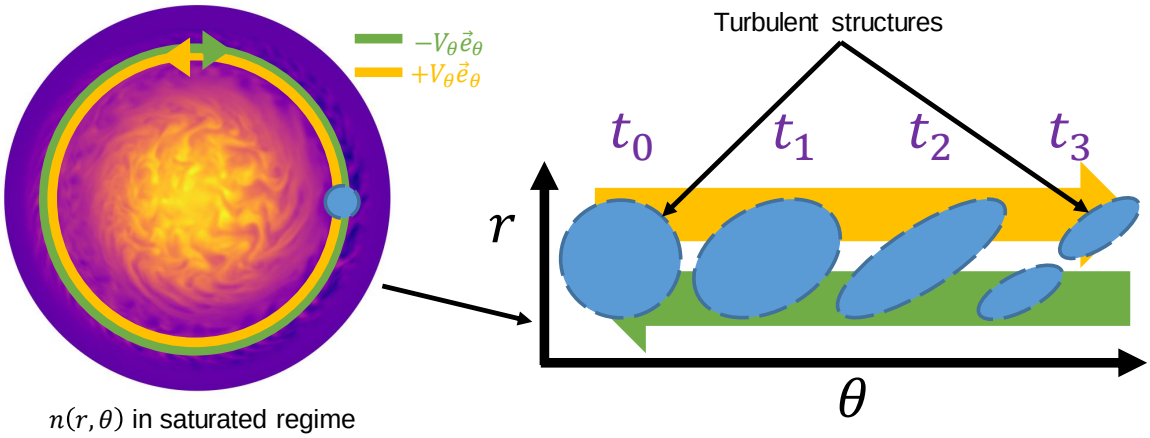

Figure 2.8: Visual representation of sheared flows in a poloidal plane. **Left:** density map in a poloidal plane in a saturated turbulence regime. Shear flow layers and a turbulent structure (i.e. a turbulent *eddy*) along which transport occurs is also represented. **Right:** The same structure is represented at different time intervals in such a r, θ plane in presence of two layers of flow shear. The structure elongation and decorrelation process is pictured.

Chapter 3

Transport barrier using a vorticity source

The results presented in this chapter are published in [75]. The chapter is therefore very similar in this manuscript with only minor modifications and additional informations when judged relevant.

3.1 Gyrokinetic modelling and GYSELA

3.1.1 Basis of gyrokinetic framework

As described in previous sections, kinetic models are among the most precise and fundamental models to describe plasmas. However, the computing accessibility of full 6D kinetic models $(r, \theta, \varphi, v_r, v_\theta, v_\varphi)$ would require computation times many orders of magnitude larger than what is currently available. A possible way to tackle this limitation is to reduce this model to a 5D gyrokinetic one by averaging on the Larmor trajectory of particles (Figure 3.1). This allows us to stay in the powerful kinetic framework by keeping crucial effects linked to micro-turbulence of time scales larger than ω_c^{-1} and discarding smaller ones.

To understand the gyrokinetic theory, the first step is to understand that the smallest scale it is able to describe will be linked to the ratio $\epsilon_B = \rho_c / L_B \ll 1$, with $L_B = \nabla B / B$ the typical gradient length scale of the magnetic field. This means the magnetic field must vary on much larger space and time scales than the Larmor radius of the considered particles. Alternatively, variations of the microscopic potential energy is small compared to the thermal energy $q_s \delta\phi / k_B T_s \ll 1$. Also, time variations of both the electric $\mathbf{E}$ and magnetic $\mathbf{B}$ fields must be negligeable during a cyclotron period, meaning $\omega_{E,B}/\omega_c \ll 1$, where $\omega_{E,B}$ is the typical pulsation for the considered fields and ω_c is the cyclotron frequency. More generally, the crucial parameter is the thermal Larmor radius of the species considered $\rho_{c,s}$ normalized to the minor radius of the tokamak a

$$\epsilon_B \sim \frac{\omega_{E,B}}{\omega_c} \sim \frac{q_s \delta\phi}{k_B T_s} \sim \mathcal{O}\left(\rho_s^\star = \frac{\rho_{c,s}}{a}\right), \tag{3.1}$$

where usually for tokamaks $\rho_{c,e^-} \approx 10^{-5}$ m and $\rho_{c,i} \approx 10^{-3}$ m.

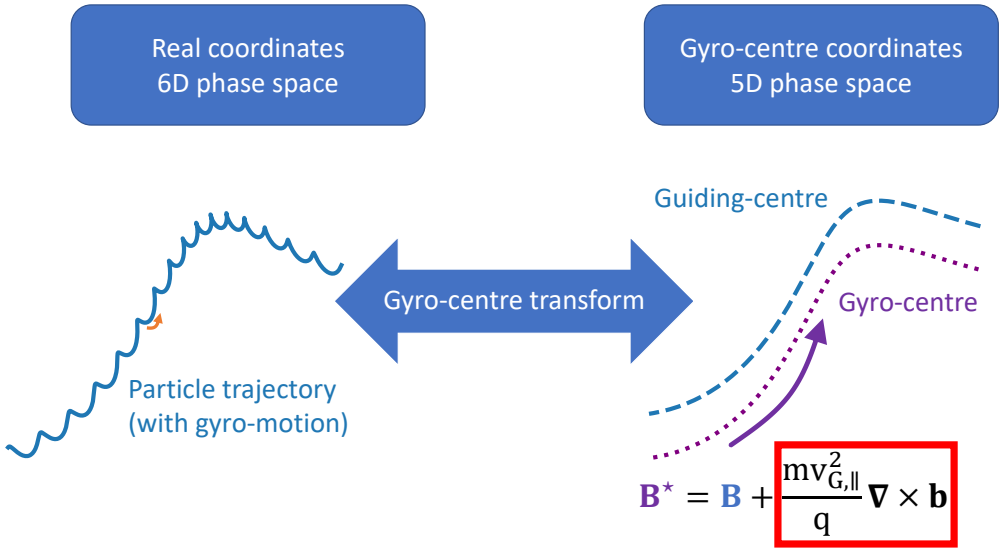

Figure 3.1: Effect of the gryro-averaging operation on the guiding-centre trajectory (6D to 5D). Figure reproduced from [76].

By keeping those limitations in mind, the gyrokinetic Vlasov equation is obtained by gyro-averaging the classic Vlasov equation using the Hamiltonian representation to conserve both symmetry and conservation properties of the used equations, namely the Vlasov and Poisson equations. This procedure is detailed with rigor in the work of A. Brizard [77] and forms the basis of the GYSELA code. In this thesis, derivation of the model will not be detailed.

3.1.2 GYrokinetic SEmi-LAgrangian

GYSELA [78] is a 5D full-f gyrokinetic electrostatic code coupling the Vlasov equation and the quasi-electroneutrality equation codevelopped by CEA/IRFM and IJL. One of the main advantage of GYSELA comes from the treatment of the entire distribution function, hence the full-f notation, meaning $\bar{F}_s$ will evolve for *each* species regardless of the scale studied, plasma being at equilibrium or subject to small fluctuations. The treatment of electrons is however less robust and is mainly limited to an adiabatic response so far. Partially kinetic electrons, more specifically the trapped ones, are under development. In this thesis, we use only adiabatic electrons, which means that up to compressional effects, the time-averaged particle transport across circular magnetic surfaces vanishes if there is only one kinetic ion species in the system. Nevertheless, main ions heat flux can still be studied with this set of assumptions. The following Vlasov equation, where the s subscript stands for the considered ion species, is solved in GYSELA for each species:

$$B^\star_{\parallel,s}\partial_t \bar{F}_s + \boldsymbol{\nabla} \cdot \left(\dot{\mathbf{x}}_{GC,s} B^\star_{\parallel,s} \bar{F}_s\right) + \partial_{v_{G_\parallel,s}} \left(\dot{v}_{G\parallel,s} B^\star_{\parallel,s} \bar{F}_s\right) = \mathcal{C}\left(\bar{F}_s\right) + \mathcal{S}\left(\bar{F}_s\right), \qquad (3.2)$$

with $\bar{F}_s$ the ion gyrocentre distribution function, $\mathbf{x}_{GC,s}$ and $v_{G_\parallel,s}$ the gyro-center position and parallel velocity respectively. They are defined through

$$B^\star_{\parallel,s}\dot{\mathbf{x}}_{GC,s} = v_{G_\parallel,s}\mathbf{B}^\star_{\mathbf{s}} + \frac{1}{Z_s}\mathbf{b}\times\boldsymbol{\nabla}\Lambda_s, \tag{3.3}$$

$$B^\star_{\parallel,s}M_s\dot{v}_{G\parallel,s} = -\mathbf{B}^\star_{\mathbf{s}}\cdot\boldsymbol{\nabla}\Lambda_s, \tag{3.4}$$

where $\Lambda_s = eZ_s\mathcal{J}\left[\phi\right] + \mu_s B$ is the gyrocenter energy with $\mu_s = M_s v^2_{\perp,s}/2B$ the magnetic moment and $\mathcal{J}$ is the gyro-average operator. The latter is important to switch from the gyro-averaged quantity (i.e. $\bar{F}_s$ or $\bar{\phi}$) to the real quantities (F_s or ϕ). When developped, equation (3.3) gives us the usual drifts mentionned in previous sections. $B^\star_{\parallel,s}$ is part of the velocity space Jacobian defined through $\mathbf{b} = \mathbf{B}/\left\|\mathbf{B}\right\|$ and $B^\star_{\parallel,s} = \mathbf{B}^\star_{\mathbf{s}}\cdot\mathbf{b} = B + \frac{M_s}{q_s}v_{G_\parallel,s}\mathbf{b}\cdot(\boldsymbol{\nabla}\times\mathbf{b})$, with

$$\mathbf{B}^\star_{\mathbf{s}} = \mathbf{B} + \frac{M_s}{q_s}v_{G_\parallel,s}\boldsymbol{\nabla}\times\mathbf{b}. \tag{3.5}$$

Equation (3.2) is coupled to the quasi-electroneutrality equation,

$$\underbrace{en_{e_0}\left(\frac{\phi - \langle\phi\rangle_{FS}}{T_e}\right)}_{\text{Adiabatic } e^- \text{ response}} - \sum_s \underbrace{Z_s\boldsymbol{\nabla}_\perp\cdot\left(\frac{n_{0,s}}{B_0\omega_{c,s}}\boldsymbol{\nabla}_\perp\phi\right)}_{\text{Polarization density}} = \sum_s \underbrace{Z_s\int dv_s\mathcal{J}\left[\bar{F}_s - \bar{F}_{eq,s}\right]}_{\text{Particle density fluctuations}}, \tag{3.6}$$

to make the GYSELA model self-consistent. A way of computing the exact or approximate polarization density in GYSELA is proposed in appendix C.2. In equation (3.6), ϕ is the *real* electrostatic potential, Z_s and M_s the charge number and particle mass of the considered ion species, B_0 the magnetic field amplitude and $\omega_{c,s} = Z_s eB_0/M_s$ the ion cyclotron pulsation. Here, dv_s is defined by $dv_s = J_{v_s}d\mu_s dv_{\parallel,s}$ with $J_{v_s} = 2\pi B^\star_{\parallel,s}/M_s$ the velocity space Jacobian. $\bar{F}_{eq,s}$ refers to the equilibrium distribution function of the species considered and is usually defined as a Maxwellian distribution. The polarization density is a correction due to the polarization drift velocity evoked in the introduction. However, the derivation made by T.S. Hahm and A.J. Brizard makes this polarization appear as a density correction of the order of the Larmor radius of the considered species. The electron polarization density is discarded since polarization is proportionnal to the particle mass ($M_e \ll M_s$).

Collisions are taken into account in the GYSELA model through the operator $\mathcal{C}\left(\bar{F}\right)$ which conserves both energy and particles [79]. Also, both *intra* and *inter* species collisions are modelled.

3.1.3 Kinetic external sources

In equation (3.2) $\mathcal{S}$ represents the source terms. This gives GYSELA the ability to run in a *flux-driven* regime where a heat source continuously heat up a select region of the plasma. This allows the pressure profile to be maintained even when

turbulence is present, the latter leading to a flattening of the pressure profile in the absence of any source. Sources have been built by projecting the parallel velocity $v_{G_\parallel,s}$ and magnetic moment μ_s onto the orthogonal basis of Hermite and Laguerre polynomials respectively [80, 81].

$$\widehat{S}_E\left(\widehat{r},\widehat{\theta},\widehat{v}_\parallel,\widehat{\mu}\right) = \sum_{l=0}^{+\infty}\sum_{h=0}^{+\infty} c_{hl} H_h\left(\bar{v}_{G,\parallel}\right) L_l\left(\bar{\mu}\right) \exp\left(-\bar{v}_{G_\parallel}^2 - \bar{\mu}\right), \tag{3.7}$$

where H_h and L_l are the Hermite and Laguerre polynomials detailed in appendix C.3, $\bar{v}_{G_\parallel,s}/\sqrt{2T_S/M_s}$ and $\bar{\mu}_s = \mu_s B/T_S$ are the normalized parallel velocity and magnetic moment. One can choose to inject particles, parallel momentum, poloidal momentum and/or energy by choosing the right c_{hl} coefficients. In the following sections, only the heat source and the poloidal momentum (equivalent to a vorticity) source are used.

The kinetic sources of heat and poloidal momentum (i.e. vorticity) are defined respectively as

$$\mathcal{S}_{\epsilon,s} = \frac{S_0^\epsilon S_r^\epsilon(r)}{\sqrt{2}\pi^{3/2}T_{S,\epsilon}^{5/2}}\left[\bar{v}_{G_\parallel,s}^2 - \frac{1}{2} + \frac{2-\bar{\mu}_s}{2-J_{\parallel,B,s}^2}J_{\parallel,B,s}\left(J_{\parallel,B,s} - 2\bar{v}_{G_\parallel,s}\right)\right]\exp\left(-\bar{v}_{G_\parallel,s}^2 - \bar{\mu}_s\right), \tag{3.8}$$

$$\mathcal{S}_\Omega = \frac{S_0^\Omega S_r^\Omega(r) B^2}{\sqrt{2}\pi^{3/2}T_{S,\Omega}^{5/2}}\left[2\bar{v}_{G_\parallel,s}^2 - \bar{\mu}_s\right]\exp\left(-\bar{v}_{G_\parallel,s}^2 - \bar{\mu}_s\right), \tag{3.9}$$

where $J_{\parallel,B,s} = \sqrt{2T_S}J_{\parallel,s}/B^2$ is defined with the parallel current $J_{\parallel,s}$ and the source temperature T_S, the latter being fixed at $T_{S,\epsilon}/T_0 = 1.5$ and $T_{S,\Omega}/T_0 = 1$ where T_0 is a reference temperature. $S_0^{\epsilon,\Omega}$ is the source amplitude and $S_r^{\epsilon,\Omega}(r)$ is the radial profile; both of them are GYSELA input parameters. The radial width of the source is chosen so that normalized values match with experimental data as presented in appendix C.1. The poloidal momentum source is built such that no heat nor particles are injected in the system. A marginal quantity of parallel momentum is injected along with the poloidal momentum as well as pressure anisotropy. This can be seen in equation (3.9) in the terms $2\bar{v}_{G_\parallel,s}^2 - \bar{\mu}_s$ which, when integrated, will respectively inject parallel pressure and pump perpendicular pressure[1] and therefore enhance the local pressure anisotropy $\Pi_{\parallel,s} = P_{\parallel,s} - P_{\perp,s}$.

Once integrated over the velocity space, one can get the fluid source of energy and vorticity for their associated fluid moment equations,

$$\mathbb{S}_\epsilon = S_0^\epsilon S_r^\epsilon\left[2 - \frac{4J_{\parallel,B,s}^2}{2-J_{\parallel,B,s}^2}\right], \tag{3.10}$$

$$\mathbb{S}_\Omega = S_0^\Omega \boldsymbol{\nabla}_\perp^2 S_r^\Omega. \tag{3.11}$$

[1] We recall that $P_{\parallel,s} = \int dv_s \frac{1}{2}\mathcal{U}^2\bar{F}_s$ with $\mathcal{U}^2 = \left(v_{G_\parallel,s} - V_{\parallel,s}\right)^2$, $P_{\perp,s} = \int dv_s \mu_s B\bar{F}_s$ and $P_{tot,s} = \frac{1}{3}P_{\parallel,s} + \frac{2}{3}P_{\perp,s}$.

To understand how the vorticity source works to inject poloidal momentum, we can look at the vorticity conservation equation,

$$\partial_t W + \partial_r \mathcal{K} = S_0 \boldsymbol{\nabla}_\perp^2 S_r^\Omega, \tag{3.12}$$

with $W = -\left\langle \boldsymbol{\nabla} \cdot \left(\frac{n_{eq,s} M_s}{B^2} \boldsymbol{\nabla}_\perp \phi \right) \right\rangle_{FS} = q_s \left\langle \int dv_s \mathcal{J} \left[\bar{F}_s \right] \right\rangle_{FS}$ the fluid vorticity, $\mathcal{K} = q_s \left\langle \int dv_s \mathcal{J} \left[(d_t \mathbf{x}_{G,s} \cdot \boldsymbol{\nabla} r) \bar{F} - s \right] \right\rangle_{FS}$ the fluid vorticity flux and $S_0 \boldsymbol{\nabla}_\perp^2 S_r^\Omega$ the fluid vorticity source. Equation (3.12) is obtained by taking the gyro average of the Vlasov equation (3.2) and integrating over the velocity space. A flux-surface average is then performed to obtain a 1D (i.e. radial) equation for vorticity. Figure 3.2a (orange dashed line) represents the normalized fluid vorticity source profile as a function of the normalized radius. One can note the main central lobe at $r/a = 0.75$ which is later referred as the source location. However, due to the nature of the gyro-average operator in GYSELA, the computed source is not purely axisymmetric. This is illustrated in Figure 3.2b where radial profiles of the fluid vorticity source at $\theta = 0$ (i.e. mid-plane, weak field side, dashed-dotted blue line) and $\theta = \pi$ (mid-plane, strong field side, dashed red line) are compared to the flux-surface averaged value (solid black line). A strong poloidal asymmetry arises in the source amplitude, varying by around $\pm 20\%$ with a clear in-out (i.e. $\cos\theta$) dependency similarly as B, the magnetic field amplitude. This information, combined with the injected anisotropy discussed before, leads to an injection of a *poloidal asymmetry of pressure anisotropy* for the main ion species (i.e. deuterium here). Said differently, the term $\partial_\theta \Pi_\parallel$ may be strongly affected by the vorticity source. Therefore, we expect the neoclassical terms of heat flux and later impurity flux to be determined mainly by this term in the vicinity of the applied vorticity source. This will be further studied in the next chapter.

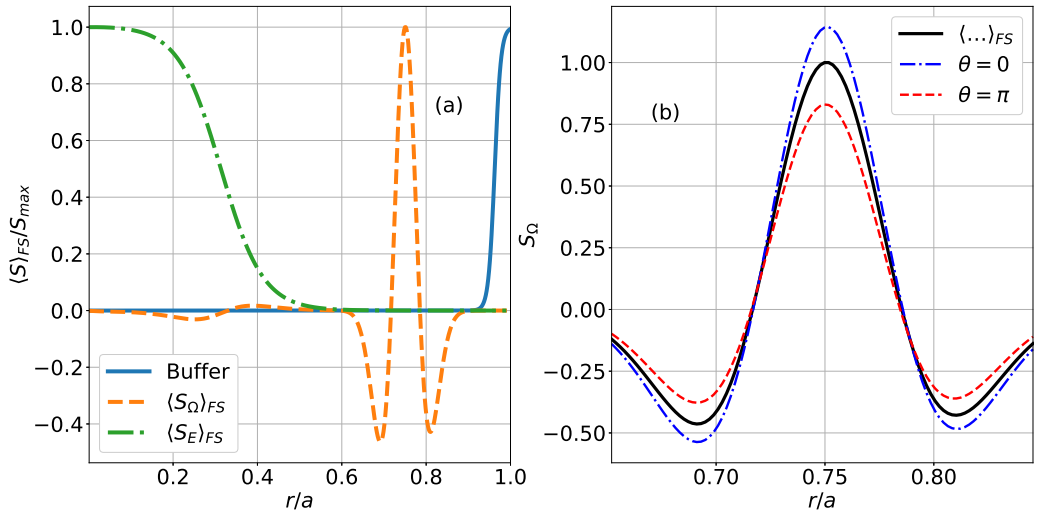

Figure 3.2: **(a):** Normalized radial profiles of the buffer diffusion (solid blue line), fluid energy source (dashed-dotted green line) and fluid vorticity source (dashed orange line). **(b):** Normalized vorticity source radial profile for $\theta = 0$ (dashed-dotted blue line), $\theta = \pi$ (dotted red line) and surface-averaged (solid black line).

It is difficult to impose a sheared radial electric field E_r in a full-f code; trying to inject such a field directly in the quasi-neutrality equation proved to be uneffective [82] due to immediate screening effect of the plasma. Two different approaches can then be considered to generate an $E \times B$ flow shear in a flux-driven gyrokinetic simulation with adiabatic electrons:

1. Use the poloidal momentum source (also referred as vorticity source hereafter) previously described. The idea is to add a term in the right-hand-side of the Vlasov equation (3.2) to polarize the plasma. It adds a small term equivalent to a polarization density, effectively biasing locally the plasma and creating a local E_r field. Ion cyclotron frequency range can be used to inject poloidal momentum in a plasma [83], like IBW (Ion Berstein Waves) [84] or MCFD (Mode Conversion Flow Drive) [85] for example. The poloidal momentum source used in this study can be viewed as the resulting effect of such experimental methods on the sole mean radial electric field. This source aims at emulating the effects of such heating systems and demonstrating the effect of a strong $E \times B$ shear flow on a turbulent plasma.

2. Locally enforce a sheared radial electric field via the radial force balance by "imposing" a large pressure gradient:

$$E_r = -\frac{1}{q_s n_s}\frac{\partial P_{\perp,s}}{\partial r} + v_\theta B_\varphi - v_\varphi B_\theta \tag{3.13}$$

   Notice that, when the pressure is anisotropic, the perpendicular pressure $P_\perp$[2] enters the radial force balance instead of the total pressure P_{tot}. Details on its derivation are given in appendix E of [80]. Since radial particle transport is negligible with adiabatic electrons, we expect the imposed density gradient to remain unchanged and a sheared E_r to be generated to balance out the pressure gradient throughout the simulation. This case is referred as the steep gradient case hereafter. We expect the steep density gradient to be the dominant stabilizing mechanism of turbulence since density gradient is long known to stabilize the ITG instabilities [29].

3.2 Parameters and saturation level

3.2.1 Simulation parameters

Three simulations with similar parameters are studied and summarized in appendix C.2; the vorticity and reference cases are two branches of the same initial simulation where in the former the source is activated from $t\omega_{c,0} = 126400$ while the source remains off in the latter. The third one is the so-called steep-gradient case. All of them use a normalized gyro radius $\rho^\star = \rho_0/a \equiv 1/200$ with ρ_0 the hydrogen

[2]More precisely, there should be an additional term to $\partial_r P_\perp$, namely $(P_\parallel - P_\perp)\boldsymbol{\kappa}$, with $\boldsymbol{\kappa} = [\boldsymbol{\nabla}_\perp B - \mathbf{b}\times(\boldsymbol{\nabla}\times\mathbf{B})]/\mathbf{B}$ the magnetic curvature (see for instance [86], eq.6.42]). This contribution is usually small and has been neglected here.

Larmor radius at mid-radius and a the minor radius. Due to the increasing cost of simulations with smaller $\rho^\star$ values, we chose one comparable to the COMPASS tokamak. The domain goes from $r/a = 0$ to $r/a = 1$ with the last 10% of the radial domain subject to a buffer diffusion region to damp out fluctuations at the edge and avoid possible numerical oscillations. Dirichlet boundary conditions are used at the outer radial position $r/a = 1$ such that $\phi(r/a = 1) = 0$. There, a buffer region located at $r/a > 0.9$ and characterized by additional diffusion and Krook terms forces the distribution function to relax towards an axisymmetric centered Maxwellian. There is no inner boundary condition since the simulated domain encompasses the magnetic axis $r/a = 0$. Note however that, because of symmetry reasons, the axisymmetric $(m, n) = (0, 0)$ component of the radial electric field is necessarily vanishing at $r/a = 0$. The buffer radial profile is shown in Figure 3.2 (solid blue line). The safety factor radial profile writes

$$q(r) = 1.5 + 2.3 \exp\left[2.5 \ln\left(r/a\right)\right]. \tag{3.14}$$

The resulting magnetic shear $s = \frac{r}{q}\frac{dq}{dr}$ stabilizes the transverse Kelvin-Helmholtz instability that could be driven by the imposed strong $E \times B$ shear [87, 88]. However we do not expect the magnetic shear to play a major role in creating the transport barrier since it is monotonic unlike in ITBs scenarios. The isotropic heat source used in those simulations, localized in the interval $r/a = 0$ to $r/a \approx 0.4$ (See Figure 3.2, dashed-dotted green line), evolves in time: for the vorticity and reference cases, the amplitude of the heat source is fixed at a "high" value until turbulent intensity saturates. The heat source amplitude is then lowered so that the pressure profile stays roughly constant (i.e., its evolution becomes very slow in time). For the steep gradient case, the source amplitude is fixed at the same "high" value throughout the whole duration of the simulation. The deuterium ions are in the banana regime with a collisionality such that $\nu^\star_{D^+} < 1$. Parameters are summarized in table 3.1.

3.2.2 Initial conditions

The initial temperature and density profiles are chosen such that ITG instabilities arise, meaning the ratio $\eta \equiv \frac{T^{-1}\partial_r T}{n^{-1}\partial_r n} = \kappa_T/\kappa_n = 3$ is constant on most of the domain except in the steep gradient case that peaks at $\kappa_n \approx 28$ at $r/a = 0.75$ (see section 5) leading to $\eta \approx 0.13$ locally. The vorticity and reference cases density profile (Figure 3.3a, dashed blue line) are close to a L-mode profile whereas the steep gradient one (Figure 3.3a, dotted orange line) is similar (i.e. in general shape and not in radial position) to what can be observed in H-mode discharges with a steep density gradient at the edge (See [51] for example). Their respective η profiles are shown in Figure 3.3b; the vorticity and reference cases are identical to the steep gradient case except at $r/a = 0.75$, where the steep gradient is located.

3.2.3 Saturation level

We denote each mode as (m, n), where m and n are the poloidal and toroidal Fourier mode numbers respectively. Figure 3.4 shows the time evolution of the $(0, 0)$ and

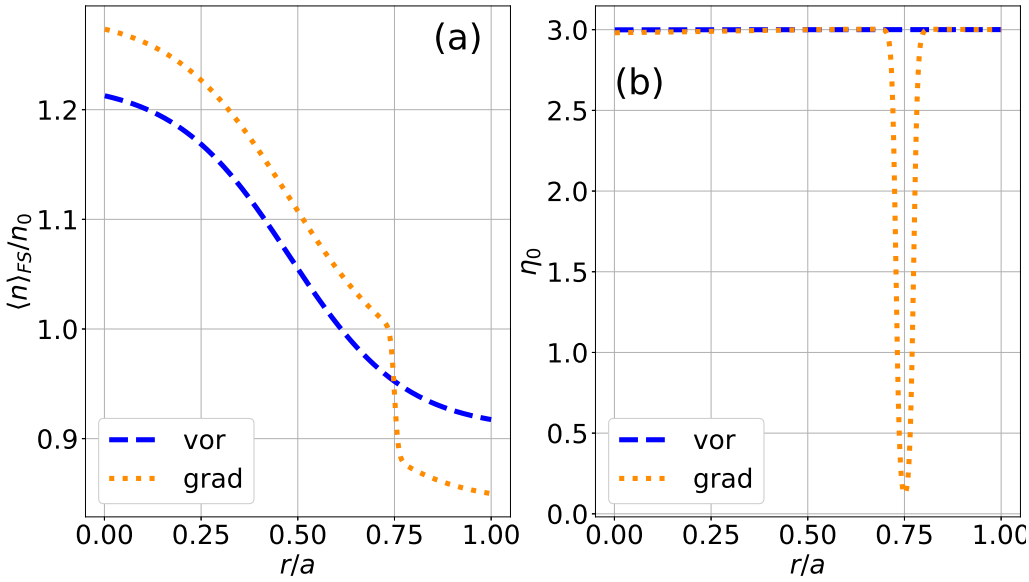

Figure 3.3: Radial profiles of the flux surface averaged guiding-center density **(a)** and η profile $\kappa_{T_0}/\kappa_{n_0}$ **(b)** at $t\omega_{c,0} = 0$ for the vorticity case (similar to the reference case, blue dotted line) and for the steep gradient case (orange dashed line).

$(0,1)$ as well as some resonant $n + m/q\,(r) = 0$ modes of the electrostatic potential, with $q\,(r)$ the safety factor profile, at $r/a = 0.5$ in the reference simulation. All three simulations exhibit very similar behaviours until saturation since the parameters are almost identical (except near the density gradient at $r/a = 0.75$). The oscillating phase of the $(0,0)$ and $(0,1)$ modes from $t\omega_{c,0} = 0$ to $t\omega_{c,0} \approx 3 \cdot 10^4$ corresponds to the relaxation of the low frequency GAMs [89] (Geodesic Acoustic Modes). These oscillations are negligible after the main plasma instability starts its linear growth, namely ITG. This linear growth phase starts at around $t\omega_{c,0} \approx 3 \cdot 10^4$ until turbulence saturation is reached at approximately $t\omega_{c,0} \approx 6 \cdot 10^4$. For each simulation, the global mean linear growth rate $\overline{\gamma}_{lin} \approx 5 \cdot 10^{-4}\omega_{c,0}$ is computed by fitting the linear part on

$$\langle \phi \rangle_{RMS} = \sqrt{\sum_{m,n \neq 0} |\phi_{m,n}|^2}. \tag{3.15}$$

Values for the different simulations are reported in table 3.1.

3.3 Poloidal momentum (vorticity) source

3.3.1 Onset of a transport barrier

The source described in equation (3.9) is used to produce a sheared poloidal momentum profile to the system once turbulent intensity saturates. Although already using about 4 million CPU hours, the simulation has not reached steady state yet, which would have required several confinement times. However, the adiabatic evolution of the flux-surface averaged profiles and the fast response of turbulence is

Parameters	Reference	Vorticity	Steep gradient
Collisionality	$\nu^\star_{D^+}\,(r/a=0.5)=0.1$		
Charge / atomic numbers	$Z_i=1, A_i=2$		
Time step	$\Delta t\omega_{c,0}=16$		
$N_r\times N_\theta\times N_\varphi\times N_{v_\parallel}\times N_\mu$	$511\times512\times64\times127\times31$		
Normalized gyroradius	$\rho^\star=\rho_{c,0}/a=1/200$		
Inverse aspect ratio	$1/\epsilon=R_0/a=4.4$		
Maximum density gradient	$\kappa_n=R_0/L_n=2.2$		$\kappa_n\approx28$
Maximum temperature gradient	$\kappa_T=R/L_T=6.6$		
Amplitude of vorticity source	$S_0^\Omega=0$*	$S_0^\Omega=0.08$*	$S_0^\Omega=0$
Average ITG linear growth rate	$\overline{\gamma}_{lin}/\omega_{c,0}\approx5\cdot10^{-4}$		

Table 3.1: Simulation parameters used in this study. *The poloidal momentum source is activated from $t\omega_{c,0}=126400$ for the vorticity case and disabled in the reference case.

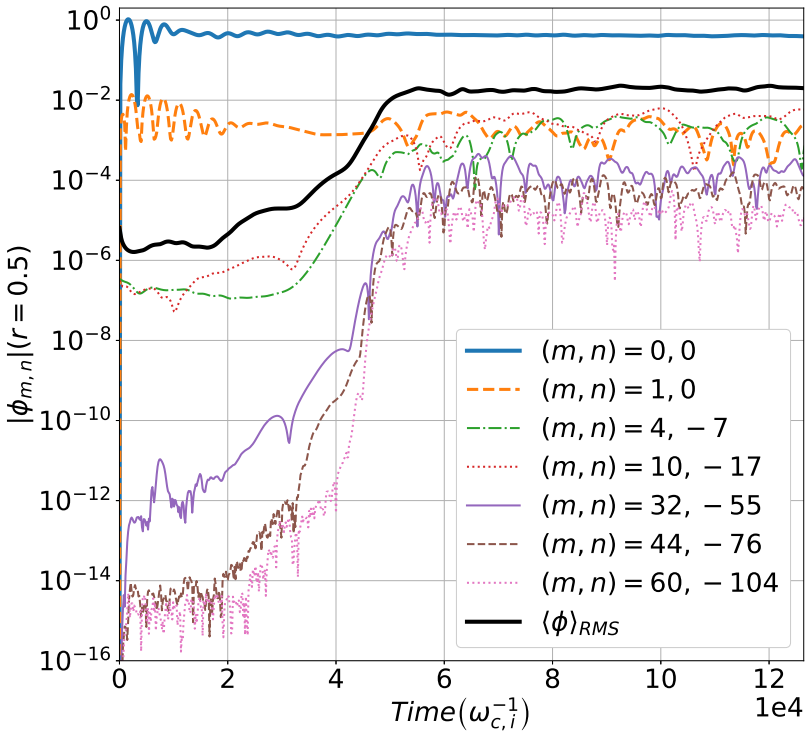

Figure 3.4: $|\phi_{m,n}|$ at $r=0.5$ plotted against time (up to $t_{vor}\omega_{c,0}=126400$, the vorticity activation time). The solid black line represents $\langle\phi\rangle_{RMS}$ (equation (3.15)) and is used to compute the average linear growth rate of ITG instability. This plot is also representative of the steep gradient case since we look at the mode evolution at $r/a=0.5$, away from the steep gradient region at $r/a=0.75$.

enough to reach critical conclusions regarding the impact of an external source of $E \times B$ shearing on turbulent transport. Figure 3.5a shows the $E \times B$ poloidal flow at the same simulation time for both the reference (green dotted line) and vorticity (blue dashed line) cases. The vorticity source effectively produces the desired $E \times B$ flow shear compared to the reference case with a significant amplitude difference at $r/a = 0.7$ and $r/a = 0.8$. As stated in [90], it is empirically found in numerical simulations that the $\omega_{E\times B}$ shearing rate should be within the same order of magnitude as γ_{lin}^{MAX}, the maximum linear growth rate of the relevant instability (i.e. ITG in this case) for turbulence stabilization. This simple rule of thumb is useful to have an idea of the amount of shear we should impose on the plasma *a priori*. Here we choose to normalize the shearing rate to $\overline{\gamma}_{lin} \leqslant \gamma_{lin}^{MAX}$ the average linear growth rate computed with $\langle\phi\rangle_{RMS}$ (equation (3.15)) which is more representative of the actual "growth rate of ITG" instability. The chosen source amplitude should establish a shear flow around one order of magnitude higher than $\overline{\gamma}_{lin}$ (i.e. $\omega_{E\times B} \approx 10\overline{\gamma}_{lin}$) to fullfil the previously discussed stabilizing conditions, consistently with previous studies [91].

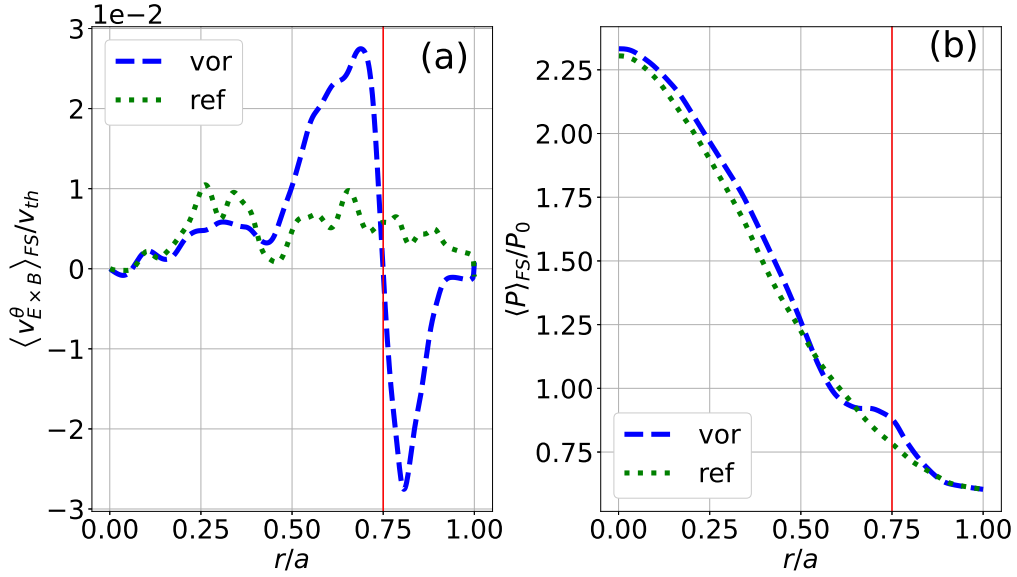

Figure 3.5: $E \times B$ velocity **(a)** and pressure **(b)** radial profiles of the vorticity (dashed blue line) and reference (dotted green line) cases at $t\omega_{c,0} = 377920$. The red vertical line represents the vorticity source position if activated.

Figure 3.5b shows the radial pressure profiles of the reference (dotted green line) and vorticity (dashed blue line) cases at the same simulation time. Three main features appear when the source is turned on: a "plateau" appears at $r/a = [0.6, 0.7]$ and the core pressure slightly increases compared to the reference case. Also, a steepening of the pressure gradient is observed on the inner side of the plateau ($r/a = 0.6$) and on the outer side of the source ($r/a = 0.8$). One must note that in the plateau region, the $\partial_t P$ term is not negligible in the heat flux balance. This means the radial pressure profile is still evolving and may be transient. The vorticity source used here does not inject energy in the system, and the core heat source is the same as the reference case which means that the increase seen on the radial

profile should result from the presence of some transport barrier.

As attested by [91], it should be noted that the vorticity source activation leads to a pressure (and therefore temperature) anisotropy that tends to destabilize the plasma and any transport barrier that could be generated by the vorticity source through quasi-periodic relaxations. This reduces locally the ITG linear threshold [92] and triggers ITG modes excitation. In previous study, this ITG modes excitation by temperature anisotropy led to periodic transport barrier crashes and consequently anisotropy collapses. However, those crashes are not observed here while a much higher temperature anistropy than previous studies is observed. A scan in collisionality at lower resolution (not shown) shows that both temperature anisotropy and shear rate saturate at a value that is independent of $\nu^\star$. The saturation value only depends on the vorticity source amplitude. Conversely, in the absence of collisions, there is no sign of saturation in the time interval that is considered, so that both temperature anisotropy and shearing rate increase to very large values. However, we did not observe the relaxation events reported by [93] possibly because of a too short simulation. The main hypothesis for the absence of relaxations is then linked to the recently upgraded collision operator used in this study [79]. Previously, only the parallel direction $v_\parallel$ was taken into account for the collisions as presented in [94], whereas the latest version takes into account the perpendicular direction μ. The derivatives in μ are then acting as an isotropizing mechanism counterbalancing the anisotropizing effect of the source, hence no relaxation mechanisms are observed in our simulations.

To quantify the effect of velocity shearing on turbulent heat transport of the main species and confinement, we choose to diagnose first the evolution of the effective heat diffusivity coefficient χ_T as a function of time in different radial regions. For this purpose, heat transport is assumed to be mainly diffusive, with the heat flux expressed as $Q = -n\chi_T \nabla T$. The radial fluxes of energy then writes:

$$Q^{neo} = \left\langle \int \mathcal{E} \left(v_D^r + v_{E_{n=0}}^r \right) \bar{F}_s dv \right\rangle_{FS}, \tag{3.16}$$

$$Q^{turb} = \left\langle \int \mathcal{E} \left(v_{E_{n\neq 0}}^r \right) \bar{F}_s dv \right\rangle_{FS}, \tag{3.17}$$

where $\mathcal{E} = \mu B + \frac{1}{2} v_{G\parallel}^2$, $v_D^r = \bar{\mathbf{v}}_D \cdot \nabla r$, $v_{E_{n=0}}^r = \langle \bar{\mathbf{v}}_{E\times B} \cdot \nabla r \rangle_\varphi$ and $v_{E_{n\neq 0}}^r = \bar{\mathbf{v}}_{E\times B} \cdot \nabla r - v_{E_{n=0}}^r$. Q^{neo} is the neoclassical heat flux, which is the sum of the curvature and gradient drift contributions as well as the toroidally axisymmetric $E \times B$ drift contribution. The turbulent heat flux Q^{turb} consists of the non toroidally axisymmetric $E \times B$ drift contribution.

The total radial heat flux is then the sum of the turbulent and neoclassical contributions:

$$Q_{tot} = Q^{turb} + Q^{neo}. \tag{3.18}$$

Figure 3.6 represents the total radial heat flux (equation (3.18)) as a function of radius and time normalized to the average gyro-Bohm heat flux $\langle Q_{GB} \rangle_{r,\theta,\varphi} =$

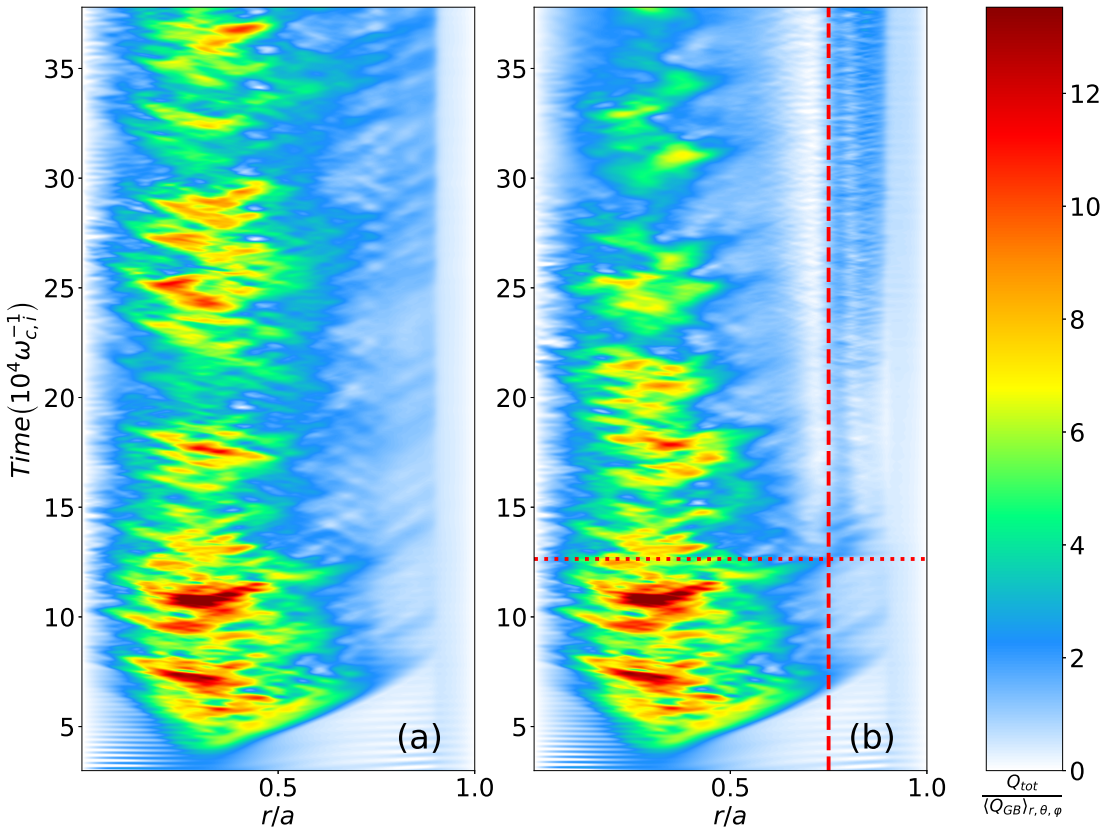

Figure 3.6: Total radial heat flux Q_{tot} (equation (3.18)) as a function of radius and time for the reference **(a)** and vorticity **(b)** cases. The vertical dashed red line represents the vorticity source position while the horizontal dotted red line is the vorticity activation time.

$\langle -n_{e,0}\chi_{GB}\nabla T_{e,0}\rangle_{r,\theta,\varphi}$ with $\chi_{GB} = \rho^{\star}\chi_B = \rho^{\star}\frac{T_{e,0}}{q_i B}$, the gyro-Bohm diffusivity [95] and $T_{e,0}(r)$ and $n_{e,0}(r)$ the initial electron temperature and density profiles. After the vorticity source is activated (i.e. $150000\omega_{c,i}^{-1}$ as shown in Figure 3.6b), a clear reduction in total heat flux is observed compared to the reference (Figure 3.6a) case. The core region ($r/a = [0.25, 0.45]$) shows lower levels of heat flux than the reference case, which explains the higher core pressure, whereas a region of $Q_{tot} \approx 0$ arises on the inner side of the source ($r/a \in [0.6, 0.7]$) hence the plateau in the pressure profile. One can note higher heat flux levels on the outer side of the source ($r/a \in [0.75, 0.85]$) due to both the previously discussed excitation of ITG modes driven by the source-induced pressure anisotropy and the increased temperature gradient. This leads to the steepening of the pressure profile observed previously. To complete those observations, a radial average is performed on equation (3.18) to get:

$$\langle Q_{tot}\rangle_{\Delta r} = \left\langle Q^{turb}\right\rangle_{\Delta r} + \langle Q^{neo}\rangle_{\Delta r}\,. \tag{3.19}$$

Assuming diffusive heat fluxes, one can define the different heat diffusivity components as follows:

$$\chi_T^{neo} = -\frac{\langle Q^{neo}\rangle_{\Delta r}}{\langle n\nabla T\rangle_{\Delta r}}, \tag{3.20}$$

$$\chi_T^{turb} = -\frac{\left\langle Q^{turb}\right\rangle_{\Delta r}}{\langle n\nabla T\rangle_{\Delta r}}, \tag{3.21}$$

$$\chi_T^{tot} = \chi_T^{turb} + \chi_T^{neo}. \tag{3.22}$$

The heat diffusivity coefficients are normalized to the local $\langle\chi_{GB}\rangle_{\Delta r,\theta,\varphi}$ gyro-Bohm diffusivity coefficients. For this analysis, we select two radial regions:

- $\Delta r = [0.7, 0.8]$, the region where the flow shear is injected.
- $\Delta r = [0.15, 0.6]$, the region where the turbulence amplitude is found maximum.

Figures 3.7a and 3.7b show the time evolution of the turbulent spatial-averaged diffusivity coefficients in the core (Figure 3.7a) and source (Figure 3.7b) regions respectively. The turbulent diffusivity $\chi_T^{turb}/\langle\chi_{GB}\rangle_{\Delta r,\theta,\varphi}$ quickly drops by a factor of about 10 in the vorticity source region (Figure 3.7b, dashed blue line) when the poloidal momentum source is activated, compared to the reference simulation (Figure 3.7b, dotted green line). In the source region, the turbulent diffusivity is the dominant factor until the vorticity source is activated. Then, the neoclassical diffusivity χ_T^{neo} becomes the dominant contribution and stays constant in both the source and core regions at approximately $\chi_T^{neo}/\langle\chi_{GB}\rangle_{\Delta r,\theta,\varphi} \approx 0.5$ for both cases. Interestingly, the turbulent diffusivity in the core is affected by the activation of the source (Figure 3.7a, dashed blue line) even if it is not as impactful as near the source itself. An overall decaying trend seems to take place especially after the source activation. This decrease in diffusivity at the source position explains the

observed pressure increase in the core as less energy is lost to the edge; this attests that a transport barrier has developed at the source location.

One can estimate the shear rate threshold above which turbulence is suppressed by checking the evolution of the turbulent diffusivity χ_T^{turb} relative to the shear rate $\omega_{E\times B}$ (Figure 3.8). This threshold, defined as the shear rate for which $\chi_T^{turb}/\langle\chi_{GB}\rangle_{\theta,\varphi,\Delta r}$ is inferior or equal to half of its average value before the source activation, is $\langle\omega_{E\times B}\rangle_{\theta,\varphi,\Delta r}^{threshold} \approx \overline{\gamma}_{lin}$, consistently with the rule of thumb discussed previously.

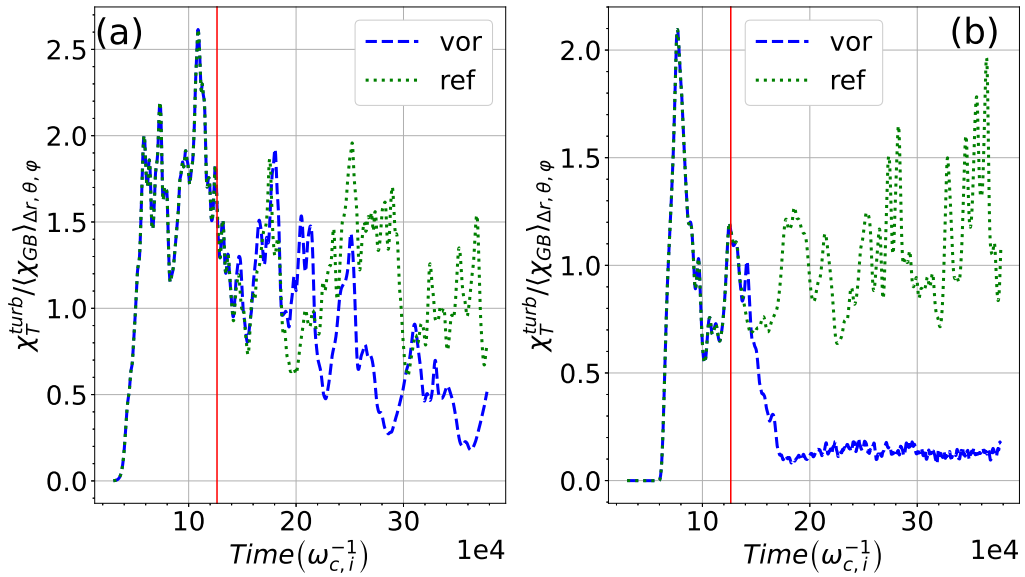

Figure 3.7: Time evolution of the turbulent heat diffusivity in the $r/a = [0.15, 0.6]$ **(a)** and $r/a = [0.7, 0.8]$ **(b)** regions for the vorticity (blue dashed line) and reference (dotted green line). The red vertical line represents the vorticity activation time for the vorticity case. The neoclassical diffusivity being almost constant in time, it is not presented here.

The observed reduction in $\langle Q^{turb}\rangle_{\Delta r}$ (see equation (3.19)) can be explained through non-linear arguments. Let us consider a simple expression for the radial turbulent heat flux with $Q^{turb} = \langle Pu^r_{E\times B}\rangle_{FS}$ with $P = (n+\delta n)(T+\delta T)$ and $\delta u^r_{E\times B} \approx \frac{1}{B_0 r}\partial_\theta \delta\phi$, the δ referring to fluctuating quantities and $\delta u^r_{E\times B}$ the perturbed $E\times B$ drift velocity. Up to the second order, this leads to:

$$Q^{turb} \approx \frac{1}{B_0 r}\left[\underbrace{\langle n\rangle_{FS}\langle\delta T\partial_\theta\delta\phi\rangle_{FS}}_{conduction} + \underbrace{\langle T\rangle_{FS}\langle\delta n\partial_\theta\delta\phi\rangle_{FS}}_{convection}\right]. \tag{3.23}$$

The convection term is negligeable in our simulations where electrons are adiabatic, hence we won't consider this term hereafter. One can write for a given fluctuating quantity the following expression:

$$\delta A = \sum_{m,n}\tilde{A}_{m,n}(r)\exp\left[i\left(m\theta + n\varphi - \omega t + \Omega_A\right)\right]. \tag{3.24}$$

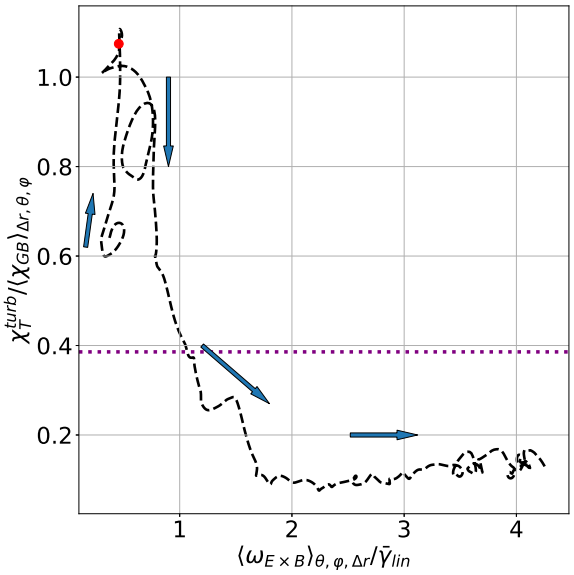

Figure 3.8: Turbulent heat diffusivity χ_T^{turb} plotted against the shear rate $\omega_{E\times B}$ in the source region $r/a = [0.7, 0.8]$ for $t\omega_{c,0} = [110400, 243200]$. The red dot represents the vorticity activation time for the vorticity case $t_{vor}\omega_{c,0} = 126400$. The arrows indicate the time evolution. The dotted horizontal line represents half of the average value of $\chi_T^{turb}/\langle\chi_{GB}\rangle_{\Delta r,\theta,\varphi}$, the threshold for turbulence suppression.

where $\tilde{A}_{m,n}(r)$ is the amplitude profile (real), m and n the poloidal and toroidal wavenumber respectively and Ω_A the phase of the quantity considered. When applied to equation (3.23), one can write

$$Q^{turb} \approx \frac{\langle n\rangle_{FS}}{B_0}\sum_{m,n} k_\theta \tilde{\phi}_{m,n}\tilde{T}_{m,n}\sin\left(\Omega_\phi - \Omega_T\right) \tag{3.25}$$

with $k_\theta = m/r$ the poloidal wavenumber. Ultimately, we consider fluctuations with similar amplitudes such as $\tilde{\phi}_{m,n} \sim \tilde{n}_{m,n} \sim \tilde{T}_{m,n}$, leading to:

$$Q^{turb} \approx \frac{\langle n\rangle_{FS}}{B_0}\sum_{m,n} k_\theta \tilde{\phi}^2_{m,n}\sin\left(\Omega_\phi - \Omega_T\right). \tag{3.26}$$

Equation (3.26) implies that Q^{turb} is proportionnal to $\tilde{\phi}^2_{m,n}$, k_θ and to the phase difference between the potential and the temperature. If the analysis presented here holds, both turbulent intensity and radial turbulent heat flux must be in phase. To verify this hypothesis, the following definition of electrostatic potential fluctuations is used:

$$\delta\phi(r,\theta,\varphi=0,t) = \phi(r,\theta,\varphi=0,t) - \langle\phi(r,\theta,\varphi)\rangle_\varphi, \tag{3.27}$$

where $\langle\phi(r,\theta,\varphi)\rangle_\varphi$ represents the toroidally axisymmetric modes of the potential and are substracted specifically to remove the contribution coming from :

- The mean potential, or the so-called $\phi_{0,0}$ Fourier mode, which is related to zonal flows [96].
- The convection cells [96], which are toroidally axisymmetric but exhibit poloidal asymmetries. They are associated with the $\phi_{m\neq 0,0}$ Fourier components.

The focus here is on a single poloidal plane $(r, \theta, \varphi = 0)$ representative of the whole simulation box. Information of interest being the local turbulent intensity and later the radial and poloidal geometric structures, this will provide sufficient information on those variables as discussed in [97, 98]. The local radial turbulent intensity is then computed by averaging the square of equation (3.27) over θ and Δr:

$$I_{turb} = \left\langle \left[\delta\phi\left(r, \theta, \varphi = 0, t\right)\right]^2 \right\rangle_{\theta,\Delta r} . \tag{3.28}$$

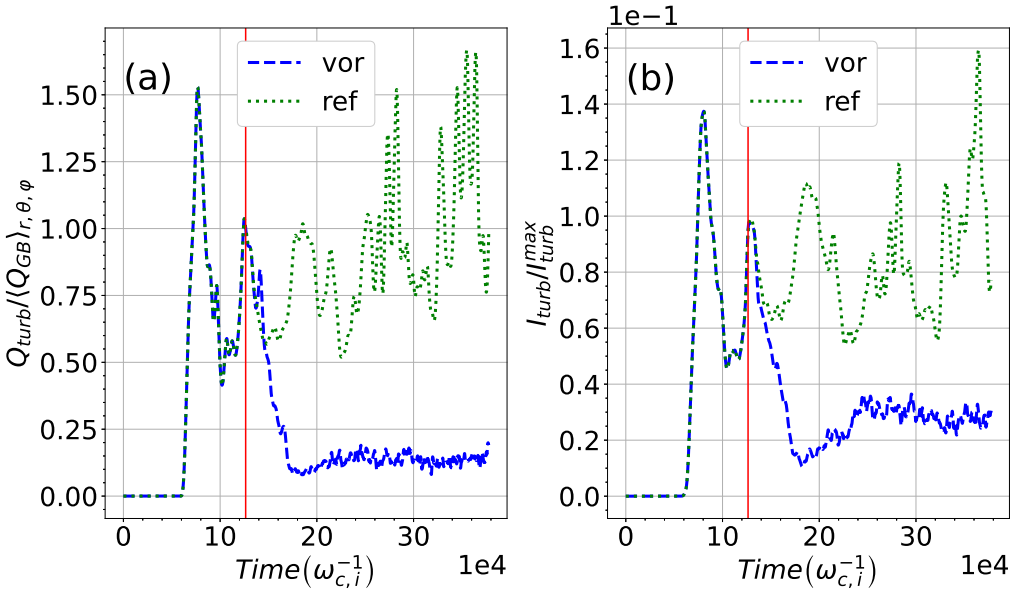

Figure 3.9: Time evolution of the turbulence heat flux **(a)** and turbulent intensity **(b)** in the $r/a = [0.7, 0.8]$ region for the vorticity (blue dashed line) and reference (dotted green line). The red vertical line represents the vorticity activation time for the vorticity case. **(a)** and **(b)** signals are in phase.

I_{turb} is normalized to I_{turb}^{max}, the maximum value reported before the source activation which is the same for both the reference and vorticity cases. Figures 3.9 and 3.10 represent the time evolution of the turbulent heat flux and turbulent intensity in the source (Figure 3.9) and core (Figure 3.10) regions respectively. As expected, I_{turb} and $\left\langle Q^{turb}\right\rangle_{\Delta r}$ are in phase in both regions, implying the previous relationship found between Q^{turb} and $I_{turb} \leftrightarrow \tilde{\phi}^2$ holds in the case of adiabatic electrons. When the vorticity source is activated, the turbulent intensity largely decreases in the source region by a factor 3 while the heat flux decreases by a factor 10. Note that there is still a small turbulence level present locally. Moreover, the turbulent intensity also decreases in the core (Figure 3.10) when the vorticity source is on. The

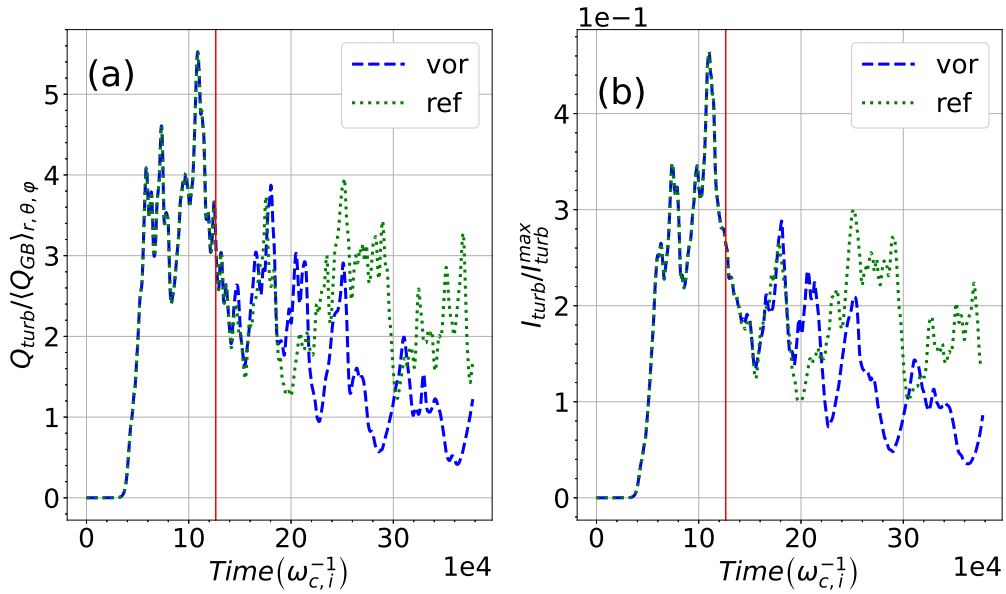

Figure 3.10: This figure shows the time evolution of the turbulent heat flux **(a)** and turbulent intensity **(b)** in the $r/a = [0.15, 0.6]$ region for the vorticity (blue dashed line) and reference (dotted green line) cases. The red vertical line represents the vorticity activation time for the vorticity case. **(a)** and **(b)** signals are in phase.

reduction in turbulent heat flux is then directly linked to the reduction of turbulent intensity.

Another way to verify the validity of the relation described in equation (3.26) is to plot $\langle Q_{tot}^{turb}\rangle_{\Delta r}$ as a function of I_{turb} in the core (Figure 3.11a) and source regions (Figure 3.11b). A linear fit $Q_{turb}/\langle Q_{GB}\rangle_{r,\theta,\varphi} = aI_{turb}/I_{turb}^{max}$ is then applied to the data to check the validity of equation (3.26). In the source region, both the turbulent intensity and turbulent heat flux in the vorticity case are at very low levels compared to the reference case. However, the fit for the reference case is more robust ($R^2 = 0.57$) with a slope of $a_{source}^{ref} \sim 11.2$ while it's only $a_{source}^{vor} \sim 4.8$ in the vorticity case ($R^2 = 0.09$). Not withstanding the small value of the R^2 value in the vorticity case, it is obvious that the plasma behaviour is different than in the reference case. This indicates large variations in k_θ and/or phase differences. In the core region, both the reference and vorticity cases show similar slopes of $a_{core}^{vor} \approx a_{core}^{ref} \sim 12.5$ with a convincing determination coefficient $R^2 > 0.8$. This means the turbulence has similar features but with a lower amplitude when the vorticity is on and verifies equation (3.26).

The neoclassical heat flux profile is slightly altered in the vorticity case as presented in Figure 3.12. When looking at the core (i.e. $r/a \leqslant 0.6$), the reference and vorticity cases are similar both in amplitude and shape. However, near the source localized at $r/a = 0.75$, the neoclassical heat flux presents a sheared profile when the transport barrier is present with part of the flux outside the source becoming negative. This behaviour is not due to the transport barrier and more to the asymmetry of pressure anisotropy injected by the vorticity source itself as discussed in section 3.1.3 . Its effect is however minor on the neoclassical heat flux as observed

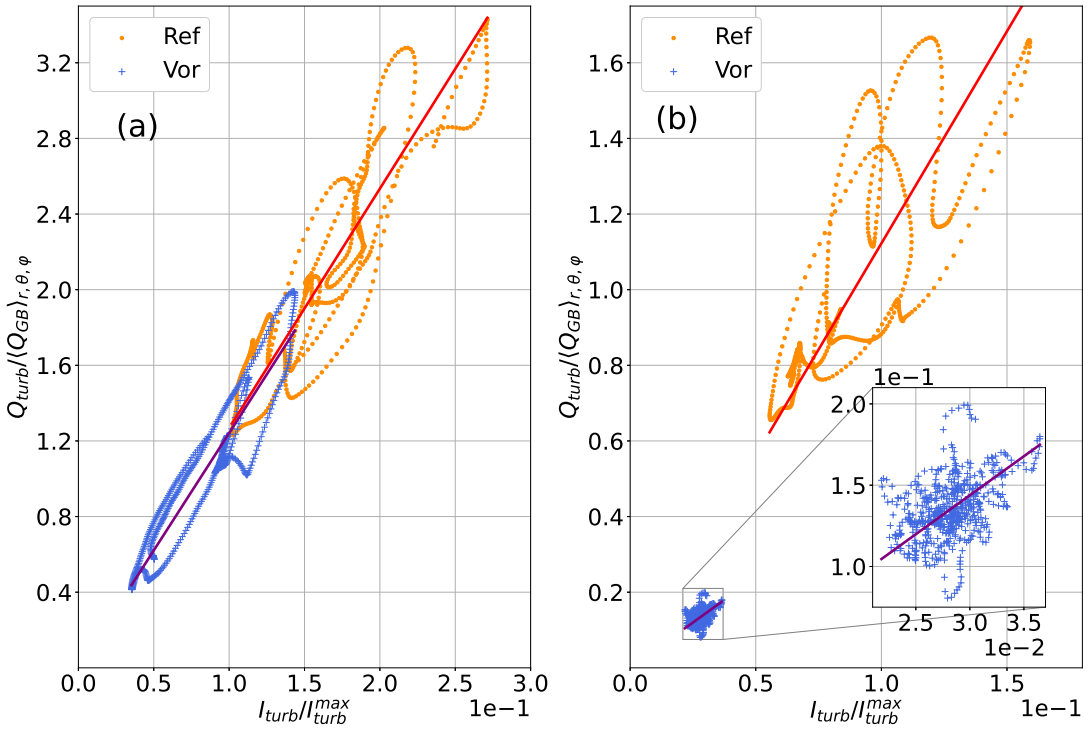

Figure 3.11: Heat flux as a function of turbulent intensity for the vorticity (blue cross) and reference (orange dots) cases in the core **(a)** and source **(b)** regions.

here.

3.3.2 Involved mechanisms: auto-correlation length and perpendicular wavenumber

As already discussed in the introduction, one of the main hypothesis is that an $E \times B$ flow shear is able to *tear* the turbulent structures locally to reduce their mean size and therefore stabilize the plasma. We propose two different approaches to verify this prediction in our simulations:

1. Compute and compare the local auto-correlation radial length of the perturbed electrostatic potential for both the reference and vorticity cases. The aim is to check any change in typical radial structure size.

2. Compute the poloidal wavenumber spectrum of the perturbed electrostatic potential to monitor what poloidal scales are specifically affected by this turbulent intensity quench.

Auto-correlation radial length

The aim in this paragraph is to quantify effect on the "mean" size of turbulent structures of the $E \times B$ shear flow. For this purpose, we calculate the fluctuations as written in equation (3.27) and then compute a correlation length Probability Density Function (PDF), following reference [97]:

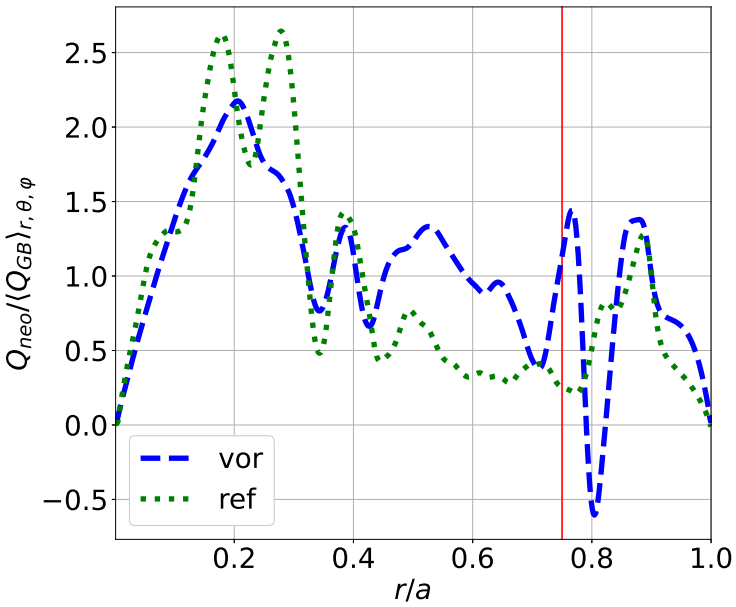

Figure 3.12: Radial profile of the neoclassical heat flux normalized to the average gyro-Bohm heat flux and averaged over the last $16000\omega_{c,i}^{-1}$ for the reference (dotted green line) and vorticity (dashed blue line) cases. The red vertical line indicates the vorticity source position.

$$C_{\delta\phi,\delta\phi}\left(r,\theta,\varphi=0,t,\delta r\right)=\frac{\delta\phi\left(r+\delta r,\theta,\varphi=0,t\right)\delta\phi\left(r,\theta,\varphi=0,t\right)}{\left[\delta\phi\left(r,\theta,\varphi=0,t\right)\right]^{2}} \tag{3.29}$$

This autocorrelation function is computed for each θ angle and radial location r on a radial window $[r-\delta r_{max}, r+\delta r_{max}]$. Here we adjust the radial extent to $\delta r_{max}=20\rho_{c,0}$, which is found to be sufficient to capture most of the turbulent radial structures. Thus we obtain a PDF for each time step, θ angle and radius $r/a\in[0.1,0.9]$. The Half Width at Half Maximum (HWHM) of this PDF is taken along δr to obtain a time dependent poloidal map of the radial correlation length:

$$C_{\delta\phi,\delta\phi}\left(r,\theta,\varphi=0,t,L_{AC}^{\delta\phi}\right)=0.5. \tag{3.30}$$

Finally, the flux-surface average of the poloidal map obtained is computed before doing a time average over the last $48000t\omega_{c,0}$ of both the simulation and reference cases

$$\langle L_{AC}\rangle_{FS}\left(r\right)=\overline{\left\langle L_{AC}^{\delta\phi}\left(r,\theta,t\right)\right\rangle_{FS}}, \tag{3.31}$$

with the overline representing the time average.

Figure 3.13a shows the flux-surface and time averaged auto-correlation length as a function of the normalized radius while Figure 3.13b shows the radial profile of

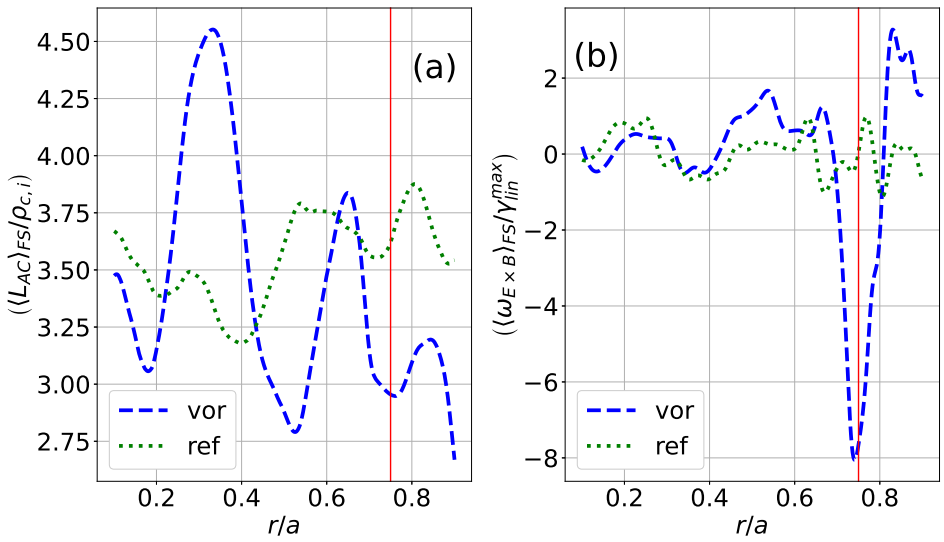

Figure 3.13: Flux surface and time average of the correlation length normalized to the local ion gyro-radius **(a)** and $E \times B$ shearing rate **(b)** as a function of radius for the reference (green dotted line) and vorticity (blue dashed line) cases. The red vertical line indicates the source location for the vorticity case.

the shear rate $\omega_{E\times B}$ at the last simulation time. The reference case (Figure 3.13a, dotted green line) represents the correlation length without the vorticity source. L_{AC} stays close to $3.5\rho_{c,i}$ with a small $E \times B$ shear rate (Figure 3.13b, dotted green line), but if the source is turned on (Figure 3.13a, dashed blue line), the radial correlation length decreases where the flow shear rate is maximum (Figure 3.13b, dashed blue line), at $r/a = 0.75$. This is consistent with the turbulent structure shearing hypothesis: the $E \times B$ shear flow reduces locally the radial extension of the turbulent structures. This ultimately leads to a spatial decorrelation of those structures and a quench in turbulent intensity as previously observed. Conversely, the correlation length increases in the range $r/a \in [0.2; 0.4]$ and decreases near $r/a = 0.5$ where shearing is not strong. Hence, the decrease of χ_T and of the turbulent intensity in those regions cannot be attributed to the auto-correlation length.

Poloidal wavenumber spectra

To complete this analysis, we compute the k_θ spectrum of the perturbed electrostatic potential to monitor the intensity evolution of the different poloidal structure scales at different radii. The k_θ spectrum is computed through

$$\left|\delta\phi_{k_\theta}\right|^2 (r, k_\theta) = \overline{\left|\delta\phi\left(r, k_\theta, \varphi = 0, t\right)\right|^2}. \tag{3.32}$$

For each time step, a 1D FFT is performed along the poloidal axis before averaging it over the last $48000 t\omega_{c,0}$ to get a cleaner signal. This is comparable to $\left|\delta\phi^{3D}_{k_\theta}\right|^2 (r, k_\theta) = \overline{\sum_{k_\varphi} \left|\delta\phi\left(r, k_\theta, k_\varphi\right)\right|^2}$ because the dominant modes are the resonant ones.

Figure 3.14a shows the core region (i.e. $r/a = 0.43$) poloidal wavenumber spectra

for the reference case (dotted green line) and vorticity case (dashed blue line). The vorticity case spectrum keeps the same features as the reference one with a slightly lower amplitude. Figure 3.14b shows the poloidal wavenumber spectrum for the source region (i.e. $r/a = 0.75$). A clear difference can be seen between the reference (dotted green line) and vorticity case (dashed blue line). The smallest poloidal scales ($k_\theta \rho_{c,i} > 0.1$) undergo a much more important decrease in intensity than the bigger scales ($k_\theta \rho_{c,i} < 0.1$). This shows a reorganisation of the turbulent structures at that location with a mean scale shifting from $\overline{k_\theta \rho_{c,i}} \approx 0.28$ to $\overline{k_\theta \rho_{c,i}} \approx 0.16$, meaning the poloidal structures got bigger but also less intense. One explanation for this local shift is that turbulent structures may get *tilted* along the poloidal direction due to shearing as shown in Figure 1 of [90]. As a result turbulent structures are radially smaller and poloidally bigger with an overall lower intensity.

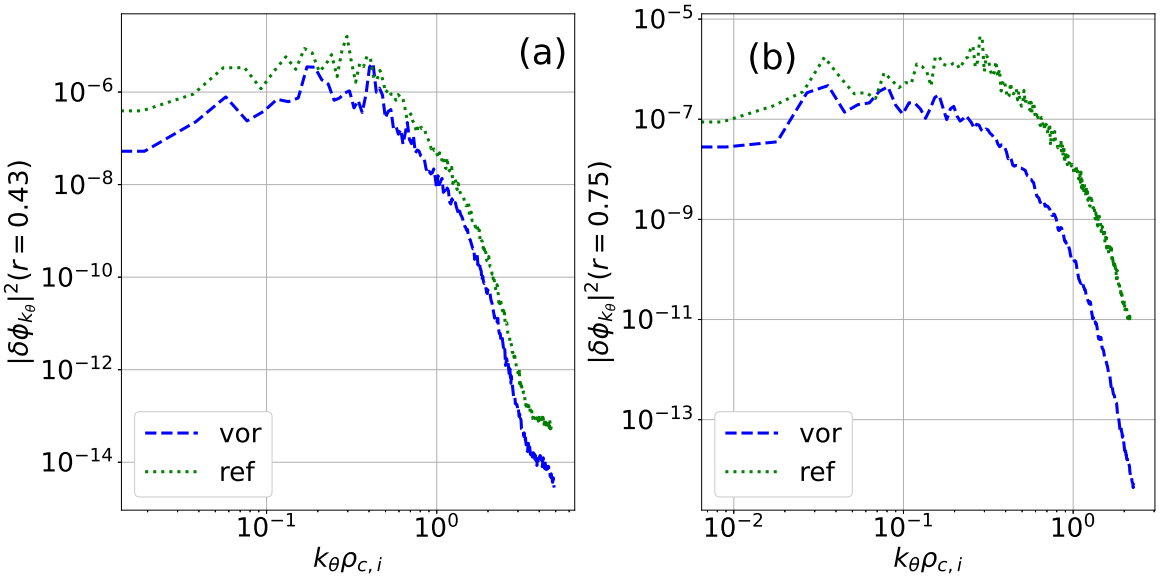

Figure 3.14: Poloidal wavenumber spectra using a 1D FFT averaged over the last 100 time steps for the reference (green dotted line) and vorticity (blue dashed line) cases for $r/a = 0.43$ **(a)** and $r/a = 0.75$ **(b)**.

3.4 Steep gradient case

Another way to generate a localized $E \times B$ poloidal shear flow is to produce a radially strong pressure gradient (Figure 3.15a) as shown with the radial density profile in Figure 3.3a. Since the temperature profile is allowed to evolve (flux-driven condition) but not the ion density profile (adiabatic electrons), we can enforce an initial density profile with a steep gradient at the desired location, the pressure gradient intensity defining the poloidal shear flow amplitude. The main interest of this approach is to determine how the heat transport coefficients behave when an H-mode pressure profile is enforced from the start.
A simulation with such gradient and characteristics detailed in table 3.1 shows that this method creates indeed the desired radial profile of poloidal $E \times B$ shear flow as shown in Figure 3.15b. Notice that, in this case, the velocity profile is different

from the vorticity-induced one (Figure 3.5b, dashed blue line) with a single lobe instead of two at $r/a = 0.75$. Outside of the steep gradient region, the $E \times B$ velocity profile is similar to what is observed in the reference case.

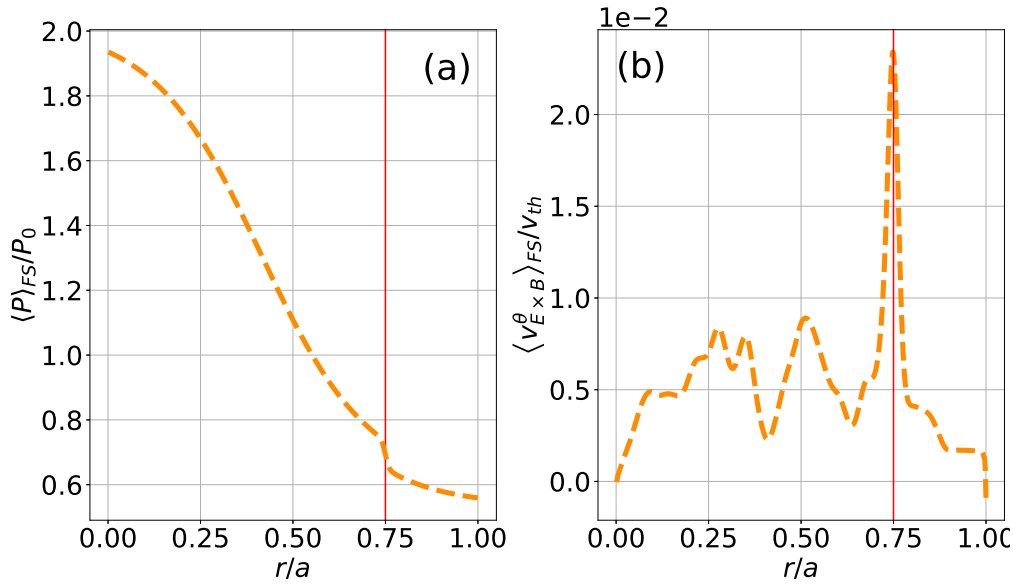

Figure 3.15: Radial profile of the total pressure **(a)** and $E \times B$ poloidal velocity **(b)** at the simulation end for the steep gradient case. The red vertical line indicates the steep gradient position.

Figure 3.16 shows the time evolution of the total heat diffusivity (Figure 3.16a), the turbulent heat flux (Figure 3.16b) and the turbulent intensity (Figure 3.16c) in the steep gradient region. The turbulent diffusivity is vanishing in that region and only marginally contributes to the total diffusivity now dominated by the neoclassical coefficient, roughly constant at $\chi_T^{neo} / \langle \chi_{GB} \rangle_{\Delta r,\theta,\varphi} \approx 0.5$. The radial turbulent heat flux (Figure 3.16b) shows the same trend as the turbulent intensity (Figure 3.16c) and drops to very low levels even smaller than the level observed in the vorticity case (Figure 3.9a).

In the core, the diffusivity is dominated by tubulence and does not show the decaying trend (Figure 3.17a). Figure 3.17b shows the time evolution of the radial turbulent heat flux which again correlates strongly with the turbulent intensity in the same region (Figure 3.17c). This approach seems effective to reduce the heat turbulent transport coefficient and turbulent intensity both near the steep gradient and in the core.

The origin of the barrier is however more ambiguous than in the vorticity case. Two main factors need to be taken into account here. The first one is the linear stabilization of ITG by the density gradient. The criteria to enable ITG to grow linearly in a tokamak geometry is given in [31]. With our parameters, we get $\kappa_T^{crit} = 22.4$, which is higher than the prescribed value of $\kappa_T = 6.6$. Therefore, the linear stabilization of ITG modes by the density gradient is primarly responsible for the transport barrier creation and the low turbulent heat flux observed in the region $r/a = [0.7, 0.8]$.

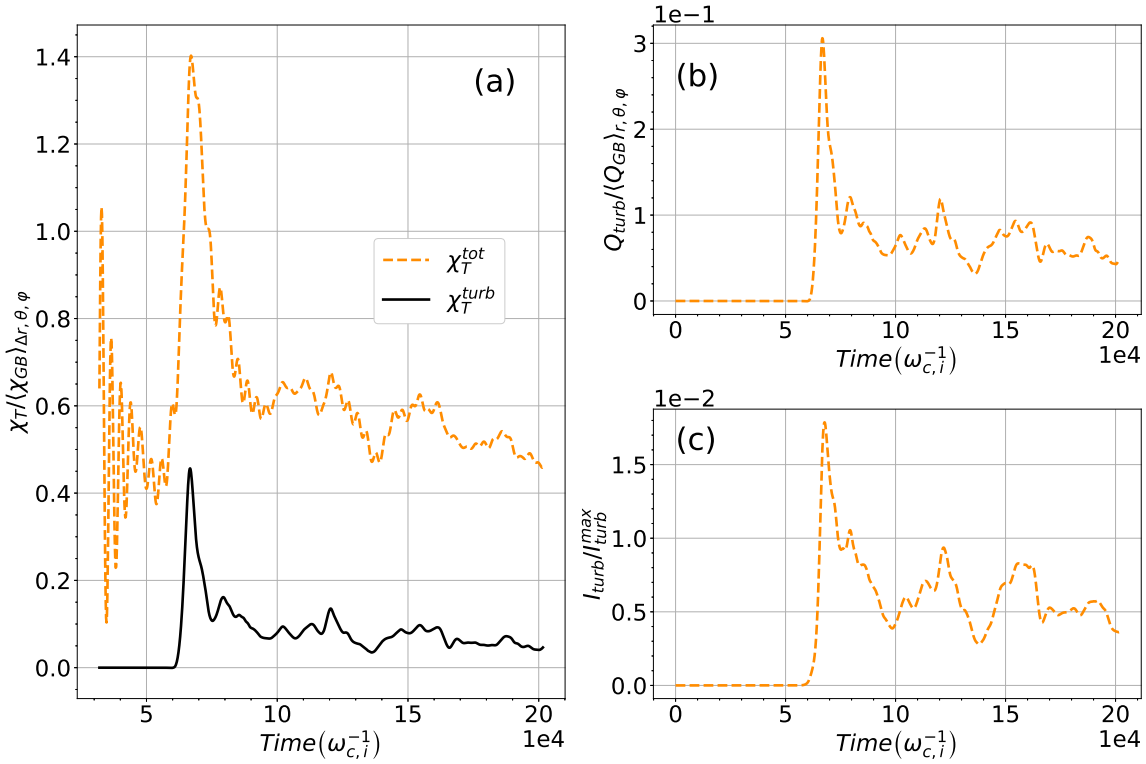

Figure 3.16: Diffusivity, turbulent heat flux and turbulent intensity time evolution averaged in the $r/a = [0.7, 0.8]$ region for the steep gradient case. **(a)** Time evolution of the total (dashed orange line) and turbulent (solid black line) heat diffusivity coefficient. **(b)** Turbulent heat flux as a function of time. **(c)** Turbulent intensity plotted against time. **(b)** and **(c)** signals are in phase.

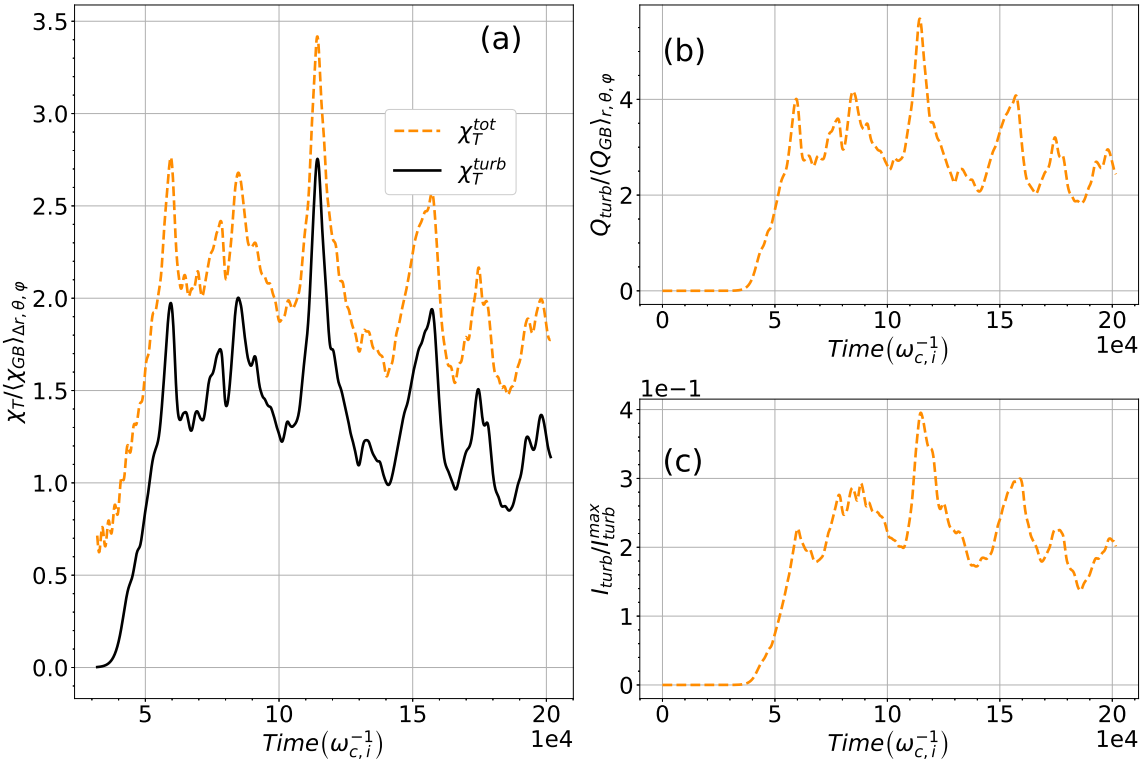

Figure 3.17: This figure is similar to Figure 3.16 except that the radial average is in the $r/a = [0.15, 0.6]$ region for the steep gradient case. **(a)** Time evolution of the total (dashed orange line) and turbulent (solid black line) heat diffusivity coefficient. **(b)** Turbulent heat flux as a function of time. **(c)** Turbulent intensity plotted against time. **(b)** and **(c)** signals are in phase.

Moreover, one cannot neglect the impact of the $E \times B$ shear flow generated by the pressure gradient. As shown in Figure 3.13b and 3.18b, the shearing levels generated by the source and the steep gradient present different shapes (i.e. two vs one lobe) but are within the same order of magnitude of $\sim 8\overline{\gamma}_{lin}$, the average linear growth rate of ITG modes at $r/a = 0.5$. The $E \times B$ flow shear is likely to prevent ITG turbulence to propagate across this region by tearing appart convective cells that could develop e.g. through turbulence spreading. This results in an even more "effective" transport barrier with two different stabilizing mechanisms taking place simultaneously.

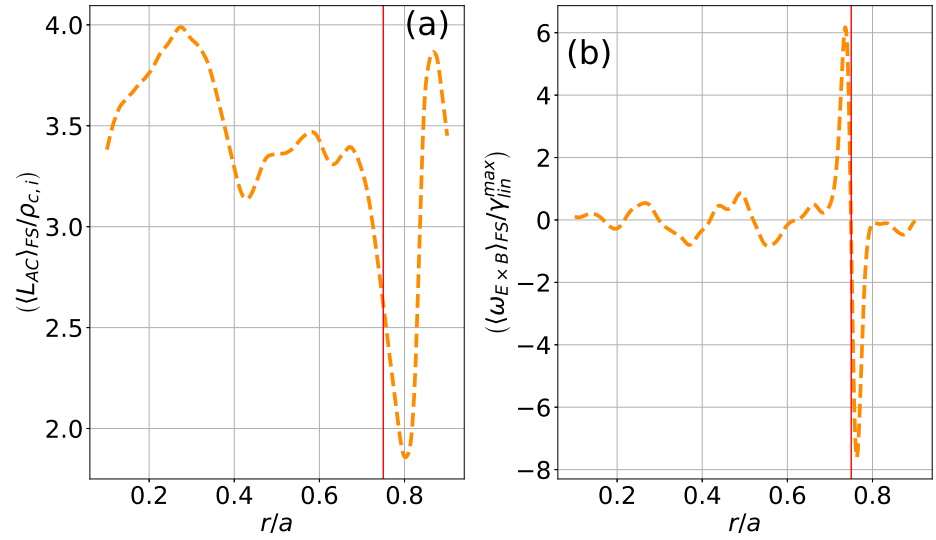

Figure 3.18: Flux surface and time average of the correlation length **(a)** and $E \times B$ shearing rate **(b)** as a function of radius for the steep gradient case. The red vertical line indicates the steep gradient location.

Figure 3.18a confirms the previous analysis by showing that the auto-correlation radial length of the perturbed potential is significantly lower near the steep gradient position at $r/a = 0.75$. This shows that almost no turbulence structures are present here while the rest of the plasma manifests a similar behaviour as evidenced in the reference case (Figure 3.13b, dotted green line).

3.5 Discussion and conclusion

We have analyzed here, by means of flux driven gyrokinetic simulations of ITG turbulence, two different ways to reduce turbulence and make the plasma bifurcate to what can be described as an improved confinement mode with the development of a transport barrier.

The first way is based on a method proposed by A. Strugarek [91, 93] that uses a vorticity source to locally polarize the plasma and generate a strong $E \times B$ shear flow comparable to what is observed experimentally for such plasmas. This method leads to the effective reduction of the turbulent heat diffusivity χ_T^{turb} in the source region when the shear rate $\omega_{E\times B}$ reaches a threshold of $\omega_{E\times B} \approx \overline{\gamma}_{lin}$, meaning no

fluctuation persists in the vicinity of the strongly sheared region. A minor reduction in χ_T^{turb} is observed as well in the core region compared to a reference case, showing that the edge-localized source has an impact on the core. This reduction in turbulent transport can be explained by the turbulent intensity quench observed when vorticity is turned on. Moreover, a shearing of the larger turbulent structures into smaller ones is observed as attested by the change of correlation length in the strong flow shear region. The k_θ spectrum analysis shows the impact of the source with lower turbulent intensity, shifting the maximum of the spectrum to the lower wavenumbers. This effect is due to the structures being tilted in the poloidal direction. This reduction in heat transport led to slightly higher pressure in the core than the reference scenario without the vorticity source.

The second way consists in enforcing an H-mode-like density profile to generate through the radial force balance a localized strong $E \times B$ shear flow. This alternative method managed to stabilize the plasma locally by linearly stabilizing ITG modes through the steep gradient profile enforced. In addition to this linear stabilization effect, the $E \times B$ flow shear generated by the steep pressure gradient also helps stabilizing the plasma by tearing apart any turbulent structures that could grow in the steep gradient region. The edge reduction in heat transport leads to higher core temperatures, meaning the created transport barrier is efficient enough to increase energy confinement.

Accounting for kinetic electrons would allow particle transport in the simulation presented here in both the vorticity and steep gradient cases. The latter case would therefore be difficult to study as we expect the enforced steep density gradient to collapse rapidly and it is not expected to generate and maintain a transport barrier. In addition, TEMs would arise in the system and combine with ITGs and probably lead to higher turbulence level since steep density gradients are destabilizing for TEMs [99]. We still expect the vorticity source to be relevant in the presence of kinetic electrons and we expect a transport barrier could still arise in those conditions, even with TEMs.

However, one may expect a different threshold in the magnitude of the vorticity source to trigger a transport barrier. Indeed, the saturation of TEM turbulence exhibits a different sensitivity to Zonal Flows as compared to ITG. In particular, their contribution to TEM saturation has been found to depend on local plasma parameters, most critically the temperature ratio T_e/T_i and $\eta = L_n/L_{Te}$, the ratio of density over temperature gradient lengths [37, 100, 101, 102].

The next chapter tackles impurity transport in presence of such transport barriers. Both helium and tungsten impurities transport in trace limit are investigated.

Chapter 4

Impurity transport with a transport barrier

4.1 Introduction

The formation of a transport barrier in nonlinear GYSELA simulations has been demonstrated to efficiently reduce ion heat flux generated by ITG turbulence (see chapter 3). In this chapter, we explore both turbulent and neoclassical impurity transport in the presence of a transport barrier, by extending the previous work of K. Lim [17]. Light impurities, such as helium (He), are known to be mainly transported by turbulent transport due to its low collisionality, while heavy impurities, argon (Ar) and tungsten (W), are mainly transported by neoclassical transport. Experiments [103, 104, 105] have demonstrated detrimental core accumulation of heavy impurities due to inward neoclassical convection [14]. These results are qualitatively consistent with the results obtained from nonlinear GYSELA simulations, highlighting the importance of controlling neoclassical transport in fusion devices. Furthermore, recent studies [21, 22, 23] have also confirmed that the need of comprehensive modelling of neoclassical channel in properly describing heavy impurities transport. For this reason, a series of nonlinear GYSELA simulations have been carried out to investigate the effects of transport barrier on turbulent and neoclassical impurity transport.

4.2 Plasma parameters

4.2.1 Parameters and initial conditions

In recent years, a scrape-off layer-like (SOL-like) operator has been implemented in GYSELA to relax the electrostatic potential ϕ towards the pre-sheath conditions expected in that region of the plasma in a poloidally axisymmetric way with $\phi_{bias} = \phi\left(r = r_{wall}\right) \equiv 0$. Additionally, GYSELA has received several critical updates regarding computational optimizations to the collision operator. By leveraging these features, a set of GYSELA simulations have been carried out with more appropriate initial conditions and input parameters compared to the previous work [17]. This modification requires the choice of a modified initial radial density profile with a steeper gradient at the separatrix ($r/a = 1$) as described in Figure 4.1a.

Other plasma parameters, as discussed in section 3.2, are applied and summarized in table 4.1.

The radial profiles of heat and vorticity source terms are shown in Figure 4.1b. The amplitude of $S_0^E = 0.0085$ is set to ensure that the temperature profile is nearly in equilibrium with the prescribed heat source. The radial domain is extended to $r/a = 1.15$ to take into account the SOL region. The values of $\rho^\star = \rho_0/a \equiv 1/200$ and the safety factor, $q\,(r)$, are kept unchanged compared to the section 3.2. With given density and temperature gradients, the value of $\eta = 3$ is applied over the most of the domain to trigger ITG instabilities. The collisionality of the main species is set to $\nu^\star_{D^+} = 0.1$ at $r/a = 0.575$ in the Banana regime.

In Figure 4.2, the time evolution of the electric potential is described for different (m, n) modes. Once the simulations reach the steady state, two different cases, one with the vorticity source ("barrier" case) and one without ("reference" case), are carried out separately. The radial profile of the vorticity source activated at $r/a = 0.7$, where turbulence is found to be sufficient to observe the effect of a transport barrier, is shown in Figure 4.1b with an amplitude of $S_0^\Omega = 0.005$. It is important to note that, in this work, the value of S_0^Ω is reduced from 0.08 to 0.05 compared to the case in chapter 3 to minimize non-physical effect of the vorticity source while maintaining sufficient levels of poloidal $\omega_{E\times B}$ shear to trigger the formation of a transport barrier.

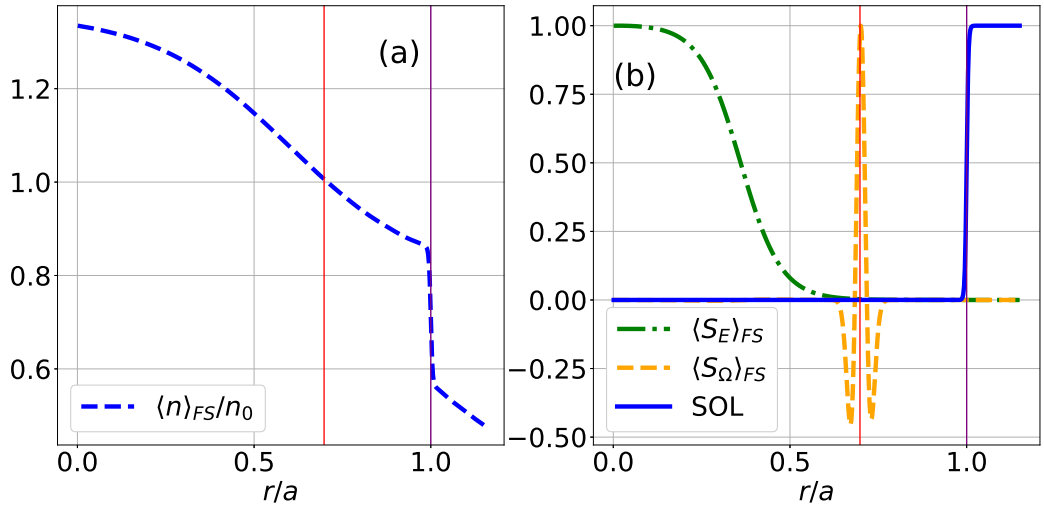

Figure 4.1: **(a):** Radial profile of the initial flux surface averaged guiding-center density. **(b):** Normalized radial profiles of the axisymmetrical SOL mask (solid blue line), fluid energy source (dotted green line) and fluid vorticity source (dashed orange line). The purple vertical line indicates the separatrix position while the red one indicates the vorticity source location if activated.

4.2.2 Triggering of the transport barrier

First, we need to assess whether the vorticity source is effective and the transport barrier is active. To this end, we measure the evolution of the heat diffusivity χ_{turb} as a function of $\omega_{E\times B}$, the poloidal shear rate. Figure 4.3a shows that when $\omega_{E\times B}$

Parameters	Reference	Vorticity
Collision rate	$\nu^{\star}_{D^+}\,(r/a = 0.575) = 0.1$	
Main species charge / atomic numbers	$Z_i = 1, A_i = 2$	
Time step	$\Delta t\omega_{c,0} = 20$	
$N_r \times N_\theta \times N_\varphi \times N_{v_\parallel} \times N_\mu$	$511 \times 1024 \times 64 \times 127 \times 51$	
Normalized gyroradius	$\rho^{\star} = \rho_{c,0}/a = 1/200$	
Inverse aspect ratio	$1/\epsilon = R_0/a = 4.4$	
Maximum density gradient for the main species	$\kappa_n = R_0/L_n = 2.2$	
Maximum Temperature gradient for the main species	$\kappa_T = R_0/L_T = 6.6$	
Amplitude of the vorticity source	$S_0^{\Omega} = 0$	$S_0^{\Omega} = 0.005$*
Amplitude of the heat source	$S_0^{E} = 0.0085$	
Average ITG linear growth rate	$\bar{\gamma}_{lin}/\omega_{c,0} \approx 3.88 \cdot 10^{-4}$	

Table 4.1: Simulation parameters used for the main simulations studied in this chapter. *The poloidal momentum (vorticity) source is activated from $t\omega_{c,0} = 100000$ for the vorticity case and disabled in the reference case.

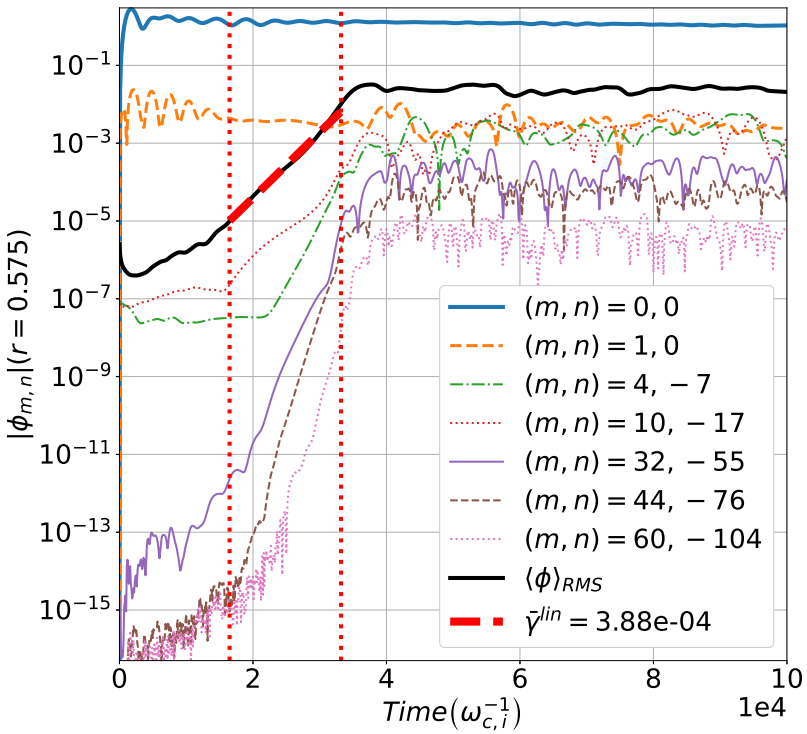

Figure 4.2: $|\phi_{m,n}|$ at $r = 0.575$ plotted against time (up to $t_{vor}\omega_{c,0} = 100000$, the vorticity activation time). $\langle\phi\rangle_{RMS}$ and some resonant modes are plotted for reference. The average linear growth rate is extracted from the $\langle\phi\rangle_{RMS}$ values in the time interval in between the red vertical dotted lines.

reaches a value close to $\bar{\gamma}_{lin}$, the turbulent heat diffusivity is quenched similarly as shown in Figure 3.8. An interesting feature is that χ_{turb} follows a much more chaotic path before dropping to its final value of $\chi_{turb} \approx 0.25$. The main reason for this behaviour is the reduced amplitude of the vorticity source which leads to a longer $\omega_{E\times B}$ shear rate saturation time as less vorticity is injected.

Different from the previous case, temperature profile at the last simulation time shows a steeper gradient and higher core temperature in the vorticity case. Unlike the vorticity case, the temperature gradient remains almost constant in the reference case from $r/a = 0$ to $r/a = 0.95$. The latter shows little change in the temperature gradient within the radial interval $r/a = 0.8$ to $r/a = 0.95$. This means that the energy confinement is enhanced up to the vorticity source location, where the shearing is at its maximum; these observations confirm that the transport barrier was well triggered. We then let both the reference and vorticity simulations reach a time of $t = 220000\omega_{c,i}^{-1}$ where they converge to a quasi steady-state with almost constant pressure radial profiles.

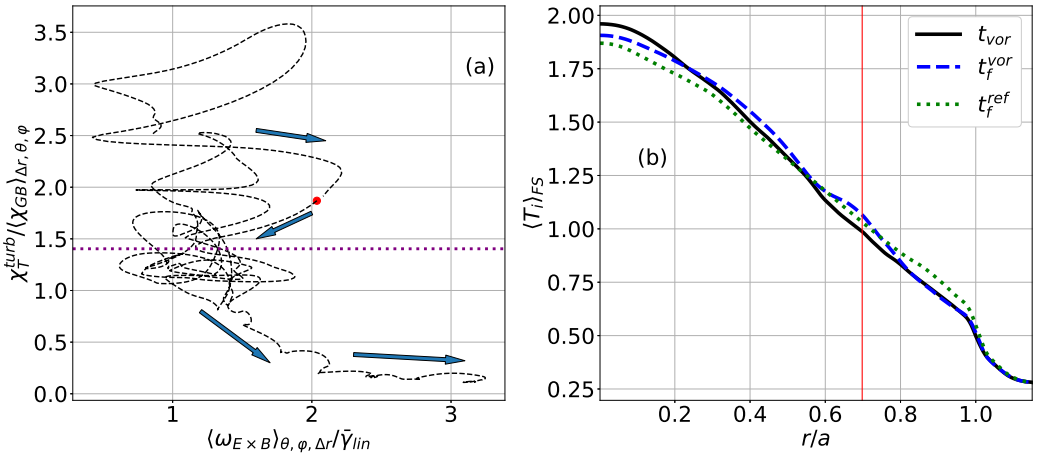

Figure 4.3: **(a)**: Turbulent heat diffusivity χ_T^{turb} plotted against the shear rate $\omega_{E\times B}$ in the source region $r/a = [0.65, 0.75]$ for $t\omega_{c,0} = [90000, 220000]$. The red dot represents the vorticity activation time for the vorticity case $t_{vor}\omega_{c,0} = 100000$. Arrows indicate the time evolution. The dotted horizontal line represents half of the average value of $\chi_T^{turb}/\langle\chi_{GB}\rangle_{\Delta r,\theta,\varphi}$ prior to the source activation, the threshold for turbulence suppression. **(b)**: Temperature profile at the source activation time ($t_{vor} = 100000\omega_{c,i}^{-1}$, solid black line) and the last simulation time of the reference ($t_f^{ref} = 220000\omega_{c,i}^{-1}$, dotted green line) and vorticity ($t_f^{vor} = 220000\omega_{c,i}^{-1}$, dashed blue line) cases.

4.2.3 Impurity injection

Different type of impurities coexist in fusion devices affecting the performance of fusion reactors. The main physical mechanism that control impurity transport depends on the atomic mass and impurity charge (i.e. their collisional regime). It is therefore important to investigate different types of impurities to obtain a more

comprehensive understanding of impurity transport. For the considered simulations, we choose the following three species:

- Helium ${}^{4}_{2}\mathrm{He}^{2+}$ ions, the ashes of the D-T fusion reaction, are light impurities which are usually in the same collisionality regime as hydrogen isotopes (${}^{1}_{1}\mathrm{H}^{1+}$, ${}^{2}_{1}\mathrm{D}^{1+}$, ${}^{3}_{1}\mathrm{T}^{1+}$, Banana-Plateau regime). This species is mainly transported by turbulence due to its smaller mass and low charge.

- Argon ${}^{40}_{18}\mathrm{Ar}^{18+}$ ions are usually injected around Plasma-Facing Components (PFC) to mitigate the power exhaust loaded on them, especially on the divertor. These species are classified as intermediate-Z species and are mainly governed by neoclassical transport. Their collisional regime is intermediate between Plateau and Pfirsch-Schlüter regimes.

- Tungsten ${}^{184}_{74}\mathrm{W}^{40+}$ ions, which composes most of modern tokamaks' divertor plates, can be sputtered after extremely high intensity burst of heat flux. They are not fully ionized even at core temperatures and are in a high collisionality regime, namely Pfirsch-Schlüter regime. The neoclassical channel is usually the dominant one for this species.

Simulation branches are summarized in appendix C.3 for clarity.

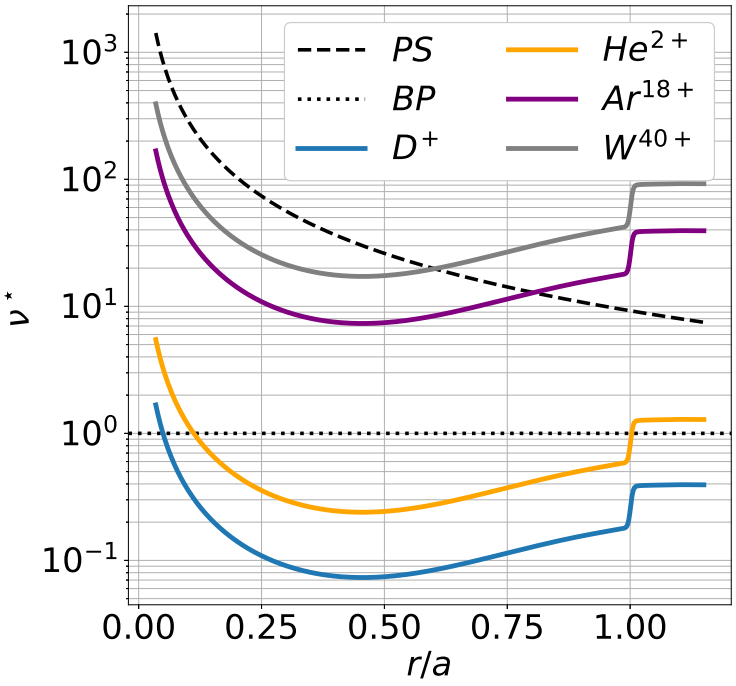

Figure 4.4: Collisionality profiles for the different species considered with the Banana-Plateau (BP) and Pfirsch-Schlüter (PS) limits plotted in dash and dotted black lines. The higher the atomic number or charge number, the higher the collisionality as computed through equation (4.1).

The density profiles of each impurity are similar to those of the main ions, as described in Figure 4.1a, while the concentrations differ, with $f_{He} = 8 \cdot 10^{-10}$, $f_{Ar} = 8.8 \cdot 10^{-11}$ and $f_W = 4 \cdot 10^{-11}$. This indicates that impurities are in the trace

limit, thereby having no impact on the background ITG turbulence [106]. The radial profiles of the collisionalities are shown in Figure 4.4 based on the following expression [14]:

$$\nu_s^\star = \frac{qR_0}{\epsilon^{3/2}} \frac{4\sqrt{\pi}}{3} \frac{e^4 \log\Lambda}{(4\pi\epsilon_0)^2} \frac{Z_{D^+}^2}{T_{D^+}^2} \left[n_{D^+} Z_{D^+}^2 + \sum_{s \neq D^+} \sqrt{2} N_s Z_s^2 \frac{(1 + M_{D^+}/M_s)}{\left(1 + v_{T_s}^2 / v_{T_{D^+}}^2\right)^{3/2}} \right], \quad (4.1)$$

where the s index represents the considered impurity species and D^+ the main species (i.e. fully ionized deuterium). Tungsten is near the Pfirsch-Schlüter limit while argon and helium are respectively in the Plateau and Banana regimes, which translates to

$$\nu_{D^+}^\star < \nu_{He^{2+}}^\star \ll 1 \ll \nu_{Ar^{18+}}^\star < \epsilon^{-3/2} \approx \nu_{W^{40+}}^\star . \quad (4.2)$$

Unlike the main ions, no sources are applied for impurities. This means that the transfer of energy and poloidal momentum from main ions to impurities will be only done through collisional effects and turbulent heating. Impurities are injected as a secondary species in the Vlasov equation after both the reference and vorticity cases have reached almost constant temperature and shearing profiles at $t = 220000\omega_{c,i}^{-1}$.

4.3 Numerical results

The numerical computation time required to evolve two species in nonlinear gyrokinetic simulations is challenging. To this end, we run a first simulation with the main ion species only (i.e. with D^+ and without impurities) for a sufficiently long time to reach the steady state. Once this state is achieved, we inject impurities at $t_{imp} = 220000\omega_{c,i}^{-1}$ for another run for $50000\omega_{c,i}^{-1}$. Impurity particle fluxes are then computed in the same way as the heat fluxes in equation (3.17) and can also be separated into two distinct channels

$$\Gamma^{neo} = \left\langle \int \left(v_D^r + v_{E_{n=0}}^r \right) \bar{F}_s dv \right\rangle_{FS}, \quad (4.3)$$

$$\Gamma^{turb} = \left\langle \int v_{E_{n\neq 0}}^r \bar{F}_s dv \right\rangle_{FS}, \quad (4.4)$$

where Γ^{neo} and Γ^{turb} are the flux-surfaced averaged neoclassical and turbulent particle fluxes respectively. Similarly as before, the neoclassical channel is the sum of the curvature and gradient drift contributions as well as the toroidally axisymmetric $E \times B$ drift contribution while the turbulent channel is the non toroidally axisymmetric $E \times B$ drift contribution. The total flux-surfaced averaged particle flux can then be written

$$\Gamma^{tot} = \Gamma^{turb} + \Gamma^{neo}. \quad (4.5)$$

Since we are interested in the dynamics near the source (i.e. $r/a = 0.7 \pm 0.05$) and the core ($r/a \leqslant 0.65$), we choose to focus on a radial region going from $r/a = 0$ to $r/a = 0.9$ since particle flux is affected by the boundary conditions after $r/a = 0.9$.

4.3.1 Density, temperature and total impurity flux profiles

Density

In the absence of the transport barrier, helium is mainly directed outward due to turbulent transport leading to a hollow density profile [17]. Whereas, with the onset of a transport barrier, the helium density profile near the source region is greatly affected as described in Figure 4.5. On the inner side of the barrier, particles accumulate, leading to the formation of a density shoulder, while at the source position the formation of a density well is observed.

Argon and tungsten show similar behaviours, an increased accumulation rate at the core, when the transport barrier is present. This is supported by Figure 4.6; in the reference case, helium is slowly flushed out from the core while argon and tungsten accumulate in the core (see top left of Figure 4.6). However, when the transport barrier is present, all species accumulate in the core, although the accumulation is very slow for helium (see bottom left of Figure 4.6). Argon and tungsten are accumulating approximately twice as fast when compared to the reference case, which unfortunately increases contamination.

Looking at the edge region gives us a better understanding of what happens. In the reference case (top right of Figure 4.6), helium levels are increasing while argon and tungsten remain approximately constant. This indicates that helium tends to be flushed out from the core towards the edge. When the transport barrier is turned on, density levels for all impurities decrease at the edge, especially for argon.

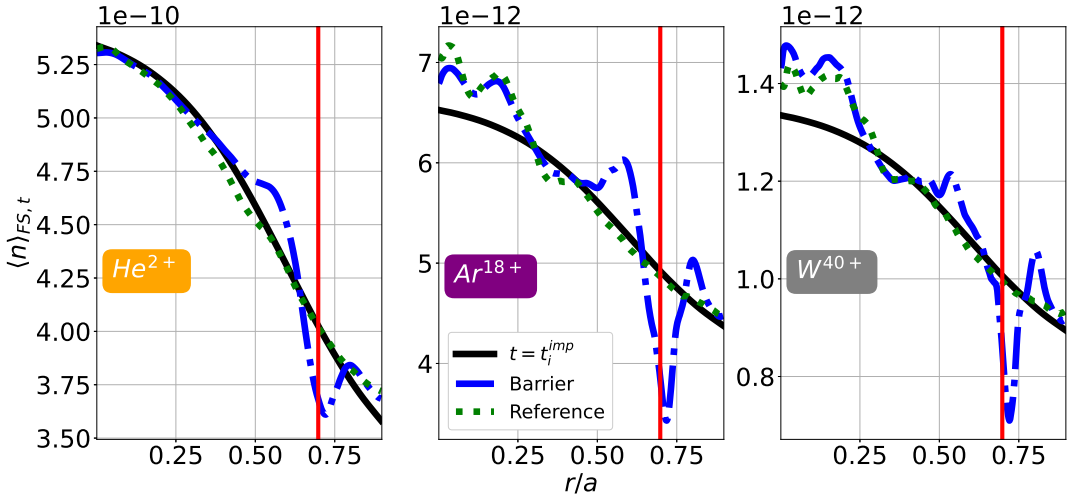

Figure 4.5: Flux-surface averaged densities of helium (left), argon (center) and tungsten (right) in the reference (dotted green lines) and vorticity (dotted-dashed blue lines) cases. Solid black lines represent the initial profile of the corresponding impurities. All profiles are time averaged over the last $5000\omega_{c,i}^{-1}$ of the simulations except for the initial profiles.

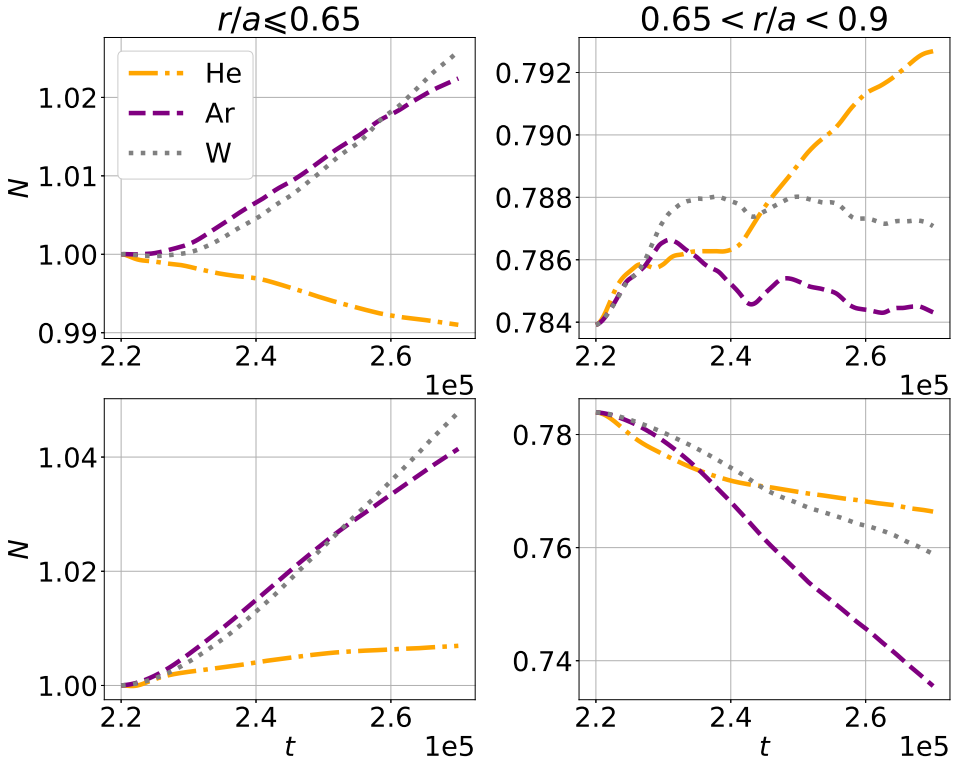

Figure 4.6: Time evolution of the average densities of helium (orange dashed-dotted lines), argon (purple dashed lines) and tungsten (gray dotted lines) in the reference (top row) and vorticity (bottom row) cases. Left column corresponds to an average over $r/a \leqslant 0.65$, representing the core particle density evolution, while the right column is averaged over $0.65 < r/a < 0.9$, representing the edge density evolution. Values are normalized with the average density over $0 < r/a < 0.9$ at $t = t_i^{imp}$, the time of impurity injection (i.e. the integral of the initial impurity density profile).

This indicates that the transport barrier separates the plasma in two regions; the inside and the outside of the barrier. Within the barrier, a strong core accumulation of impurities is observed due to an inward radial particle flux, as these impurities cannot cross the transport barrier. On the outside of the barrier, an outward particle flux flushes impurities out of the plasma, preventing these impurities from penetrating into the core region (see Figure 4.6, bottom right).

Poloidal asymmetry of density, defined as

$$\delta N_s = \left\langle N_s^f - N_s^0 \right\rangle_\varphi / \left\langle N_s^0 \right\rangle_\varphi \tag{4.6}$$

with N_s^f and N_s^0 the density of the species s at the final and initial time of the simulation respectively, are plotted in Figure 4.7. Poloidal asymmetries are found to be more prominent for heavy impurities due to their high charge numbers. For instance, argon and tungsten exhibit $\sim 20\%$ and $\sim 30\%$ of asymmetries respectively, while the degree of asymmetry for helium remains below 3%.

However, when the transport barrier is turned on, the distribution of impurity density is strongly affected in the vicinity of the barrier. The use of the vorticity source results in the formation of strong convection cells near the transport barrier, thereby increasing the poloidal asymmetry in this region. Non-homogenous distribution of impurity density are known to significantly modify neoclassical transport, typically accelerating the core accumulation [15].

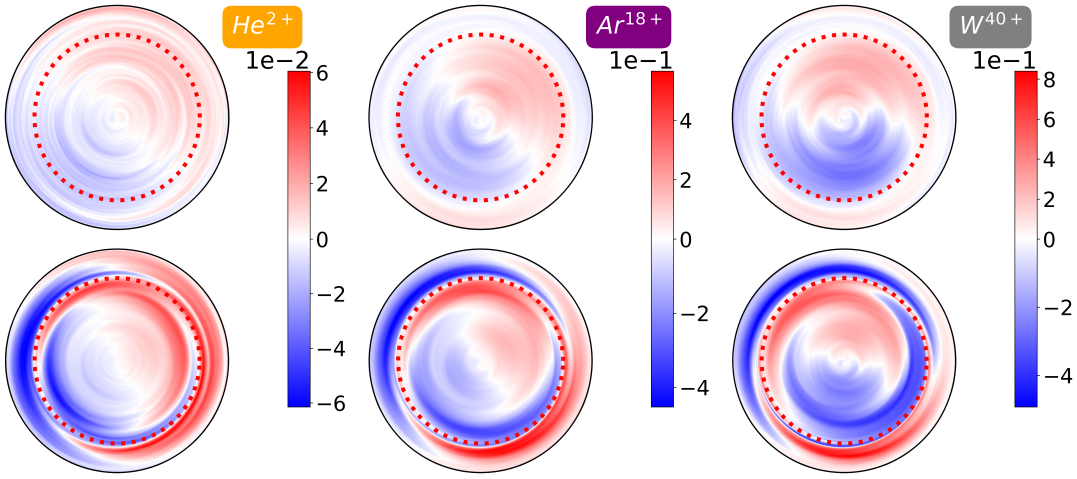

Figure 4.7: Density fluctuations $\delta N = \left\langle N_s^f - N_s^0 \right\rangle_\varphi / \left\langle N_s^0 \right\rangle_\varphi$ for helium (left column), argon (center column) and tungsten (right column) with (bottom row) and without (top row) the transport barrier. The dotted red circle represents the vorticity source position at $r = 0.7$.

Temperature

The temperature profile of helium (Figure 4.8, left plot) remains very similar, regardless of whether the vorticity source is activated with only a slight increase in core temperature and its gradient in the case of the transport barrier. The effect of the transport barrier is more pronounced for high-Z impurities (Figure 4.8, center

and right plots) as their response to the polarized electric potential is proportionnal to $\propto Z_s\phi$. This might indicate that the effect of the transport barrier on heat flux is more efficient for heavy impurities, while the temperature profile of helium remains similar to that of the main ions.

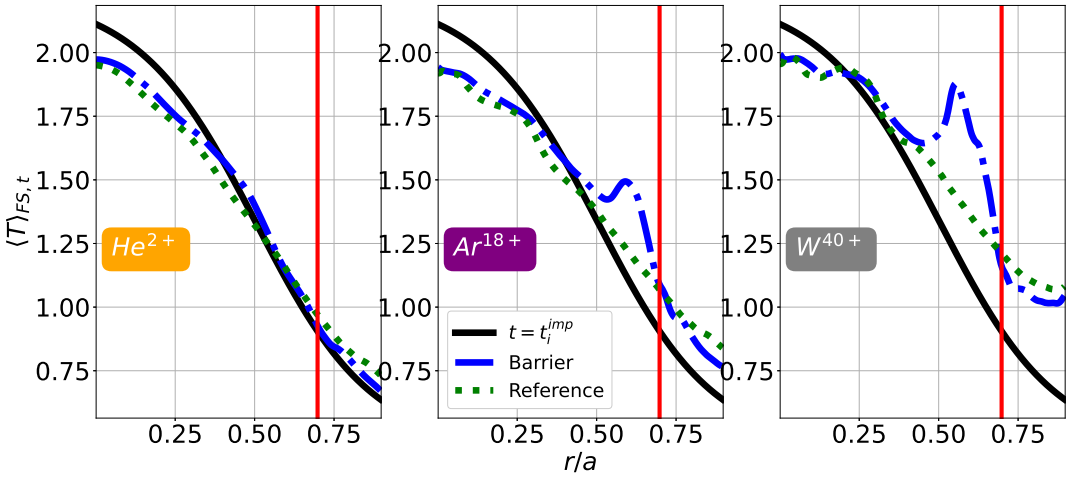

Figure 4.8: Flux-surface averaged temperatures of helium (left), argon (center) and tungsten (right) in the reference (dotted green lines) and vorticity (dotted-dashed blue lines) cases. Solid black lines represent the initial profile of the corresponding impurities. All profiles are time averaged over the last $5000\omega_{c,i}^{-1}$ of the simulations except for the initial profiles.

Total impurity flux

In this subsection, we focus on the total particle fluxes described in equation (4.5). Hereafter, the impurity flux is normalized to the integrated flux $\left|\int dr \left\langle \Gamma_{ref}^{tot,s} \right\rangle_{t,\Delta r}\right|$ of the reference case where no transport barrier is present. The radial range $\Delta r \in [0, 0.9]$ and the time window $\Delta t = 5000\omega_{c,i}^{-1}$ are set for the analysis of numerical results. For helium (Figure 4.9, left), the total particle flux switches from outward to inward. Helium on the inner side of the transport barrier (i.e. $r/a \leqslant 0.7$) is then accumulated toward the core while a thin layer of outward radial flux is present on the outer side of the source (i.e. $r/a \geqslant 0.75$) shows that particles cannot penetrate the plasma core when they come from the outside of the transport barrier.

Both argon and tungsten (Figure 4.9, center and right respectively) simulations show similar behaviour as they both had radially inward directed particle fluxes in the reference case. The transport barrier creates an enhanced layer of inward radial particle flux on the inner side of the transport barrier (i.e. $r/a \in [0.5, 0.7]$), increasing the accumulation rate of those heavy impurities in the core. However, an outward radial particle flux is created on the outer side of the transport barrier (i.e. $r/a \geqslant 0.7$) which requires more analysis by looking at the neoclassical and turbulent channels separately.

The results presented here provide evidence that the transport barrier generated by $E \times B$ shearing through the vorticity source acts as a barrier not only for the heat flux of the main ions, but also for the impurity flux. This observation is

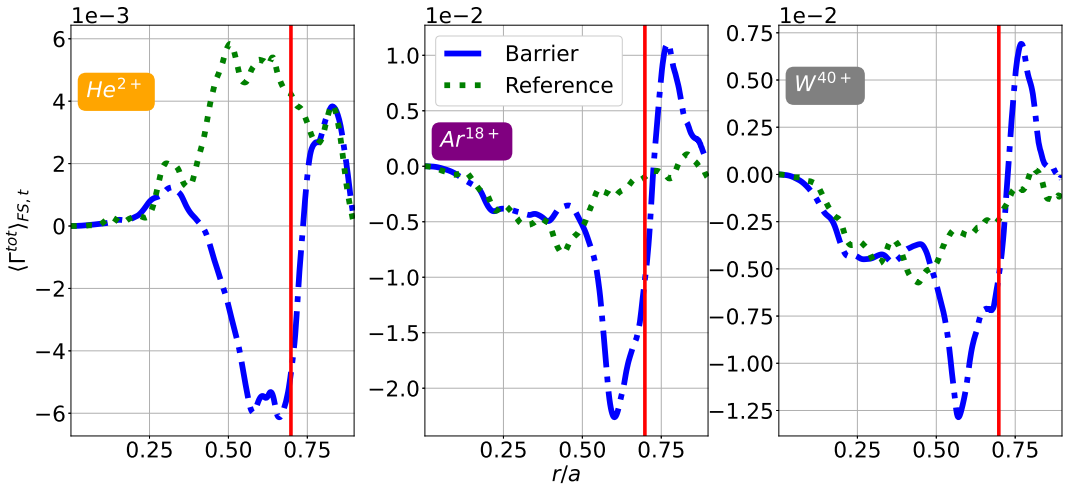

Figure 4.9: Total particle flux-surface averaged fluxes for helium (left), argon (center) and tungsten (right) in the reference (dotted green lines) and vorticity (dotted-dashed blue lines) cases. All profiles are time averaged over the last $5000\omega_{c,i}^{-1}$ of the simulations.

especially true for heavy and highly collisional impurities (i.e. argon and tungsten). The presence of the transport barrier allows particles already on the inside of the transport barrier to accumulate in the core, while particles coming from the outside are repelled.

Considering that both tungsten and argon are coming from the walls or divertor, this may show that if an intense enough $E \times B$ poloidal shearing is maintained throughout the experiment, heavy impurities will not contaminate the core. However, concerns may be expressed regarding helium since it usually needs to be flushed towards the separatrix and divertor region. Those results suggest that strong $E \times B$ poloidal shearing may contradict this specific requirement.

In the next subsections, we propose to look at the different components of the radial impurity fluxes using equations (4.3) and (4.4) to study the neoclassical and turbulent impurity flux channels separately.

4.3.2 Neoclassical impurity flux

The neoclassical channel, defined in equation (4.5), is usually dominant for heavy impurities and is strongly affected by poloidal asymmetries as shown by previous calculations on section 2.2.3. Since the vorticity source injects both poloidal asymmetry of perpendicular *and* parallel pressure in addition to a pressure anisotropy, poloidal asymmetry is expected to play an important role in the neoclassical particle flux profiles, especially for the banana-plateau component.

As expected, we retrieve known results [17] in the reference cases (green dotted lines) as Figure 4.10 shows that helium (left) presents very low level of neoclassical transport while the opposite is observed for both argon (center) and tungsten (right). When the transport barrier is activated, a similar trend is observed for all species - a strongly sheared particle flux profile at the source location (i.e., $r/a = 0.7$). On both inner and outer sides of the transport barrier, particle fluxes show similar magnitudes but opposite signs, with the inner side driving inward flux

(negative) and the outer side an outward flux (positive). This demonstrates that neoclassical flux predominates over turbulent flux within the transport barrier region.

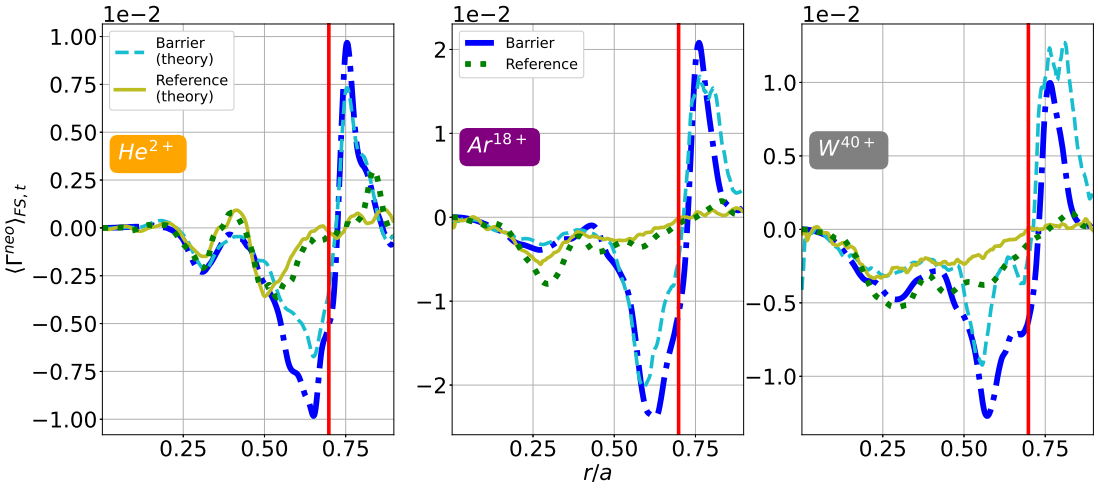

Figure 4.10: Neoclassical particle flux-surface averaged fluxes for helium (left), argon (center) and tungsten (right) in the reference (dotted green lines) and vorticity (dotted-dashed blue lines) cases. Theoretical neoclassical fluxes are computed through equations (2.21) to (2.26) for the barrier (dashed cyan lines) and reference (solid olive lines) cases. All profiles are time averaged over the last $5000\omega_{c,i}^{-1}$ of the simulations.

As shown in Figure 4.10, theoretical predictions, computed using GYSELA profiles (n, P, T etc...) with equations (2.21) to (2.26), are found to be accurate in the reference cases. Additionaly, it captures the correct features of the transport barrier characteristics in our case with a relatively good agreement of profiles in the source region, namely the sheared aspect and extrema amplitude on both sides of the barrier. A more in-depth analysis of the different components of the neoclassical flux (Figure 4.11) shows different behaviours depending on the species examined.

For all species in the reference case, we retrieve similar results to those of K. Lim [17] with BP fluxes dominating in the case of helium. Furthermore, the highest levels of PS fluxes are observed for the tungsten, as expected since this component highly depends on collisionality levels which tend to increase with atomic mass number. A strong BP flux is still observed for heavy impurities inside the barrier.

For helium, the PS flux remains extremely low whether the barrier is in place or not; the BP flux mainly determines the radial profile of the neoclassical flux and hence the total flux when the transport barrier is present. The sheared aspect of the radial profile is retrieved solely in this channel. Argon shows the same trend regarding the BP flux, which becomes 5 times larger in the source region when activated. A substantial increase in the PS flux in the source region is also observed, especially on the outer side of the transport barrier where both PS and BP flux reach the same amplitude levels while also presenting the sheared profile. This behaviour is amplified for the tungsten; this time, the PS flux amplitude is almost twice as big as the BP flux on the outside of the source when activated.

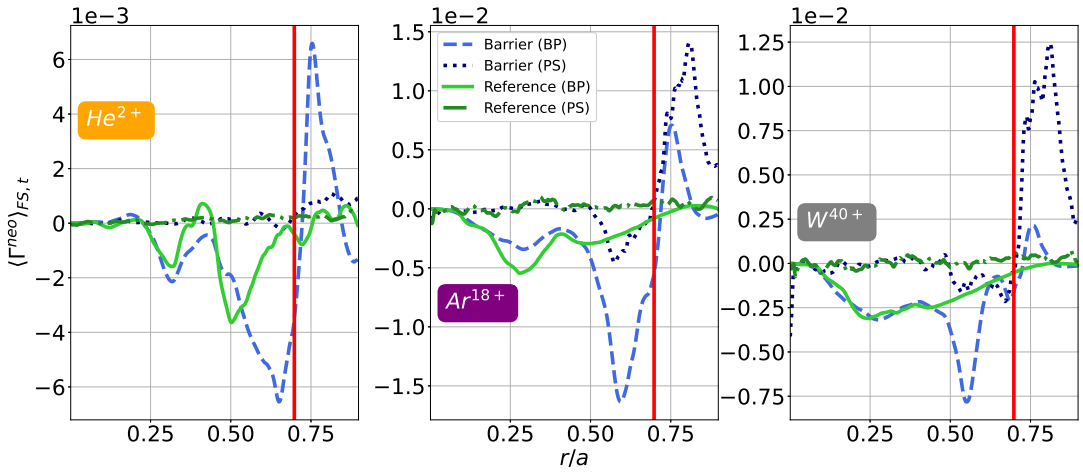

Figure 4.11: Theoretical neoclassical particle flux-surface averaged fluxes for helium (left), argon (center) and tungsten (right). Banana-plateau and Pfirsch-Schlüter fluxes for both the reference (solid light green and dotted-dashed lines for BP and PS fluxes respectively) and barrier (dashed light blue and dotted lines for BP and PS fluxes respectively) are presented separately. All profiles are time averaged over the last $5000\omega_{c,i}^{-1}$ of the simulations.

To better understand what is responsible for the behaviour observed, we plot the major components of the neoclassical flux separately in Figure 4.12 with the BP components on the top row and the PS components on the bottom row. For helium, the increase in BP flux (Figure 4.12, top left) is exclusively due to the term

$$\Gamma^{\Pi_\parallel} = -\frac{I}{Ze}\left\langle \frac{B^2}{N_z}\right\rangle_\psi^{-1}\left\langle \frac{\mathbf{B}\cdot\nabla\theta}{N_z} B \frac{\partial}{\partial\theta}\left(\frac{\Pi_{\parallel,z}}{B}\right)\right\rangle_\psi , \tag{4.7}$$

which is directly linked to the poloidal asymmetry of pressure anisotropy $\partial_\theta\left(\Pi_{\parallel,z}/B\right) = \partial_\theta\left[\left(P_{\parallel,z} - P_{\perp,z}\right)/B\right]$. As expected, this is a direct result of the vorticity source. The same effect can still be seen on both argon and tungsten (Figure 4.12, top center and top right) but with a smaller impact on the outer side of the transport barrier as atomic mass and charge number increases.

However, argon and tungsten also undergo major modification in PS fluxes. This change is mainly due to the main ion species pressure gradient term

$$\Gamma^{\nabla N_i} = \frac{I^2 T_i m_z \nu_{z,i}}{Ze^2}\frac{1}{L_{\psi,i}}\left(\left\langle\frac{N_z}{B^2}\right\rangle_\psi - \left\langle\frac{B^2}{N_z}\right\rangle_\psi^{-1}\right), \tag{4.8}$$

with $1/L_{\psi,i} = \partial_\psi \ln P_i - \frac{3}{2}\partial_\psi \ln T_i$. This behaviour can be explained by the temperature profile steepening as a result of the transport barrier at the source location.

Drawing conclusion about neoclassical transport is therefore challenging due to the impact of the vorticity source on the asymmetry of pressure anisotropy (i.e. the $\Gamma^{\Pi_\parallel}$ term), especially for helium which is the most affected because of its light mass.

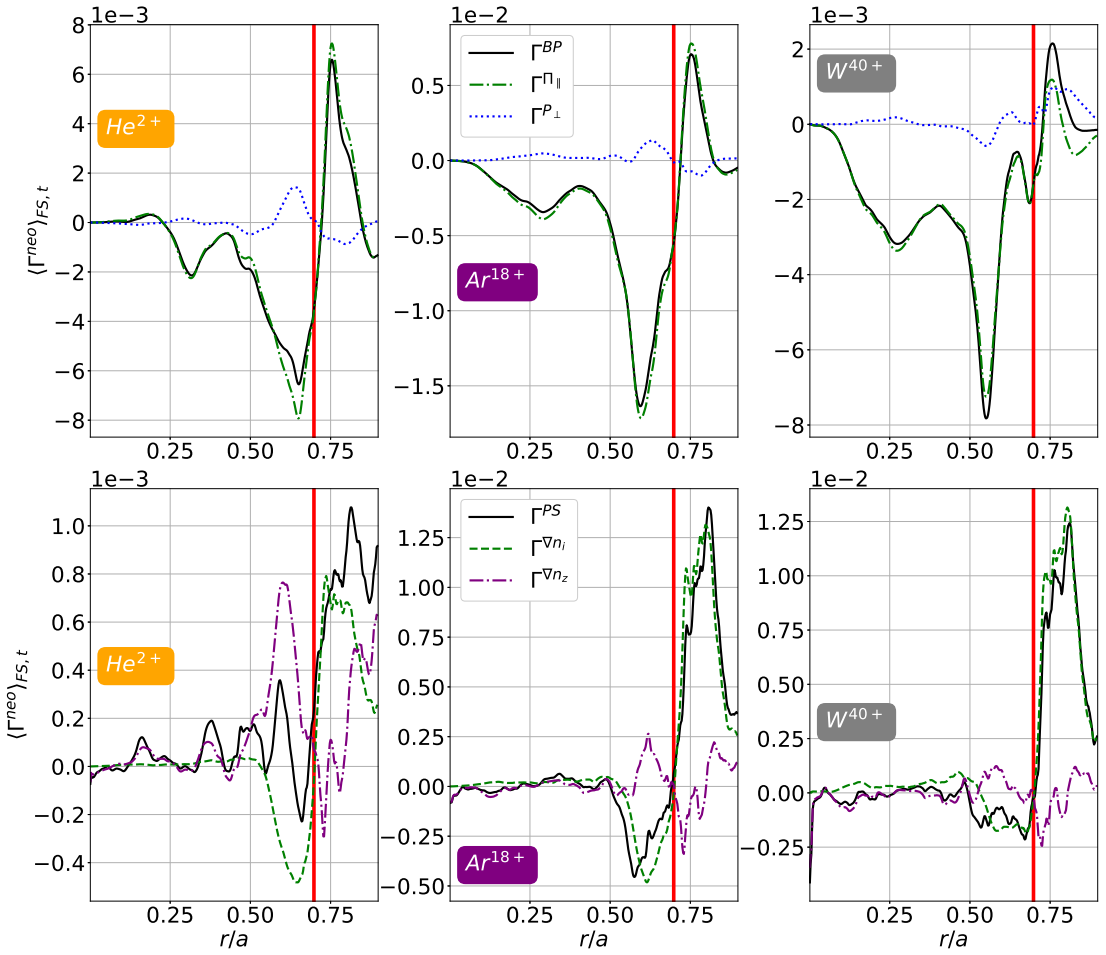

Figure 4.12: Components of the theoretical neoclassical fluxes in the vorticity case. Top row represents the total banana-plateau flux (solid black lines) and its components while the bottom row shows the Pfirsch-Schlüter flux (solid black line) and the dominant terms composing it, Γ^u and Γ^K being discarded since they are small compared to $\Gamma^{\nabla_{N_i}}$ and $\Gamma^{\nabla_{N_z}}$. Detailed terms are given in equations (2.21), (2.22), (2.23) and (2.25). All profiles are time averaged over the last $5000\omega_{c,i}^{-1}$ of the simulations.

In real tokamak experiments with ETBs, such a high level of asymmetry in pressure anisotropy is unlikely. Therefore, the neoclassical impurity flux observed here, particularly for helium, might not be realistic. However, for argon and tungsten, the fact that the pressure terms become more important is more encouraging as these terms are expected to be important in experiments. Poloidal maps of the pressure anisotropy of impurities $\Pi_{s,\parallel} = P_{s,\parallel} - P_{s,\perp}$ are given in Figure 4.13 for the reference and barrier cases. As expected, poloidal asymmetries are strongly enhanced in the transport barrier region when the poloidal momentum source is activated, hence the increase observed in $\Gamma^{\Pi_\parallel}$.

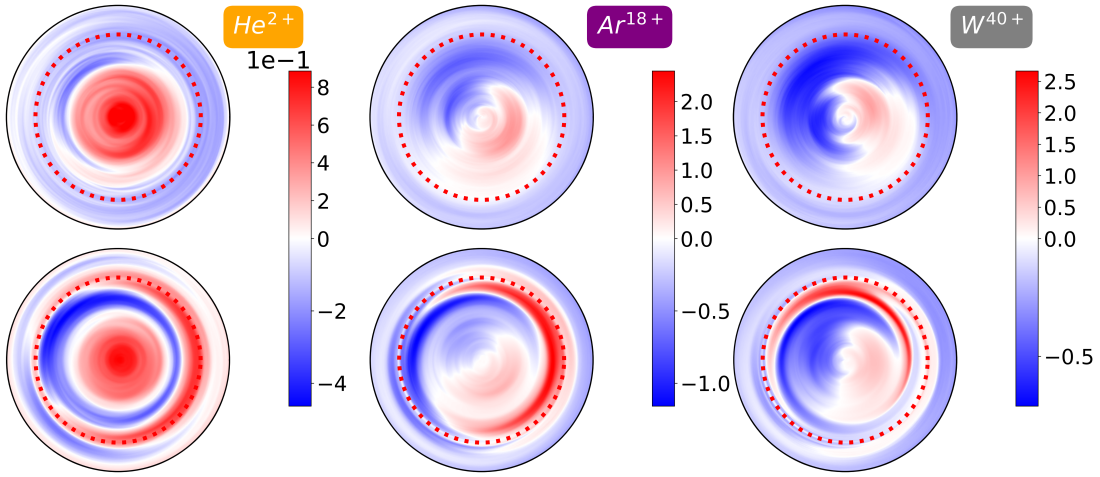

Figure 4.13: Pressure anisotropy $\Pi_{s,\parallel} = P_{s,\parallel} - P_{s,\perp}$ poloidal maps for helium (left column), argon (center column) and tungsten (right column) with (bottom row) and without (top row) the transport barrier. The dotted red circle represents the vorticity source position at $r = 0.7$. Maps are normalized to the maximum absolute value of the reference poloidal map of the impurity considered at the last simulation time (i.e. top row).

The choice of impurity profile can also be discussed. For helium, the choice of a negative density gradient (i.e. decreasing with respect to r/a, similarly as for the main species) is supported by the fact that helium should be generated in the core plasma. However, argon and tungsten are not coming from the core but rather from the edge and should therefore have a *reversed* density profile, larger at the edge and smaller in the core. Simulations with reversed density profiles are under investigation.

Turbulent channel

The turbulent impurity flux, defined in equation (4.4), can be significantly affected by the transport barrier, as highlighted in section 3. Light and low-Z impurities are mainly transported by turbulence. Given that the transport barrier can efficiently reduce turbulence levels, helium is expected to be strongly affected among the different impurities explored in this study.

A first way to look at the turbulent impurity flux is to monitor its radial profile evolution. For this purpose, we plot a 2D colour map of Γ^{turb} as a function of time

(y-axis) and space (x-axis, radius) as shown in Figures 4.14 (helium), 4.15 (argon) and 4.16 (tungsten).

In the reference case, the particle flux of helium is directed outward (positive) from $r/a = 0.2$ to the edge, indicating that helium is mainly transported outward by turbulence. This trend changes completely in the presence of the transport barrier, similarly to the heat flux shown in Figure 3.6. The flux amplitude on the inside of the vorticity source, from $r/a = 0.38$ to $r/a = 0.65$, is greatly lowered while the outside, $r/a \geqslant 0.7$, reverses its sign. The core plasma, from $r/a = 0.2$ to $r/a = 0.38$, remains unaffected by the transport barrier with a constant band of turbulent flux stabilizing at values close to the reference one.

Argon and tungsten exhibit similar behaviours in both the reference and vorticity cases. In the reference case, the sign of particle transport is changed after $2000\omega_{c,i}^{-1}$ (i.e. the time required for additionnal species to be affected by turbulence). With the vorticity source, the turbulent flux in the core region, from $r/a = 0.2$ to $r/a = 0.5$, remains negative during the entire simulation time, while a small radial band (i.e. from $r/a = 0.5$ to $r/a = 0.6$) shows very little turbulent transport. Interestingly, the vicinity of the transport barrier is similar across all three impurity species tested, with a thin layer of outward flux inside the barrier, and inward flux outside the barrier, similarly to Figure 3.6.

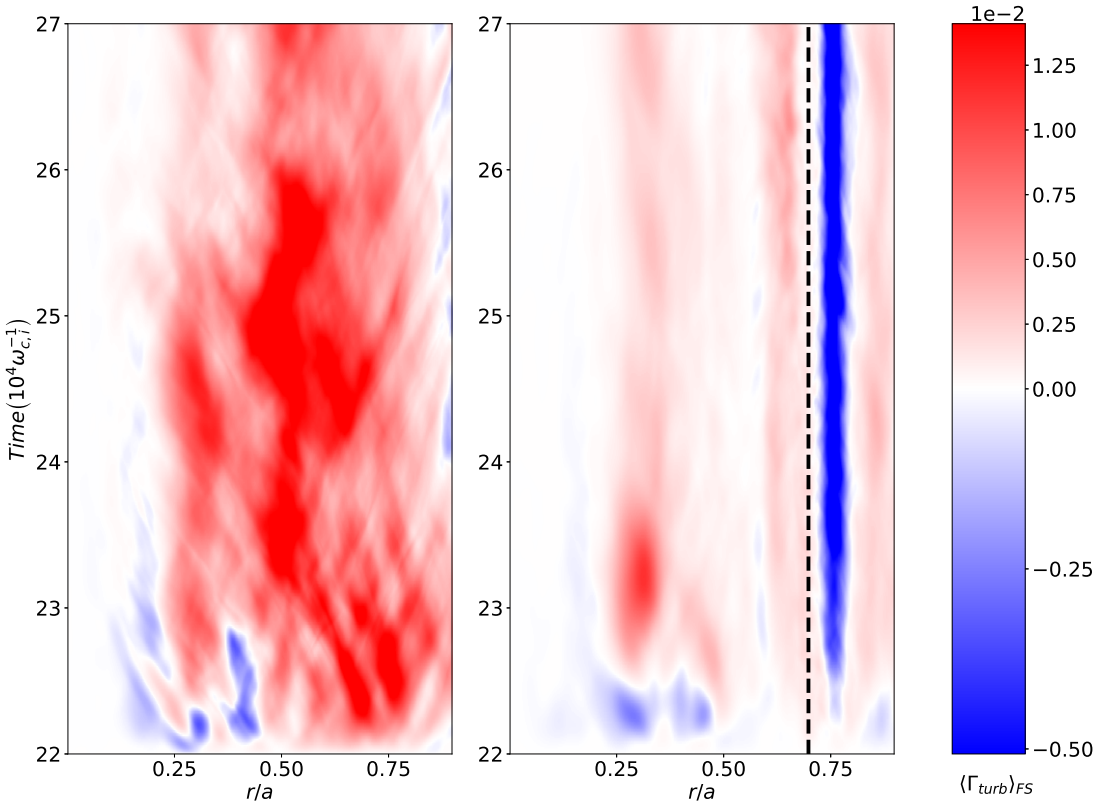

Figure 4.14: Turbulent flux as a function of time (y-axis) and space (x-axis) for helium impurities. Left plot is for the reference case while the right one is when the vorticity source is turned on. The dotted black vertical line indicates the vorticity source position.

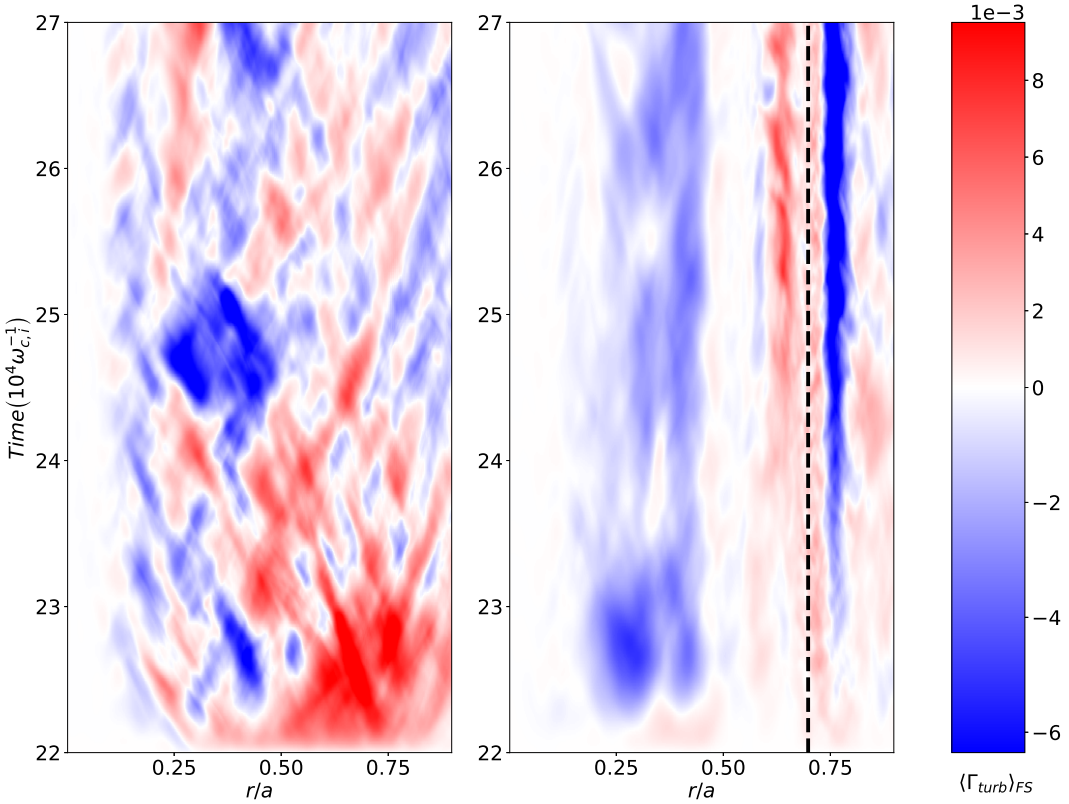

Figure 4.15: Turbulent flux as a function of time (y-axis) and space (x-axis) for helium impurities. Left plot is for the reference case while the right one is when the vorticity source is turned on. The dotted black vertical line indicates the vorticity source position.

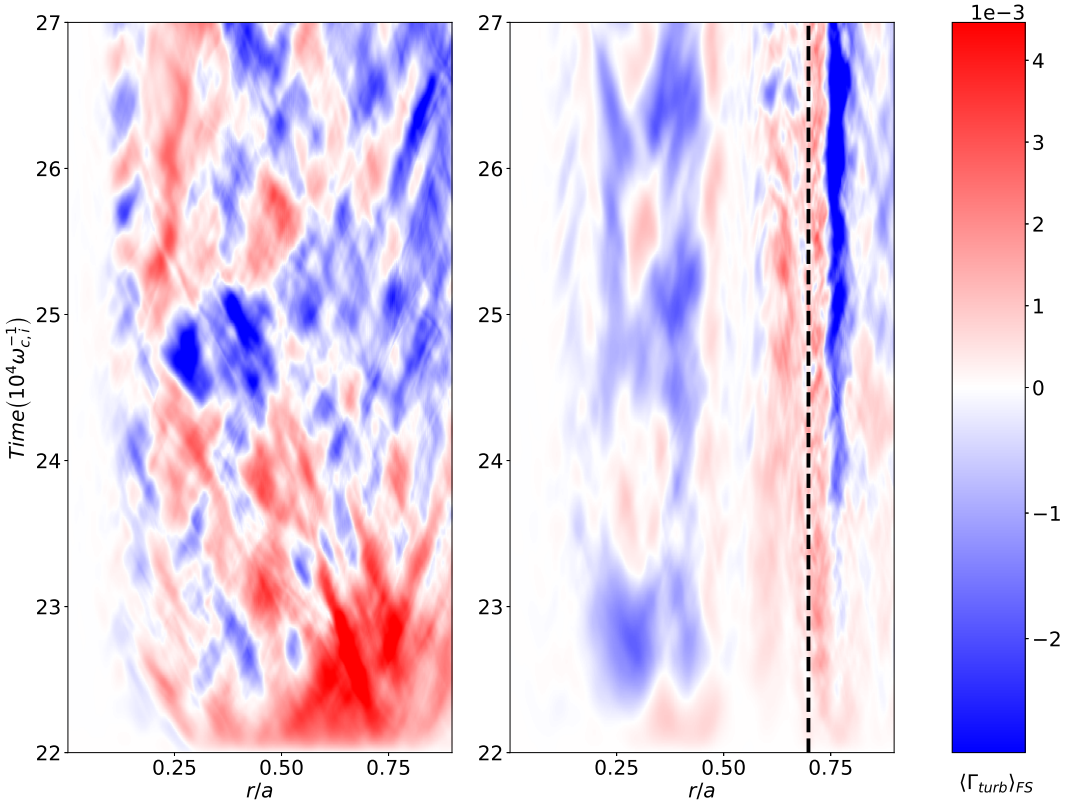

Figure 4.16: Turbulent flux as a function of time (y-axis) and space (x-axis) for helium impurities. Left plot is for the reference case while the right one is when the vorticity source is turned on. The dotted black vertical line indicates the vorticity source position.

In the reference case, the time-averaged turbulent impurity flux for helium over the last $5000\omega_{c,i}^{-1}$ (Figure 4.17, left) peaks at $r/a \approx 0.5$. As observed in chapter 3 for turbulent heat flux, the transport barrier affects not only the source region (i.e. from $r/a = 0.65$ to $r/a = 0.75$), but also in the core from $r/a = 0.37$ to $r/a \sim 0.65$. When the transport barrier is turned on, the turbulent particle flux remains unaffected from $r/a = 0$ to $r/a = 0.37$. Beyond this point, it significantly diminishes, nearing zero where it was previously at its maximum. An interesting characteristics observed here is the presence of a positive turbulent particle flux region with intermediate levels (i.e. $\sim$ half the maximum value) on the inside of the transport barrier while the outside presents an intense negative particle flux (i.e. approximately same levels of the maximum value, but radially inward).

For argon and tungsten, the turbulent particle flux levels were already low in the reference case and further decrease in the transport barrier case. However, a region of slightly increased turbulent flux on the inside of the transport barrier is still observed, especially for tungsten, while the intense negative flux on the outside is kept for both argon and tungsten.

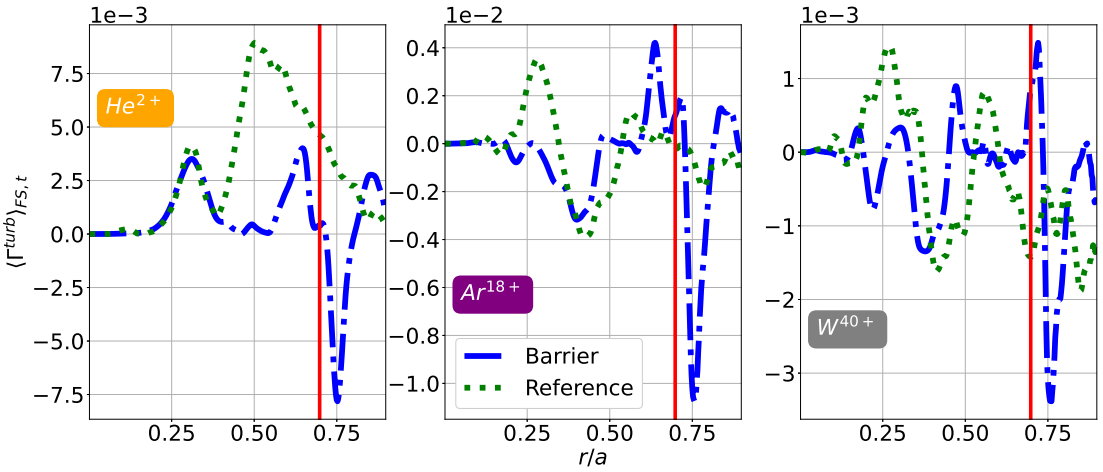

Figure 4.17: Turbulent particle flux-surface averaged fluxes for helium (left), argon (center) and tungsten (right) in the reference (dotted green lines) and vorticity (dotted-dashed blue lines) cases. All profiles are time averaged over the last $5000\omega_{c,i}^{-1}$ of the simulations.

By considering how the transport barrier affects turbulence in the system, particularly the turbulent intensity, it is possible to understand the phenomena occurring in the core region. Reduced turbulent intensity leads to diminished impurity and heat fluxes, as both are directly proportionnal to turbulence intensity. With the reduction of the latter in the presence of the transport barrier, as previously evidenced in chapter 3, the consequent effect can be easily evaluated.

The variations near the transport barrier still need to be addressed. The main hypothesis to explain the observed behaviour when the transport barrier is active is linked to the density gradient κ_n. As presented in Figure 4.18, the peaks of turbulent particle flux near the transport barrier, both negative and positive, coincide with the κ_n peaks observed. This indicates that the observed reversal in turbulent flux may be linked to turbulent diffusion. The fact that both the density gradient and turbulent flux reverse their signs when the transport barrier is activated provides

evidence for this hypothesis. A similar observation can be made for the slight increase in turbulent flux on the inner side as it aligns with enhanced turbulent diffusion via steep density gradient. However, the reversal of the gradient sign in this region should be approached with caution. This is due to the influence of neoclassical transport, which, being heavily influenced by $\Gamma^{\Pi_\parallel}$, modifies the density profile near the source. The inward turbulent diffusion is likely an artefact caused by the vorticity source rather than an effect of the transport barrier.

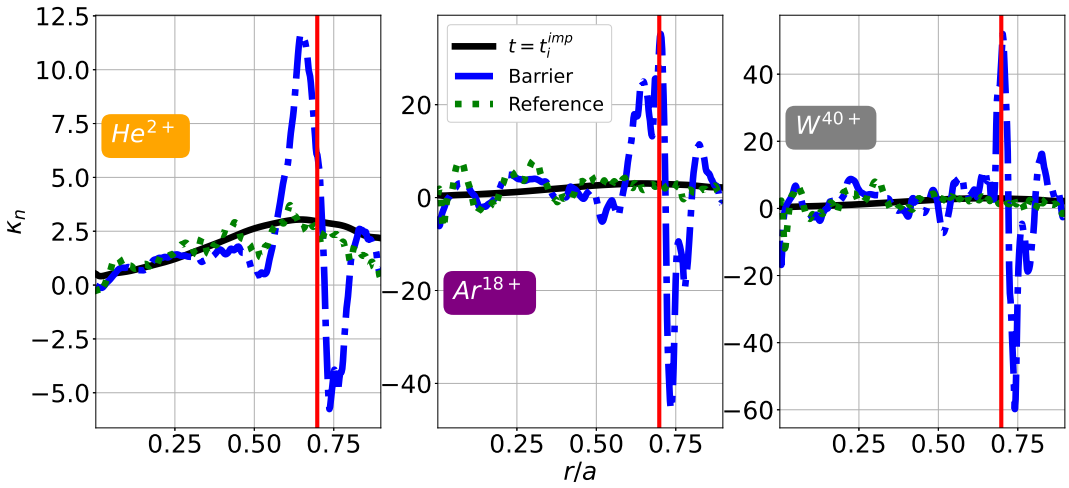

Figure 4.18: Inverse density gradient length $\kappa_n = -\partial_r \ln \langle n_{GC} \rangle_{FS}$ for helium (left), argon (center) and tungsten (right) in the reference (dotted green lines) and vorticity (dotted-dashed blue lines) cases. Solid black lines represent the initial profile at t_0^{imp}. Profiles are time averaged over the last $5000\omega_{c,i}^{-1}$ of the simulations.

Radial averages of turbulent impurity fluxes are then performed $\langle \Gamma^{turb} \rangle_{\Delta r}$ in two distinct radial regions:

- $\Delta r = [0.65, 0.75]$, the region where the transport barrier is located.
- $\Delta r = [0.2, 0.65]$, the region where the turbulent particle flux amplitude usually reaches a maximum.

This analysis provides a more comprehensive understanding of the overall behaviour of turbulent impurity fluxes, as it smoothes out small variations in space, particularly for argon and tungsten.

In the core region (Figure 4.19), $\langle \Gamma^{turb} \rangle_{\Delta r}$ stabilizes itself at approximately a third of the reference case for helium. This confirms the previous statement that despite being localized near the edge, the vorticity source still reduces turbulent impurity flux in the core region. This result is similar to that of heat diffusivity χ_T in chapter 3.

However, argon behaves differently and stabilizes at negative values when the source is present while remaining at zero on average in the reference case. This indicates that when the transport barrier is turned on, argon undergoes an inward turbulent transport in addition to the previously observed enhanced inward neoclassical convection.

This behaviour is not as obvious with tungtsen which, in the reference case, behaves similarly to argon, but fluctuates more significantly in time when the transport barrier is present. Nevertheless, it seems that $\langle \Gamma^{turb} \rangle_{\Delta r}$ stabilizes at lower negative values in the presence of the vorticity source, similar to argon.

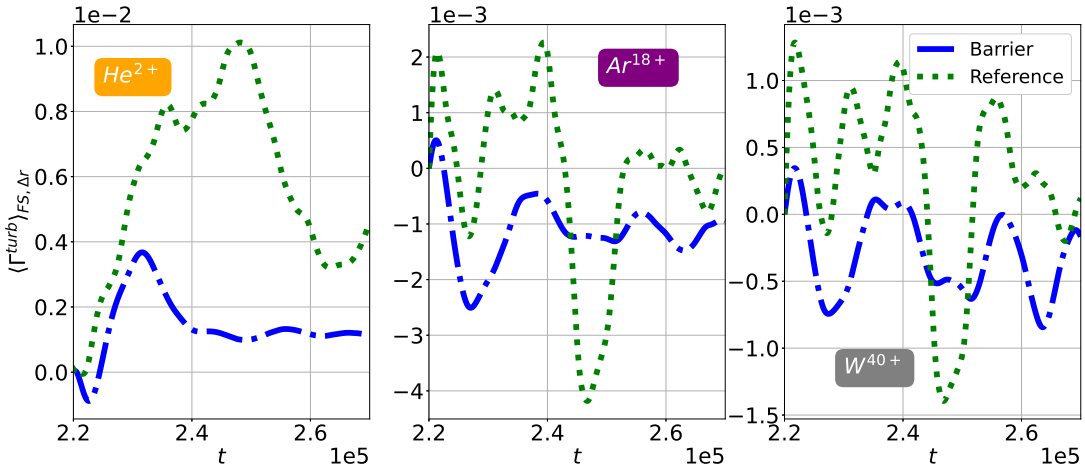

Figure 4.19: Turbulent impurity flux in the core as a function of time, radially averaged over $0.2 \leqslant r/a \leqslant 0.65$ for helium (left), argon (center) and tungsten (right) for the reference (dotted green lines) and vorticity (dotted-dashed blue lines).

In the source region (Figure 4.20), the results for helium are straightforward . $\langle \Gamma^{turb} \rangle_{\Delta r}$ drops to zero on average with the transport barrier activated. This is similar to the diffusivity results shown in Figure 3.7. This behaviour was expected since helium behaves similarly as deuterium and is mainly subject to the same type of turbulent transport.

Argon undergoes small levels of particle flux, dropping to zero on average with some inward transport taking place during short time intervals. This transport is entirely stabilized when the vorticity source is turned on with values dropping to zero on average in the same manner as helium.

Tungsten behaves similarly but shows values staying below zero in the reference case, indicating inward turbulent transport in that region. Again, this diffusion coefficient is stabilized to zero in presence of the vorticity source, effectively stopping turbulent transport in this region.

To conclude on turbulent transport, the effect of the vorticity source is not limited to its vicinity, it also reduces the core turbulent transport. More specifically, helium turbulent transport is stabilized to substantially lower values when the transport barrier is present as opposed to the reference case. Since heavier impurities are less subject to turbulent transport, the transport barrier has less effect on them. However, turbulent transport is still affected with values stablizing at negative values, increasing the inward transport for heavy impurities.

The nature of turbulent transport is also a topic of interest. Although turbulent diffusion seems to be a predominant factor in turbulent particle flux, the

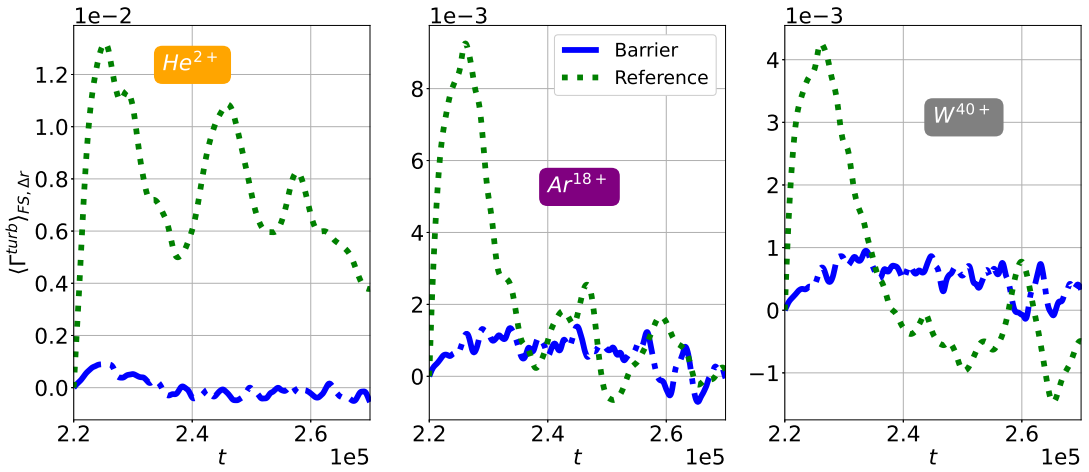

Figure 4.20: Turbulent impurity flux in the vorticity source region as a function of time, radially averaged over $0.65 \leqslant r/a \leqslant 0.75$ for helium (left), argon (center) and tungsten (right) for the reference (dotted green lines) and vorticity (dotted-dashed blue lines).

contributions from other turbulent convection terms such as thermo-diffusion, roto-diffusion or curvature pinch, cannot be overlooked. In this regard, we are adopting an approach similar to that employed by K. Lim [107] to separately evaluate each component during the nonlinear simulations with the transport barrier. The main idea involves treating the curvature pinch as constant for all simulations, and also neglecting the roto-diffusion term as the toroidal rotation of impurities remains in the subsonic regime. This work requires numerous simulations with different density and temperature gradients, demanding a significant amount of computing time. Recent optimizations in GYSELA have resulted in a reduction of simulation costs by approximately 70% in comparison to the version used for chapter 3, thus making this investigation feasible with the computing power provided by our current HPC facilities. It should be noted, however, that this study falls outside the scope of this thesis.

4.4 Tests with a steep gradient

Another way of generating poloidal shear and a transport barrier is, as already discussed in chapter 3, to use an initial density profile for the main ion species presenting a strong gradient on a thin radial layer. This method is effective as the local strong density gradient stabilizes ITG modes by lowering the η factor locally while poloidal shear prevents any turbulent structure to develop in the considered region. We propose here to use this approach with the updated version of GYSELA in presence of helium impurities as a preliminary test to see how particle flux is impacted by the steep gradient of the main ion species and the resulting poloidal shear. Another interesting scope of this study is to investigate how a transport barrier less affected by the injected asymmetry of pressure anisotropy $\Gamma^{\Pi_\parallel}$ term in neoclassical transport behaves.

4.4.1 Parameters and initialization

Initial parameters are similar to the ones presented in section 4.2.1 to the exception of the radial density profile and outer boundary region. Both are presented in Figure 4.21; The density steep gradient is located either at $r/a = 0.9375$ (hereafter referred as case a) or at $r/a = 0.75$ (case b) with the same amplitude as the tests conducted in section 3.4. A simpler boundary condition is chosen like in chapter 3, which consists in a buffer diffusion on the last 13% of the radial domain, modified as $r/a \in [0; 1.25]$, to stabilize any numerical instabilities arising at the edge.

As you can see in Figure 4.21, the buffer mask is close to the steep gradient in case a; this proximity raised concerns about the turbulence that could arise outside the steep gradient without the buffer. This led us to perform the same tests with a steep gradient located further away from the buffer mask, hence the b case presented here.

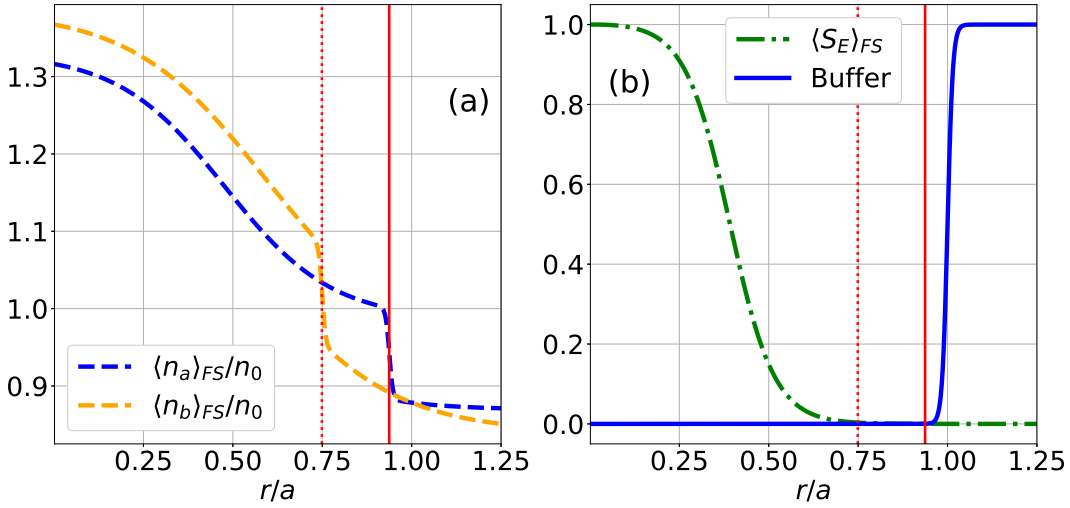

Figure 4.21: **(a):** radial profile of the inital flux surface averaged guiding-center density for the a (dashed blue line) and b (dashed orange line) cases. **(b):** Normalized radial profiles of the axisymmetric buffer mask (blue line) and fluid energy source (dotted green line). The red vertical lines indicate the steep gradient positions; the solid one corresponds to the a case ($r/a = 0.9375$) while the dotted one corresponds to the b case ($r/a = 0.75$).

All the other parameters are kept the same as shown in table 3.1 except for the vorticity source which is kept deactivated throughout all the following results.

A first simulation is run so that ITG modes are triggered on most of the radial domain except for the steep gradient region (i.e. $r/a = 0.9375$ for case a, $r/a = 0.75$ for case b) which is, as presented in chapter 3, linearly stabilized by the density gradient. However, we noted that almost no turbulence was able to grow outside the steep gradient location in case b ($r/a > 0.75$) even if $\eta > 2$. This indicates that the temperature gradient chosen here may not be large enough to trigger ITG modes [108] since the buffer does not apply in this region. Further tests are being performed with a constant radial temperature gradient with $\kappa_T = 6.6$ fixed at all radial positions.

Once saturation of the modes are reached for at least inside the strong density

gradient location, we let the system evolve until the temperature gradient remains relatively constant. After this quasi steady-state is reached, we inject impurities (helium, $f_{He} = 2 \cdot 10^{-5}$) with standard density and temperature profiles with $\kappa_n = 2.2$ and $\kappa_T = 6.6$ at $r/a = 0.575$ without any steep gradient, the goal being to observe how does helium would pass - or not - this kind of transport barrier.

4.4.2 Numerical results

A first look at the radial density profile of helium (Figure 4.22a) shows an accumulation of helium immediately inside the barrier while a depletion is observed on the outer side (i.e. $0.94 \leqslant r/a$). Both a and b cases behave similarly with a sheared density profile at the steep gradient positions. The steep gradient has a greater effect on helium density than the vorticity source and seems to affect transport differently. However, temperature profile (Figure 4.22b) is altered in a similar fashion as the vorticity case by aligning with the main ion temperature profile and a steepening inside the barrier, indicating energy is more efficiently confined in the core region (i.e. inside the transport barrier location) for both cases explored here.

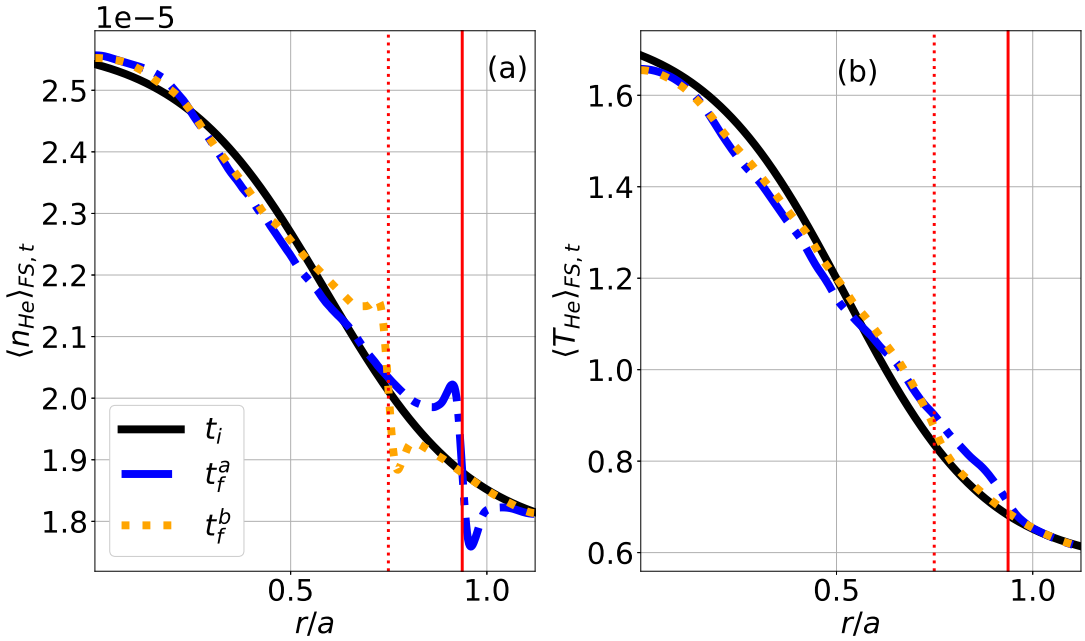

Figure 4.22: Initial (t_i, solid black lines) and final radial profiles of helium density **(a)** and temperature **(b)**. Dashed-dotted blue lines are for the a case (t_f^a) where the steep gradient is located at $r/a = 0.9375$ while the dotted orange lines correspond to the b case (t_f^b) with the steep gradient located at $r/a = 0.75$. All the final profiles are averaged over the last $5000\omega_{c,i}^{-1}$. The red vertical lines indicate the steep gradient position; the solid one corresponds to the a case ($r/a = 0.9375$) while the dotted one corresponds to the b case ($r/a = 0.75$).

All helium fluxes presented afterward are normalized to the integrated flux $\left| \int dr \, \langle \Gamma_a^{tot,s} \rangle_{t,\Delta r} \right|$ of the a case (i.e. steep gradient located at $r/a = 0.9375$) over a radial range $\Delta r \in [0, 1.125]$ and last time steps $\Delta t = 5000\omega_{c,i}^{-1}$.

The radial profile of helium flux (Figure 4.23) shows that both a and b cases are very similar inside the barrier location with flux mainly outward and dominated by turbulence. A slightly negative radial region of turbulent flux is observed immediately inside the barrier and can be attributed to a local reversal of the density gradient. Outside the transport barrier, both cases show no turbulent transport; For the a case, this can be attributed to the presence of the diffusion buffer. However, for the b case, we can explain the absence of turbulent transport to an insufficient temperature gradient to trigger ITG modes.

Neoclassical transport is negative on most of the domain except immediately inside the transport barrier with a positive region. Curiously, the neoclassical flux is of lower amplitude in the b case in the core region.

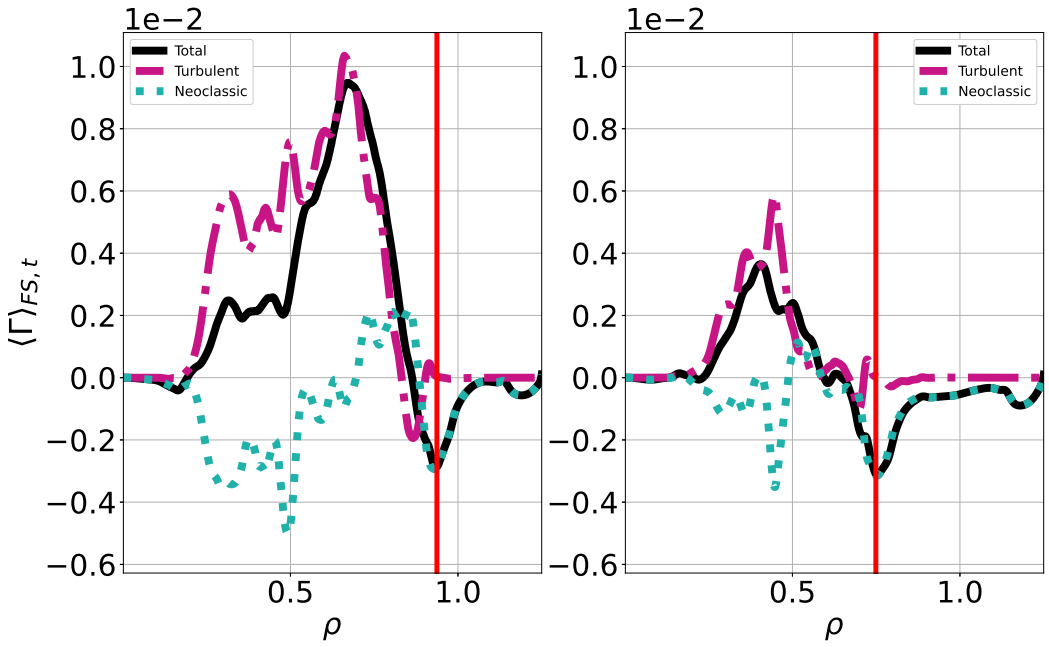

Figure 4.23: Total (solid black line), turbulent (dashed-dotted violet-red line) and neoclassic (dotted blue line) radial particle flux time averaged over the last $5000\omega_{c,i}^{-1}$ for the a (left) and b (right) cases. The red vertical lines indicate the steep gradient position for each corresponding case.

Similarly as in the vorticity case, the negative turbulent particle flux observed on the inside of the transport barrier can be attributed - at least partly - to a density gradient reversal as shown in Figure 4.24a. Diffusion then happens to be directed inward in that region. However, the amplitude of the density gradient of the main ions at the transport barrier position is stabilizing enough so that almost no turbulence can develop here, hence the absence of turbulent particle flux. Similarly, the negative gradient part on the outside of the source leads to almost no diffusion since no turbulence could develop in the first place.

Theoretical impurity flux for the a case gives again a good match with the GYSELA results (Figure 4.25a) with a correct description of the "sheared" region on the inside of the transport barrier. As shown in Figure 4.25b, this is almost entirely due to the BP component and more specifically the pressure anisotropy term $\Gamma^{\Pi_\parallel}$ (Figure 4.25c). This anisotropy is however relatively small compared to what can

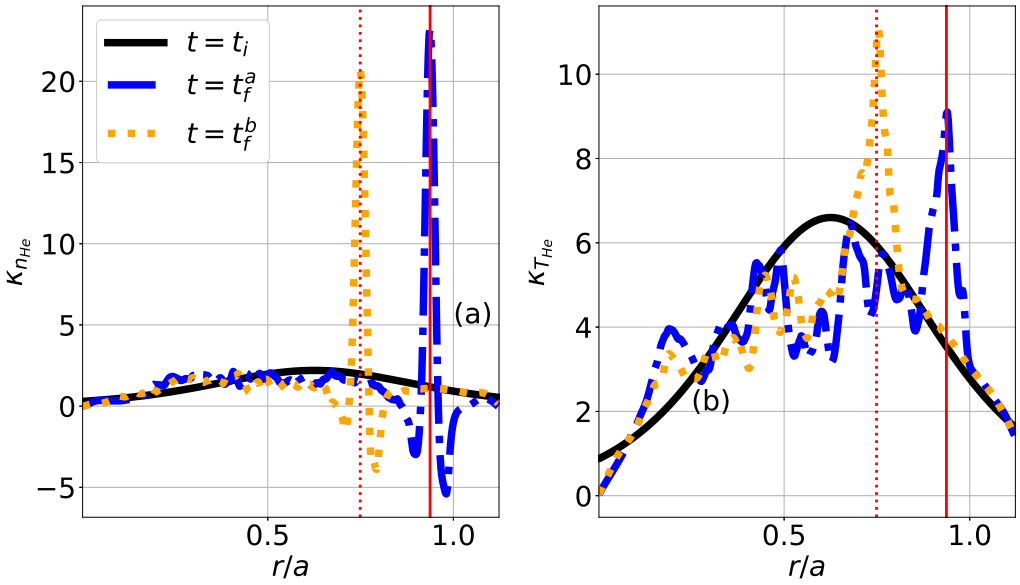

Figure 4.24: Initial (t_i, solid black lines) and final density (**(a)**, left) and temperature (**(b)**, right) gradient length profiles for the a case (dashed-dotted blue lines, t_f^a) where the steep gradient is located at $r/a = 0.9375$ and for the b case (dotted orange lines, t_f^b) with the steep gradient located at $r/a = 0.75$. Final profiles are averaged over the last $5000\omega_{c,i}^{-1}$. The red vertical lines indicate the steep gradient position; The solid one corresponds to the a case ($r/a = 0.9375$) while the dotted one corresponds to the b case ($r/a = 0.75$).

be observed in the vorticity case.

4.5 Discussion and conclusions

In this chapter, we studied the effects of the vorticity source, as well as the transport barrier, on impurity transport in a trace regime. In addition, a brief test was conducted, using helium and a transport barrier generated by the steep gradient method.

Compared to the reference simulation without the vorticity source, helium undergoes a global sign change across the entire radial domain, due to the reduced turbulent particle flux. This flux is significantly diminished by the transport barrier, making neoclassical transport, mainly driven by the poloidal asymmetry of pressure anisotropy $\Gamma^{\Pi_\parallel}$, the dominant component for helium particle flux. This leads to an accumulation of helium in the core due to inward neoclassical convection and local inward turbulent diffusion on the inside of the transport barrier, the latter originating from a density gradient sign reversal. This local negative turbulent particle flux can also be observed for argon and tungsten.

In the presence of the vorticity source, neoclassical inward convection, which is dominant over the turbulent particle flux for heavy impurities, also increases for argon and tungsten compared to their reference cases respectively (i.e., without

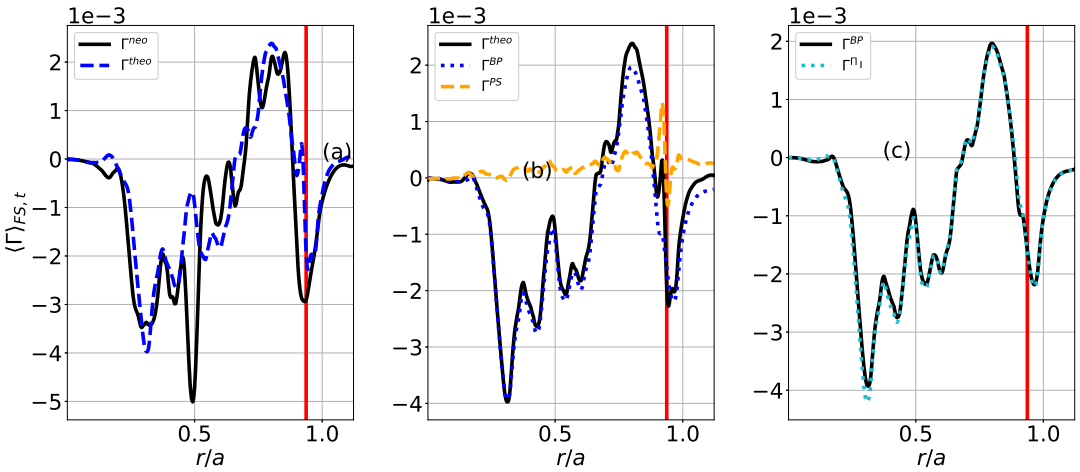

Figure 4.25: Radial profile of radial particle flux time averaged over the last $5000\omega_{c,i}^{-1}$. **(a):** GYSELA (solid black line), theoretical (dashed blue line) radial particle flux. **(b):** theoretical (solid black line), Banana-Plateau (dotted blue line) and Pfirsch-Schlüter (dashed orange line) particle flux. **(c):** Theoretical banana-plateau particle flux (solid black line) and its pressure anisotropy component (dotted cyan line).

the source). The anisotropy term $\Gamma^{\Pi_\parallel}$ in the banana-plateau component still plays a major role for heavy impurities, but with greater mass number the main ion pressure term $\Gamma^{\nabla N_i}$ in the Pfirsch-Schlüter component of the neoclassical particle flux becomes dominant. This can be explained by the fact that this component is directly proportionnal to the ratio $M_s\nu_{zs,i}/q_s$, which increases by many orders of magnitude for tungsten when compared to helium for example.

The additional test for helium with a steep gradient for the main ion species density profile gives similar results. However, core turbulence is still present, leading to an outward turbulent particle flux. The transport barrier then effectively stops particles on the inner side, leading to accumulation of impurities at this radial position.

The transport barrier created through the vorticity source leads to increased neoclassical convection of particles which are already on the inner side of the barrier independantly of the species considered. However we can still consider this barrier as *effective* since it creates the desired effect; Particles cannot pass the transport barrier in one way or another, meaning that we increased confinement in the core (i.e. inner side of the barrier) by isolating it from the edge (i.e. outer side of the barrier). Caution is however advised regarding the neoclassical fluxes obsreved in presence of the transport barrier as well as the inward turbulent diffusion observed on the outside of the transport barrier, the latter being the consequence of the former. The barrier created through the vorticity source may be efficient in our simulations but may be unrealistic regarding those two elements (i.e. asymmetries of pressure anistropy and inward turbulent diffusion on the outside of the source).

However, the barrier created through the main species density gradient is imperfect since impurity fluxes become inward at the steep gradient position; this means particles are more confined in the core plasma (i.e. inner side of the steep gradient) but particles from the edge (i.e. outer side of the steep gradient) can enter even

more efficiently in the core and contaminate it.

Chapter 5

Conclusion, limits and future work

In tokamaks, the presence of impurities results in a significant challenge, as they have the potential to disrupt the plasma and stop fusion reaction, leading to a decrease in reactor efficiency. These impurities can arise directly from the fusion reactions (helium), be seeded at the walls to mitigate heat fluxes received by PFC (argon, neon) or be sputtered from the divertor (tungsten). Tungsten is especially problematic in tokamaks due to its high charge number ($Z = 74$). It does not fully ionize even at the core temperature and therefore radiates the majority of the absorbed energy as light, reducing the energy available for fusion reactions. As a result, even a small concentration of tungsten in the core can completely extinguish the burning plasma. Therefore, understanding and controlling impurity transport is crucial.

To avoid contamination and enhance plasma confinement, L-H transitions and transport barrier in general are useful mechanisms to tackle this confinement and contamination problem. More precisely, $E \times B$ flow shear is the best candidate to explain how the transport barriers can reduce turbulence level and increase confinement time.

GYSELA, a 5D gyrokinetic code, has been used throughout this thesis to study transport mechanisms in tokamak plasmas. Its main advantage is to be a full-f code massively parallelized, mandatory to tackle kinetic problems of this scale. Another advantage of GYSELA is its ability to access precise transport coefficients determined self-consistently, taking into account possible synergies between the neoclassical and turbulent channels as already investigated [109]. A synthetic source of poloidal momentum is used to mimic the conditions of a transport barrier by imposing a sheared radial electric field on a small radial region. This source reduces locally the turbulent diffusivity χ_T^{turb} thus creating a transport barrier mechanism on the radial heat flux of deuterium ions resulting in higher confinement times. The turbulence amplitude both locally and at the core plasma is efficiently quenched and the auto-correlation length of electrostatic potential fluctuations is also notably reduced. A shift in k_θ towards larger scale is observed in the vicinity of the source, implying that turbulent eddies are stretched in the poloidal direction and become radially smaller. These observations fit well with the presented mechanism in Figure 2.8.

In chapter 3, an alternative way of generating a transport barrier has also been explored by locally imposing a strong density gradient. Through the force equilib-

rium, this strong density gradient creates a sheared radial electric field and shear flow in the poloidal direction. This method is efficient since it means the strong density gradient linearly stabilizes ITG modes while the $E \times B$ flow shear prevents any structure from growing. This method is proved to be efficient by maintaining very low turbulence intensity levels in the vicinity of the strong density gradient.

After successfully creating a transport barrier in GYSELA, the investigation of impurity transport through the barrier was carried out. For this purpose, an updated version of GYSELA with better edge physics and significant numerical optimizations have been used for this study. In chapter 4, transport of helium, argon and tungsten, which all experience a different collisionality regime while being encountered in real experiments, are studied in a trace regime with density profiles similar to the main ion species. The transport barrier has a significant impact on impurity transport, especially the neoclassical channel. This is mainly due to two distinct effects; First, the vorticity source injects pressure anisotropy in a non-axisymmetric way, artificially enhancing the banana-plateau flux for all species. Second, in the case of argon and tungsten, the Pfirsch-Schluter flux prevents impurities inside the barrier from leaving the core plasma, while impurities from outside the barrier are repelled. This was due to the temperature screening effect, which effectively prevents impurities from contaminating the core plasma [21]. Additionaly, the reduced turbulence intensity leads to lower turbulent impurity fluxes, especially for helium. As a result, the transport barrier created through the vorticity source is able to both keep the core particles within the barrier and repel particles coming from the edge to the outside of the barrier.

The transport of trace helium through a steep gradient of the main ion species (i.e. deuterium) was also studied since this method was proven to be efficient in creating a transport barrier. The resulting transport of helium was similar to the reference cases up to the steep gradient position with turbulent flux being dominant. However, the steep gradient of density increased neoclassical convection, leading to a semipermeable barrier. This barrier allowed impurities from the edge to penetrate and reach the inner region of the transport barrier, while prohibiting the outward escape of particles already inside. Simulations with other species, i.e. argon and tungsten, are currently in progress.

Several improvements of the presented study could enhance its quality. The use of kinetic - or at least partially - electrons (i.e. trapped kinetic electrons) would allow the study of TEM/ITG synergies for transport as well as the transport of *both* electrons and ions. However, this indicates that the transport barrier created through the density gradient of the main ion species would collapse in the absence of an external source to maintain this gradient.

Additionaly, the study of impurity transport in more realistic boundary conditions, including both the SOL and limiter configuration, would be an interesting topic for future research. Indeed, a more realistic magnetic configuration with a divertor and D-shape plasma is desirable but is beyond the scope of this thesis.

The use of more appropriate source terms might be required for more comprehensive modelling. The poloidal momentum source used in this thesis exhibits an asymmetric injection of pressure anisotropy, thus modifying both turbulent and neoclassical flux of impurities. Numerical development of this source could improve

the reliability of this kind of study.

The use of more realistic density profiles for impurities is also a topic of improvement. For example, the initial density gradient of tungsten should be positive, indicating more tungsten at the edge than at the core. To this end, an additional source term for impurity seeding could be useful.

Transport coefficient - like C_T and D (i.e. thermo-diffusion and turbulent diffusion respectively) - can be derived by scanning a different range of impurity gradients of both temperature and density for each impurity species. This work has been partially done by D. Esteve et al. [110] and could be further explored. Although this work requires substantial computational time, the recent upgrades of GYSELA allow us to compute these transport coefficients.

Recently, a study on the effect of toroidal rotation on both turbulent and neoclassical transport of tungsten was carried out using nonlinear GYSELA simulations. The injection of toroidal momentum accelerates tungsten to the supersonic regime, significantly affecting impurity transport via enhanced poloidal asymmetry and steep toroidal velocity gradient [111]. Building upon this work, the study of parallel velocity gradient (PVG) instabilities, which are triggered above a certain parallel velocity gradient, is currently being investigated within the framework of T. Rouyer's PhD thesis. The purpose of this study is to clarify the interaction between PVG and ITG instabilities, as well as their potential impact on impurity transport.

To study impurity transport, one can also look at the integrated models combining multiple codes like EDGE2D-EIRENE-DIVIMP [112] or JINTRAC [113] which combine both core and edge physics codes to simulate a full discharge scenario with multiple physics modules, ranging from target sputtering to turbulent transport coefficient or even impurity transport. For now, the most advanced codes are combining gyrokinetic flux-tube simulations at specific radii inside the core and use fluid transport equations to get transport profiles [114] with very promising results. One can think of integrating edge-divertor codes in a suite with GYSELA for core physics modelling. This would lead to better determination of transport coefficient and scenario development since the core code would be self-consistent and full-f while the edge boundary conditions would be more realistic. A first test between two major codes, GENE (full-f gyrokinetic, core physics) and XGC (PIC gyrokinetic, edge and x point physics) has already been conducted and proved to be a feasible objective [115].

Bibliography

[1] S. Li, H. Jiang, Z. Ren, C. Xu, *et al.*, "Optimal tracking for a divergent-type parabolic PDE system in current profile control," in *Abstract and Applied Analysis*, vol. 2014, Hindawi, 2014.

[2] "DOE national laboratory makes history by achieving fusion ignition," *DOE newsletter*, 2022.

[3] R. Mackenbach, "Flux surface," 2007. From Wikipedia.org.

[4] G. Federici, W. Biel, M. Gilbert, R. Kemp, N. Taylor, and R. Wenninger, "European DEMO design strategy and consequences for materials," *Nuclear Fusion*, vol. 57, no. 9, p. 092002, 2017.

[5] S. Braginskii, "Transport processes in a plasma," *Reviews of plasma physics*, vol. 1, p. 205, 1965.

[6] A. Galeev and R. Sagdeev, "Transport phenomena in a collisionless plasma in a toroidal magnetic system," *Sov. Phys. JETP*, vol. 26, no. 1, pp. 233–240, 1968.

[7] F. Hinton and R. D. Hazeltine, "Theory of plasma transport in toroidal confinement systems," *Reviews of Modern Physics*, vol. 48, no. 2, p. 239, 1976.

[8] P. Donnel, *Impurity transport in tokamak plasmas: gyrokinetic study of neoclassical and turbulent transport.* PhD thesis, 2018.

[9] D. Estève, *Etude gyrocinétique du transport multi-espèces néoclassique et turbulent dans un plasma de fusion.* PhD thesis, Aix-Marseille, 2015.

[10] E. Joffrin, M. Baruzzo, M. Beurskens, C. Bourdelle, S. Brezinsek, J. Bucalossi, P. Buratti, G. Calabro, C. Challis, M. Clever, *et al.*, "First scenario development with the JET new ITER-like wall," *Nuclear fusion*, vol. 54, no. 1, p. 013011, 2013.

[11] P. Helander and D. J. Sigmar, *Collisional transport in magnetized plasmas*, vol. 4. Cambridge university press, 2005.

[12] B. D. Esham, "Inertial confinement fusion," 2022. From Wikipedia.org.

[13] G. Chew, M. Goldberger, and F. Low, "The Boltzmann equation and the one-fluid hydromagnetic equations in the absence of particle collisions," *Proceedings of the Royal Society of London. Series A. Mathematical and Physical Sciences*, vol. 236, no. 1204, pp. 112–118, 1956.

[14] S. Hirshman and D. Sigmar, "Neoclassical transport of impurities in tokamak plasmas," *Nuclear Fusion*, vol. 21, no. 9, p. 1079, 1981.

[15] C. Angioni and P. Helander, "Neoclassical transport of heavy impurities with poloidally asymmetric density distribution in tokamaks," *Plasma Physics and Controlled Fusion*, vol. 56, no. 12, p. 124001, 2014.

[16] P. Donnel, X. Garbet, Y. Sarazin, V. Grandgirard, N. Bouzat, E. Caschera, G. Dif-Pradalier, P. Ghendrih, C. Gillot, G. Latu, *et al.*, "Neoclassical impurity flux in presence of turbulent generated poloidal asymmetries and pressure anisotropy," *Plasma Physics and Controlled Fusion*, vol. 61, no. 4, p. 044006, 2019.

[17] K. Lim, X. Garbet, Y. Sarazin, V. Grandgirard, K. Obrejan, M. Lesur, and E. Gravier, "Gyrokinetic modelling of light to heavy impurity transport in tokamaks," *Nuclear Fusion*, vol. 61, no. 4, p. 046037, 2021.

[18] P. Helander, S. L. Newton, A. Mollén, and H. M. Smith, "Impurity transport in a mixed-collisionality stellarator plasma," *Physical review letters*, vol. 118, no. 15, p. 155002, 2017.

[19] F. Reimold *et al.*, "From the core to the divertor: Status of the impurity transport investigations at wendelstein 7-x," 2023.

[20] R. Dux, A. Loarte, C. Angioni, D. Coster, E. Fable, and A. Kallenbach, "The interplay of controlling the power exhaust and the tungsten content in ITER," *Nuclear Materials and Energy*, vol. 12, pp. 28–35, 2017.

[21] A. Field, F. Casson, D. Fajardo, C. Angioni, C. Challis, J. Hobirk, A. Kappatou, H.-T. Kim, E. Lerche, A. Loarte, *et al.*, "Peripheral temperature gradient screening of high-Z impurities in optimised 'hybrid' scenario H-mode plasmas in JET-ILW," *Nuclear Fusion*, vol. 63, no. 1, p. 016028, 2022.

[22] S. Di Genova, A. Gallo, N. Fedorczak, H. Yang, G. Ciraolo, J. Romazanov, Y. Marandet, H. Bufferand, C. Guillemaut, J. Gunn, *et al.*, "Modelling of tungsten contamination and screening in WEST plasma discharges," *Nuclear Fusion*, vol. 61, no. 10, p. 106019, 2021.

[23] D. Fajardo, C. Angioni, P. Maget, and P. Manas, "Analytical model for collisional impurity transport in tokamaks at arbitrary collisionality," *Plasma Physics and Controlled Fusion*, vol. 64, no. 5, p. 055017, 2022.

[24] D. Del Sarto and A. Ghizzo, "Hasegawa–Wakatani and modified Hasegawa–Wakatani turbulence induced by ion-temperature-gradient instabilities," *Fluids*, vol. 2, no. 4, p. 65, 2017.

[25] L. Rudakov and R. Sagdeev, "Microscopic instabilities of spatially inhomogeneous plasma in a magnetic field," tech. rep., Kurchatov Inst. of Atomic Energy, Moscow, 1962.

[26] B. Kadomtsev and O. Pogutse, "Instabilities and related macroscopic effects in toroidal discharges," *IAEA conference proceedings*, vol. 1, no. 1, p. 365, 1966.

[27] O. Pogutse, "Magnetic drift instability in a collisionless plasma," *Plasma Physics*, vol. 10, no. 7, p. 649, 1968.

[28] B. Coppi, M. Rosenbluth, and R. Sagdeev, "Instabilities due to temperature gradients in complex magnetic field configurations," *The Physics of Fluids*, vol. 10, no. 3, pp. 582–587, 1967.

[29] P. Guzdar, L. Chen, W. Tang, and P. Rutherford, "Ion-temperature-gradient instability in toroidal plasmas," *The Physics of Fluids*, vol. 26, no. 3, pp. 673–677, 1983.

[30] P. Morel, E. Gravier, N. Besse, R. Klein, A. Ghizzo, P. Bertrand, X. Garbet, P. Ghendrih, V. Grandgirard, and Y. Sarazin, "Gyrokinetic modeling: A multi-water-bag approach," *Physics of Plasmas*, vol. 14, no. 11, p. 112109, 2007.

[31] F. Jenko, W. Dorland, and G. Hammett, "Critical gradient formula for toroidal electron temperature gradient modes," *Physics of Plasmas*, vol. 8, no. 9, pp. 4096–4104, 2001.

[32] E. Gravier, M. Lesur, X. Garbet, Y. Sarazin, J. Médina, K. Lim, and M. Idouakass, "Diffusive impurity transport driven by trapped particle turbulence in tokamak plasmas," *Physics of Plasmas*, vol. 26, no. 8, p. 082306, 2019.

[33] F. Jenko, D. Told, T. Görler, J. Citrin, A. B. Navarro, C. Bourdelle, S. Brunner, G. Conway, T. Dannert, H. Doerk, *et al.*, "Global and local gyrokinetic simulations of high-performance discharges in view of ITER," *Nuclear Fusion*, vol. 53, no. 7, p. 073003, 2013.

[34] H. Arnichand, J. Citrin, S. Hacquin, R. Sabot, A. Krämer-Flecken, X. Garbet, C. Bourdelle, C. Bottereau, F. Clairet, J. Giacalone, *et al.*, "Identification of trapped electron modes in frequency fluctuation spectra," *Plasma Physics and Controlled Fusion*, vol. 58, no. 1, p. 014037, 2015.

[35] D. Ernst, N. Basse, W. Dorland, C. Fiore, L. Lin, A. Long, M. Porkolab, K. Zeller, and K. Zhurovich, "Identification of TEM turbulence through direct comparison of nonlinear gyrokinetic simulations with phase contrast imaging density fluctuation measurements," 2007.

[36] T. Drouot, E. Gravier, T. Reveille, A. Ghizzo, P. Bertrand, X. Garbet, Y. Sarazin, and T. Cartier-Michaud, "A gyro-kinetic model for trapped electron and ion modes," *The European Physical Journal D*, vol. 68, no. 10, pp. 1–7, 2014.

[37] Y. Xiao and Z. Lin, "Turbulent transport of trapped-electron modes in collisionless plasmas," *Physical review letters*, vol. 103, no. 8, p. 085004, 2009.

[38] I. P. E. G. o. C. Transport, , I. P. E. G. o. C. M. Database, , and I. P. B. Editors, "Chapter 2: Plasma confinement and transport," *Nuclear Fusion*, vol. 39, no. 12, pp. 2175–2249, 1999.

[39] N. D'Angelo, "Kelvin-helmholtz instability in a fully ionized plasma in a magnetic field," *The Physics of Fluids*, vol. 8, no. 9, pp. 1748–1750, 1965.

[40] X. Garbet, C. Fenzi, H. Capes, P. Devynck, and G. Antar, "Kelvin-Helmholtz instabilities in tokamak edge plasmas," *Physics of Plasmas*, vol. 6, no. 10, pp. 3955–3965, 1999.

[41] G. I. Kent, N. C. Jen, and F. F. Chen, "Transverse Kelvin-Helmholtz instability in a rotating plasma," *The Physics of Fluids*, vol. 12, no. 10, pp. 2140–2151, 1969.

[42] D. M. Fisher, B. N. Rogers, G. D. Rossi, D. S. Guice, and T. A. Carter, "Three-dimensional two-fluid Braginskii simulations of the large plasma device," *Physics of Plasmas*, vol. 22, no. 9, p. 092121, 2015.

[43] F. Wagner, G. Becker, K. Behringer, D. Campbell, A. Eberhagen, W. Engelhardt, G. Fussmann, O. Gehre, J. Gernhardt, G. v. Gierke, *et al.*, "Regime of improved confinement and high beta in neutral-beam-heated divertor discharges of the ASDEX tokamak," *Physical Review Letters*, vol. 49, no. 19, p. 1408, 1982.

[44] K. Burrell, S. Ejima, D. Schissel, N. Brooks, R. Callis, T. Carlstrom, A. Colleraine, J. DeBoo, H. Fukumoto, R. Groebner, *et al.*, "Observation of an improved energy-confinement regime in neutral-beam–heated divertor discharges in the DIII-D tokamak," *Physical review letters*, vol. 59, no. 13, p. 1432, 1987.

[45] K. Burrell, S. Allen, G. Bramson, N. Brooks, R. Callis, T. Carlstrom, M. Chu, A. Colleraine, D. Content, J. DeBoo, *et al.*, "Confinement physics of H-mode discharges in DIII-D," *Plasma Physics and Controlled Fusion*, vol. 31, no. 10, p. 1649, 1989.

[46] K. Ida, S. Hidekuma, Y. Miura, T. Fujita, M. Mori, K. Hoshino, N. Suzuki, T. Yamauchi, J.-M. group, *et al.*, "Edge electric-field profiles of H-mode plasmas in the JFT-2M tokamak," *Physical Review Letters*, vol. 65, no. 11, p. 1364, 1990.

[47] P. Gohil, K. Burrell, and T. Carlstrom, "Parametric dependence of the edge radial electric field in the DIII-D tokamak," *Nuclear fusion*, vol. 38, no. 1, p. 93, 1998.

[48] E. Viezzer, T. Pütterich, G. Conway, R. Dux, T. Happel, J. Fuchs, R. McDermott, F. Ryter, B. Sieglin, W. Suttrop, *et al.*, "High-accuracy characterization of the edge radial electric field at ASDEX upgrade," *Nuclear Fusion*, vol. 53, no. 5, p. 053005, 2013.

[49] J. Schirmer, G. Conway, H. Zohm, W. Suttrop, *et al.*, "The radial electric field and its associated shear in the ASDEX Upgrade tokamak," *Nuclear fusion*, vol. 46, no. 9, p. S780, 2006.

[50] R. Dermott, B. Lipschultz, J. Hughes, P. Catto, A. Hubbard, I. Hutchinson, M. Greenwald, B. Bombard, K. Marr, M. Reinke, *et al.*, "Edge radial electric field structure and its connection to H-mode confinement in Alcator C-Mod," 2009.

[51] R. Panek, J. Adámek, M. Aftanas, P. Bílková, P. Böhm, F. Brochard, P. Cahyna, J. Cavalier, R. Dejarnac, M. Dimitrova, *et al.*, "Status of the COMPASS tokamak and characterization of the first H-mode," *Plasma Physics and Controlled Fusion*, vol. 58, no. 1, p. 014015, 2015.

[52] Y. Andrew, N. Hawkes, T. Biewer, K. Crombe, D. Keeling, E. De La Luna, C. Giroud, A. Korotkov, A. Meigs, A. Murari, *et al.*, "Evolution of the radial electric field in a JET H-mode plasma," *EPL (Europhysics Letters)*, vol. 83, no. 1, p. 15003, 2008.

[53] H. Meyer, C. Bunting, P. Carolan, N. Conway, M. Dunstan, A. Kirk, R. Scannell, D. Temple, M. Walsh, *et al.*, "The structure, evolution and role of the radial edge electric field in H-mode and L-mode on MAST," in *Journal of Physics: Conference Series*, vol. 123, p. 012005, IOP Publishing, 2008.

[54] F. Levinton, M. Zarnstorff, S. Batha, M. Bell, R. Bell, R. Budny, C. Bush, Z. Chang, E. Fredrickson, A. Janos, *et al.*, "Improved confinement with reversed magnetic shear in TFTR," *Physical Review Letters*, vol. 75, no. 24, p. 4417, 1995.

[55] E. Strait, L. Lao, M. Mauel, B. Rice, T. Taylor, K. Burrell, M. Chu, E. Lazarus, T. Osborne, S. Thompson, *et al.*, "Enhanced confinement and stability in DIII-D discharges with reversed magnetic shear," *Physical review letters*, vol. 75, no. 24, p. 4421, 1995.

[56] S. Ding, G. Xu, Q. Wang, W. Solomon, Y. Zhao, X. Gong, A. Garofalo, C. Holcomb, G. McKee, Z. Yan, *et al.*, "Scenario development for high β_p low torque plasma with q_{min} above 2 and large-radius internal transport barrier in DIII-D," *Nuclear Fusion*, vol. 57, no. 2, p. 022016, 2016.

[57] T. Fujita, S. Ide, H. Kimura, Y. Koide, T. Oikawa, S. Takeji, H. Shirai, T. Ozeki, Y. Kamada, S. Ishida, and J.-. Team, "Enhanced core confinement in JT-60U reversed shear discharges," May 1997.

[58] S. Ide, T. Suzuki, Y. Sakamoto, H. Takenaga, T. Fujita, N. Oyama, A. Isayama, Y. Koide, Y. Kamada, *et al.*, "Studies of the influence of electron heating on ITB subject to advanced tokamak operation in JT-60U," *Nuclear fusion*, vol. 44, no. 1, p. 87, 2003.

[59] C. Gormezano and A. Fasoli, "Optimisation of JET plasmas with current profile control," in *Proc. 16th IAEA International Conference on Fusion Energy*, vol. 1, 1997.

[60] D. Frigione, L. Garzotti, C. Challis, M. De Baar, P. De Vries, M. Brix, X. Garbet, N. Hawkes, A. Thyagaraja, L. Zabeo, *et al.*, "Pellet injection and high density ITB formation in JET advanced tokamak plasmas," *Nuclear fusion*, vol. 47, no. 2, p. 74, 2007.

[61] Y. Yang, X. Gao, H. Liu, G. Li, T. Zhang, L. Zeng, Y. Liu, M. Wu, D. Kong, T. Ming, *et al.*, "Observation of internal transport barrier in ELMy H-mode plasmas on the EAST tokamak," *Plasma Physics and Controlled Fusion*, vol. 59, no. 8, p. 085003, 2017.

[62] J. Chung, H. Kim, Y. Jeon, J. Kim, M. Choi, J. Ko, K. Lee, H. Lee, S. Yi, J. Kwon, *et al.*, "Formation of the internal transport barrier in KSTAR," *Nuclear Fusion*, vol. 58, no. 1, p. 016019, 2017.

[63] J. Team *et al.*, "Towards steady state tokamak operation with double transport barriers," *Nuclear Fusion*, vol. 39, no. 11Y, p. 1883, 1999.

[64] W. Chen, L. Yu, M. Xu, Z. Shi, X. He, D. Yu, X. Ji, Y. Li, M. Jiang, P. Shi, *et al.*, "High-β_p scenario realized by the integration of internal and external transport barriers in the HL-2A tokamak," *Physics Letters A*, vol. 440, p. 128141, 2022.

[65] Z. Lin, T. S. Hahm, W. Lee, W. M. Tang, and R. B. White, "Turbulent transport reduction by zonal flows: Massively parallel simulations," *Science*, vol. 281, no. 5384, pp. 1835–1837, 1998.

[66] P. H. Diamond, S. Itoh, K. Itoh, and T. Hahm, "Zonal flows in plasma—a review," *Plasma Physics and Controlled Fusion*, vol. 47, no. 5, p. R35, 2005.

[67] R. L. Dewar and R. F. Abdullatif, "Zonal flow generation by modulational instability," in *Frontiers in Turbulence and Coherent Structures*, pp. 415–430, World Scientific, 2007.

[68] S. Kobayashi, Ö. D. Gürcan, and P. H. Diamond, "Direct identification of predator-prey dynamics in gyrokinetic simulations," *Physics of Plasmas*, vol. 22, no. 9, p. 090702, 2015.

[69] H. Biglari, P. Diamond, and P. Terry, "Influence of sheared poloidal rotation on edge turbulence," *Physics of Fluids B: Plasma Physics*, vol. 2, no. 1, pp. 1–4, 1990.

[70] K. Itoh and S.-I. Itoh, "The role of the electric field in confinement," *Plasma physics and controlled fusion*, vol. 38, no. 1, p. 1, 1996.

[71] P. Terry, "Suppression of turbulence and transport by sheared flow," *Reviews of Modern Physics*, vol. 72, no. 1, p. 109, 2000.

[72] C. Bourdelle, "Staged approach towards physics-based L-H transition models," *Nuclear Fusion*, vol. 60, no. 10, p. 102002, 2020.

[73] T. Kobayashi, "The physics of the mean and oscillating radial electric field in the L-H transition: the driving nature and turbulent transport suppression mechanism," *Nuclear Fusion*, vol. 60, no. 9, p. 095001, 2020.

[74] R. Waltz, G. Kerbel, and J. Milovich, "Toroidal gyro-Landau fluid model turbulence simulations in a nonlinear ballooning mode representation with radial modes," *Physics of Plasmas*, vol. 1, no. 7, pp. 2229–2244, 1994.

[75] G. Lo-Cascio, E. Gravier, T. Réveillé, M. Lesur, Y. Sarazin, X. Garbet, L. Vermare, K. Lim, A. Guillevic, and V. Grandgirard, "Transport barrier in 5D gyrokinetic flux-driven simulations," *Nuclear Fusion*, vol. 62, no. 12, p. 126026, 2022.

[76] X. Garbet, Y. Idomura, L. Villard, and T. Watanabe, "Gyrokinetic simulations of turbulent transport," *Nuclear Fusion*, vol. 50, no. 4, p. 043002, 2010.

[77] A. Brizard and T. Hahm, "Foundations of nonlinear gyrokinetic theory," *Reviews of modern physics*, vol. 79, no. 2, p. 421, 2007.

[78] V. Grandgirard, J. Abiteboul, J. Bigot, T. Cartier-Michaud, N. Crouseilles, G. Dif-Pradalier, C. Ehrlacher, D. Esteve, X. Garbet, P. Ghendrih, *et al.*, "A 5D gyrokinetic full-f global semi-Lagrangian code for flux-driven ion turbulence simulations," *Computer Physics Communications*, vol. 207, pp. 35–68, 2016.

[79] P. Donnel, X. Garbet, Y. Sarazin, V. Grandgirard, Y. Asahi, N. Bouzat, E. Caschera, G. Dif-Pradalier, C. Ehrlacher, P. Ghendrih, *et al.*, "A multi-species collisional operator for full-f global gyrokinetics codes: Numerical aspects and verification with the GYSELA code," *Computer Physics Communications*, vol. 234, pp. 1–13, 2019.

[80] J. Abiteboul, X. Garbet, V. Grandgirard, S. Allfrey, P. Ghendrih, G. Latu, Y. Sarazin, and A. Strugarek, "Conservation equations and calculation of mean flows in gyrokinetics," *Physics of Plasmas*, vol. 18, no. 8, p. 082503, 2011.

[81] Y. Sarazin, V. Grandgirard, J. Abiteboul, S. Allfrey, X. Garbet, P. Ghendrih, G. Latu, A. Strugarek, G. Dif-Pradalier, P. Diamond, *et al.*, "Predictions on heat transport and plasma rotation from global gyrokinetic simulations," *Nuclear Fusion*, vol. 51, no. 10, p. 103023, 2011.

[82] Y. Sarazin, V. Grandgirard, P. Angelino, A. Casati, G. Dif-Pradalier, X. Garbet, P. Ghendrih, O. Gürcan, P. Hennequin, and R. Sabot, "Turbulence spectra and transport barriers in gyrokinetic simulations," in *AIP Conference Proceedings*, vol. 1069, pp. 325–330, American Institute of Physics, 2008.

[83] J. Rice, *Driven Rotation, Self-Generated Flow, and Momentum Transport in Tokamak Plasmas*, vol. 119. Springer Nature, 2022.

[84] J. Wilson, R. Bell, S. Bernabei, K. Hill, J. Hosea, B. LeBlanc, R. Majeski, R. Nazikian, M. Ono, C. Phillips, *et al.*, "Ion cyclotron range of frequencies

heating and flow generation in deuterium-tritium plasmas," *Physics of Plasmas*, vol. 5, no. 5, pp. 1721–1726, 1998.

[85] Y. Lin, J. Rice, S. Wukitch, M. Greenwald, A. Hubbard, A. Ince-Cushman, L. Lin, M. Porkolab, M. Reinke, and N. Tsujii, "Observation of ion-cyclotron-frequency mode-conversion flow drive in tokamak plasmas," *Physical review letters*, vol. 101, no. 23, p. 235002, 2008.

[86] R. D. Hazeltine and J. D. Meiss, *Plasma confinement*. Courier Corporation, 2003.

[87] Y. Kim, P. Diamond, H. Biglari, and P. Terry, "Theory of resistivity-gradient-driven turbulence in a differentially rotating plasma," *Physics of Fluids B: Plasma Physics*, vol. 2, no. 9, pp. 2143–2150, 1990.

[88] B. D. Scott, P. Terry, and P. Diamond, "Saturation of Kelvin-Helmholtz fluctuations in a sheared magnetic field," *The Physics of fluids*, vol. 31, no. 6, pp. 1481–1491, 1988.

[89] N. Winsor, J. L. Johnson, and J. M. Dawson, "Geodesic acoustic waves in hydromagnetic systems," *The Physics of Fluids*, vol. 11, no. 11, pp. 2448–2450, 1968.

[90] K. Burrell, "Effects of ExB velocity shear and magnetic shear on turbulence and transport in magnetic confinement devices," tech. rep., General Atomic Co., 1996.

[91] A. Strugarek, Y. Sarazin, D. Zarzoso, J. Abiteboul, A. Brun, T. Cartier-Michaud, G. Dif-Pradalier, X. Garbet, P. Ghendrih, V. Grandgirard, *et al.*, "Ion transport barriers triggered by plasma polarization in gyrokinetic simulations," *Plasma Physics and Controlled Fusion*, vol. 55, no. 7, p. 074013, 2013.

[92] J. Kim, W. Horton, D. Choi, S. Migliuolo, and B. Coppi, "Temperature anisotropy effect on the toroidal ion temperature gradient mode," *Physics of Fluids B: Plasma Physics*, vol. 4, no. 1, pp. 152–158, 1992.

[93] A. Strugarek, Y. Sarazin, D. Zarzoso, J. Abiteboul, A. Brun, T. Cartier-Michaud, G. Dif-Pradalier, X. Garbet, P. Ghendrih, V. Grandgirard, *et al.*, "Unraveling quasiperiodic relaxations of transport barriers with gyrokinetic simulations of tokamak plasmas," *Physical review letters*, vol. 111, no. 14, p. 145001, 2013.

[94] G. Dif-Pradalier, P. Diamond, V. Grandgirard, Y. Sarazin, J. Abiteboul, X. Garbet, P. Ghendrih, G. Latu, A. Strugarek, S. Ku, *et al.*, "Neoclassical physics in full distribution function gyrokinetics," *Physics of Plasmas*, vol. 18, no. 6, p. 062309, 2011.

[95] R. Waltz, J. Candy, and M. Rosenbluth, "Gyrokinetic turbulence simulation of profile shear stabilization and broken gyroBohm scaling," *Physics of Plasmas*, vol. 9, no. 5, pp. 1938–1946, 2002.

[96] P. Donnel, X. Garbet, Y. Sarazin, Y. Asahi, F. Wilczynski, E. Caschera, G. Dif-Pradalier, P. Ghendrih, and C. Gillot, "Turbulent generation of poloidal asymmetries of the electric potential in a tokamak," *Plasma Physics and Controlled Fusion*, vol. 61, no. 1, p. 014003, 2018.

[97] P. Ghendrih, G. Dif-Pradalier, C. Norscini, T. Cartier-Michaud, D. Estève, X. Garbet, V. Grandgirard, G. Latu, C. Passeron, and Y. Sarazin, "Self organisation of plasma turbulence: impact on radial correlation lengths," in *Journal of Physics: Conference Series*, vol. 561, p. 012008, IOP Publishing, 2014.

[98] P. Ghendrih, C. Norscini, T. Cartier-Michaud, G. Dif-Pradalier, J. Abiteboul, Y. Dong, X. Garbet, O. Gürcan, P. Hennequin, V. Grandgirard, *et al.*, "Phase space structures in gyrokinetic simulations of fusion plasma turbulence," *The European Physical Journal D*, vol. 68, no. 10, pp. 1–17, 2014.

[99] P. Helander, C. Beidler, T. Bird, M. Drevlak, Y. Feng, R. Hatzky, F. Jenko, R. Kleiber, J. Proll, Y. Turkin, *et al.*, "Stellarator and tokamak plasmas: a comparison," *Plasma Physics and Controlled Fusion*, vol. 54, no. 12, p. 124009, 2012.

[100] F. Merz and F. Jenko, "Nonlinear saturation of trapped electron modes via perpendicular particle diffusion," *Physical review letters*, vol. 100, no. 3, p. 035005, 2008.

[101] J. Lang, S. E. Parker, and Y. Chen, "Nonlinear saturation of collisionless trapped electron mode turbulence: Zonal flows and zonal density," *Physics of Plasmas*, vol. 15, no. 5, p. 055907, 2008.

[102] D. Ernst, J. Lang, W. Nevins, M. Hoffman, Y. Chen, W. Dorland, and S. Parker, "Role of zonal flows in trapped electron mode turbulence through nonlinear gyrokinetic particle and continuum simulation," *Physics of Plasmas*, vol. 16, no. 5, p. 055906, 2009.

[103] K. Ida, R. Fonck, S. Sesnic, R. Hulse, and B. LeBlanc, "Observation of z-dependent impurity accumulation in the PBX tokamak," *Physical review letters*, vol. 58, no. 2, p. 116, 1987.

[104] M. Tokar, J. Rapp, G. Bertschinger, L. Konen, H. Koslowski, A. Kramer-Flacken, V. Philipps, U. Samm, and B. Unterberg, "Nature of high-Z impurity accumulation in tokamaks," *Nuclear fusion*, vol. 37, no. 12, p. 1691, 1997.

[105] R. Neu, R. Dux, A. Geier, A. Kallenbach, R. Pugno, V. Rohde, D. Bolshukhin, J. Fuchs, O. Gehre, O. Gruber, *et al.*, "Impurity behaviour in the ASDEX Upgrade divertor tokamak with large area tungsten walls," *Plasma physics and controlled fusion*, vol. 44, no. 6, p. 811, 2002.

[106] M. Lesur, C. Djerroud, K. Lim, E. Gravier, M. Idouakass, J. Moritz, J. Médina, T. Réveillé, T. Drouot, T. Cartier-Michaud, *et al.*, "Validity limits of the passive treatment of impurities in gyrokinetic tokamak simulations," *Nuclear Fusion*, vol. 60, no. 3, p. 036016, 2020.

[107] K. Lim, E. Gravier, M. Lesur, X. Garbet, Y. Sarazin, and J. Médina, "Impurity pinch generated by trapped particle driven turbulence," *Plasma Physics and Controlled Fusion*, vol. 62, no. 9, p. 095018, 2020.

[108] A. M. Dimits, G. Bateman, M. Beer, B. Cohen, W. Dorland, G. Hammett, C. Kim, J. Kinsey, M. Kotschenreuther, A. Kritz, *et al.*, "Comparisons and physics basis of tokamak transport models and turbulence simulations," *Physics of Plasmas*, vol. 7, no. 3, pp. 969–983, 2000.

[109] Y. Asahi, V. Grandgirard, Y. Sarazin, P. Donnel, X. Garbet, Y. Idomura, G. Dif-Pradalier, and G. Latu, "Synergy of turbulent and neoclassical transport through poloidal convective cells," *Plasma Physics and Controlled Fusion*, vol. 61, no. 6, p. 065015, 2019.

[110] D. Esteve, Y. Sarazin, X. Garbet, V. Grandgirard, S. Breton, P. Donnel, Y. Asahi, C. Bourdelle, G. Dif-Pradalier, C. Ehrlacher, *et al.*, "Self-consistent gyrokinetic modeling of neoclassical and turbulent impurity transport," *Nuclear Fusion*, vol. 58, no. 3, p. 036013, 2018.

[111] K. Lim, X. Garbet, Y. Sarazin, E. Gravier, M. Lesur, G. Lo-Cascio, and T. Rouyer, "Self-consistent gyrokinetic modelling of turbulent and neoclassical tungsten transport in toroidally rotating plasmas," *Physics of Plasma*, 2023.

[112] H. Kumpulainen, M. Groth, G. Corrigan, D. Harting, F. Koechl, A. Jaervinen, B. Lomanowski, A. Meigs, M. Sertoli, and J. Contributors, "Validation of EDGE2D-EIRENE and DIVIMP for W SOL transport in JET," *Nuclear Materials and Energy*, vol. 25, p. 100866, 2020.

[113] E. M. Asp, G. Corrigan, P. d. S. A. Belo, L. Garzotti, D. Harting, F. Köchl, V. Parail, M. Cavinato, A. Loarte, M. Romanelli, *et al.*, "JINTRAC integrated simulations of ITER scenarios including fuelling and divertor power flux control for H, He and DT plasmas," *Nuclear Fusion*, vol. 62, no. 12, p. 126033, 2022.

[114] P. Rodriguez-Fernandez, N. Howard, and J. Candy, "Nonlinear gyrokinetic predictions of SPARC burning plasma profiles enabled by surrogate modeling," *Nuclear Fusion*, vol. 62, no. 7, p. 076036, 2022.

[115] G. Merlo, S. Janhunen, F. Jenko, A. Bhattacharjee, C. Chang, J. Cheng, P. Davis, J. Dominski, K. Germaschewski, R. Hager, *et al.*, "First coupled GENE-XGC microturbulence simulations," *Physics of Plasmas*, vol. 28, no. 1, 2021.

[116] L. Vermare, P. Hennequin, C. Honoré, M. Peret, G. Dif-Pradalier, X. Garbet, J. Gunn, C. Bourdelle, F. Clairet, J. Morales, *et al.*, "Formation of the radial electric field profile in the WEST tokamak," *Nuclear Fusion*, vol. 62, no. 2, p. 026002, 2021.

Appendix A

Neoclassical fluxes

A.1 Useful relations for the magnetic field

By starting from [11]

$$\mathbf{B} = I(\psi)\,\boldsymbol{\nabla}\varphi + \boldsymbol{\nabla}\varphi \times \boldsymbol{\nabla}\psi, \tag{A.1}$$

one can deduce two very useful equations. By taking its norm, we can write $|\mathbf{B}|^2 = I(\psi)^2 |\boldsymbol{\nabla}\varphi|^2 + |\boldsymbol{\nabla}\varphi \times \boldsymbol{\nabla}\psi|^2$. This equation can be further reduced by using $\boldsymbol{\nabla}\varphi = \frac{1}{R}\mathbf{e}_\varphi$, giving

$$|\mathbf{B}|^2 = \frac{I(\psi)^2}{R^2} + \frac{|\boldsymbol{\nabla}\psi|^2}{R^2}. \tag{A.2}$$

Another useful relation comes from the operation $\mathbf{B} \times \boldsymbol{\nabla}\psi$, which gives

$$\mathbf{B} \times \boldsymbol{\nabla}\psi = I(\psi)\,\boldsymbol{\nabla}\varphi \times \boldsymbol{\nabla}\psi + (\boldsymbol{\nabla}\varphi \times \boldsymbol{\nabla}\psi) \times \boldsymbol{\nabla}\psi. \tag{A.3}$$

The term $\boldsymbol{\nabla}\varphi \times \boldsymbol{\nabla}\psi = \mathbf{B} - I(\psi)\,\boldsymbol{\nabla}\varphi$ is given by equation (A.1) while $(\boldsymbol{\nabla}\varphi \times \boldsymbol{\nabla}\psi) \times \boldsymbol{\nabla}\psi = -|\boldsymbol{\nabla}\psi|^2 \boldsymbol{\nabla}\varphi$ is given by vector properties. Using those relations, we can write

$$\begin{aligned} \mathbf{B} \times \boldsymbol{\nabla}\psi &= I(\psi)\,\mathbf{B} - \boldsymbol{\nabla}\varphi \overbrace{\left[I^2(\psi) + |\boldsymbol{\nabla}\psi|^2\right]}^{|\mathbf{B}|^2 R^2}, \\ \mathbf{b} \times \boldsymbol{\nabla}\psi &= I(\psi)\,\mathbf{b} - |B|\,R^2 \boldsymbol{\nabla}\varphi. \end{aligned} \tag{A.4}$$

One can also compute

$$\mathbf{B} \times \boldsymbol{\nabla}\varphi = (\boldsymbol{\nabla}\varphi \times \boldsymbol{\nabla}\psi) \times \boldsymbol{\nabla}\varphi = \frac{1}{R^2}\boldsymbol{\nabla}\psi \tag{A.5}$$

by using vector properties as well as $|\boldsymbol{\nabla}\varphi|^2 = \frac{1}{R^2}$.

A.2 Main ion particle flux

A.2.1 Flux channels

By starting from equation (2.8) and assuming both stationary state ($\partial_t = 0$) and an axisymmetric torus ($\partial_\varphi = 0$), we get

$$\langle q_i \boldsymbol{\Gamma}_i \cdot \boldsymbol{\nabla}\psi \rangle_{FS} = -\left\langle N_i q_i R^2 \mathbf{E} \cdot \boldsymbol{\nabla}\varphi \right\rangle_{FS} - \left\langle R^2 \boldsymbol{\mathcal{F}} \cdot \boldsymbol{\nabla}\varphi \right\rangle_{FS}. \tag{A.6}$$

By using equation (A.4) to extract $-\left(\mathbf{b} \times \boldsymbol{\nabla}\psi + I\left(\psi\right)\mathbf{b}\right)/B = R^2 \boldsymbol{\nabla}\varphi$ and dividing everything by q_i, we can rewrite equation (A.6) as

$$\langle \boldsymbol{\Gamma}_i \cdot \boldsymbol{\nabla}\psi \rangle_{FS} = \overbrace{-\left\langle \frac{I}{B}\left(N_i E_\parallel + \frac{\mathcal{F}_\parallel}{q_i}\right)\right\rangle_{FS}}^{\text{Neoclassic}} + \overbrace{\frac{\boldsymbol{\nabla}\psi \cdot (\boldsymbol{\mathcal{F}} \times \mathbf{B})}{q_i B^2}}^{\text{Classic}} + \overbrace{N_i \boldsymbol{\nabla}\psi \cdot \frac{\mathbf{E} \times \mathbf{B}}{B^2}}^{\text{Turbulent}}, \tag{A.7}$$

where we recognize three terms respectively linked to the neoclassical parallel friction, the classic perpendicular friction and the turbulent $\mathbf{E} \times \mathbf{B}$ drift flux. The neoclassical part of this flux can be rewritten using the identity $1 = 1 - \frac{B^2}{\langle B^2 \rangle_{FS}} + \frac{B^2}{\langle B^2 \rangle_{FS}}$:

$$\langle \boldsymbol{\Gamma}_i \cdot \boldsymbol{\nabla}\psi \rangle_{FS}^{neo} = -\left\langle \frac{I}{B}\left(N_i E_\parallel + \frac{\mathcal{F}_\parallel}{q_i}\right)\left[1 - \frac{B^2}{\langle B^2 \rangle_{FS}} + \frac{B^2}{\langle B^2 \rangle_{FS}}\right]\right\rangle_{FS} \tag{A.8}$$

$$= \underbrace{-I\left\langle \frac{1}{q_i B}\left(q_i N_i E_\parallel + \mathcal{F}_\parallel\right)\left(1 - \frac{B^2}{\langle B^2 \rangle_{FS}}\right)\right\rangle_{FS}}_{\langle \boldsymbol{\Gamma}_i \cdot \nabla\psi \rangle_{FS}^{PS}} \underbrace{-I\frac{\left\langle B\left(q_i N_i E_\parallel + \mathcal{F}_\parallel\right)\right\rangle_{FS}}{q_i \langle B^2 \rangle_{FS}}}_{\langle \boldsymbol{\Gamma}_i \cdot \nabla\psi \rangle_{FS}^{BP}}, \tag{A.9}$$

to make the two main components of the neoclassical appear, namely the banana-plateau and Pfirsch-Schlüter components.

A.2.2 Link between BP flux and anisotropy

Starting from the fluid momentum conservation equation

$$\frac{\partial M_i N_i \mathbf{V}_i}{\partial t} + \boldsymbol{\nabla} \cdot \bar{\boldsymbol{\Pi}}_i = N_i q_i \left(\mathbf{E} + \mathbf{V} \times \mathbf{B}\right) + \boldsymbol{\mathcal{F}}, \tag{A.10}$$

with $\bar{\boldsymbol{\Pi}}_i$ the pressure tensor written with the CGL notation[13]. This is helpful to describe the anisotropy by separating the perpendicular and parallel components such that $\bar{\boldsymbol{\Pi}}_i = P_\parallel b_l b_j + P_\perp\left(\delta_{lj} + b_l b_j\right)$. By projecting this equation along $\mathbf{B}$, we get

$$\mathbf{B} \cdot \left[\frac{\partial M_i N_i \mathbf{V}_i}{\partial t} + \boldsymbol{\nabla} \cdot \bar{\boldsymbol{\Pi}}_i\right] = N_i q_i \mathbf{B} \cdot \mathbf{E} + \mathbf{B} \cdot \boldsymbol{\mathcal{F}}. \tag{A.11}$$

After we consider a steady-state, simplify notations and take the flux-surface average of this equation, we can write

$$\left\langle \mathbf{B}\cdot\boldsymbol{\nabla}\cdot\bar{\bar{\mathbf{\Pi}}}_i\right\rangle_{FS} = \left\langle B\left(N_i q_i E_\parallel + \mathcal{F}_\parallel\right)\right\rangle_{FS}. \tag{A.12}$$

This enables us to rewrite the BP flux as

$$\langle \mathbf{\Gamma}_i\cdot\boldsymbol{\nabla}\psi\rangle_{FS}^{BP} = -I\frac{\left\langle \mathbf{B}\cdot\boldsymbol{\nabla}\cdot\bar{\bar{\mathbf{\Pi}}}_i\right\rangle_{FS}}{q_i\left\langle B^2\right\rangle_{FS}}, \tag{A.13}$$

making the link between the BP component of the flux with anisotropy appear directly.

A.3 Impurity particle flux

We start from

$$\mathbf{\Gamma}_{\perp,s} = \underbrace{N_s\mathbf{v_E}}_{\mathbf{\Gamma}_{E,s}} + \underbrace{N_s\left\langle\mathbf{v}_{D,s}\right\rangle_v}_{\mathbf{\Gamma}_{D,s}} - \underbrace{\boldsymbol{\nabla}\times\left[N_s\left\langle\frac{\mu_s}{q_s}\mathbf{b}\right\rangle_v\right]}_{\mathbf{\Gamma}_{mag,s}} \tag{A.14}$$

with

$$\mathbf{v}_E = \frac{\mathbf{B}\times\boldsymbol{\nabla}\bar{\phi}}{B^2}, \tag{A.15}$$

$$\mathbf{v}_{D,s} = \mathbf{v}_{\nabla,s} + \mathbf{v}_{c,s} = \frac{\mu_s}{q_s}\frac{\mathbf{B}\times\boldsymbol{\nabla}B}{B^2} + \frac{M_s v_{\parallel,GC,s}^2}{qB^2}\frac{\mathbf{R_c}\times\mathbf{B}}{R_c^2}, \tag{A.16}$$

$$\mathbf{v}_{\parallel,GC,s} = v_{\parallel,GC,s}\mathbf{b}. \tag{A.17}$$

We can rewrite $\frac{\mathbf{R_c}\times\mathbf{B}}{R_c^2} = \mathbf{B}\times(\mathbf{b}\cdot\boldsymbol{\nabla})\,\mathbf{b} = -\kappa\times\mathbf{B}$ before integrating both $\mathbf{v}_{\nabla,s}$ and $\mathbf{v}_{c,s}$ over the velocity space. First, for the gradient drift we get

$$\begin{aligned}\left\langle\mathbf{v}_{\nabla,s}\right\rangle_v &= \frac{1}{N_s}\int d^3\mathbf{v}_{GC,d}\bar{f}_s\frac{\mu_s}{q_s}\frac{\mathbf{B}\times\boldsymbol{\nabla}B}{B^2} = \frac{\mathbf{B}\times\boldsymbol{\nabla}B}{N_s q_s B^3}\int d^3\mathbf{v}_{GC,s}\bar{f}_s\mu_s B,\\ \left\langle\mathbf{v}_{\nabla,s}\right\rangle_v &= \frac{P_{\perp,s}}{N_s}\frac{\mathbf{B}\times\boldsymbol{\nabla}B}{q_s B^3}.\end{aligned} \tag{A.18}$$

For the curvature drift we write

$$\begin{aligned}\left\langle\mathbf{v}_{c,s}\right\rangle_v &= -\frac{1}{N_s}\int d^3\mathbf{v}_{GC,s}\bar{f}_s\frac{M_s v_{\parallel,GC,s}^2}{q_s B}\frac{\kappa\times\mathbf{B}}{B^2} = -\frac{\kappa\times\mathbf{B}}{N_s q_s B^2}\int d^3\mathbf{v}_{GC,s}\bar{f}_s M_s v_{\parallel,GC,s}^2,\\ \left\langle\mathbf{v}_{c,s}\right\rangle_v &= -\frac{P_{\parallel,s}}{N_s}\frac{\kappa\times\mathbf{B}}{q_s B^2}.\end{aligned} \tag{A.19}$$

For the magnetization, it is straightforward

$$\left\langle \frac{\mu_s}{q_s}\mathbf{b} \right\rangle_v = \frac{1}{N_s}\int d^3\mathbf{v}_{GC,s}\frac{\mu_s B}{q_s}\frac{\mathbf{b}}{B}\bar{f}_s = \frac{P_{\perp,s}}{N_s}\frac{\mathbf{b}}{q_s B}. \tag{A.20}$$

Equation (A.14) becomes, by combining equations (A.18),(A.19) and (A.20):

$$\mathbf{\Gamma}_{D,s} = \mathbf{\Gamma}_{\nabla,s} + \mathbf{\Gamma}_{c,s} + \mathbf{\Gamma}_{mag,s} = P_{\perp,s}\frac{\mathbf{B}\times\boldsymbol{\nabla}B}{q_s B^3} - P_{\parallel,s}\frac{\kappa\times\mathbf{B}}{q_s B^2} - \boldsymbol{\nabla}\times\left[P_{\perp,s}\frac{\mathbf{b}}{q_s B}\right] \tag{A.21}$$

The magnetization term can be further developped as

$$\boldsymbol{\nabla}\times\left[P_{\perp,s}\frac{\mathbf{b}}{q_s B}\right] = \boldsymbol{\nabla}\left(\frac{P_{\perp,s}}{q_s B}\right)\times\mathbf{b} + (\boldsymbol{\nabla}\times\mathbf{b})\frac{P_{\perp,s}}{q_s B}. \tag{A.22}$$

We remind that $\nabla\times\mathbf{b}$ can be recast as

$$\boldsymbol{\nabla}\times\mathbf{b} = \mathbf{b}\times(\boldsymbol{\nabla}\times\mathbf{b}) + \mathbf{b}\left[\mathbf{b}\cdot(\boldsymbol{\nabla}\times\mathbf{b})\right] = -\kappa + \mathbf{b}\left[\mathbf{b}\cdot(\boldsymbol{\nabla}\times\mathbf{b})\right]. \tag{A.23}$$

Moreover, we can compute

$$\mathbf{b}\times\kappa = \mathbf{b}\times\left[\mathbf{b}\times(\boldsymbol{\nabla}\times\mathbf{b})\right] = -\mathbf{b}\left[\mathbf{b}\cdot(\boldsymbol{\nabla}\times\mathbf{b})\right] + \boldsymbol{\nabla}\times\mathbf{b}, \tag{A.24}$$

which leads to

$$\boldsymbol{\nabla}\times\mathbf{b} = \mathbf{b}\times\kappa + \mathbf{b}\left[\mathbf{b}\cdot(\boldsymbol{\nabla}\times\mathbf{b})\right]. \tag{A.25}$$

Also, we have

$$\boldsymbol{\nabla}\left(\frac{P_{\perp,s}}{q_s B}\right) = \frac{1}{q_s B}\boldsymbol{\nabla}P_{\perp,s} + \frac{P_{\perp,s}}{q_s}\boldsymbol{\nabla}\left(\frac{1}{B}\right) = \frac{1}{q_s B}\boldsymbol{\nabla}P_{\perp,s} - \frac{P_{\perp,s}}{q_s}\frac{\boldsymbol{\nabla}B}{B^2}, \tag{A.26}$$

which ultimately leads to

$$\mathbf{\Gamma}_{D,s} = \frac{1}{q_s B}\left[P_{\perp,s}\frac{\mathbf{B}\times\boldsymbol{\nabla}B}{B^2} - P_{\parallel,s}\frac{\kappa\times\mathbf{B}}{B} - \frac{\boldsymbol{\nabla}P_{\perp,s}\times\mathbf{B}}{B} + P_{\perp,s}\frac{\boldsymbol{\nabla}B\times\mathbf{B}}{B^2} - (\boldsymbol{\nabla}\times\mathbf{b})P_{\perp,s}\right],$$

$$\mathbf{\Gamma}_{D,s} = \frac{1}{q_s B}\left[P_{\parallel,s}\mathbf{b}\times\kappa + \mathbf{b}\times\boldsymbol{\nabla}P_{\perp,s} - (\boldsymbol{\nabla}\times\mathbf{b})P_{\perp,s}\right]. \tag{A.27}$$

We can transform the last term by using equations (A.24) and (A.25) to get

$$-(\boldsymbol{\nabla}\times\mathbf{b})P_{\perp,s} = -\left(\mathbf{b}\times\kappa + \mathbf{b}\left[\mathbf{b}\cdot(\boldsymbol{\nabla}\times\mathbf{b})\right]\right)P_{\perp,s}, \tag{A.28}$$

which we can further decompose in perpendicular and parallel components

$$\mathbf{\Gamma}_{D,\perp,s} = \frac{\mathbf{b}}{q_s B}\times\left[\underbrace{\left(P_{\parallel,s} - P_{\perp,s}\right)}_{\Pi_{\parallel,s}}\kappa + \boldsymbol{\nabla}P_{\perp,s}\right], \tag{A.29}$$

$$\mathbf{\Gamma}_{D,\parallel,s} = -\frac{\mathbf{b}\left[\mathbf{b}\cdot(\boldsymbol{\nabla}\times\mathbf{b})\right]}{q_s B}P_{\perp,s}. \tag{A.30}$$

A.4 Poloidal asymmetries

In equation (2.19), the K_s term can be developped[8] as $K_s = K_{s0}(\psi) + K_{s1}(\psi, \theta)$ with

$$K_{s0}(\psi) = \langle K_s \rangle_\psi , \tag{A.31}$$

$$K_s(\psi, \theta) = -\frac{1}{B}\frac{\partial}{\partial \psi}\left(\frac{I\Pi_{\parallel,s}}{q_s B}\right) + \left\langle \frac{1}{B}\frac{\partial}{\partial \psi}\left(\frac{I\Pi_{\parallel,s}}{q_s B}\right)\right\rangle_{FS} . \tag{A.32}$$

One can also project equation (2.7) along the toroidal direction and average it over flux surfaces to extract the link between the particle flux and parallel friction force

$$\left\langle R\mathbf{e}_\varphi \cdot \frac{\partial (M_s \mathbf{\Gamma}_s)}{\partial t}\right\rangle_{FS} + \langle R\mathbf{e}_\varphi \cdot \boldsymbol{\nabla} \cdot \mathbf{\Pi}_s \rangle_{FS} - \langle q_s R\mathbf{e}_\varphi \cdot (N_s \mathbf{E} + \mathbf{\Gamma}_s \times B)\rangle_{FS} + \left\langle R\mathcal{F}_{\parallel,si}\right\rangle_{FS} . \tag{A.33}$$

By assuming a steady state, toroidal axisymmetry and neglecting the stress tensor term $\mathbf{\Pi}_s$, we can write[11]

$$\langle \mathbf{\Gamma}_s \cdot \boldsymbol{\nabla}\psi \rangle_{FS}^{neo} = -\left\langle \frac{I\mathcal{F}_{\parallel,si}}{q_s B}\right\rangle_{FS} , \tag{A.34}$$

where the parallel friction term is detailed by Hirshman and Sigmar[14] and P. Donnel[8]

$$\mathcal{F}_{\parallel,si} = M_s \nu_{si}\left[-N_s \frac{T_i}{q_s}\frac{I}{L_\psi} + B(N_s u - K_s)\right] . \tag{A.35}$$

We note that $L_\psi^{-1} = L_{\psi,i}^{-1} + L_{\psi,s}^{-1}$ with $L_{\psi,s}^{-1} = -\partial_\psi P_{\perp,s}/T_i Z_s N_s$ and $L_{\psi,i}^{-1} = \partial_\psi \ln P_i - H_{TS}\partial_\psi \ln T_i$. u is linked to the poloidal velocity of ions.

Appendix B

Turbulent flux

B.1 Linear and quasi-linear theory

B.1.1 Link between ϕ_1 and f_1

We start by using a developpement like equation (1.23) for both the electrostatic potential ϕ and the distribution function f in equation 2.27

$$\begin{aligned}\frac{\partial\left(f_0+f_1\right)}{\partial t}+\frac{\mathbf{b}}{B}\times\boldsymbol{\nabla}\left(\phi_0+\phi_1\right)\cdot\boldsymbol{\nabla}\left(f_0+f_1\right)+\mathbf{b}v_\parallel\cdot\boldsymbol{\nabla}\left(f_0+f_1\right)\\ -\frac{q}{M}\boldsymbol{\nabla}\left(\phi_0+\phi_1\right)\cdot\frac{\partial}{\partial\mathbf{v}}\left(f_0+f_1\right)=0.\end{aligned}\tag{B.1}$$

By keeping the first order in perturbations, we get the linear relationship

$$\begin{aligned}\frac{\partial f_1}{\partial t}+\frac{\mathbf{b}\times\nabla\phi_0}{B}\cdot\boldsymbol{\nabla}f_1+\frac{\mathbf{b}\times\nabla\phi_1}{B}\cdot\boldsymbol{\nabla}f_0+\mathbf{b}v_\parallel\cdot\boldsymbol{\nabla}f_1\\ -\frac{q}{M}\boldsymbol{\nabla}\phi_0\cdot\frac{\partial}{\partial\mathbf{v}}f_1-\frac{q}{M}\boldsymbol{\nabla}\phi_1\cdot\frac{\partial}{\partial\mathbf{v}}f_0=0,\end{aligned}\tag{B.2}$$

in which we can inject the usual expression for perturbations (equation (1.23)). This ultimately leads to the following relationship

$$f_{k_\parallel,m,\omega}=-\frac{q\phi_{k_\parallel,m,\omega}}{Mv_{T,i}^2}f_0\frac{k_\theta\rho_c v_{T,i}\left[\frac{\partial_r n_0}{n_0}+\frac{\partial_r T_0}{2T_0}\left(\frac{v_\parallel^2}{v_{T,i}^2}-1\right)\right]-k_\parallel v_\parallel}{\omega-\frac{k_\theta}{B}\partial_r\phi_0-k_\parallel v_\parallel}.\tag{B.3}$$

Here, the only effect of the axisymmetrical part of the potential (i.e. ϕ_0) is to shift the resonnance (i.e. Doppler effect).

B.1.2 Quasi-linear fluxes

To estimate the quasi-linear fluxes, the linear relationship derived just before is considered to be true. Starting from equation (B.1) from which we remove the linear part,

$$\frac{\partial f_0}{\partial t} + \frac{\mathbf{b}}{B} \times \boldsymbol{\nabla}(\phi_1) \cdot \boldsymbol{\nabla}(f_1) + \mathbf{b} v_\parallel \cdot \boldsymbol{\nabla} f_0 - \frac{q}{M} \boldsymbol{\nabla}(\phi_0) \cdot \frac{\partial f_0}{\partial \mathbf{v}} - \frac{q}{M} \boldsymbol{\nabla}(\phi_1) \cdot \frac{\partial f_1}{\partial \mathbf{v}} = 0, \tag{B.4}$$

before averaging over θ. All the equilibrium quantities won't be affected (i.e. $\langle f_0 \rangle_\theta = f_0$ for example) while $\langle f_1 \rangle_\theta = 0$ since perturbed quantities are periodic over θ. This gives

$$\frac{\partial f_0}{\partial t} + \frac{1}{r} \frac{\partial}{\partial r} \left(r \Lambda^r_{QL} \right) - \frac{q}{M} \left\langle \partial_z \phi_1 \partial_{v_\parallel} f_1 \right\rangle_\theta = 0, \tag{B.5}$$

with $\Lambda^r_{QL} = \langle -f_1 \partial_\theta \phi_1 / Br \rangle_\theta$ a radial phase-space flux which writes

$$\Lambda^r_{QL} = \left\langle \sum_{k_\parallel, k_\theta, \omega} \sum_{k'_\parallel, k'_\theta, \omega'} -\frac{i k_\theta}{B} \hat{\phi}_{k_\parallel, k_\theta, \omega} \hat{f}_{k'_\parallel, k'_\theta, \omega'}(r) \exp\left[i \left(k_\parallel z + m\theta - \omega \right) \right] \exp\left[i \left(k'_\parallel z + m'\theta - \omega' \right) \right] \right\rangle_\theta . \tag{B.6}$$

The average operator will select all the $\left(k'_\parallel, k'_\theta, \omega' \right)$ terms that are identical but with opposite signs, thus selecting the complex conjugate

$$\Lambda^r_{QL} = \sum_{k_\parallel, k_\theta, \omega} \left(-\frac{i k_\theta}{B} \hat{\phi}_{k_\parallel, k_\theta, \omega} \right)^\star \hat{f}_{k_\parallel, k_\theta, \omega}(r), \tag{B.7}$$

which is written

$$\Lambda^r_{QL} = \sum_{k_\parallel, k_\theta, \omega} -\frac{i k_\theta}{B} \left| \hat{\phi}_{k_\parallel, k_\theta, \omega} \right|^2 f_M \frac{q_i}{T_0} \frac{k_\theta \rho_c v_{T,i} \left[\frac{\partial_r n_0}{n_0} + \frac{\partial_r T_0}{2 T_0} \left(\frac{v_\parallel^2}{v_{T,i}^2} - 1 \right) \right] - \frac{k_\theta}{B} \partial_r \phi_0 - k_\parallel v_\parallel}{\omega - \frac{k_\theta}{B} \partial_r \phi_0 - k_\parallel v_\parallel}. \tag{B.8}$$

Once integrated over the velocity space, equation (B.5) gives the usual writing

$$\frac{\partial n_0}{\partial t} + \frac{1}{r} \frac{\partial}{\partial r} \left(r \Gamma^r_{QL} \right) = 0 \tag{B.9}$$

with $\Gamma^r_{QL} = \int dv_\parallel \Lambda^r_{QL}$. We recall that in cylindrical coordinates, the divergence writes

$$\boldsymbol{\nabla} \times \mathbf{A} = \frac{1}{r} \frac{\partial (r A_r)}{\partial r} + \frac{1}{r} \frac{\partial A_\theta}{\partial \theta} + \frac{\partial A_z}{\partial z}, \tag{B.10}$$

hence the identification performed in equation B.9.

B.1.3 Turbulent flux

By using equation (B.8), the particle flux Γ^r_{QL} can be expressed as

$$\Gamma^r_{QL} = \Re\left[\int dv_\parallel \sum_{k_\parallel,k_\theta,\omega} -\frac{ik_\theta}{B}\left|\hat{\phi}_{k_\parallel,k_\theta,\omega}\right|^2 f_M \frac{q}{T_0}\frac{k_\theta\rho_c v_{T,i}\left[\frac{\partial_r n_0}{n_0}+\frac{\partial_r T_0}{2T_0}\left(\frac{v_\parallel^2}{v_{T,i}^2}-1\right)\right]-\frac{k_\theta}{B}\partial_r\phi_0-k_\parallel v_\parallel}{\omega-\frac{k_\theta}{B}\partial_r\phi_0-k_\parallel v_\parallel}\right]. \tag{B.11}$$

The *actual* flux of particle is then the real part of this expression, which can be simplified by separating $\omega = \omega_r + i\gamma$ and noting for the denominator $\Omega_R = \omega_r - \frac{k_\theta}{B}\partial_r\phi_0$

$$\Gamma^r_{QL} = \Re\left[\int dv_\parallel \sum_{k_\parallel,k_\theta,\omega} -\frac{ik_\theta}{B}\left|\hat{\phi}_{k_\parallel,k_\theta,\omega}\right|^2 f_M \frac{q}{T_0}\frac{k_\theta\rho_c v_{T,i}\left[\frac{\partial_r n_0}{n_0}+\frac{\partial_r T_0}{2T_0}\left(\frac{v_\parallel^2}{v_{T,i}^2}-1\right)\right]-\frac{k_\theta}{B}\partial_r\phi_0-k_\parallel v_\parallel}{\Omega_R-k_\parallel v_\parallel+i\gamma}\right]. \tag{B.12}$$

This expression can be simplified by multiplying it by $\left(\Omega_R - k_\parallel v_\parallel - i\gamma\right) / \left(\Omega_R - k_\parallel v_\parallel - i\gamma\right)$, which is the complex conjugate of the denominator. This leads to to the final expression of the turbulent particle flux

$$\Gamma^r_{QL} = \int dv_\parallel \sum_{k_\parallel,k_\theta,\omega} -\frac{\gamma k_\theta}{B}\left|\hat{\phi}_{k_\parallel,k_\theta,\omega}\right|^2 f_M \frac{q}{T_0}\frac{k_\theta\rho_c v_{T,i}\left[\frac{\partial_r n_0}{n_0}+\frac{\partial_r T_0}{2T_0}\left(\frac{v_\parallel^2}{v_{T,i}^2}-1\right)\right]-\frac{k_\theta}{B}\partial_r\phi_0-k_\parallel v_\parallel}{\left(\Omega_R-k_\parallel v_\parallel\right)^2+\gamma^2}. \tag{B.13}$$

B.2 Fluid moments from Vlasov equation

From

$$\underbrace{\int_{-\infty}^{+\infty} A dv_\parallel \frac{\partial f_s}{\partial t}}_{1} + \underbrace{\int_{-\infty}^{+\infty} A dv_\parallel \mathbf{v}_s\cdot\boldsymbol{\nabla} f_s}_{2} + \underbrace{\int_{-\infty}^{+\infty} A dv_\parallel \frac{q_s\mathbf{E}}{m_s}\cdot\nabla_{\mathbf{v_s}} f_s}_{3} = 0, \tag{B.14}$$

one can compute the fluid moments for ions ($s = i$) with the following definition:

$$n = \int_{-\infty}^{+\infty} f_i dv_\parallel \tag{B.15}$$

$$Mnu_\parallel = \int_{-\infty}^{+\infty} Mv_\parallel f_i dv_\parallel, \tag{B.16}$$

$$P_\parallel = \int_{-\infty}^{+\infty} M\left(v_\parallel - u_\parallel\right)^2 f dv_\parallel \leftrightarrow \int_{-\infty}^{+\infty} Mv_\parallel^2 f_i dv_\parallel = P_\parallel + Mnu_\parallel^2, \tag{B.17}$$

$$Q_\parallel = \int_{-\infty}^{+\infty} M\left(v_\parallel - u_\parallel\right)^3 f_i dv_\parallel \leftrightarrow \int_{-\infty}^{+\infty} Mv_\parallel^3 f dv_\parallel = P_\parallel + 3u_\parallel P_\parallel + Mnu_\parallel^3 \tag{B.18}$$

$$\mathbf{v}_\alpha = \mathbf{v}_{E\times B} + v_\parallel \mathbf{b} \tag{B.19}$$

First moment, $A = 1$

By taking $A = 1$, the first term of equation (B.14) is straightforward as the time derivative and velocity integral can be swapped since variables are independant from each other. This leads to

$$\int_{-\infty}^{+\infty} dv_\parallel \frac{\partial f_i}{\partial t} = \frac{\partial}{\partial t}\int_{-\infty}^{+\infty} f_i dv_\parallel = \frac{\partial n}{\partial t}. \tag{B.20}$$

The second term of equation (B.14) can be separated in two terms; the $\mathbf{E}\times\mathbf{B}$ drift, which only depends on space, and the parallel velocity which does not depend on space and therefore can be swapped with the space gradient. This gives

$$\int_{-\infty}^{+\infty} dv_\parallel \mathbf{v}\cdot\boldsymbol{\nabla} f_i = \int_{-\infty}^{+\infty} dv_\parallel \left(\mathbf{v}_{E\times B} + v_\parallel \mathbf{b}\right)\cdot\boldsymbol{\nabla} f_i,$$

$$\mathbf{v}_{E\times B}\cdot\boldsymbol{\nabla}\int_{-\infty}^{+\infty} dv_\parallel f_i + \boldsymbol{\nabla}\cdot\int_{-\infty}^{+\infty} dv_\parallel v_\parallel \mathbf{b} f_i = \frac{\mathbf{E}\times\mathbf{B}}{B^2}\cdot\boldsymbol{\nabla} n + \frac{\partial}{\partial z}\left(nu_\parallel\right). \tag{B.21}$$

The last term of equation (B.14) is also straightfroward as $\mathbf{E}$ does not depend on velocity and the parallel velocity is the only one of interest:

$$\int_{-\infty}^{+\infty} dv_\parallel \frac{\mathbf{E}}{M}\cdot\boldsymbol{\nabla}_\mathbf{v} f_i = \frac{q_i E_z}{M}\int_{-\infty}^{+\infty} dv_\parallel \frac{\partial f_i}{\partial v_\parallel} = \frac{q_i E_z}{M}\left[f_i\right]_{-\infty}^{+\infty} = 0 \tag{B.22}$$

since $\lim_{v_\parallel\to\pm\infty}(f_i) = 0$ by definition. Combining equations (B.20), (B.21) and (B.22) gives the continuity equation

$$\frac{\partial n}{\partial t} + \frac{\mathbf{E}\times\mathbf{B}}{B^2}\cdot\boldsymbol{\nabla} n + \frac{\partial}{\partial z}\left(nu_\parallel\right) \quad = 0 \tag{B.23}$$

Second moment, $A = Mv_\parallel$

Similarly as for $A = 1$, the first term of equation (B.14) simple to compute since the time derivative and velocity terms can be swapped. This gives

$$\int_{-\infty}^{+\infty} dv_\parallel Mv_\parallel \frac{\partial f_i}{\partial t} = \frac{\partial}{\partial t}\int_{-\infty}^{+\infty} Mv_\parallel f_i dv_\parallel = \frac{\partial Mnu_\parallel}{\partial t}. \tag{B.24}$$

The second term also requires to separate the $\mathbf{E}\times\mathbf{B}$ drift term to the parallel velocity term to get

$$\int_{-\infty}^{+\infty} dv_\parallel Mv_\parallel \mathbf{v}\cdot\boldsymbol{\nabla} f_i = \int_{-\infty}^{+\infty} dv_\parallel Mv_\parallel \left(\mathbf{v}_{E\times B} + v_\parallel \mathbf{b}\right)\cdot\boldsymbol{\nabla} f_i,$$
$$\mathbf{v}_{E\times B}\cdot\boldsymbol{\nabla}\int_{-\infty}^{+\infty} dv_\parallel Mv_\parallel f_i + \boldsymbol{\nabla}\cdot\int_{-\infty}^{+\infty} dv_\parallel Mv_\parallel^2 \mathbf{b} f_i = \frac{\mathbf{E}\times\mathbf{B}}{B^2}\cdot\boldsymbol{\nabla}\left(Mnu_\parallel\right) + \frac{\partial}{\partial z}\left(Mnu_\parallel^2\right) + \frac{\partial P_\parallel}{\partial z}, \tag{B.25}$$

where $\int_{-\infty}^{+\infty} dv_\parallel Mv_\parallel^2 f_i$ is replaced by equation (B.17).

The third term is computed requires an integral by part to get

$$\int_{-\infty}^{+\infty} dv_\parallel Mv_\parallel \frac{q_i\mathbf{E}}{M}\cdot\boldsymbol{\nabla}_\mathbf{v} f_i = q_i E_z \int_{-\infty}^{+\infty} v_\parallel dv_\parallel \frac{\partial f_i}{\partial v_\parallel},$$
$$q_i E_z\left(\left[v_\parallel f_i\right]_{-\infty}^{+\infty} - \int_{-\infty}^{+\infty} dv_\parallel f_i\right) = -q_i E_z n. \tag{B.26}$$

One can get a first momentum conservation equation by combining equations (B.24), (B.25) and (B.26)

$$\frac{\partial Mnu_\parallel}{\partial t} + \frac{\mathbf{E}\times\mathbf{B}}{B^2}\cdot\boldsymbol{\nabla}\left(Mnu_\parallel\right) + \frac{\partial Mnu_\parallel^2}{\partial z} = q_i E_z n - \frac{\partial P_\parallel}{\partial z}, \tag{B.27}$$

which can be further developped by combining it with equation (B.23) to get

$$Mn\left[\frac{\partial}{\partial t} + \frac{\mathbf{E}\times\mathbf{B}}{B^2}\cdot\boldsymbol{\nabla} + u_\parallel\frac{\partial}{\partial z}\right]u_\parallel = q_i E_z n - \frac{\partial P_\parallel}{\partial z}. \tag{B.28}$$

Third moment, $A = Mv_\parallel^2$

To compute the first term, we swap the time derivative and velocity terms again in equation (B.17), which gives

$$\int_{-\infty}^{+\infty} dv_\parallel Mv_\parallel^2 \frac{\partial f_i}{\partial t} = \frac{\partial}{\partial t}\int_{-\infty}^{+\infty} Mv_\parallel^2 f_i dv_\parallel = \frac{\partial\left(Mnu_\parallel^2 + P_\parallel\right)}{\partial t}. \tag{B.29}$$

Similarly as before, the second term can be computed using equation (B.18)

$$\int_{-\infty}^{+\infty} dv_\parallel M v_\parallel^2 \mathbf{v}\cdot\boldsymbol{\nabla} f_i = \int_{-\infty}^{+\infty} dv_\parallel M v_\parallel^2 \left(\mathbf{v}_{E\times B} + v_\parallel \mathbf{b}\right)\cdot\boldsymbol{\nabla} f_i,$$
$$\frac{\mathbf{E}\times\mathbf{B}}{B^2}\cdot\boldsymbol{\nabla}\left(Mnu_\parallel^2 + P_\parallel\right) + \frac{\partial}{\partial z}\left(Mnu_\parallel^3 + 3u_\parallel P_\parallel + Q_\parallel\right), \tag{B.30}$$

The last term is computed similarly as equation (B.26) and requires to integrate by part:

$$\int_{-\infty}^{+\infty} dv_\parallel M v_\parallel^2 \frac{q_i\mathbf{E}}{M}\cdot\boldsymbol{\nabla}_{\mathbf{v}} f_i = q_i E_z \int_{-\infty}^{+\infty} v_\parallel^2 dv_\parallel \frac{\partial f_i}{\partial v_\parallel},$$
$$q_i E_z\left(\left[v_\parallel^2 f_i\right]_{-\infty}^{+\infty} - 2\int_{-\infty}^{+\infty} dv_\parallel v_\parallel f_i\right) = -2q_i E_z n u_\parallel. \tag{B.31}$$

By combining equations (B.29), (B.30), (B.31) and (B.28), the energy conservation equation can then be written

$$\left[\frac{\partial}{\partial t} + \frac{\mathbf{E}\times\mathbf{B}}{B^2}\cdot\boldsymbol{\nabla}\right] P + \frac{\partial Q_\parallel}{\partial z} + \frac{\partial u_\parallel P_\parallel}{\partial z} + 2P_\parallel\frac{\partial u_\parallel}{\partial z} \quad = 0. \tag{B.32}$$

B.3 Linearisation of gyrofluid moments

Using equation (1.23) and

$$\mathbf{v}_{E\times B} = -\frac{1}{B}\begin{pmatrix}\frac{\partial\phi}{\partial r}\\ \frac{1}{r}\frac{\partial\phi}{\partial\theta}\\ \frac{\partial\phi}{\partial z}\end{pmatrix}\times\begin{pmatrix}0\\0\\1\end{pmatrix} = \frac{1}{B}\begin{pmatrix}-\frac{1}{r}\frac{\partial\phi}{\partial\theta}\\ \frac{\partial\phi}{\partial r}\\ 0\end{pmatrix}$$

, one can develop the coninuity equation (2.38) as

$$-i\omega n_1 + ik_\theta\phi_1\frac{\partial n_0}{\partial r} + n_0 ik_\parallel u_1 = 0.$$

By dividing this equation by n_0 and using $\omega_{n,T}^\star = \frac{k_\theta\rho_c v_T}{\{n_0,T_0\}}\frac{\partial\{n_0,T_0\}}{\partial r}$, $\Omega_\parallel = k_\parallel v_T$ and $v_T = \sqrt{\frac{T_0}{M}}$, this can be reduced to

$$\omega\frac{n_1}{n_0} = \frac{q_i\phi_1}{T_0}\omega_n^\star + \frac{\Omega_\parallel u_1}{v_T} = 0. \tag{B.33}$$

Linearizing the momentum conservation equation (2.39) gives

$$-i\omega M n_0 u_1 = -q_i n_0 ik_\parallel\phi_1 - ik_\parallel\left(n_0T_1 + n_1T_0\right).$$

This equation can be simplified by dividing it by $n_0\sqrt{T_0M}$:

$$\omega \frac{u_1}{v_T} = \Omega_\parallel \frac{q_i \phi_1}{T_0} + \Omega_\parallel \left(\frac{T_1}{T_0} + \frac{n_1}{n_0} \right). \tag{B.34}$$

The linearization of the energy conservation equation (2.40) gives

$$-i\omega \left(n_0 T_1 + n_1 T_0 \right) + i \frac{k_\theta \phi_1}{B} \frac{\partial \left(n_0 T_0 \right)}{\partial r} + 3 i k_\parallel n_0 T_0 u_1 = 0,$$

which can be rewritten as

$$\omega \left(\frac{T_1}{T_0} - \frac{n_1}{n_0} \right) + i \frac{q_i \phi_1}{T_0} \left[\omega_n^\star + \omega_T^\star \right] - 3 \Omega_\parallel \frac{u_1}{v_T} = 0. \tag{B.35}$$

Poisson equation (2.31) is also linearized using the same method and gives

$$\frac{n_1}{n_0} = \frac{q_i \phi_1}{T_0} \left[\frac{\tau_i}{Z_i^2} + \rho_L^2 k_\perp^2 \right]. \tag{B.36}$$

Combining equations (B.33), (B.34), (B.35 and (B.36) as well as normalizing frequencies to $\Omega_\parallel$, one get the linear dispersion relation for ITG in a cylindrical geometry :

$$\hat{\omega}^3 \left[\frac{\tau_i}{Z_i^2} + \rho_c^2 k_\perp^2 \right] - \hat{\omega}^2 \hat{\omega}_n^\star - \hat{\omega} \left[3 \left(\frac{\tau_i}{Z_i^2} + \rho_c^2 k_\perp^2 \right) + 1 \right] + \left(2 \hat{\omega}_n^\star - \hat{\omega}_T^\star \right) = 0. \tag{B.37}$$

Appendix C

GYSELA and source computation

C.1 Electric field well scaling in H mode operations

The electric field well width of different tokamaks in H mode are compared to their gyroradii in table C.1. This gives us a simple - and optimistic - link between a given normalized gyroradius we choose in GYSELA and the expected vorticity source width necessary to match experiments *in normalized units*.

Tokamak	WEST [116]	COMPASS [51]	D3D [47]	ALCATOR C-mod[50]	ASDEX-U [49]	JET [52]	JFT-2M [46]	MAST [53]	ITER
a (m)	0.5	0.23	0.62	0.22	0.65	1.25	0.35	0.65	2
B (T)	3.7	1.2	2.1	8	3.1	3.45	2.2	0.51	5.3
T_i^{core} (eV)	800	720	300	3000	1600	1850	450	300	10000
A_i, Z_i	2,1	2,1	2,1	2,1	2,1	2,1	2,1	4,2	2,1
$\rho_{c,i}$ (mm)	1.105	3.232	1.192	0.989	1.865	1.802	1.394	3.471	2.727
L_E (cm)	1.5	1.15	1	0.75	3.25	1.5	1	1.625	2.67
$1/\rho^\star$ $a/\rho_{c,i}$	453	71	520	222	349	694	251	187	733
$1/L_E^\star$ $L_E/\rho_{c,i}$	33.33	20	62	29.33	20	83.33	35	40	75

Table C.1: Characteristics of different tokamaks, including their normalized gyroradii and width of electric field well at the edge transport barrier position during H-mode operations. $1/L_E^\star$ for ITER are estimated based on a linear fit of all the measurements and is therefore a rough estimate.

C.2 Polarization density

In GYSELA normalized units, polarization density for a species s is defined as

$$n_{pol} = \boldsymbol{\nabla}_\perp \cdot \left(\frac{A_s n_{0,s}}{B_0^2} \boldsymbol{\nabla}_\perp \phi \right), \tag{C.1}$$

with A_s and $n_{0,s}$ the mass number and initial density profile of the considered species respectively and ϕ the electrostatic potential. B_0 is always taken equal to 1 in GYSELA and can be ignored hereafter.

C.2.1 Nabla operators

The exact computation consists in taking the full gradient and divergence terms in toroidal coordinates. First, we need to define the said operators in order to proceed with the computations. In simplified toroidal coordinates, we get

$$\boldsymbol{\nabla} = \begin{pmatrix} \partial_r \\ \frac{1}{r}\partial_\theta \\ \frac{1}{R}\partial_\varphi \end{pmatrix}. \tag{C.2}$$

By writing $\zeta = \frac{r}{qR_0}$, $\mathbf{B}$ can be written as

$$\mathbf{B} = \frac{B_0 R_0}{R} \begin{pmatrix} 0 \\ \zeta \\ 1 \end{pmatrix}. \tag{C.3}$$

By rewriting $\mathbf{b} = \mathbf{B}/B$ the unit vector along $\mathbf{B}$ where $B = \sqrt{1+\zeta^2}\, B_0 R_0/R$ is the magnetic field norm, the parallel gradient can be written as

$$\begin{aligned} \boldsymbol{\nabla}_\parallel &= \mathbf{b}\,(\mathbf{b}\cdot\boldsymbol{\nabla}) = \mathbf{b}\left[\frac{\zeta\mathbf{e}_\theta + \mathbf{e}_\varphi}{\sqrt{1+\zeta^2}} \cdot \left(\mathbf{e}_r\,\partial_r + \mathbf{e}_\theta\,\frac{1}{r}\partial_\theta + \mathbf{e}_\varphi\,\frac{1}{R}\partial_\varphi\right)\right] \\ &= \frac{\mathbf{b}}{\sqrt{1+\zeta^2}}\left(\frac{\zeta}{r}\partial_\theta + \frac{1}{R}\partial_\varphi\right). \end{aligned} \tag{C.4}$$

Consequently, the perpendicular gradient will be written

$$\begin{aligned} \boldsymbol{\nabla}_\perp &= \boldsymbol{\nabla} - \boldsymbol{\nabla}_\parallel \\ &= \begin{pmatrix} \partial_r \\ \frac{1}{r}\left[1 - \frac{\zeta^2}{1+\zeta^2}\right]\partial_\theta - \frac{1}{R}\frac{\zeta}{1+\zeta^2}\partial_\varphi \\ \frac{1}{R}\left[1 - \frac{1}{1+\zeta^2}\right]\partial_\varphi - \frac{1}{r}\frac{\zeta}{1+\zeta^2}\partial_\theta \end{pmatrix} \end{aligned} \tag{C.5}$$

C.2.2 Exact computation

To compute accurately the polarization density, we use equation (C.5) in equation (C.1) and using the full 3D electrostatic potential map $\phi(r,\theta,\varphi,t)$

$$\begin{aligned} n_{pol}(r,\theta,\varphi,t) &= A_s \boldsymbol{\nabla}_\perp \cdot [n_{0,s} \boldsymbol{\nabla}_\perp \phi(r,\theta,\varphi,t)] \\ &= A_s \partial_r \left[n_{0,s} \partial_r \phi(r,\theta,\varphi,t)\right] \\ &+ F_r n_{0,s} \partial_\theta \left[F_r \partial_\theta \phi(r,\theta,\varphi,t) - G_R \partial_\varphi \phi(r,\theta,\varphi,t)\right] \\ &- G_R n_{0,s} \partial_\varphi \left[F_r \partial_\theta \phi(r,\theta,\varphi,t) - G_R \partial_\varphi \phi(r,\theta,\varphi,t)\right] \\ &+ F_R n_{0,s} \partial_\varphi \left[F_R \partial_\varphi \phi(r,\theta,\varphi,t) - G_r \partial_\theta \phi(r,\theta,\varphi,t)\right] \\ &- G_r n_{0,s} \partial_\theta \left[F_R \partial_\varphi \phi(r,\theta,\varphi,t) - G_r \partial_\theta \phi(r,\theta,\varphi,t)\right] \\ &+ F_r n_{0,s} \partial_r \phi(r,\theta,\varphi,t) \\ &- G_R \sin\theta n_{0,s} \left[F_R \partial_\varphi \phi(r,\theta,\varphi,t) - G_r \partial_\theta \phi(r,\theta,\varphi,t)\right] \\ &+ F_R \cos\theta n_{0,s} \partial_r \phi(r,\theta,\varphi,t) \\ &+ F_R \sin\theta n_{0,s} \partial_\varphi \left[F_r \partial_\theta \phi(r,\theta,\varphi,t) - G_R \partial_\varphi \phi(r,\theta,\varphi,t)\right] \end{aligned} \quad \text{(C.6)}$$

with $F_r = \frac{1}{r}\left[1 - \frac{\zeta^2}{1+\zeta^2}\right]$, $F_R = \frac{1}{R}\left[1 - \frac{1}{1+\zeta^2}\right]$, $G_r = \frac{1}{r}\frac{\zeta}{1+\zeta^2}$ and $G_R = \frac{1}{R}\frac{\zeta}{1+\zeta^2}$. We finally take the surface average of the above expression to compute the polarization density of the considered species

$$\langle n_{pol}(r) \rangle_{FS} = \frac{\iint (\mathbf{B} \cdot \boldsymbol{\nabla}\theta)^{-1} n_{pol}(r,\theta,\varphi) d\theta d\varphi}{\iint (\mathbf{B} \cdot \boldsymbol{\nabla}\theta)^{-1} d\theta d\varphi}. \quad \text{(C.7)}$$

C.2.3 Approximation used in GYSELA

In GYSELA, the quasi-neutrality equation (3.6) is solved in a 2D Fourier space by using

$$\boldsymbol{\nabla}_\perp^{approx} \approx \begin{pmatrix} \partial_r \\ \frac{1}{r}\partial_\theta \\ 0 \end{pmatrix}, \quad \text{(C.8)}$$

and the full 3D potential array. This operator is equivalent to neglecting the poloidal component of the magnetic field. More details are available in V. Grandgirard's work[78].

We propose to apply this operator to the 2D map of potential written simultaneously with radial density profile $\phi(r,\theta,\varphi=0)$ by making the assumption than $\langle \phi(r,\theta,\varphi) \rangle_{FS} \approx \langle \phi(r,\theta,\varphi=0) \rangle_{FS}$. The following expression can be obtained

$$\begin{aligned} \langle n_{pol} \rangle_{FS}(r,t) &\simeq A_s \langle \boldsymbol{\nabla}_\perp^{approx} \cdot (n_{0,s} \boldsymbol{\nabla}_\perp^{approx} \phi(r,\theta,\varphi=0,t)) \rangle_{FS} \\ &= A_s \left\langle \partial_r \left(n_{0,s}\, \partial_r \phi\right) + \frac{n_{0,s}}{r}\, \partial_r \langle \phi \rangle_\varphi + \frac{n_{0,s}}{r^2}\, \partial_\theta^2 \langle \phi \rangle_\varphi \right\rangle_{FS} \end{aligned} \quad \text{(C.9)}$$

C.2.4 Comparison

We select two time steps for which we posess all data, especially the 3D potential, to compare equations (C.6) and (C.9) and see if the proposed approximations hold depending if we are injecting vorticity (i.e. polarization) or a steep gradient. We

select two times, $t = 100800\omega_{c,0}^{-}1$ and $t = 416000\omega_{c,0}^{-}1$ for the steep gradient and vorticity cases respectively. Details about those simulation are described in section 3.2.

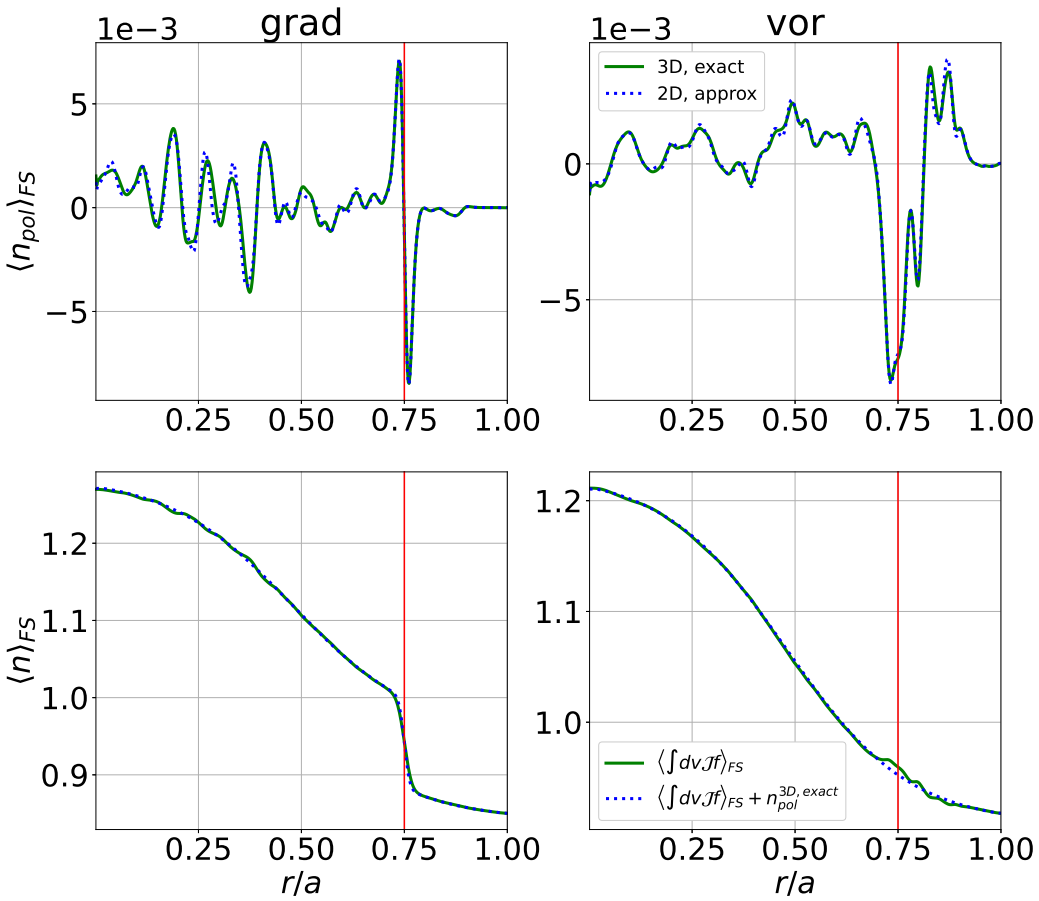

Figure C.1: **Top row:** radial profile of polarization density computed with equation (C.6) (green solid lines) and equation (C.6) for the steep gradient (top left) and vorticity cases (top right). **Bottom row:** Particle density profile computed with the gyroaverage applied on the gyrocenter distribution function only (green solid lines) and with the exact polarization density computation through equation (C.6) for the steep gradient (bottom left) and vorticity (bottom right) cases.

As shown on Figure C.1, the agreement between the full 3D exact computation and 2D approximation used in GYSELA is satisfying in both the steep gradient (top left) and vorticity cases (top right). This is confirmed when we look at the gyroaveraged density of gyrocenters (i.e. the *real* particle density); the polarization correction flattens all the density fluctuations observed. This is due to the fact that only one species is present in those simulations and therefore, all the density flucuations are potential fluctuations arising from the polarization term in equation (3.6). Thus, the corrected *particle* density profile is, at all times, the same as the initial profile provided only one kinetic species is present in the system.

C.3 Lorraine's polynomials

Integrals of Hermite and Laguerre, both born in Lorraine, whom polynomials respectively give

$$L_l(x) \longrightarrow \int_0^{+\infty} L_l L_{l'} \exp(-x)\, dx = \delta_{ll'} |L_l|^2, \tag{C.10}$$

$$H_h(x) \longrightarrow \int_{-\infty}^{+\infty} H_h H_{h'} \exp\left(-x^2\right) dx = \delta_{hh'} |H_h|^2, \tag{C.11}$$

and form a range of orthogonal basis normalized such that $|L_l|^2 = 1$ and $|H_h|^2 = \int_{-\infty}^{+\infty} H_h^2 \exp(-x^2)\, dx = \sqrt{\pi} 2^h h!$. The first polynomials are

$$\begin{aligned}
L_0(x) &= 1, \\
L_1(x) &= 1 - x, \\
L_2(x) &= \frac{1}{2}\left(2 - 4x + x^2\right), \\
L_3(x) &= \frac{1}{6}\left(6 - 18x + 9x^2 - x^3\right)
\end{aligned}$$

for the Laguerre ones, and

$$\begin{aligned}
H_0(x) &= 1 \longrightarrow |H_0|^2 = \sqrt{\pi}, \\
H_1(x) &= 2x \longrightarrow |H_1|^2 = 2\sqrt{\pi}, \\
H_2(x) &= -2 + 4x^2 \longrightarrow |H_2|^2 = 8\sqrt{\pi}, \\
H_3(x) &= -12x + 8x^3 \longrightarrow |H_3|^2 = 48\sqrt{\pi}
\end{aligned}$$

for the Hermite ones.

C.4 Simulation branches

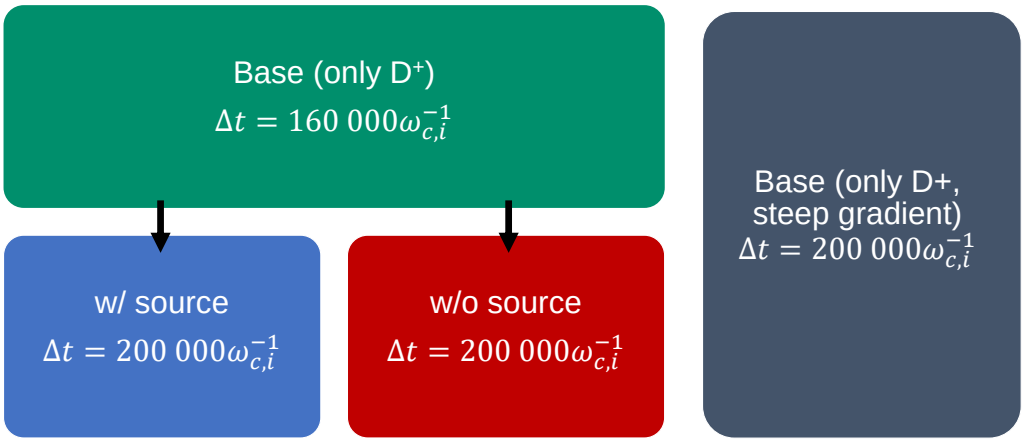

Figure C.2: Visual representation of the simulation branches ran for chapter 3. The total represents around 7 million CPU hours. Since the transport barrier is present from the begining in the steep gradient case, there was no need for multiple branches.

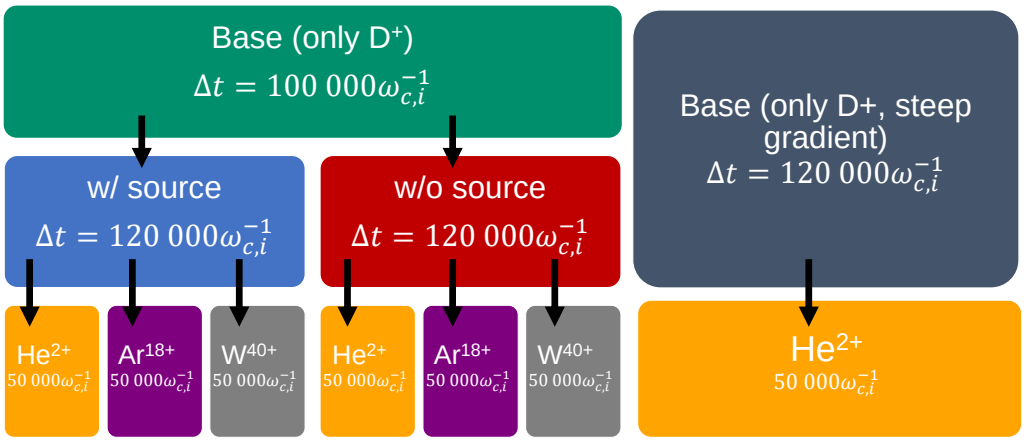

Figure C.3: Visiual representation of the simulation branches ran for chapter 4. The total represents around 5.5 million CPU hours. The reduced amount of CPU hours is due to GYSELA optimizations. For now, only one branch with helium is completed for the steep gradient case.